FATIGUE PROPERTIES OF HEAVILY DRAWN STEEL WIRES

Kasper LAMBRIGHS

Examencomissie:
Prof. dr. ir.- arch. Herman Neuckermans, chairman
Prof. dr. ir. Martine Wevers, promotor
Prof. dr. ir. Bert Verlinden, promoter
Prof. dr. ir. Ignaas Verpoest
Prof. dr. ir. Dirk Vandepitte
Prof. dr. Andrew Godfrey
(Tsinghua University, Beijing, P.R. China)
Dr. ir. Willem Dekeyser
(NV Bekaert SA, Zwevegem)

Dissertation presented
in partial fulfillment of
the requirements for
the degree of
Doctor of engineering

November 2010

ISBN 978-94-6018-273-0
D/2010/7515/112

Voorwoord

Tijdens mijn doctoraatsstudie heb ik kunnen rekenen op erg veel hulp, daarom eerst een woord van dank.

Ik wil mijn promotoren, prof. Martine Wevers en prof. Bert Verlinden, bedanken voor het vertrouwen dat ze in mij gesteld hebben, voor de uitmuntende begeleiding, de waardevolle wetenschappelijke suggesties, de kritische reflecties en voor het nalezen en verbeteren van mijn artikels en het manuscript.

Verder wil ik NV Bekaert SA bedanken voor de ondersteuning van dit project. De samenwerking verliep erg vlot, er was veel ruimte voor overleg. Ik kon steeds met al mijn vragen bij de desbetreffende experts terecht. Speciale dank gaat uit naar dr. Willem Dekeyser voor de goede coördinatie van het project en om tijd vrij te maken voor het manuscript na te lezen en deel uit te maken van de examencommissie.

Graag wil ik mijn assessoren, prof. Ignaas Verpoest en prof. Dirk Vandepitte, bedanken voor de interessante en waardevolle opmerkingen.
Ik zou prof. Andy Godfrey van Tsinghua University willen bedanken om tijd te maken om het manuscript na te lezen en om speciaal naar Leuven te komen voor mijn private en publieke doctoraatsverdediging.

Ook wil ik prof. Herman Neuckermans bedanken om de examencommissie voor te zitten.

Verder bedank ik mijn familie voor de vele kansen die ze mij gegeven hebben en voor de steun.

Om af te sluiten zou ik Kobe Thys nog veel succes willen wensen met de verderzetting van dit project.

Abstract English

The fatigue behavior of heavily drawn steel wires with a diameter ranging from 175 to 300 μm and a total strain of about 3.5 has been studied. It is observed that the fatigue data of heavily drawn steel wires shows a very large scatter compared to normal fatigue data. A fractographical study revealed different fatigue crack initiation mechanisms, resulting into different fatigue lives. Two different crack growth mechanisms were observed, namely short and long crack growth.

A new approach is developed and used to estimate the threshold stress intensity factor range for crack growth ($\Delta K_{th,R}$) which is based on fatigue crack initiations at internal non-metallic inclusions. At these internal crack initiations a characteristic area is formed around the inclusion (in literature this region is called optical dark area, granularly bright facet or facet). This area corresponds to the short crack growth regime. The transition between short and long crack growth, which can be seen clearly by fractography, is used to estimate $\Delta K_{th,R}$.

$\Delta K_{th,R}$ is estimated for different stress amplitudes (σ_a) and load ratios (R). It is observed that $\Delta K_{th,R}$ is independent of σ_a and that the fatigue crack growth is K_{max} controlled for $R < 0.16$ and ΔK controlled for $R > 0.16$. The two asymptotes of the (ΔK, K_{max}) graph, ΔK^*_{th} and K^*_{max}, are calculated to be 3.82 ± 0.09 and 4.47 ± 0.16 MPa$\sqrt{m}$ respectively.

The influence of non-metallic inclusions on the fatigue properties of heavily cold drawn steel wires is studied. Through a fractography study it is possible to link the inclusion properties, such as chemical composition, geometry, size and location, to the fatigue properties.

Comparing the Stress Intensity Factors (SIF) of non-metallic inclusions to the threshold value for crack growth shows that the defect size that should be used to calculate the SIF is larger than the inclusion size itself. This is validated using Scanning Electron Microscopy (SEM) in combination with a Focused Ion Beam (FIB). This SEM/FIB study shows that the region around non-metallic inclusions is characterized by alterations in the microstructure that should be taken into account. It is calculated that the SIF increases with 16.5 ± 3.6 % compared to Murakami's way of calculating SIF of non-metallic inclusions.

Samenvatting (Dutch)

De vermoeiingseigenschappen van sterk vervormde staaldraden met een diameter van 175 tot 300 μm en een totale vervorming van ongeveer 3.5 zijn onderzocht. De vermoeiingslevensduur van deze sterk vervormde staaldraden heeft een zeer grote spreiding. Een fractografiestudie toont aan dat er verschillende scheurinitiatiemechanisme werkzaam zijn die elk een eigen vermoeiingslevensduur hebben. Er zijn twee verschillende scheurgroeimechanismes werkzaam, namelijk korte en lange scheurgroei.
Er is een nieuwe methode ontwikkeld om de drempelwaarde voor scheurgroei ($\Delta K_{th,R}$) te bepalen die gebaseerd is op interne scheuren aan niet-metallische insluitsels. Rond deze insluitsels bevindt zich een zeer ruw gebied dat overeenstemt met de groei van korte scheuren. De overgang tussen het korte en lange scheurgroeigebied kan duidelijk waargenomen worden in de elektronenmicroscoop en wordt gebruikt om $\Delta K_{th,R}$ te bepalen.
$\Delta K_{th,R}$ is bepaald voor verschillende spanningsamplitudes (σ_a) en spanningsverhoudingen (R). $\Delta K_{th,R}$ is onafhankelijk van σ_a en de scheurgroei is K_{max} gecontroleerd als $R < 0.16$ en ΔK gecontroleerd als $R > 0.16$. ΔK^*_{th} and K^*_{max}, de twee asymptoten uit de (ΔK, K_{max}) grafiek, zijn respectievelijk gelijk aan 3.82 ± 0.09 en 4.47 ± 0.16 MPa$\sqrt{m}$.
De invloed van niet-metallische insluitsels op de vermoeiingseigenschappen van sterk vervormde staaldraden is onderzocht. Met behulp van fractografische studies was het mogelijk om verschillende eigenschappen van de insluitsels zoals de grootte, de locatie, de samenstelling en de vorm, te koppelen aan de vermoeiingseigenschappen.
Wanneer de spanningsintensiteitsfactoren (SIF) van de niet-metallische insluitsels vergeleken worden met de drempelwaarde voor scheurgroei blijkt dat de defectgrootte die gebruikt zou moeten worden om de SIF te berekenen groter is dan de grootte van het insluitsel. Dit is gevalideerd met behulp van de elektronen en ionenmicroscoop waaruit blijkt dat het gebied rond de insluitsels scheuren aanwezig zijn en dat het een verschillende microstructuur heeft in vergelijking met de microstructuur in de bulk van het materiaal. Wanneer deze defecten en aangepaste microstructuur worden meegenomen in de berekening van de SIF blijkt dat de SIF 16.5 ± 3.6 % groter zal zijn dan wordt berekend met Murakami's formules.

List of abbreviations

AC	Alternating Current
ANOVA	Analysis Of Variance
APFIM	Atom Probe Field Ion Microscopy
BTA	Benzotrialzole
CE	Carbon Equivalent
EDX	Energy Dispersive X-ray spectroscopy
FCT	Facet
FGA	Fine Granular Area
FIB	Focudes Ion Beam
GBF	Granular Bright Facet
HAC	Hydrogen Assisted Cracking
HCF	High Cycle Fatigue
HELP	Hydrogen Induced Localized Plasticity
HK	Knoop Hardness
HRTEM	High Resolution Transmission Electron Microscopy
LAD	Localized Anodic Dissolution
LC	Long fatigue Crack
LCF	Low Cycle Fatigue
LCL	Lower Confidence Limit
MSC	Microstructurally Short Crack
MVC	Micro Void Coalescence
ODA	Optical Dark Area
PSC	Physically Short Crack
SEM	Scanning Electron Microscopy
SN curve	Stress amplitude – fatigue life curve
SSRT	Slow Strain Rate Test
TEM	Transmission Electron Microscopy
UCL	Upper Confidence Limit
UTS	Ultimate Tensile Strength
VHCF	Very High Cycle Fatigue
XRD	X-Ray Diffraction

List of symbols

a	crack length, depth (fatigue general), longest semi-axis of the ellipse (inclusions)
a_0	El haddad parameter (fatigue general), initial defect depth (Verpoest)
a_f	crack length at failure
a*	critical crack length defined in the unified damage approach
b	shortest semi-axis of the ellipse
c	half of the crack width
d	distance between the crack initiation site and the strongest microstructural barrier
da/dN	crack growth rate (growth increment per cycle)
k_t	stress-concentration factor
m	Paris constant
r	fractional drawing reduction (wire drawing), radius (general)
A	constant
A_0	wire cross-sectional area before drawing
A_1	wire cross-sectional area after drawing
B	constant
C	specific heat (wire drawing), Paris constant (fatigue)
C*	constant
D_0	wire diameter before drawing
D_1	wire diameter after drawing
E	Youngs modulus
$K_{applied}$	applied stress intensity factor
$K_{closure}$	stress intensity due to closure
K_{int}	stress intensity factor due to internal stresses
K_{max}	maximum stress intensity factor
$K_{max,th}$	maximum threshold stress intensity factor
K_{min}	minimum stress intensity factor
K_{total}	total stress intensity factor at the crack tip
K^*_{max}	intrinsic maximum stress intensity threshold according to the unified damage approach
L_0	El Haddad parameter
M	amount of datapoints in the x-direction
N	number of cycles (fatigue), amount of datapoints in the y-direction (roughness measurements)
N_f	cycles to failure
Q	quartile
R	Load ratio
R_a	average roughness
R_p	maximum profile peak height compared to the mean
R_t	difference between the lowest valley and the highest peak
R_v	maximum profile valley depth compared to the mean

T_i	cementite plate thickness at a strain of i
Y	geometrical factor
Z	difference in height compared to the mean plane
α	approach semi-angle of a die (wire drawing), geometrical factor (fatigue)
γ	constant
ε	true drawing strain
ρ	density
λ	Interlamellar distance
σ_a	stress amplitude
σ_{cyc}	cyclic yield stress
σ_d	drawing stress
σ_e	endurance limit
σ_F	fatigue limit
$\bar{\sigma}$	average strength or flow stress of a wire during drawing
Δ	typical parameter for wire drawing
ΔK	stress intensity factor range
ΔK_{dR}	microstructural threshold for crack propagation
ΔK_{th}	threshold stress intensity factor range
$\Delta K_{th,int}$	intrinsic threshold stress intensity factor range
ΔK^*_{th}	intrinsic stress intensity threshold range according to the unified damage approach
ΔK_{CR}	extrinsic component of ΔK that is governed by crack closure
ΔK_{FCT}	stress intensity factor range of the FCT area
ΔT_d	temperature increase due to plastic deformation in a single pass
$\Delta\sigma$	stress range, $\sigma_{max} - \sigma_{min}$
$\Delta\sigma_{e,R}$	conventional fatigue limit for a given R
$\Delta\sigma_{incl,max}$	maximum inclusion stress
$\Delta\sigma_n$	nominal applied stress range
Φ	redundant work factor
$\sqrt{area}$	the root of the area of the fatigue crack projected on the plane perpendicular to the applied load

Table of Contents

Preface III
Abstract IV
Samenvatting (Dutch) V
List of abbreviations VI
List of symbols VII
Table of contents IX

1 Introduction and thesis outline 1
1.1 Introduction 1
1.2 Objectives 2
1.3 Approach 2
1.4 Outline 3
1.5 Contributions to the state of the art 3
2 Literature review 5
2.1 Wire drawing production process 5
2.2 Microstructure of heavily drawn steel wires 9
2.2.1 Lamellae alignment and thinning 9
2.2.2 Cementite decomposition 15
2.2.3 Texture development 16
2.2.4 Localization of plastic flow 17
2.2.5 Dynamic aging 19
2.2.6 Residual stresses 20
2.2.7 Conclusions 22
2.3 Fatigue general 22
2.3.1 Low and high cycle fatigue 22
2.3.2 Fatigue thresholds 28
2.3.3 Short and long fatigue crack growth 32
2.3.4 Unified damage approach 37
2.3.5 Influencing parameters 42
2.3.6 Conclusions 46
2.4 Fatigue of drawn wires 47
2.5 Conclusions 60
3 Materials and methods 61
3.1 Materials 61
3.2 Methods 61
3.2.1 Fatigue tests 61
3.2.2 Fractography 63
4 Fatigue mechanisms 67
4.1 Fatigue crack initiation mechanisms 67
4.1.1 Fracture modes 67
4.1.2 Environmentally assisted fatigue crack initiation 68
4.1.3 Stress concentrations 84

4.1.4 Influence of the fatigue crack initiation mechanism on the fatigue life ... 88
4.1.5 Conclusions ... 91
4.2 Fatigue crack growth mechanisms ... 91
4.2.1 Growth of short and long fatigue cracks ... 91
4.2.2 Environmentally assisted fatigue crack growth ... 98
4.2.3 Conclusions ... 99
5 Fatigue thresholds ... 101
5.1 Threshold determination method ... 101
5.2 Kitagawa-Takahashi diagram ... 103
5.2.1 Threshold determination method ... 103
5.2.2 Short crack growth ... 104
5.3 Conclusions ... 109
6 Surface roughness ... 111
6.1 Experimental methods ... 111
6.1.1 Polishing method ... 111
6.1.2 Roughness measurements ... 113
6.2 Results ... 114
6.2.1 Polishing method ... 114
6.2.2 Fatigue tests ... 117
6.3 Conclusions ... 120
7 Influence of non-metallic inclusions ... 121
7.1 Introduction ... 121
7.2 Inclusions in wire rod ... 122
7.2.1 Wire rod A ... 122
7.2.2 Wire rod B ... 124
7.3 Inclusion properties ... 125
7.3.1 Inclusion size and location ... 125
7.3.2 Inclusion composition ... 131
7.3.3 Inclusion geometry ... 133
7.4 Stress intensity factor calculation ... 134
7.5 Conclusions ... 140
8 Load ratio effects ... 141
8.1 Introduction ... 141
8.2 Influence of the load ratio on the fatigue thresholds ... 142
8.3 Conclusions ... 145
9 Conclusions ... 147
9.1 Results and evaluation ... 147
9.2 Applicability of the results ... 149
9.3 Recommendations for future work ... 150

1 Introduction and thesis outline

1.1 Introduction

High carbon pearlitic steel wires have the highest strength of all mass-produced steel materials. The steel wires are generally produced via several steps of cold drawing from wires containing 0.6 to 0.9 wt. % C. Over the past few years, many efforts have been made to improve the strength, and a maximum experimentally obtained value of 5.7 GPa [1] has been reported.
High carbon pearlitic steel wires are usually twisted together to form steel cords that are used for the radial tires for busses and trucks due to their outstanding strength as well as their acceptable ductility. The steel wires that will be investigated in this study are brass coated steel cord filaments which are supplied by NV Bekaert SA. The filaments are first twisted together to a cord and are used for the carcass of radial tires. Figure 1.1 shows a section of a radial tire.

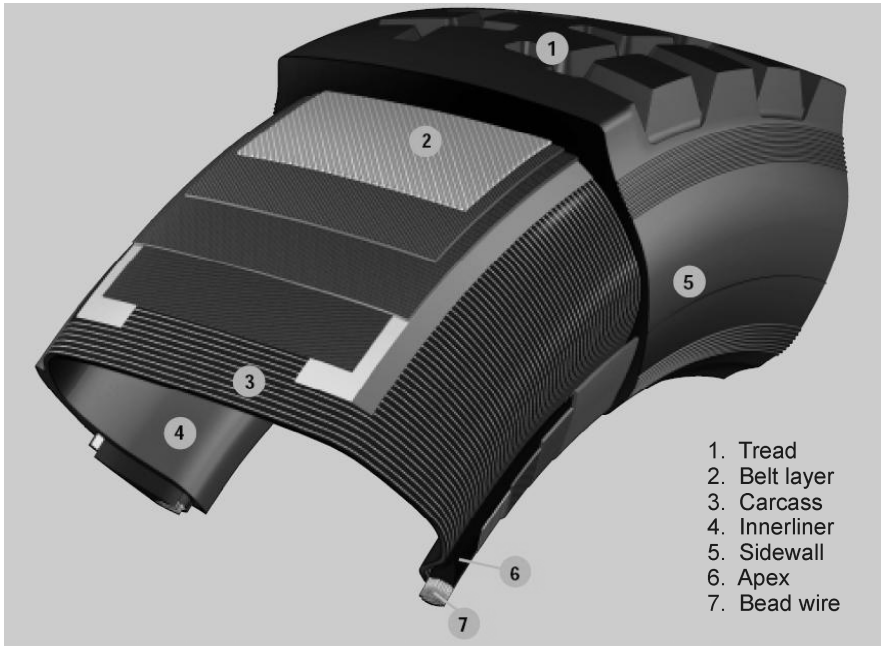

Figure 1.1: Section of a radial tire.

As can be seen in figure 1.1 the carcass of the tire goes from one side of the rim to the other side. In fact, the carcass holds the complete tire together and makes sure that the forces are passed on from the rim to the belt layers and forward on to the road and vice versa. First of all the carcass has to take up the inflation pressure of the tire. Next, when the vehicle starts moving, a dynamic load is

superimposed on the static load. Therefore the dynamic properties of the carcass layer are of crucial importance.
Due to the very complex composite structure of the tire, it is not possible to relate the fatigue properties of the carcass layer to the fatigue properties of the steel cord filaments in a direct way. A lot of influencing factors such as the rubber/steel cord adhesion, the penetration of the rubber into the cords, the fatigue properties of the rubber, the fatigue properties of the cord etc. should be taken into account. Nevertheless, it is chosen to study the fatigue properties of the steel cord filaments in this study since it is believed that, if one wants to obtain good fatigue properties of the carcass layer, it is essential that the fatigue properties of the individual steel cord filaments (which carry the majority of the load) are good.
Therefore the fatigue properties of steel cord filaments are fundamentally investigated in this study. The aim is to understand the fatigue mechanisms that are active for these heavily drawn steel cord filaments, and, if possible, to improve the fatigue properties based on the knowledge gained by the fundamental study.

1.2 Objectives

The objectives of this study are:

- To develop a basic understanding of the fatigue mechanisms that are active in heavily drawn steel wires by investigating the different crack initiation and propagation mechanisms.
- If possible, find ways to improve the fatigue properties of heavily drawn steel wires by the knowledge gained on the different fatigue mechanisms.

1.3 Approach

The approach of the problem is straightforward and is shown schematically in figure 1.2.

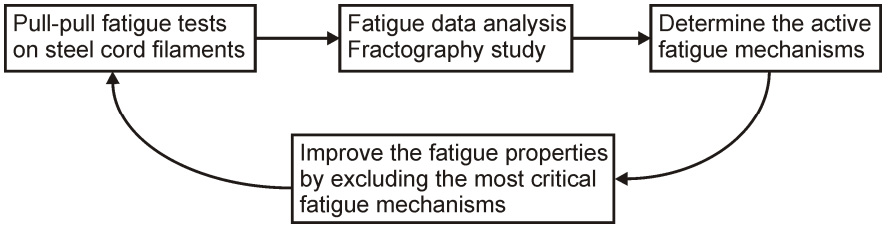

Figure 1.2: Schematic overview of the research approach.

To investigate the fatigue mechanisms of heavily drawn steel wires, pull-pull fatigue tests are performed. Each fatigue fracture surface is investigated in the SEM and if possible, the fatigue crack origin is determined. These data are coupled with the fatigue life of the sample and efforts are made to determine the active fatigue crack initiation mechanism for this fracture. This is repeated for a large number of samples in order to determine the fatigue crack initiation

mechanisms for the investigated batch of wires. Once the fatigue initiation mechanisms are known the most critical fatigue crack initiation mechanism, which leads to the lowest fatigue lives, is determined. If possible the fatigue properties of the wires are improved by excluding the most critical fatigue mechanism. Possibly this can be done by adaptations to the production process or by using another wire rod quality. To validate the improvement, pull-pull fatigue tests are done on the new batch of wires and the approach starts again from the beginning.

1.4 Outline

In chapter 2 a state of the art literature review is given. The emphasis in this literature review is put on the microstructural developments during wire drawing and on the properties of heavily drawn steel wires. Some aspects of fatigue are explained in depth and all relevant articles about the fatigue properties of heavily drawn steel wires are discussed extensively. Chapter 3 describes the used materials and experimental procedures. In chapter 4, all the active fatigue mechanisms are described. Two different fracture modes are observed, namely surface and internal fatigue crack initiation. For surface crack initiations two different fatigue crack initiation mechanisms are active: environmentally assisted fatigue crack initiation and fatigue crack initiation at surface stress concentrations. For internal crack initiations only one fatigue crack initiation mechanism is observed namely fatigue crack initiation at internal stress concentrations. Based on fractographical results and existing literature, two different fatigue crack propagation mechanisms were observed: the growth of short and long fatigue cracks. Chapter 5 describes a newly developed method to determine the fatigue threshold for steel wires based on internal fatigue crack initiation. The influence of the surface roughness is described in chapter 6 and the influence of non-metallic inclusions is investigated in chapter 7. Chapter 8 shows the influence of the load ratio on the fatigue threshold using the unified damage approach. In chapter 9 a general conclusion is given and suggestions for further work are done.

1.5 Contributions to the state of the art

Through multiple experiments it was possible to determine the different fatigue crack initiation mechanisms that are active for the heavily drawn steel wires investigated in this study. Besides the crack initiations at stress concentrations, which are already described in literature, it was observed that fatigue cracks can also initiate due to environmental influences, more particularly due to the presence of chlorides on the wire surface. It was found that this fatigue mechanism is the most critical one active, and, that it always leads to a very fast crack initiation with correspondingly low fatigue lives.

Similar as for high strength steels, the heavily drawn steel wires fracture at internal non-metallic inclusions in the high cycle fatigue regime. In this study, efforts are made to explain the growth of short cracks in the high cycle fatigue

regime. There are two possible crack growth mechanisms for short cracks, namely the existence of a single fatigue threshold in combination with internal stresses (unified damage approach), and mixed mode crack growth. Due to a lack of experimental evidence none of both short crack growth mechanisms could be excluded. It is important to note that it is possible that a combination of both mechanisms is active, as is described in chapter 5.

Based on experimental results it was possible to model the complete crack growth region based on the equation according to Paris, but with different C and m values for the short and the long crack growth regime. The C and m values were calculated for both wires that were used in this study and an equation is derived to calculate the complete fatigue life of these wires.

The influence of non-metallic inclusions on the fatigue properties of heavily drawn wires was investigated. Besides the influence of the inclusion size and location, it was also possible to observe some trends for the inclusion composition and geometry.
Through an extensive experimental investigation of the microstructure around non-metallic inclusions it was observed that microcracks can be present around inclusions in drawn steel wires. Further it was observed that the microstructure around the inclusions was different from the bulk of the wire. Based on these observations and on a discrepancy between the fatigue data and the threshold value for long crack growth it was concluded that the actual defect size of an inclusion that is used to calculate ΔK is about 18% larger than the inclusion size itself. Therefore, an adaptation of Murakami's formula is suggested for heavily drawn steel wires.

Since crack growth rate measurements are not applicable for such small diameter wires, a new method was developed to determine the threshold value for long crack growth. This method is based on internal fatigue crack initiations and was experimentally validated. This method was used to determine the influence of the load ratio (R) on the fatigue threshold. It was possible to determine the two intrinsic threshold values, ΔK^*_{th} and K^*_{max}, for one of the wires investigated in this study (unified damage approach).

2 Literature review

2.1 Wire drawing production process

In the wire drawing process the cross-sectional area of a wire is reduced by pulling it through a die (figure 2.1), creating a long product with a constant cross section that has an excellent surface finish and closely controlled dimensions. Drawing is usually conducted at room temperature using a number of passes or reductions through consecutively located dies. Annealing may be necessary after a number of drawing passes before the drawing operation is continued in order to eliminate the effects of strain hardening (reducing the flow stress and increasing the ductility). During wire drawing the deformation is accomplished by a combination of tensile and compressive stresses that are created by the pulling force (applied at the exit of the die) and by the die geometry.

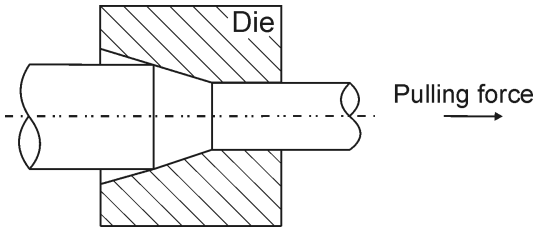

Figure 2.1: Wire drawing principle.

From a theoretical point of view the pulling force (or drawing stress) is limited by the strength of the wire that is being drawn in order to avoid fracture or unstable deformation behavior during wire drawing. Practical considerations however limit the drawing stress to about 60% of the wire strength. This means that in practice the area reduction per drawing pass rarely exceeds 30%. Therefore it is necessary to apply many reductions or drawing passes to achieve a large overall reduction.

A typical drawing die is shown in figure 2.2 [2]. The wire makes contact in the drawing cone along the approach angle and is reduced to the dimensions of the drawing cone exit. The bearing area involves no further reduction and allows the die to be refinished without a change in the exit dimensions of the drawing cone. The back relief reduces the amount of abrasion that takes place if the drawing stops or if the die is out of alignment. A lubricant is introduced at the bell portion of the die and is pulled into the die/wire interface by the moving wire.

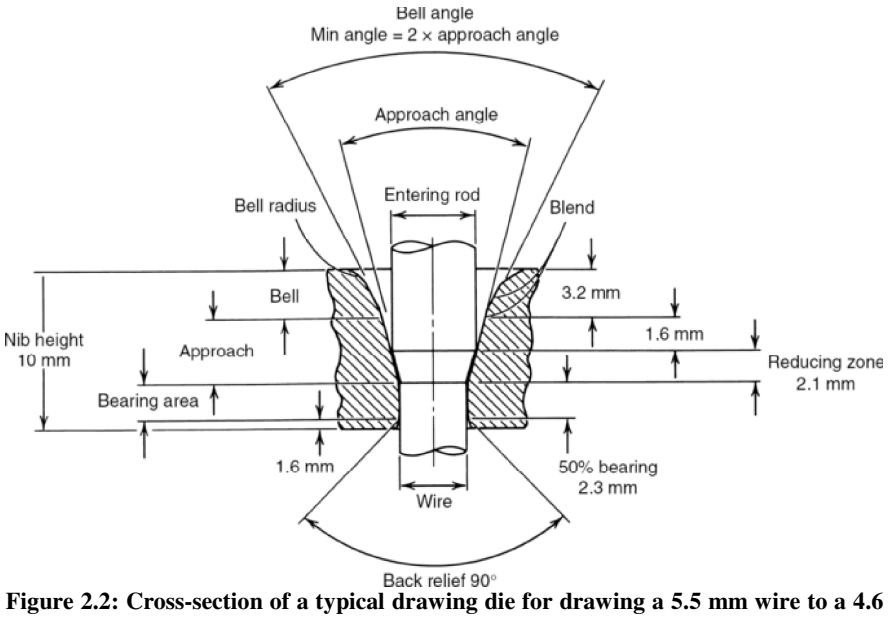

Figure 2.2: Cross-section of a typical drawing die for drawing a 5.5 mm wire to a 4.6 mm wire [2].

The approach angle is perhaps the most important feature of the die. The effect of the approach angle on the material flow cannot easily be considered independent of the drawing reduction. Therefore modern drawing theory incorporates both into the Δ parameter [2]:

$$\Delta \approx \left(\frac{\alpha}{r}\right)\left[1+\left(1-r\right)^{1/2}\right]^2 \tag{2.1}$$

where α is the approach semi-angle (half the included angle) in radians and r is the fractional drawing reduction given by:

$$r = 1 - \frac{A_1}{A_0} \tag{2.2}$$

where A_0 and A_1 are respectively the starting and finishing cross-sectional areas. In most publications the true drawing strain ε is used to indicate the level of reduction.

$$\varepsilon = \ln\frac{A_0}{A_1} = 2\ln\frac{D_0}{D_1} \tag{2.3}$$

where D_0 and D_1 are respectively the starting and the finishing wire diameters.

Commercial die design often involves approach semi-angles in the range of 4 to 10° and drawing reductions of about 20% [2]. The corresponding Δ values typically range from 1.5 to 3, with higher values corresponding to lower reductions and higher die angles, and lower values corresponding to higher reductions and lower die angles.
Basically, low Δ values may involve excessive frictional work between the wire and the drawing cone, and high Δ values involve redundant work (work that isn't used for wire diameter reduction) or plastic strain beyond that calculable from the reduction in area of the pass. Some degree of redundant work exists for $\Delta > 1$. The redundant work increases when Δ increases and the frictional work will increase as Δ decreases. The net effect is that some intermediate value of Δ involves the minimum work and therefore the minimum drawing force. This is the case because the drawing force multiplied by the drawing velocity is the work consumed per unit time (power). Similarly, the drawing stress equals the work per unit volume of wire drawn. The Δ value for a minimum drawing stress [2] can be approximated by:

$$\Delta_{\min} \approx 4.9\left[\frac{\mu}{\ln\left(1/1-r\right)}\right]^{1/2} \tag{2.4}$$

where μ is the coefficient of friction between the wire and the drawing cone. The drawing stress σ_d [2] can be approximated by:

$$\sigma_d \approx \sigma_f\left(\frac{3.2}{\Delta}+0.9\right)\left(\alpha+\mu\right) \tag{2.5}$$

where σ_f is the flow stress of the wire during the drawing pass. Siebel [3] estimates the drawing stress using equation 2.6. Siebel's formula results in an estimated drawing stress that is about 10% larger than the one estimated by equation 2.5.

$$\sigma_d \approx \sigma_f\left[\varepsilon+\left(\frac{\mu}{\alpha}\right)\cdot\varepsilon+\left(\frac{2}{3}\right)\alpha\right] \tag{**2.6**}$$

The redundant work is expressed in terms of the redundant work factor or the ratio of total plastic deformation work to the work imposed by dimensional change. Experimental studies suggest that the redundant work factor Φ [2] can be estimated to be:

$$\Phi \approx \frac{\Delta}{6}+1 \tag{2.7}$$

Hosford and Caddell [4] used the redundant work factor to estimate the drawing force (equation 2.8). It is important to note that α is in degrees in equation 2.8.

$$\sigma_d \approx \Phi \cdot \sigma_f \cdot \varepsilon \left(1 + \mu \cdot \text{cotg}\alpha\right) \qquad (\alpha \text{ in degrees}) \qquad \textbf{(2.8)}$$

The management of heat is of great concern in drawing because practical cold-drawing operations can involve that the wire temperature increases a few hundred degrees Celsius. Much heat is generated directly by the plastic deformation, and this heat is only partially removed by interpass cooling. The dies extract little heat under commercial conditions and become very hot. Under adiabatic conditions, the temperature increase ΔT_d associated with plastic deformation in a single pass is approximately:

$$\Delta T_d = \frac{\Phi \cdot \bar{\sigma} \cdot \ln\left(\frac{1}{1-r}\right)}{C \cdot \rho} \qquad (2.9)$$

where C and ρ are respectively the specific heat and density of the wire. Additional heat generation is associated with frictional work. This heat is concentrated at the die-wire interface and can lead to diminished lubrication, further heating, and catastrophic lubricant breakdown. Accompanying problems include poor wire surface quality and metallurgical changes near the wire surface. If the coefficient of friction is not influenced by Δ, frictional heating is aggravated by low Δ processing. Fortunately, there is a tendency for low approach angles (and thus low Δ) to foster hydrodynamic lubrication and a reduced coefficient of friction [2].

A typical commercial wire drawing production process of (hyper) eutectoid steels consists of following steps:

1. Chemical or mechanical descaling
2. Dry wire drawing
3. Patenting (intermediate heat treatment)
4. Brass coating
5. Wet wire drawing

The *descaling* process is done before cold drawing to prevent damage to the wire surface or the drawing die during cold drawing. The wire rod (starting material) must first be cleaned of surface contaminants, such as glass and heavy rust. This cleaning process can be done by chemical pickling, where an acid is used to remove the surface contaminations, or by mechanical descaling, where the surface layer of the wire rod is mechanically removed by scraping.
The *dry drawing* process is normally used for wire with a diameter that is larger than 0.5 mm and for which the relatively rough surface produced is acceptable.

The lubricant is usually a dry soap powder, placed in a die box and picked up by the wire surface upon its passage through the box.
After the dry drawing a *patenting* heat treatment is necessary to eliminate the effects of strain hardening. The wire is uncoiled and heated to the austenite region to obtain a complete austenite microstructure. The wire is then cooled rapidly from above the austenite transformation range in a molten medium (usually lead at about 540 °C) for a period of time sufficient to allow complete transformation to a fine pearlitic structure. Salt baths and fluidized beds have also been used for this purpose. In any case, this treatment increases considerably the amount of subsequent wire-drawing reduction that the product can withstand and permits the production of high-strength wire. Successive drawing and patenting steps can be used to obtain the desired size and strength level.
In some cases the wires are *brass coated* before the wet wire drawing (the wires that were investigated in this study are brass coated steel wires). The brass coating has a two-fold function: lubrication and adhesion (not related to the wire drawing process). Since the brass coating is much softer than the steel wire itself it acts as some kind of lubricant during the wet wire drawing process, ensuring a smooth deformation. The adhesion properties of the brass coating are only important when the steel wires are used as steel cord in tire applications. In these applications the brass coating will react with the sulfur in the rubber and provide a strong interlocking between the rubber and the steel wire.
The *wet wire drawing* is normally used for smaller diameter wires (less than 0.5 mm). The drawing process itself is performed in a bath of lubricant (oil-based or aqueous). Hereby it is important to note that the lubricant is not only chosen for its tribological properties but also for its cooling properties.

2.2 Microstructure of heavily drawn steel wires

Due to the severe plastic deformation which is applied during wire drawing, the microstructure will evolve from randomly oriented pearlite colonies (after the patenting heat treatment) to a strongly oriented nanoscale microstructure. Since this change in microstructure is responsible for the exceptional mechanical properties of heavily drawn steel wires, the microstructural development during wire drawing is described in depth. Lamellae alignment and thinning, cementite decomposition, texture development, localization of plastic flow, dynamic aging and residual stress development are relevant processes occurring in heavily drawn steel wires and are described in the following paragraphs.

2.2.1 Lamellae alignment and thinning

Although the microstructural evolutions during wire drawing were already described successfully by G. Langford [5] and G. Sevillano et al. [6] this part of the literature review is mostly based on the work of X. Zhang et al. [7] since they studied the microstructural evolutions of pearlitic steel wires during wet wire drawing on a very similar wire as was used in this PhD study. They used a high strength near eutectoid steel with a carbon content of 0.7 wt.% which was supplied by NV Bekaert SA. Microstructural investigations were performed at

various steps of the overall wire drawing process from the as patented wire (1.26 mm) to the final drawn wire (0.2 mm).
The microstructural developments of heavily drawn steel wires find their origin in the very fine pearlitic microstructure which is obtained by the intermediate patenting heat treatment. This microstructure is taken as a reference state at a strain (ε) of 0.
Figure 2.3 shows the longitudinal and the transverse section of the wire in the as-patented condition. It is observed that the cementite plates within each pearlite colony are not parallel or continuous. X. Zhang et al. [7] suggest that this could be related to the patenting process for which a high speed is used. This makes sure that the transformation from austenite to pearlite is completed quickly. As a result two types of pearlite can be observed in the microstructure: plate-like pearlite and particle-like pearlite. The particle-like pearlite represents a 2D-section through cementite with a rod like morphology. It was observed that these two types can exist within one pearlite colony (indicated with the arrow in figure 2.3). The majority of the cementite is, however, of the expected plate-like morphology.

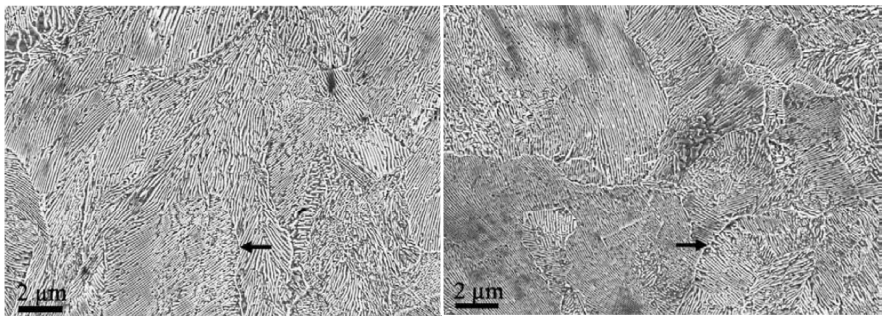

Figure 2.3: SEM image of longitudinal (left) and transverse (right) section of a wire in the as patented condition (ε = 0) [7].

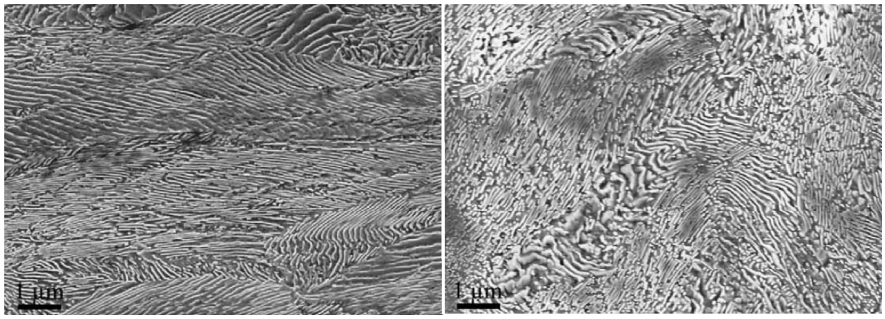

Figure 2.4: SEM image of longitudinal (left) and transverse (right) section of a wire at ε = 0.7 [7].

Figure 2.4 shows the longitudinal and the transverse section of the wire at a strain of 0.7. It is observed that the cementite plates have begun to rotate into the

drawing direction. In the transverse section, the twisting (curling) is severe and break-up of the cementite plates takes place.

For a drawing strain of 1.5 (figure 2.5) almost all the cementite plates have rotated to the near drawing direction and have stretched to such a degree that 97% of the cementite in the longitudinal section has an angle with respect to the drawing direction that is smaller than 30°. In the transverse section a typical curled structure can be observed clearly. X. Zhang et al. [7] also observed some cracks parallel to the drawing direction in the longitudinal section.

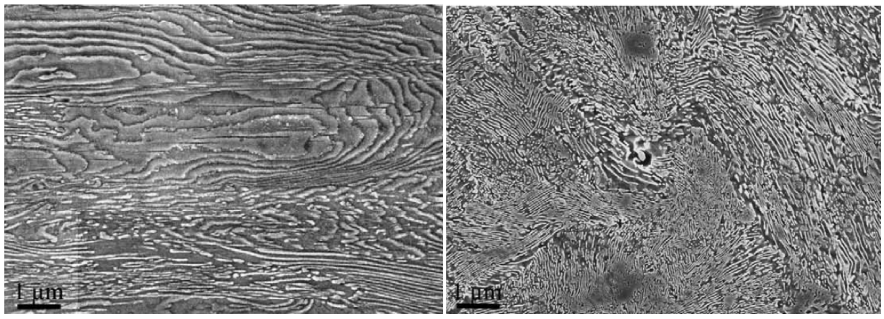

Figure 2.5: SEM image of longitudinal (left) and transverse (right) section of a wire at ε = 1.5 [7].

At a strain of 2.7 (figure 2.6) it is observed that in the longitudinal section all the cementite plates have rotated to near the drawing direction and that they are greatly stretched compared to the lower strains. In the transverse section the twisting of cementite is severe and the cementite plates are much thinner compared with those seen at strain 1.5. The typical curling morphology is obvious. In some places where the cementite plates are comparatively long (above 1 μm) shear bands are seen to develop across the cementite plates (inset on the right side of figure 2.6).

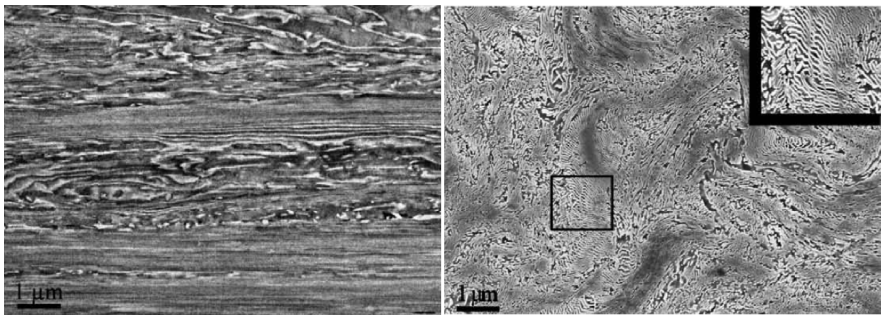

Figure 2.6: SEM image of longitudinal (left) and transverse (right) section of a wire at ε = 2.7 [7].

Zelin [8] calculated the evolution of the angle (α) between the longest pearlite colony axis and the wire axis based on the uni-axial stretching law (figure 2.7). The α angle determines the pearlite colony orientation. These calculated results correspond well with the above described experimental observation of X. Zhang et al. [7].

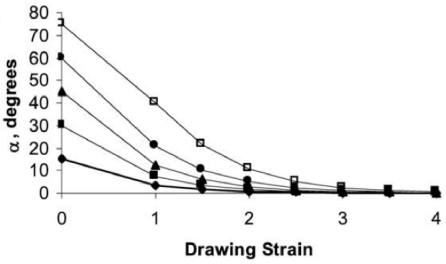

Figure 2.7: Evolution of the α angle as a function of the drawing strain predicted by the uni-axial stretching law for plates with different original orientations [8].

X. Zhang et al. [7] observed that the thickness of the cementite plates as a function of drawing strain decreases to the same extent as can be expected from the geometrical reduction due to the change in wire diameter (figure 2.8). The experimentally measured values from figure 2.8 are based on TEM observations and calculated using equation 2.10 under the assumption that the deformation is homogeneous throughout the wire and that the cementite deforms in proportions to the drawing strain.

$$T_i = T_0 e^{(-\varepsilon/2)} \tag{2.10}$$

Where T_0 and T_i are the cementite plate thickness at a strain of 0 and i. Figure 2.8 shows that the cementite plate thickness decreases from 19 nm in the as patented condition (ε = 0) to 2 nm at a strain of 3.7.

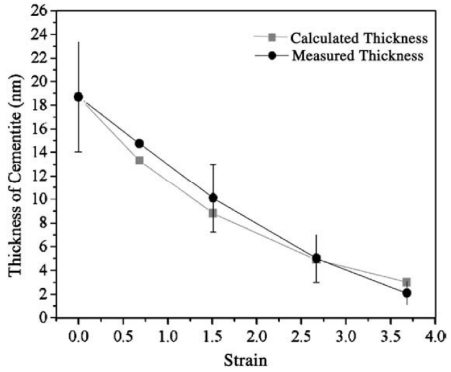

Figure 2.8: Cementite plate thickness as a function of drawing strain [7].

M. Zelin [8] also described the evolution of the cementite plate thickness during wire drawing of a steel with a carbon content of 0.8 – 0.96 wt.%. As can be seen in figure 2.9 the same degree of thinning during wire drawing as X. Zhang et al. [7] was observed. The measured thickness is based on TEM measurements of Taniyama et al. [9] while the calculated values are calculated with equation 2.10 for uni-axial stretching and equation 2.11 for plain strain stretching. Zelin [8] also observed that the uni-axial tension approach corresponds well with the experimental results. In the wire drawn to a strain of 3.7 the thickness of ferrite and cementite plates is approximately 10 and 2 nm. Assuming a lattice parameter of 2.8 Å for ferrite and 4.5 Å for cementite [10] this corresponds to approximately 40 atoms and 5 atoms, respectively. Such a small thickness of ferrite/cementite plates should have an important effect on properties of heavily drawn steel wires.

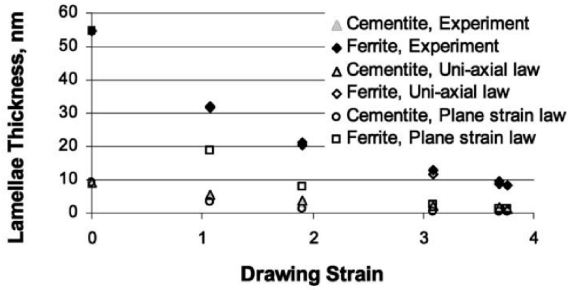

Figure 2.9: Cementite and ferrite plate thickness as a function of the drawing strain [8].

$$T_i = T_0 e^{-\varepsilon} \tag{2.11}$$

Figure 2.10 shows two example TEM images of the wire drawn to a strain of 0 and 0.7.

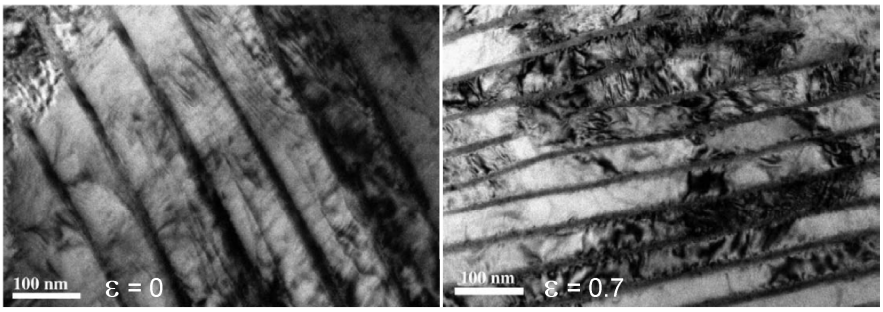

Figure 2.10: TEM images showing cementite plates in an edge-on condition at strains of ε = 0 and ε = 0.7 [7].

The observations of Borchers et al. [11] do not correspond completely with the observations of Zhang et al. [7] and Zelin [8]. They reported that the

microstructure of a wire that is drawn to a strain of 3.46 is a partially amorphous nanocomposite consisting of amorphous fibers (the former cementite lamellae) in a supersaturated ferrite matrix. The amorphization of the cementite is governed by the decrease in carbon concentration of the ferrite which is described extensively in literature as cementite dissolution (paragraph 2.2.2).
Figure 2.11 shows a TEM image of a wire drawn to a strain of 0.93 and 3.46. The cementite can be indentified as the thin grey filaments that separate the ferrite lamellae for both strains.

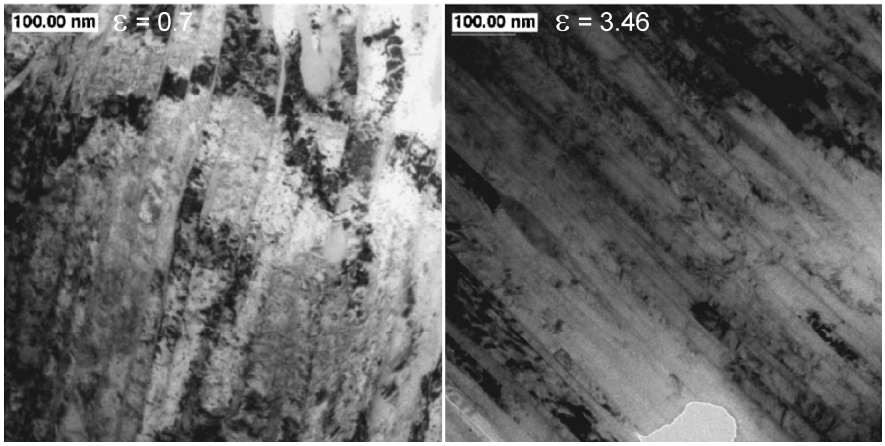

Figure 2.11: TEM image of a wire drawn to a strain of 0.93 (left) and 3.46 (right) [11].

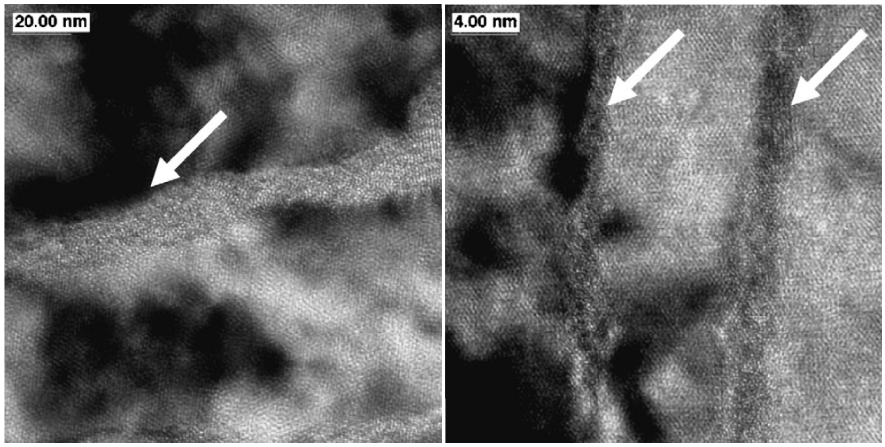

Figure 2.12: HRTEM image of a wire drawn to a strain of 3.46. Left: two ferrite grains separated by a strip of amorphous material (white arrow). Right: three ferrite grains separated by thin strips of amorphous or nanocrystalline material (white arrows) [11].

A more in depth analysis of the cementite phase using high resolution TEM (figure 2.12) shows that the ferrite grains are separated by an amorphous or

nanocrystalline material (former cementite). The partial amorphization of the cementite was also observed by Tarui et al. [12].

Hono K. et al. [13] reported that when a wire is drawn to a strain of 5.1 almost no cementite lamellae are observed, leaving a nanoscale microstructure that is only composed of ferrite fibers supersaturated with carbon. This means that at these very high strains almost all cementite is dissolved. In the next paragraph the dissolution of cementite is described thorough.

2.2.2 Cementite decomposition

In the last two decades a number of studies have focused on the importance of understanding the evolution of the cementite phase during wire drawing [7,8] and especially on the possible dissolution of the cementite phase [11,13-23]. The studies on cementite dissolution are mostly based on (3D) atom probe field ion microscopy (APFIM) of the carbon concentration in the cementite, which is generally found to be lower than the expected stoichiometric value of 25 at.% for heavily drawn steel wires [11,13,14,21,12,24]. These results were validated by thermomagnetic analysis, Mössbauer spectroscopy and internal friction measurements [15,17].

Two possible mechanisms for the dissolution of the cementite are proposed, namely the interactions between dislocations and carbon atoms in the ferrite phase or the destabilization of the cementite due to the increase of its interfacial energy. In both mechanisms, the carbon atoms move across the interface to realize the dissolution.

Most studies found experimental data which suggest that cementite decomposition is controlled by the transfer of carbon atoms from cementite to dislocations accumulated near the interface during deformation. Hong et al. [14] and Gavriljuk [25] both observed that the binding enthalpy between carbon atoms and dislocations in ferrite exceeds the solution heat of cementite, Gavriljuk [17] experimentally observed that the fraction of the cementite decomposed increases with the increase of the interfacial area between ferrite and cementite and Sauvage et al. [21] experimentally showed the existence of C atmospheres around dislocations.

Hong et al. [14] showed that the C distribution in deformed ferrite is not uniform and ranges from 0.2 to 3 at.%. For a small interlamellar spacing the C content varies between 2-3 at.% and for a big interlamellar spacing between 0.2-2 at.% while undeformed ferrite has a C content of only 0.07 at.%. The oversaturation of C results from the dissolution of cementite that has a C content < 18 at.% after wire drawing. This heterogeneous dissolution of carbon in ferrite confirms that carbon is segregated to dislocations or dislocation pile-ups.

There is however one article [23] that concluded that the destabilization of the cementite due to the increase of its interfacial energy is the most probable mechanism for the cementite decomposition. They based their conclusion on the observation that the spacing between the cementite lamellae affects their stability to dissolution. It is however not possible to explain the observed saturation in the dissolution at large strains by the destabilization mechanism, as was discussed in

detail by Gavriljuk [25]. In this discussion it was concluded that, based on the experimental results of Nam et al. [23], the strong interaction between carbon atoms and dislocations at the interface is the most probable reason for the decomposition of the cementite lamellae.
The observations of Umemoto et al. [18] question both proposed mechanisms based on the experimentally observed complete dissolution of cementite particles (± 0.5 μm) during a ball drop experiment on eutectoid specimens. Due to the very short time in which the cementite dissolves completely, a possible diffusionless transformation of the cementite is suggested.

Hono et al. [13] reported that when a wire is drawn to a strain of 5.1 almost all cementite lamellae are decomposed, leaving a nanoscale microstructure that is only composed of ferrite fibers supersaturated with carbon. This nanoscale fiber structure is responsible for the high strength of these wires. Borchers et al. [11] observed the same microstructure for a wire that was drawn to a strain of only 3.46. They described it however as a partially amorphous nanocomposite consisting of amorphous fibers (the former cementite lamellae) in a supersaturated ferrite matrix. They proposed a new mechanism to explain their observation which is based on the destabilization of the cementite by the C segregation to vacancies in the ferrite phase.

Some recent studies show the relation between cementite decomposition and some mechanical properties [20,26]. It was observed that the bending fatigue resistance and the torsional ductility are strongly degraded by the presence of dissolved cementite. It was also found that the lamellar spacing is the major factor in determining torsional ductility and tensile strength.

Up to this moment no consensus is reached on the active mechanism for the dissolution of the cementite lamellae in heavily deformed pearlite. The possible mechanisms are:
- The interactions between dislocations and carbon atoms in the ferrite phase.
- Destabilization of the cementite by the C segregation to vacancies in the ferrite phase.
- A diffusionless transformation of the cementite.

2.2.3 Texture development

Due to the wire drawing process both a metallographic and crystallographic texture is formed. The evolution of the metallographic texture has already been described in paragraph 2.2.1, the crystallographic texture will be described in this paragraph.
It is well documented that an axial [110] texture develops during wire drawing of pearlitic steels. Work performed on relatively large diameter wires [6,27] indicates that a [110] fiber texture results in an alignment of (001) planes, which are cleavage planes in ferrite, along the wire axis. These cleavage planes enhance crack propagation. Heizmann et al. [28] reported that a cyclic texture can develop

in the surface layers and at the wire center and that this can possibly also contribute to delamination under torsion loading.
The development of a strong crystallographic texture results in anisotropic mechanical behavior. Zelin [8] showed this by doing micro-hardness indentations with a Knoop diamond indentor on a drawn wire (Figure 2.13). It was measured that the micro-hardness is 900 HK in the direction perpendicular to the wire axis and only 760 HK parallel to the wire axis. This difference in micro-hardness can be attributed to a larger number of interlamellar interfaces acting as barriers for dislocation movement in a normal direction as compared with axial direction.

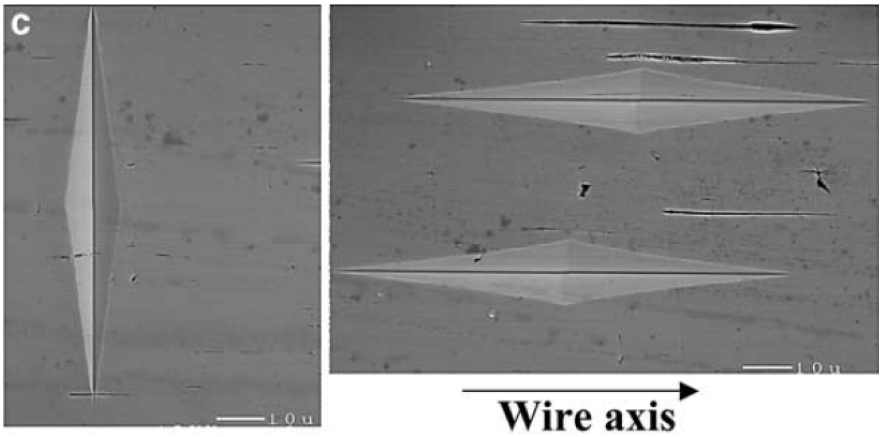

Figure 2.13: Indentations imprinted on a pre-polished surface by using a Knoop diamond pyramid along and normal to the wire axis [8].

2.2.4 Localization of plastic flow

The observed changes in lamellae dimensions and alignment suggest that the cementite plates deform during the wire drawing process. Zhang et al. [7] studied the deformation mechanisms behind the changes in the cementite plate morphology (figure 2.14) by performing local SEM/EBSD measurements.
Figure 2.14 shows the traces of the {110} and {112} slip planes in ferrite in a longitudinal section in a wire that is deformed to a strain of 0.7. Trace analysis show that in colony A and colony C local shear bands develop that are parallel to the $(\bar{1}01)$ slip plane trace in the ferrite, and that in colonies B, D and E shearing occurs in more than one direction, though in each case still parallel to either a {110} or {112} ferrite slip plane trace. It was concluded that slip initially takes place in the ferrite lamellae and is then transferred into the cementite lamellae. The conclusions were based on the observations of coarse slip, shear bands and cracks across cementite plates parallel to $\{110\}_{\alpha-Fe}$ and $\{112\}_{\alpha-Fe}$ planes.
Zelin [8] observed that the plastic deformation during wire drawing is non-uniform and that two systems of localized shear bands formed by coarse slip and fine slip surfaces are oriented between 30 and 45° with respect to the drawing direction. Based on microstructural investigations and finite element modeling it

was concluded that the localized shear bands divide the material into cells with a size that is comparable with the former austenite grain size and that the spacing of the localized shear bands decreases with increasing drawing strain.

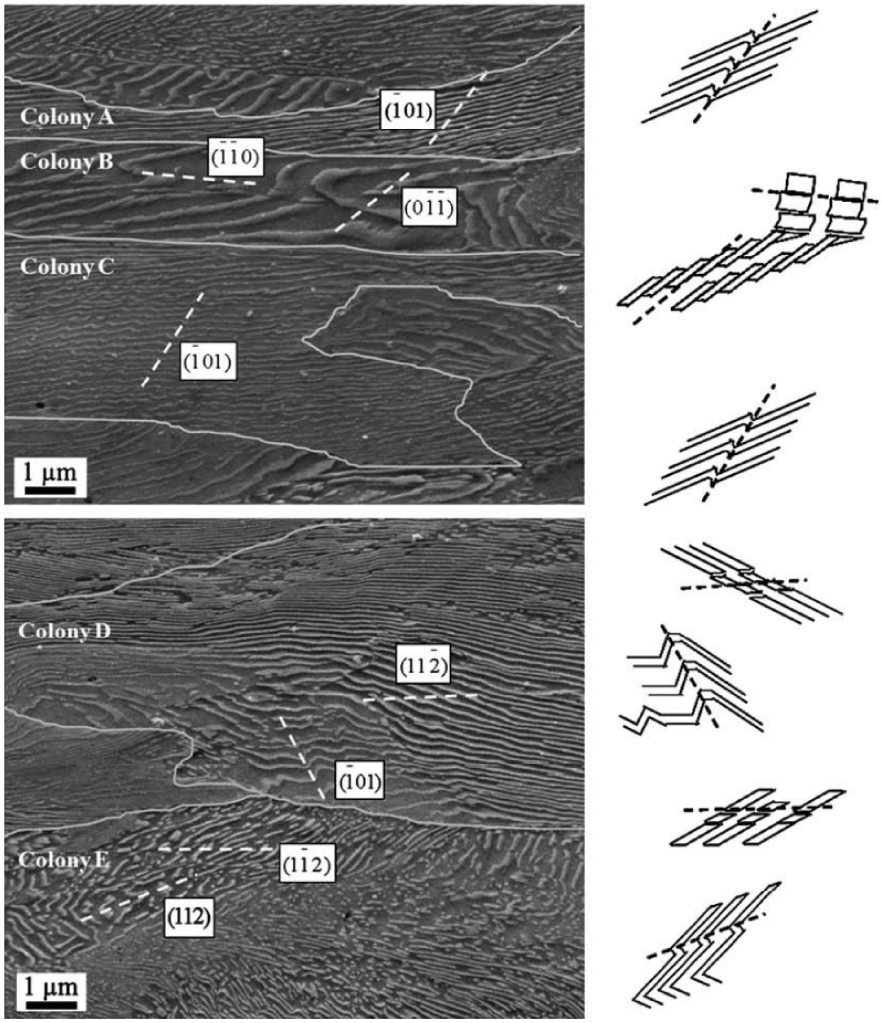

Figure 2.14: SEM micrographs showing cementite morphology at strain ε=0.7 (longitudinal section). The thick grey lines are added to indicate pearlite colony boundaries with a misorientation angle higher than 15°. The dashed white lines show the crystallographic orientations inside the pearlite colonies. The right side of the figure gives a schematic illustration of the possible deformation mechanisms of the cementite together with the crystallographic orientations [7].

2.2.5 Dynamic aging

The dissolution of cementite results in an oversaturation of ferrite by carbon atoms. This oversaturation of carbon atoms in combination with the increased wire temperature during wire drawing (150 – 250 °C) causes dynamic aging. Zelin [8] reported that dynamic aging increases the ultimate tensile strength (UTS) and decreases the ductility with approximately 5 % (figure 2.15). This aging also increases the susceptibility to delamination. Figure 2.16 shows the different fracture behavior of a wire that is drawn with different wire drawing speeds. The left side of the figure shows that the wire that is produced with a low drawing speed doesn't delaminate under torsional loading. The right side shows a clear delamination of a wire that was produced at a high drawing speed. The higher drawing speed causes a higher wire temperature during the production process which accelerates the aging and causes delamination.

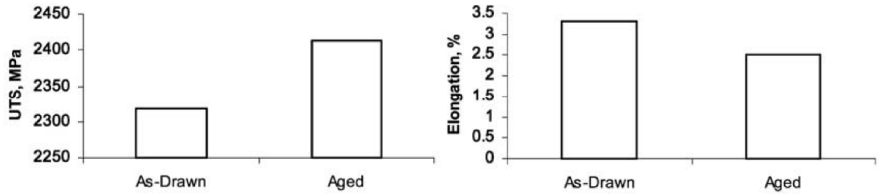

Figure 2.15: Ultimate tensile strength and elongation to failure of an as drawn and an aged wire [8].

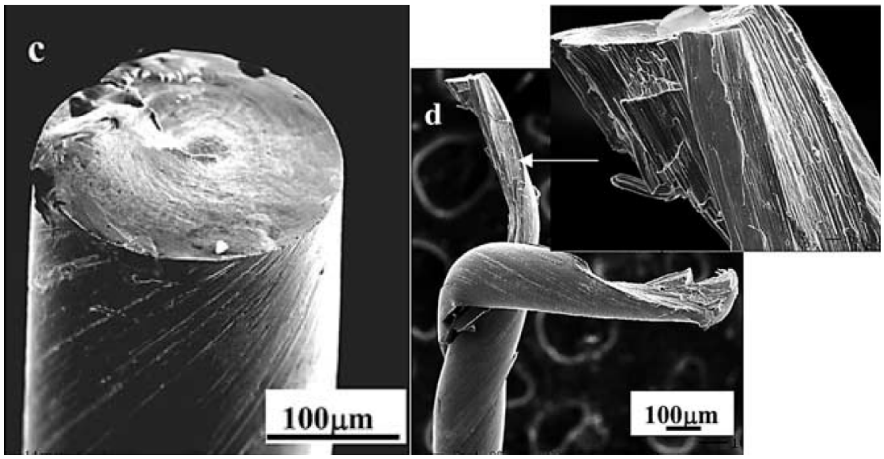

Figure 2.16: Delamination behavior of a wire produced with a low (left) and high (right) drawing speed under torsional loading [8].

2.2.6 Residual stresses

Steel wires are subjected to large plastic deformations during the drawing process. After drawing, strains tend to recover but when they are obstructed somewhere by previous plastic deformation, a field of residual strains and stresses can appear.

The residual stresses can be modeled, using finite element modeling, and measured using X-ray or neutron diffraction. The average macroscopic residual stresses in pearlite eutectoid steels are difficult to measure because the diffraction techniques provide separate values for the ferrite and the cementite phase. Further, the diffraction peaks of cementite are very weak and hard to interpret. The severe plastic deformation that is applied during the wire drawing further increases the difficulties.

Van Acker et al. [29] measured the average residual stress in the cementite and ferrite phase of two drawn wires with a total strain of 1.96 and 2.59 using neutron diffraction measurements. They observed that the residual stress inside the cementite phase is highly tensile, with values of 2000 MPa for the wire drawn to a strain of 1.96. In the ferrite phase the residual stress is compressive with values around -140 MPa. This phase microstress was found to be uniform throughout the wire cross section. For the wire drawn to a strain of 2.56 it was observed that the stresses in the cementite phase are lower, about 1750 MPa.

Elices [30] investigated the influence of residual stresses on some mechanical properties of cold drawn pearlitic wires that are drawn to a strain of 0.2. He found that the presence of residual stresses due to standard cold drawing (tensile stresses on the surface) favors the onset of yielding (figure 2.17) by the comparison of as drawn wires with wires that had a treatment to lower the residual stresses. One wire was further drawn with a very small area reduction (skin-pass – about 1%) and the other wire was heated and stretched at the same time (400 °C under a tensile load of 0.4 UTS). It was observed that the higher the residual stresses, the lower the yield stress is in a tensile test.

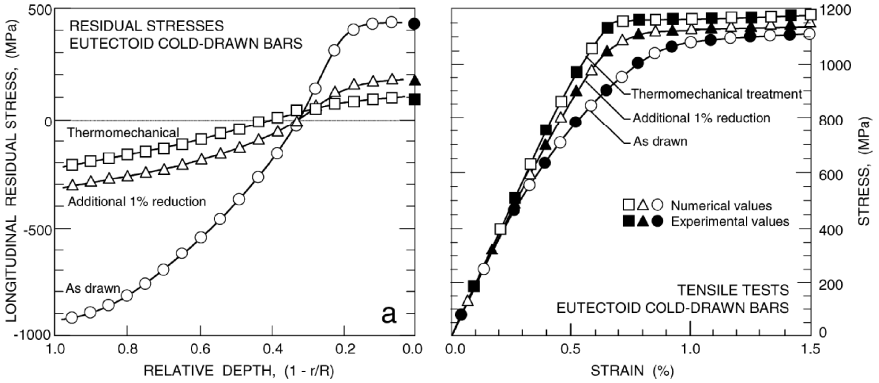

Figure 2.17: Left: profile of computed longitudinal residual stresses. Right: measured and computed stress strain curve for the three types of wires [30].

Elices [30] experimentally showed that there exists a clear relationship between stress relaxation and the presence of residual stresses: stress relaxation increases with the increase of surface tensile residual stresses.
Since the development of a fatigue crack (initiation stage) from the wire surface in the high cycle fatigue regime determines the fatigue life, it is necessary to acquire an accurate knowledge of the surface stresses which are determined by external loads and residual stresses. It is observed that the fatigue life in the high stress range shows little influence of the residual stresses. Around the threshold value however, the fatigue life shows a strong dependence on the residual stresses. Katagiri et al. [31] also observed that residual stress is one of the controlling parameters of the fatigue threshold.
Yang et al. [32] determined the residual stress profile in the ferrite phase of wires that were drawn to a total strain of 1.8 by the use of X-ray diffraction (XRD) and the layer removal technique. Figure 2.18 shows the stress profiles as a function of the relative depth (r/R) in the cold drawn wire along the different directions.

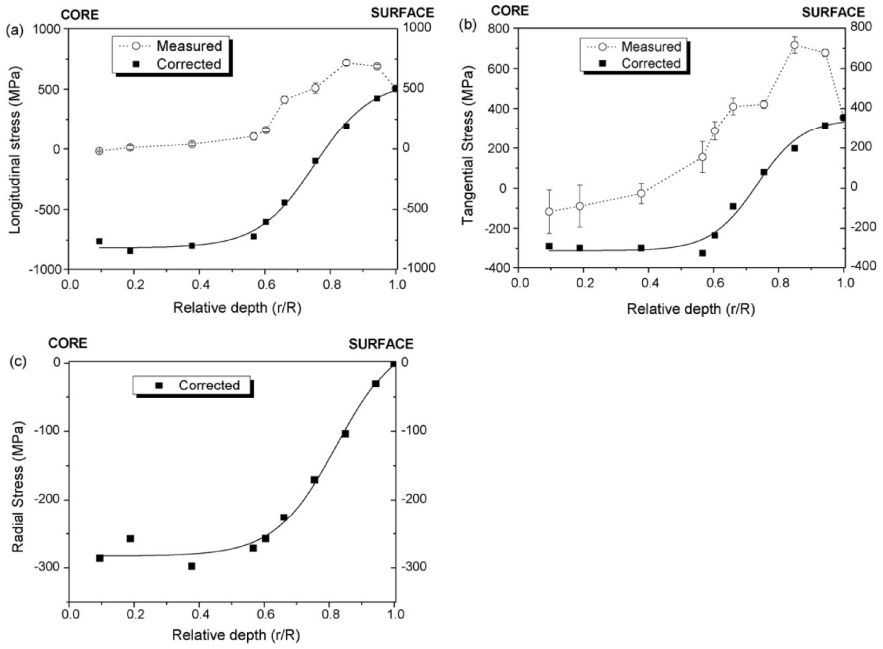

Figure 2.18: Ferrite stress profiles as a function of relative depth (r/R) in a cold drawn wire (ε = 1.8) along different directions (a) longitudinal, (b) tangential and (c) radial. The measurements needed to be corrected due to the change in residual stress state due to the sample preparation technique that was used [32].

In another article Yang et al. [33] measured the residual surface stress in the ferrite for different drawing strains up to 1.8 and used these results to calculate the macrostresses. Figure 2.19 shows the calculated macrostresses as a function of the drawing strain.

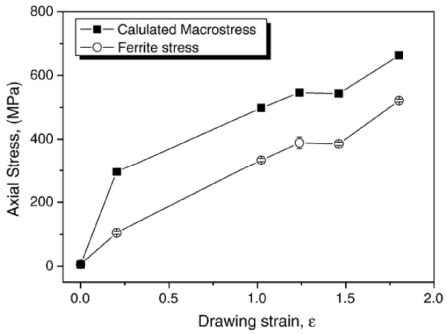

Figure 2.19: Calculated macrostresses at the surface of cold drawn wires as a function of the drawing strain together with the ferrite axial stress [33].

2.2.7 Conclusions

Although a lot of information is already available on the microstructure of heavily drawn steel wires, it is not yet fully characterized. The evolution of the pearlite colonies, the ferrite and the cementite phase during wire drawing is described, but the importance of the cementite decomposition and its influence on the mechanical properties remains unclear.

There are some publications on residual stresses of drawn steel wires, but none of them describe a similar material as is used in this study since a straightening operation is used after wire drawing.

At the moment the author is not aware of any publications that relate the microstructure to the fatigue properties of heavily drawn steel wires. Since this information is crucial for the complete understanding of the fatigue properties of heavily drawn steel wires, a research proposal on this topic is described in paragraph 9.3.

2.3 Fatigue general

Due to the massive amount of available publications in the fatigue domain, this literature review will only focus on some specific aspects of fatigue that are necessary to understand the interpretations of the experimental work done by the author of this thesis. If necessary the author would recommend consulting the reference works of S. Suresh [34] or J. Schijve [35].

2.3.1 Low and high cycle fatigue

Stress amplitude – fatigue life graphs (S-N curves) are often used to present fatigue data. Figure 2.20 gives a schematic representation of an S-N curve.

When a material is subjected to a dynamic load that is higher than the conventional fatigue limit it will fail after a finite number of cycles, called the fatigue life. When the dynamic load decreases, the fatigue life will increase. When the dynamic load is further decreased it will reach a point at which the fatigue life will become infinite, which is observed as a horizontal asymptote in the SN-curve (Figure 2.20). This asymptotic value is called the conventional

fatigue limit. It is however important to understand that this conventional fatigue limit finds its origin in fatigue tests that were terminated after a finite lifetime (mostly around 10^6 to 10^7 cycles). Therefore, the experimentally determined no failure stress level does not need to be a fatigue limit. Actually, the conventional fatigue limit was also called the endurance limit associated with a certain number of cycles.

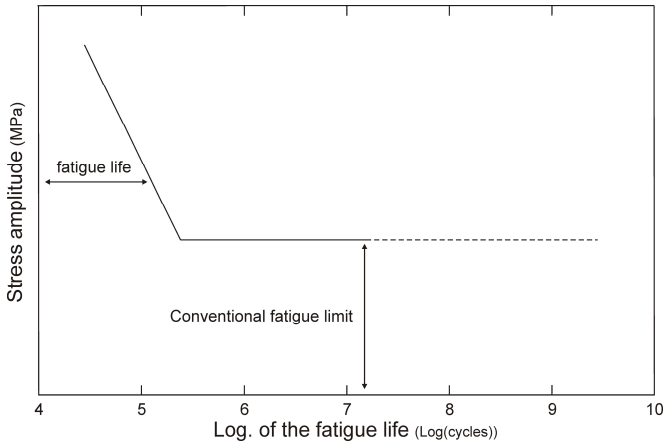

Figure 2.20: Schematic representation of an SN-curve.

At the end of the last century it was discovered for high strength steels that fatigue failures can occur at stresses below the conventional fatigue limit [36-38]. Therefore it was necessary to introduce the term very high cycle fatigue (VHCF, $N_f > 10^7$ cycles) in addition to the terms low cycle fatigue (LCF, $N_f < 10^5$ cycles) and high cycle fatigue (HCF, $10^5 < N_f < 10^7$ cycles).
The fractures that occur in the VHCF region are always related to internal non-metallic inclusions leading to the existence of two different fracture modes: surface and internal fatigue fractures. This leads to the existence of duplex SN-curves. Shiozawa et al. [39] made a schematic overview of the possible appearances of S-N curves including the possibility of fatigue failures in the VHCF region (Figure 2.21). Each S–N curve reveals results corresponding to the relative position on the probability distribution for the occurrence of surface and internal fatigue fracture modes of individual materials as shown in Figure 2.21a. This position will depend on the stress amplitude level. Type A is the common S–N curve of low-carbon steels governed by the surface fracture mode with the internal fracture mode occurring at infinite lifetime. Type B is the well known step-wise S–N curve. In this case, the probability distribution for the surface fracture mode is separated from that of the internal fracture mode. Type C is called a duplex S–N curve. The position of the probability distribution for the internal fracture mode is close to that of the surface failure mode, and both partially overlap. Finally Type D is the S–N curve governed only by the internal fracture mode because the probability distribution for internal fracture is at a shorter lifetime than that of the surface fracture mode.

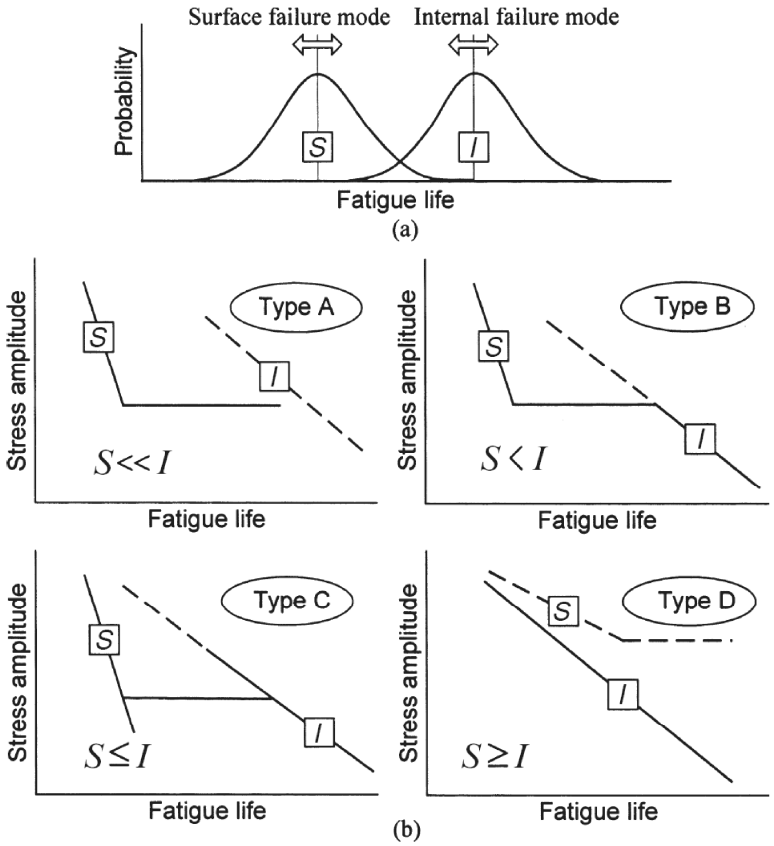

Figure 2.21: Schematic representation of the different types of duplex SN-curves [39].

Murakami et al. [38] were the first authors who made efforts to describe the internal fracture mode. Figure 2.22 gives an SEM image of a typical internal fatigue fracture, also referred to as a fish eye. Murakami et al. [38] observed that in a number of high strength steels failure in the VHCF-region always started from a non-metallic inclusion from inside the specimen. Around the inclusion an optical dark area (ODA) can be seen which shows a different fractographical appearance in comparison to its direct surrounding. The fish eye region can typically be divided into two regions: a rough area around the inclusion and a rather flat area of normal fatigue crack growth. The rough area is named ODA (optically dark area) by Murakami et al. [38], GBF (granular bright facet) by Shiozawa et al. [39-41] FGA (fine granular area) by Sakai et al. [42], and FCT (facet) by Tanaka et al. [43]. In the following text the name FCT will be used.

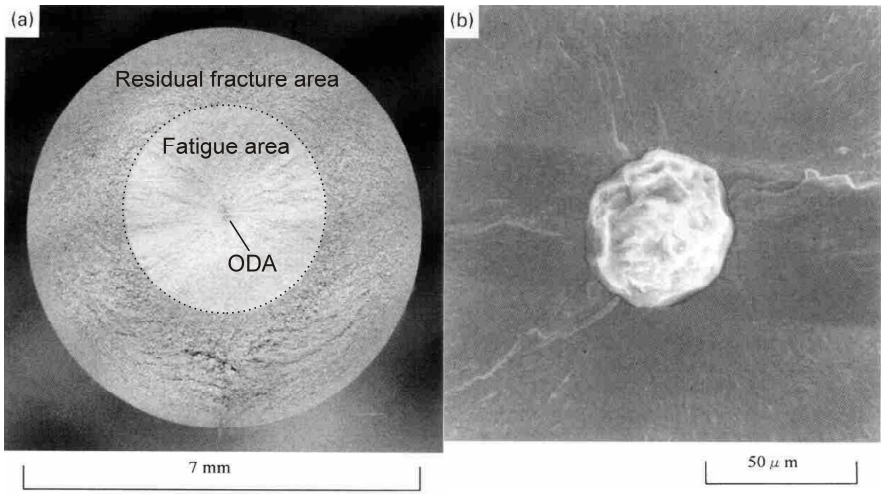

Figure 2.22: Left: typical fish eye appearance of an internal fatigue fracture. Right: Internal non-metallic inclusion inside the ODA.

Shiozawa et al. [41] suggested that the FCT area is formed by the growth and coalescence of microcracks around the inclusion. These microcracks would propagate along the boundary between spherical carbide and the matrix.
Murakami et al. [38] were first to suggest the possible influence of hydrogen on the formation of the FCT area. The conclusion of Murakami et al. is that hydrogen trapped by inclusions crucially influences the formation of a FCT area, and thus the particular fracture morphology observed around inclusions at the fracture origin. They also addressed that although the coupling mechanism of hydrogen and stress is not clear, the possible mechanism may be related to enhancing the mobility of dislocations and reducing internal friction by hydrogen. Whenever a critical crack size is reached (size of the FCT) the fatigue crack can continue its growth without the assistance of hydrogen. This can only happen when the crack growth speed becomes faster than the hydrogen diffusion speed inside the steel (figure 2.23).

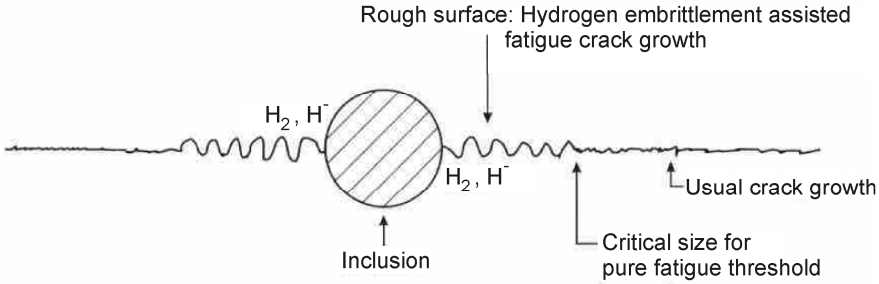

Figure 2.23: Hydrogen assisted fatigue crack growth around internal non-metallic inclusions [38].

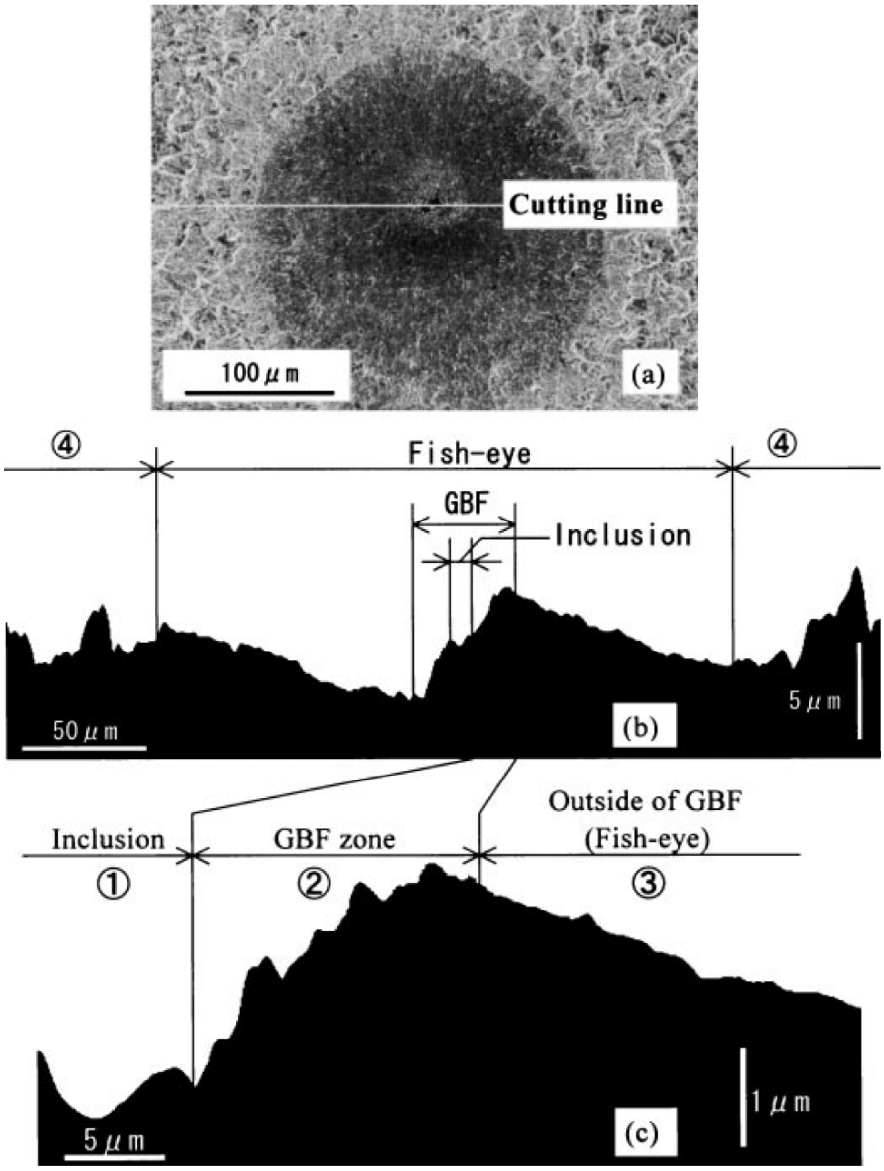

Figure 2.24: Surface roughness plot of an internal fatigue fracture [39]. The FCT area is indicated by GBF.

Sadananda et al. [44] suggested that due to the presence of high internal stresses around inclusions, short cracks can initiate very early. The term 'internal stress' is used for the local residual stress state of the material. The term will however be used in this work since it is used frequently in literature. After initiation these short cracks get arrested when they grow away from the inclusion due to the

rapidly decreasing internal stresses. Thus, a non propagating short crack forms at an early stage. Then, localized plasticity slowly builds-up near the inclusion, and along with deformation the internal stresses get enhanced. The deformation also alters the sub-microstructure and therefore, the short crack can grow slowly along the low-energy path contributing to a rough fracture surface. The presence of hydrogen can help in early localization of slip and can also reduce the cohesive energy.

Almost all publications on internal fatigue fractures in the VHCF regime use Murakami's formulae [45] for inclined fatigue cracks with an arbitrary shape:

$$\Delta K_{surface} = 0.65 \cdot \Delta\sigma \cdot \sqrt{\pi\sqrt{area}} \tag{2.12}$$

$$\Delta K_{internal} = 0.5 \cdot \Delta\sigma \cdot \sqrt{\pi\sqrt{area}} \tag{2.13}$$

with ΔK the stress intensity factor range, $\Delta\sigma$ the applied stress range and $\sqrt{area}$ the root of the area of the fatigue crack projected on the plane perpendicular to the wire axis.

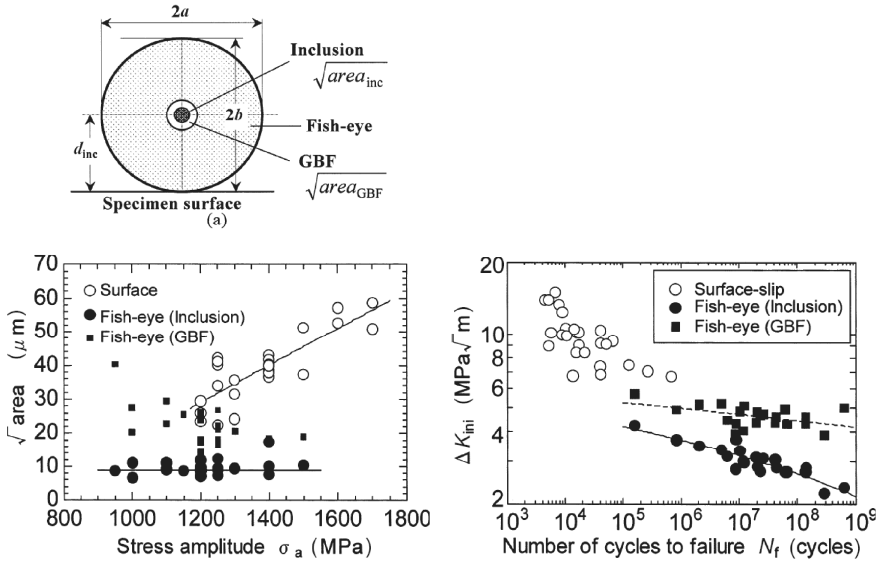

Figure 2.25: Left: experimental relationship between the size of the crack initiation site and the applied load. Right: Experimental relationship between the stress intensity factor range of the crack initiation sites and the fatigue life [39].

Schiozawa et al. [39] characterized the FCT area in depth and observed that the roughness inside the FCT area is twice as high as outside the FCT area (figure 2.24). They further showed that the size of the FCT area decreases when the applied load increases (left side of figure 2.25) and that the ΔK value of the FCT area is almost independent of the fatigue life (right side of figure 2.25). The

fatigue life increases with a decreasing ΔK value of the inclusion that initiated the internal fatigue crack (right side of figure 2.25).

Akinawa et al. [46] observed the same behavior of two different bearing steels some years later. They observed that the fatigue life increases when the ΔK value of the internal inclusions decreases (left size of figure 2.26) and that the ΔK value of the FCT area is independent of the fatigue life (right side of figure 2.26).

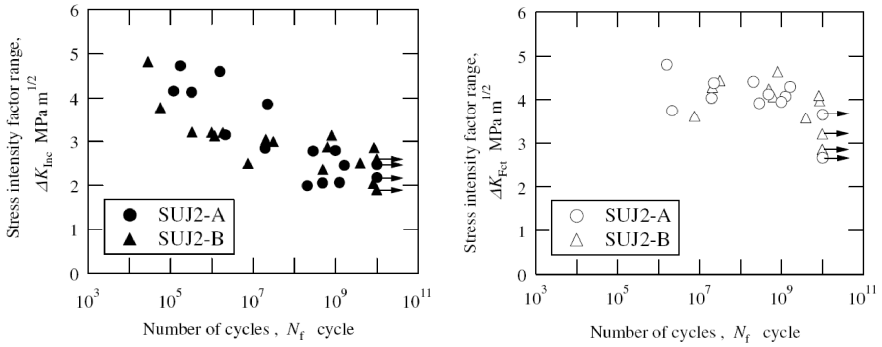

Figure 2.26: Left: experimental relationship between the inclusion size of the crack initiation site and the fatigue life. Right: Experimental relationship between the stress intensity factor range of the FCT area and the fatigue life [46].

2.3.2 Fatigue thresholds

At the moment two types of thresholds are in use for fatigue. One is the fatigue crack propagation threshold which defines a loading criterion under which cracks will not grow significantly. The other is the fatigue limit which defines a stress level under which no cracks will form, or in other words the fatigue crack initiation threshold. The fatigue crack propagation threshold presumes the existence of the crack and is used in damage tolerant design. The fatigue crack initiation threshold is traditional and was associated with the 'safe life' approach where the emphasis is on initiation rather than propagation. Both types of thresholds are functions of the loading cycle parameters and environment and both tend to decrease with increasing stress ratio.

At the moment it is not possible yet to determine the fatigue crack initiation threshold and its existence is even questioned by some [47]. This is unquestionably related to the fact that, at the moment, not everything is understood yet on the mechanisms active for fatigue crack initiation. Furthermore, there are no successful predictive fatigue models available that can take the initiation stage into account. Therefore, this paragraph only deals with the fatigue crack propagation threshold. When 'fatigue threshold' is mentioned in the text this will only refer to the fatigue crack propagation threshold.

Further it is important to note that the fatigue crack propagation threshold is conventionally determined by the use of crack growth rate measurements. In general, the fatigue crack propagation threshold is the stress level for which the

fatigue crack growth speed drops below 10^{-10} m/cycle. Therefore, this fatigue crack propagation threshold can not be applied for the VHCF region because the average crack growth rate (measured over the complete fracture surface) in the VHCF region is much smaller than 10^{-10} m/cycle (depending on the loading conditions, between 10^{-13} to 10^{-11} for the heavily drawn wires investigated in this study).

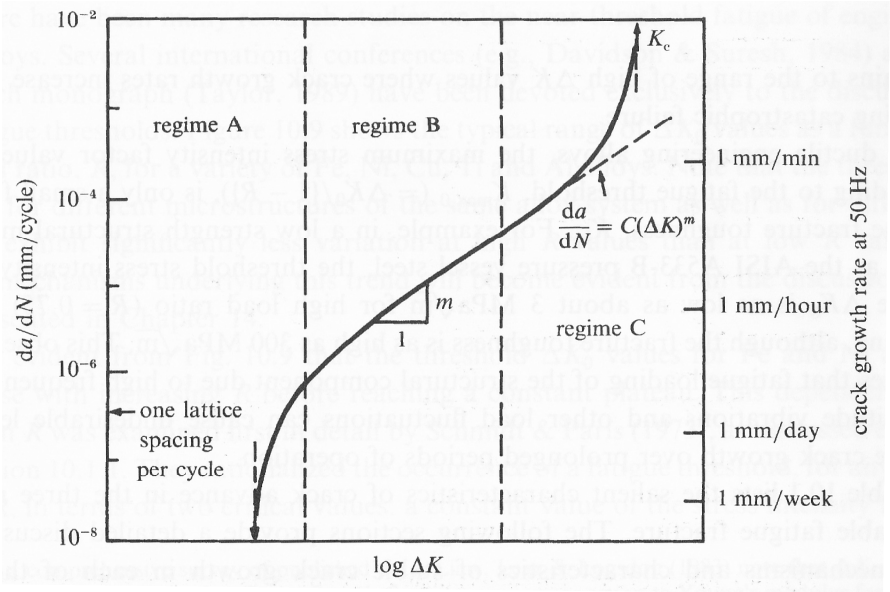

Figure 2.27: Schematic illustration of the different regimes of fatigue crack propagation [34].

Based on the crack growth rate the fatigue behavior can be divided in three regimes (figure 2.27): A near threshold regime (regime A), a stable fatigue crack growth regime, also known as the Paris regime (regime B), and a regime where the crack growth rates increase rapidly causing catastrophic failure (regime C). Regime B which shows a linear relation between log (da/dN) and log (ΔK) can be modeled successfully by the Paris law:

$$\frac{da}{dN} = C\left(\Delta K\right)^m \tag{2.14}$$

where a is the crack length, N is the number of cycles, da/dN is the crack growth rate (growth increment per cycle) and C and m are constants. In the lower end of the Paris regime (regime A) the crack growth rate decreases rapidly with a decreasing ΔK and approaches a vertical asymptote. This asymptotic value is often referred to as the threshold stress intensity factor range ΔK_{th}. It is important to note that this ΔK_{th} depends on the accuracy of the crack growth speed

measurement technique and therefore, as mentioned before, can only be applied for the LCF and HCF region. Further ΔK_{th} strongly depends on the load ratio ($R = \sigma_{min} / \sigma_{max}$), the microstructure and the environment [48].

The left side of figure 2.28 shows the influence of the load ratio (R) on ΔK_{th} for steels using the data of Bulloch [49]. A considerable scatter is observed even when the data is normalized. Nevertheless, there is an overall negative slope showing a trend towards lower thresholds for higher load ratios. An evolving series of semi-empirical approaches to understanding R-effects have been put forward which do not assume crack closure. The most important fittings are the Barsom [50] linear fit (equation 2.15) and the Klesnil and Lucas [51] power fit (equation 2.16).

$$\Delta K_{th} = A - B \cdot R \tag{2.15}$$

$$\Delta K_{th} = A \cdot (1 - R)^{\gamma} \tag{2.16}$$

where A, B and γ are constants.

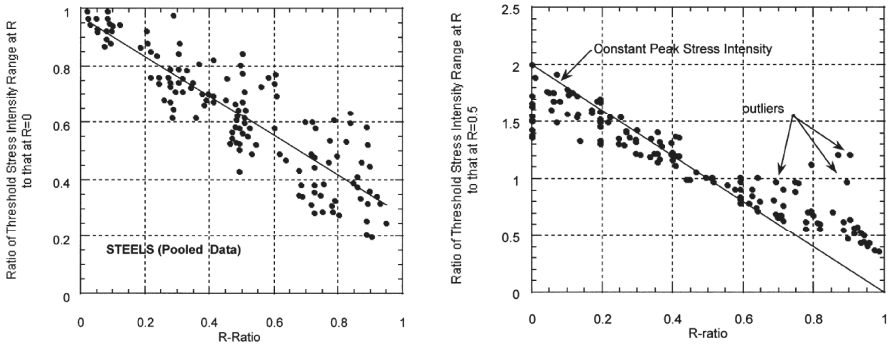

Figure 2.28: Normalized ΔK_{th} as a function of R. Left: showing the general trend for steels [48]. Right: for a variety of metal alloys [52]. The line shows the Barsom fit.

The dependence of ΔK_{th} on R is conventionally explained by the occurrence of crack closure. Because closure is an extrinsic or test-dependent variable it could give at least a qualitative explanation for the large scatter observed and illustrated in figure 2.28. Crack closure was first studied by Christensen [53] who matched photo-elastic models to fatigue experiments in which fretting-generated debris accumulated, limiting the opening displacement range of cracks. The propagation rates were strongly affected by whether or not the debris was allowed to work itself out of the crack. Nearly a decade later Elber [54,55] explained the phenomena with the plastically-deformed wake of the crack making contact with itself while some tensile loading was still applied. Some other causes of crack closure have been mentioned [56]:

1. plastic deformation of the wake
2. roughness
3. oxidation or corrosion products
4. viscous liquids
5. martensitic transformations
6. metal particles from fretting
7. hydrogen-induced deformation

Not all data for stress ratio effects take the form illustrated in the left side of figure 2.28. The right side shows some outliers which indicate a possible different functional relationship.
A key line of reasoning began when Schmidt and Paris [57] plotted the threshold stress intensity of 2124-T3 aluminum as a function of R (left side of figure 2.29). By overprinting lines corresponding to a constant K_{max} and a constant ΔK on their diagram they were able to show that the sloping portion of the curve related to a constant K_{max}, while the flat portion of the curve related to a constant ΔK. It was a short step to argue that the part of the curve controlled by K_{max} was governed by the need to open the crack while the constant ΔK portion represented the true threshold hidden under closure. This follows from the simple relation:

$$K_{\max} \geq \Delta K_{th,\text{int}} + K_{closure} \tag{2.17}$$

where $\Delta K_{th,int}$ is an intrinsic threshold stress intensity. This relation must be satisfied in order to satisfy the closure condition and the intrinsic threshold simultaneously. Application of this relation to explain the left side of figure 2.29 includes the assumption that $\Delta K_{th,int}$, a suitably chosen effective stress intensity at which the crack opens, does not vary with R. Later Döker [58] plotted threshold stress intensity range as a function of the maximum stress intensity and obtained a square plot as did Marci [59] using Schmidt and Paris's data. The right side of figure 2.29 shows such a plot.

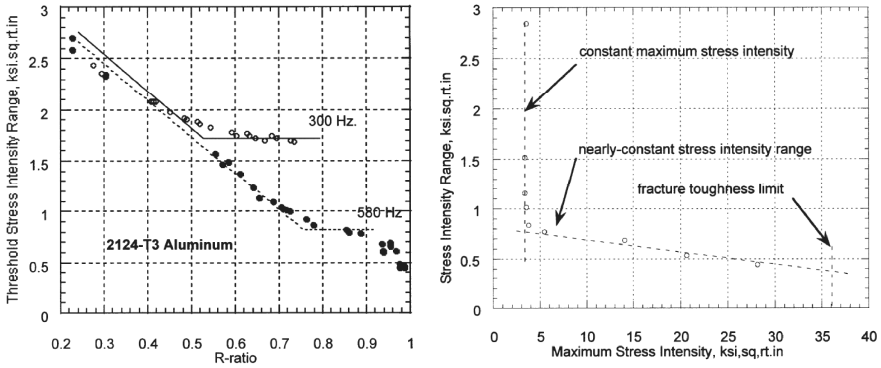

Figure 2.29: Left: ΔK_{th} as a function of R for 2124-Al at two different test frequencies [57]. Right: Döker plot of Schmidt and Paris's data [59].

The next step was made by Vasudevan, Sadananda and Louat [60] when they postulated that such a square plot could be reduced to two nearly constant thresholds which they contended were intrinsic properties of the material rather than effects of closure [61]. These two thresholds are K^*_{max} and ΔK^*_{th} corresponding to the intercepts with the axes when the two nearly orthogonal lines in the Döker plot (right side of figure 2.29) are extended. Vasudevan and Sadananda named their approach the 'Unified damage approach' and since their approach will be used to analyze the threshold data of the present study, it will be explained in depth in paragraph 2.3.4.

2.3.3 Short and long fatigue crack growth

Kitagawa and Takahashi [62] made the first successful attempt in bridging the fatigue crack-growth thresholds with endurance limits by combining crack-nucleation and crack propagation results. For their study they performed crack growth rate measurements on HT-80 steel for different crack lengths and determined their threshold values (at R = 0). They experimentally observed that ΔK_{th} is constant when the fatigue cracks are longer than 0.5 mm and called this the long crack growth region (figure 2.30). When the fatigue crack was however smaller than 0.5 mm it was observed that ΔK_{th} gradually decreases and approaches a horizontal asymptote, which was approximately equal to the fatigue limit of an unnotched smooth specimen of the material they used. The region for crack length smaller than 0.5 mm was called the short crack growth region.

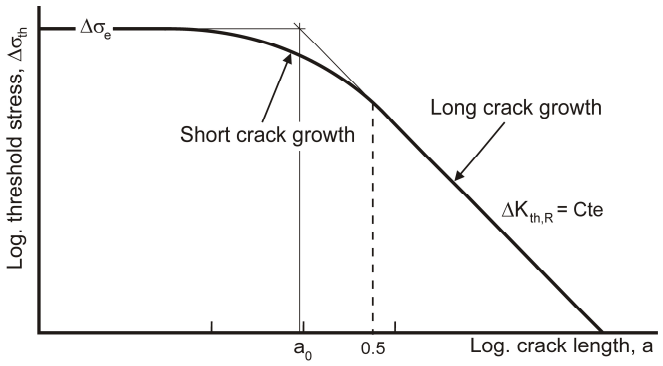

Figure 2.30: Schematic representation of the Kitagawa-Takahashi diagram.

The crack length a_0, which corresponds with the intersection between the $\Delta\sigma_e$ line and the ΔK_{th} line, is called the El Haddad parameter [63]. It was experimentally observed that the long crack growth regime starts around a crack length of approximately $10a_0$ [64]. El haddad et al. [63] proposed equation 2.18 to calculate ΔK_{th} in the short crack regime:

$$\Delta K_{th} = \Delta K_{th,R}\sqrt{\frac{a}{a+a_0}} \tag{2.18}$$

El haddad et al. [63] also derived equation 2.19 which can be used to calculate a_0.

$$a_0 = \left(\frac{\Delta K_{th}}{\Delta\sigma_e}\right)^2 \frac{1}{\pi} \tag{2.19}$$

Chapetti [65] investigated the fatigue crack propagation threshold of short cracks and observed that the initiation and early propagation of fatigue cracks is strongly influenced by the microstructure and the grain size, and that they seem to be related to the fatigue limit of metals. Both the fatigue limit and the high cycle fatigue resistance depend on the effective resistance of the microstructural barriers that has to be overcome by the cracks. Each of these barriers has a characteristic dimension and a critical stress range associated with its resistance to crack propagation. The plain fatigue limit is determined by the strongest microstructural barrier, since that resistance is generally greater than the resistance to crack nucleation. On the other hand, above the fatigue limit and for a given stress range, each barrier has an associated number of cycles that is necessary to propagate the crack.

Based on these findings Chapetti [65] created an adapted form of the Kitagawa-Takihashi diagram (figure 2.31). Please note that Chapetti used L_0 instead of a_0 for the El Haddad parameter. If the strongest microstructural barrier for fatigue crack propagation is placed at a given distance d from the material surface, the crack is non-damaging with respect to the plain fatigue limit up to a crack size a = d. For a microstructurally short crack (MSC, the crack length is of the order of the microstructural dimensions) initiated from a plain surface the fatigue limit at a given stress ratio R ($\Delta\sigma_{eR}$) defines the critical nominal stress range needed for continued crack growth (microstructural threshold). If the applied stress range $\Delta\sigma$ is smaller than $\Delta\sigma_{eR}$, cracks included in the MSC regime, are arrested at microstructural barriers placed at depths smaller than d.

For long fatigue cracks (LC) the diagram remains the same as the original Kitagawa-Takahashi diagram where fatigue cracks can only grow when the applied stress intensity factor range ΔK is greater than ΔK_{thR}.

In the physically short crack (PSC) regime (called short crack growth regime by Kitagawa et al. [62]), a transition between the microstructurally short and long crack regimes (MSC and LC), the threshold is below $\Delta\sigma_{eR}$ and ΔK_{thR}. Although the influence of microstructure is still important, Chapetti stated that the development of crack closure defines the threshold level in this regime. Since both $\Delta\sigma_{eR}$ and ΔK_{thR} depend on the stress ratio for a given material, the sub-index R is included.

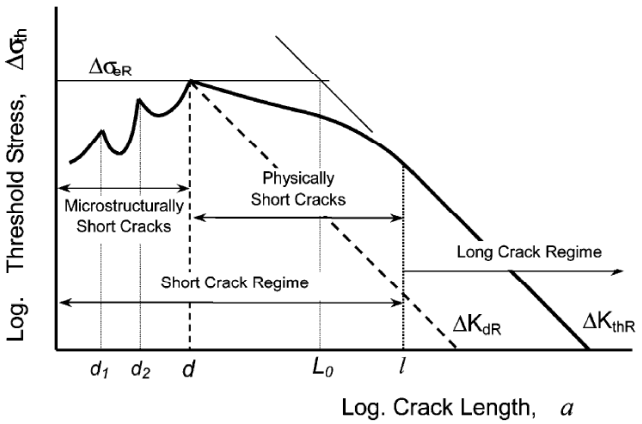

Figure 2.31: Kitagawa-Takahashi type diagram showing the threshold between propagating and non-propagating cracks [65].

Based on the effective driving force for crack growth Chapetti estimated the threshold for fatigue crack propagation as a function of the crack length using only $\Delta\sigma_{eR}$, ΔK_{thR} and the microstructural dimensions. He defined the intrinsic resistance to microstructural crack propagation as a microstructural threshold for crack propagation which is given by:

$$\Delta K_{dR} = Y \Delta \sigma_{eR} \sqrt{\pi d} \tag{2.20}$$

where Y is the geometrical correction factor and the value of d is usually given by the microstructural characteristic dimension, M (e.g. ferrite grain size, bainite or martensite lath length, etc.). For the LC regime the total extrinsic component ΔK_{CR} (the part that is governed by crack closure) is defined as (figure 2.32):

$$\Delta K_{CR} = \Delta K_{thR} - \Delta K_{dR} \tag{2.21}$$

Since the extrinsic part (crack closure) builds up in the PSC regime the extrinsic component ΔK_C is defined as (assuming an exponential build up):

$$\Delta K_C = \Delta K_{CR} \left(1 - e^{-ka}\right) \tag{2.22}$$

where the material constant k defines the development of the extrinsic component ΔK_C for each stress ratio, and a is the crack length expressed in mm. Since the material threshold for crack growth ΔK_{th} is the sum of the total intrinsic and extrinsic component it can be defined as:

$$\Delta K_{th} = \Delta K_{dR} + \left(\Delta K_{thR} - \Delta K_{dR}\right)\left(1 - e^{-k(a-d)}\right) \quad a \geq d \tag{2.23}$$

Figure 2.32 gives a schematic representation of the threshold curve given by equation 2.23. Chapetti observed a good correlation between the predictions of equation 2.23 and experimentally obtained values of ΔK_{th} in the PSC regime.

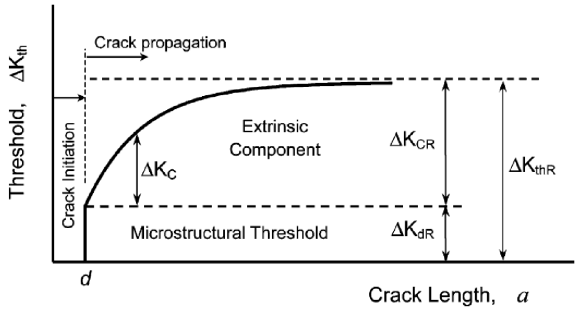

Figure 2.32: Fatigue crack propagation threshold as a function of crack length given by equation 2.23 [65].

When equation 2.23 is combined with the Paris threshold law [66] which is given in equation 2.24 it is possible to predict the complete short crack growth behavior for cracks with a ≥ d.

$$\frac{da}{dN} = C^{*}\left(\Delta K - \Delta K_{th}\right)^{m} \tag{2.24}$$

Figure 2.33 shows the da/dN - ΔK plot with some experimental data corresponding to short cracks propagating from notches in a JIS SM41B steel, obtained by Akiniwa et al. [67]. The figure shows the propagation behavior of a surface crack in smooth material for a nominal stress range equal to 400 MPa (just above the plain fatigue limit of the material), estimated by integrating equation 2.24 from a crack length equal to d, using equation 2.23 and taking the geometrical parameter Y equal to 1.12 to consider through thickness cracks.
Figure 2.33 reveals that a short crack propagates faster than a long crack at a given ΔK, and still propagates in the region below ΔK_{thR}. When the ΔK value exceeds ΔK_{thR} the propagation rate of the short crack comes closer to that of the long crack. The dashed line shows the microstructural threshold, ΔK_{dR}, which represents the minimum ΔK for crack propagation. It is actually possible to observe fatigue propagation of MSCs at $\Delta K < \Delta K_{dR}$, but any propagation at a < d is considered part of the crack initiation period.
Figure 2.34 shows the estimated fatigue propagation behavior of short cracks initiated at three notches with different geometries for the same material. Two of those notches have the same stress-concentration factor k_t (equal to 3), but different notch root radius, r = 3 and 0.5 mm (r = ρ in figure 2.34 and 2.35). The third notch is the same as the one used to obtain the experimental results shown in figure 2.33: D = 3 mm, r = 0.16 mm and k_t = 8.48.

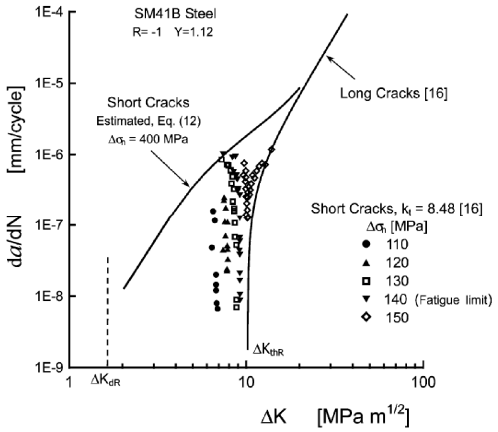

Figure 2.33: da/dN - ΔK plot for long and short fatigue cracks calculated using equations 2.23 and 2.24 [65].

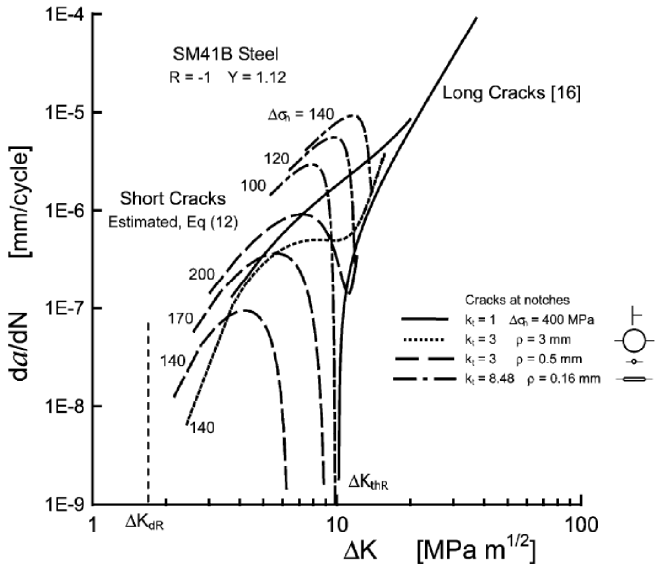

Figure 2.34: Estimated fatigue crack propagation behavior of short cracks for three different notched SM41B(S) steel specimens [65].

For the r = 3 mm notch only the nominal applied stress range equal to 140 MPa is considered. This stress level is just 10 MPa above the estimated fatigue limit for the same notch geometry (equal to 130 MPa), for which mechanically short non-propagating cracks cannot be formed. This fact can be analyzed in figure 2.35, which shows a Kitagawa–Takahashi type diagram with the threshold stress for the propagation of fatigue crack estimated using equation 2.23 and the applied stress distributions estimated for the three notch geometries. The stress distribution corresponding to r = 3 mm notch and $\Delta\sigma_n$ = 140 MPa propagates the

initiated crack of length d without arresting, since the applied stress is greater than the threshold stress for any crack length.

In the case of the r = 0.5 mm notch and $\Delta\sigma_n$ = 140 MPa the estimated stress distribution can also drive the initiated crack of length d but only to a depth of about 0.09 mm, at which the stress level becomes smaller than the threshold stress. By increasing the applied stress level, the crack can propagate further. The fatigue limit is estimated to be about 180 MPa, for which a non-propagation crack length as long as 0.5 mm can be observed. Figure 2.35 shows the stress distribution for $\Delta\sigma_n$ = 200 MPa. It can be seen that the crack can propagate without arresting, since the applied stress is greater than the threshold stress for any crack length. The estimated fatigue limit associated to this notch is 190 MPa, 60 MPa greater than the estimated one for r = 3 mm notch. The difference is due to the notch size effect. Different notch geometries define different stress gradients in the short crack regime.

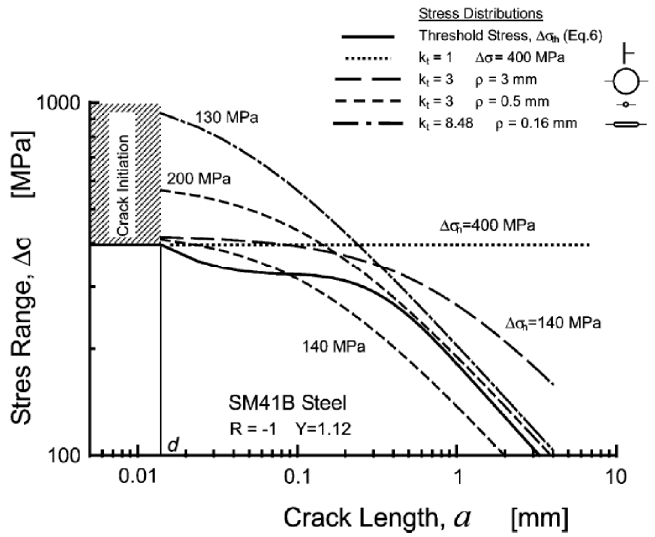

Figure 2.35: Kitagawa–Takahashi type diagram showing the estimated threshold stress for fatigue crack propagation for SM41B(S) steel [65].

2.3.4 Unified damage approach

Sadananda et al. [44] successfully applied the unified damage approach to the very high cycle fatigue regime. In this paragraph their approach is explained.

Figure 2.36 shows a schematic representation of a Kitagawa-Takahashi diagram for two R ratios. In the unified damage approach the linear segment is extrapolated to lower crack lengths to show that the triangular area is the 'internal stress' regime. In this region, the internal stresses are generated in situ via cyclic plasticity [68]. These internal tensile stresses help to nucleate and sustain a short crack that can grow to become a long crack, finally approaching failure. At lower amplitudes near the endurance limit, a large number of cycles are required to

generate sufficient magnitude of internal stresses needed for a crack to nucleate and sustain its growth. The presence of preexisting stress concentrations, such as inclusions or porosities can markedly reduce these required numbers of cycles for crack nucleation. Figure 2.36 shows that with an increase in load ratio from R = 0 to 0.8, the curve shifts to a lower critical crack length with a lower threshold and endurance limit. Figure 2.36 also shows the minimum internal stresses and their gradients required in a given system to keep a nucleated crack growing continuously until it becomes self-sustaining in the presence of external loads.
Sadananda et al. [69] observed that when experimental data is normalized in a Kitagawa-Takahashi diagram it falls on a unique curve for all the different R values. Figure 2.37 uses the experimental data of Usami [70] and shows that the critical crack length a* scales proportionately with the transition of crack nucleation to crack propagation. In the presence of aggressive environment (for example humidity that enters the tire trough defects in case of tire cord), the internal stresses can be further reduced for crack initiation and growth.

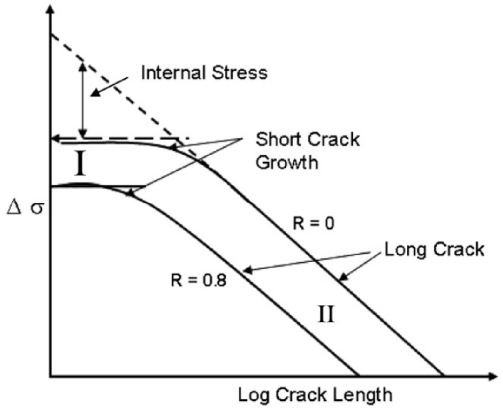

Figure 2.36: Schematic representation of the Kitagawa-Takahashi diagram for two different R values showing the internal stress regime of the unified damage approach [44].

Figure 2.37 not only defines the minimum internal stresses and their gradients required for crack initiation and growth but also defines the critical crack length (a*) needed for a crack to sustain its continuous growth. Cracks with a length less than a* will not grow if the applied stresses are less than the endurance limit. This implies that for stresses smaller than their endurance limit, the cyclic plasticity does not generate sufficient internal stresses and/or its gradients for the crack to exceed the critical size. Cracks can still form but not propagate if the internal stresses decrease rapidly as the crack moves out of their internal stress source. This means that in addition to the magnitude of the internal stress, the gradient is equally important to sustain the crack growth after nucleation. Internal stress gradients are significantly affected by the localized plasticity at the notches. Sharp notches combined with the steep internal stress gradients resulting from localized plasticity contribute to the presence of non-propagating cracks.

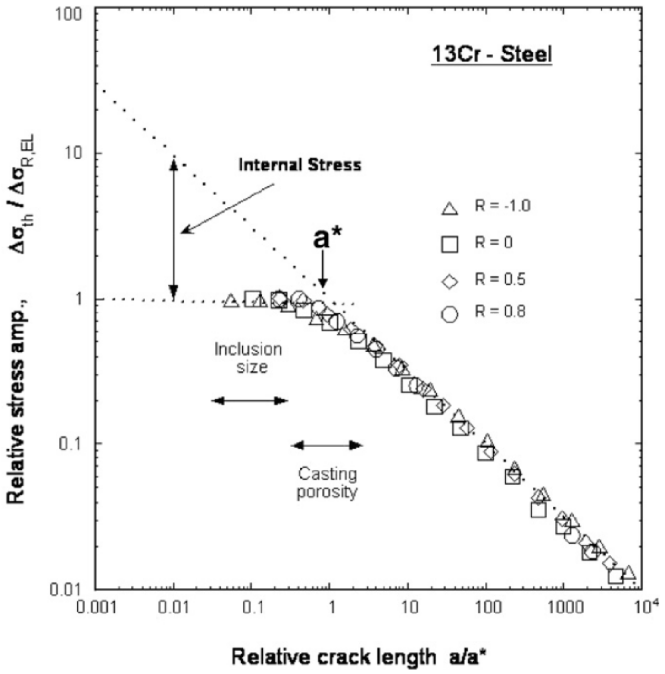

Figure 2.37: Experimental data for 13Cr steel from Usami represented in normalized coordinates [44].

It is important to note that pre-existing stress concentrations such as holes or inclusions are helpful but not necessary to localize plastic deformation and thus to the accumulation of internal stresses. Heterogeneity in deformation can occur in smooth tensile fatigue specimen due to grain orientations or microstructural inhomogeneities leading to build-up of internal stresses. Formation of persistent slip bands leading to intrusions and extrusions are examples of in situ generated sources of internal stresses. Therefore, crack nucleation will only continue in crack propagation (for a given stress) if the internal stresses and their gradients are sufficient for a nucleated crack to grow without any arrest.

To make their approach clear Sadananda et al. [44] composed figure 2.38 where they show three possible cases of internal stress profiles that could be present at the surface due to protrusions or intrusions. In Case 1, the internal stresses are higher than the required minimum (threshold for crack growth) and hence the crack initiated will always propagate without any arrest. For example, shallow notches at high applied stresses, or holes of large diameter, can have such internal stresses. For Case 2, initially the internal stresses are quite high close to their source but rapidly decrease to a level less than the required threshold minimum. In such cases, the crack grows up to some extent but gets arrested soon because the total driving force is less than the crack-growth threshold, $K^*_{max,th}$. Such non-propagating short cracks have been observed for cracks emanating from sharp

notches. These cracks can only continue their growth when the applied stresses are increased above the minimum required threshold. For Case 3, the internal stresses are not sufficient enough for both crack initiation and growth, since the magnitude and the gradients are less than the required minimum threshold for crack growth. This means that cracks can only propagate when the total internal stresses reach the minimum threshold required:

$$K_{total} = K_{applied} + K_{\text{int}} \geq K^{*}_{\max,th} \tag{2.25}$$

where K_{total} is the total stress intensity factor at the crack tip, $K_{applied}$ is the applied stress intensity factor, K_{int} is the stress intensity factor due to internal stresses and $K^{*}_{max,th}$ is the threshold required for long crack growth. It is important to note that both $K^{*}_{max,th}$ and ΔK^{*}_{th} are required threshold values (material properties) which form the basis of the unified damage approach. Since $K^{*}_{max,th} \geq \Delta K^{*}_{th}$ for almost all materials especially at low R ratios, $K^{*}_{max,th}$ becomes the controlling parameter for crack propagation.

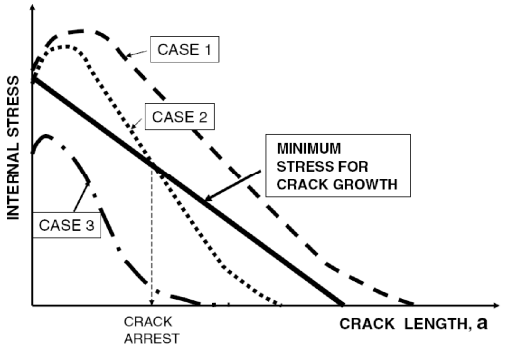

Figure 2.38: Possible internal stress profiles in relation the required minimum for steady crack growth [44].

Figure 2.39 shows a $\Delta K - K_{max}$ curve for different crack growth rates which results in L shaped curves defining the two critical values for ΔK and K_{max} for a given crack growth rate. At the threshold (taken at a crack growth rate of 10^{-10} m/cycle) they represent the fundamental values required to overcome the material crack growth resistance: $K^{*}_{max,th}$ and ΔK^{*}_{th}. It is important to note that both ΔK and K_{max} consist of three components: a part caused by the applied stresses and a part caused by the internal stresses but also a part that is caused by environmental interactions. For example, hydrogen can enhance the localized plasticity (HELP mechanism) and therefore lower the $K^{*}_{max,th}$ requirement for crack growth.

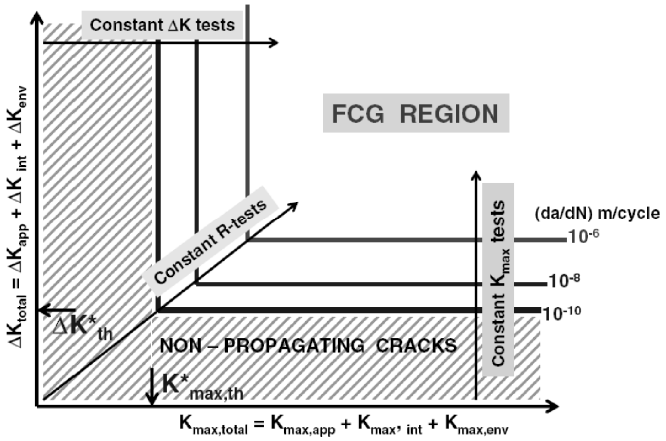

Figure 2.39: ΔK – K_{max} curve for different crack growth rates [44].

Based on the experimental data of Tanaka et al. [71] Sadananda et al. [44] calculated the total K value of a crack that nucleates from a sharp notch as a function of its length (figure 2.40). K = 0 when the crack length is zero and with increasing crack length K increases due to both the applied and the internal stresses. Because of notch tip plasticity, the K value increases to a peak value and then decreases to a minimum. The further increase in K value is small and occurs mainly due to the increase in crack length in the presence of the applied stress. This is due to the rapid decrease in notch tip internal stress as the crack grows away from the notch.

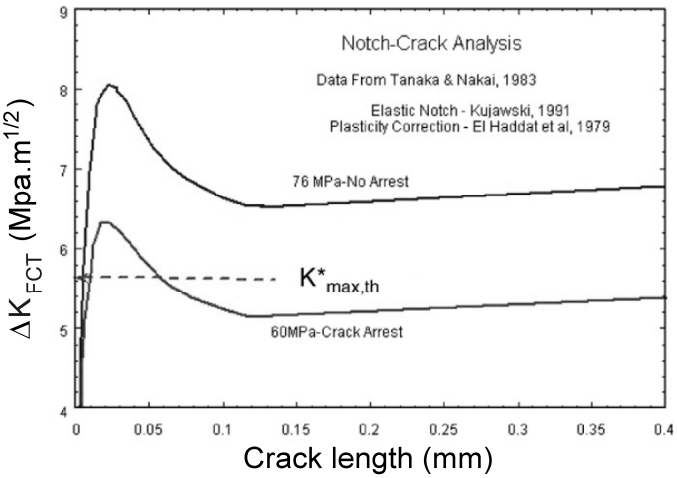

Figure 2.40: Analysis of crack growth from a stress concentration region showing that crack arrest occurs when $K_{max,total} < K^*_{max,th}$ [44].

Figure 2.40 shows that crack arrest occurs when the minimum falls below $K^*_{max,th}$. When the applied stress is increased from 60 to 76 MPa the minimum does not fall below $K^*_{max,th}$ and the crack continues growing.
This methodology can easily be used for the VHCF regime where internal fatigue cracks always initiate from internal stress concentration sites such as an inclusion. The difference with other approaches is the existence of two thresholds for fatigue crack growth instead of one and it is $K^*_{max,th}$ that causes crack arrest since $K^*_{max,th} > \Delta K^*_{th}$. In addition both thresholds are independent of the crack length, meaning that they are the same for both long and short cracks. Therefore it can be concluded that the short crack growth behavior is only a reflection of changing internal stress fields that affect their growth.

Based on the existing literature on VHCF properties Sadananda et al. [44] concluded that the FCT area around internal non-metallic inclusions is formed by the formation of a sub-microstructure. Localized plasticity slowly builds up near the inclusion, and along with deformation the internal stresses get enhanced. Deformation also alters the sub-microstructure and the crack grows slowly along the low-energy path contributing to a rough fracture surface. The presence of hydrogen (which can be trapped by non-metallic inclusions) can help in the early localization of slip and also in reducing the cohesive energy.

2.3.5 Influencing parameters

In this paragraph the influence of different parameters on the fatigue thresholds is discussed. Figure 2.41 shows the variations of both the K_{max} and the ΔK thresholds for different steels [72]. It is observed that ΔK^*_{th} is constant (2.6 ± 0.2 MPa$\sqrt{m}$) for all the different steels while $K^*_{max,th}$ varies significantly for all the steels. In addition $K^*_{max,th}$ is equal to or greater than ΔK^*_{th} and should therefore be the major controlling parameter for fatigue crack growth.

Figure 2.42 shows the variation of $K^*_{max,th}$ as a function of the square root of the yield stress for different steels in ambient air. Although the different steels that were used for figure 2.42 have different compositions and microstructures a general trend of a decreasing threshold stress with an increasing yield strength. Since steels are very sensitive to relative humidity, it is possible that the decrease of $K^*_{max,th}$ with the yield stress is due to environmental contributions.

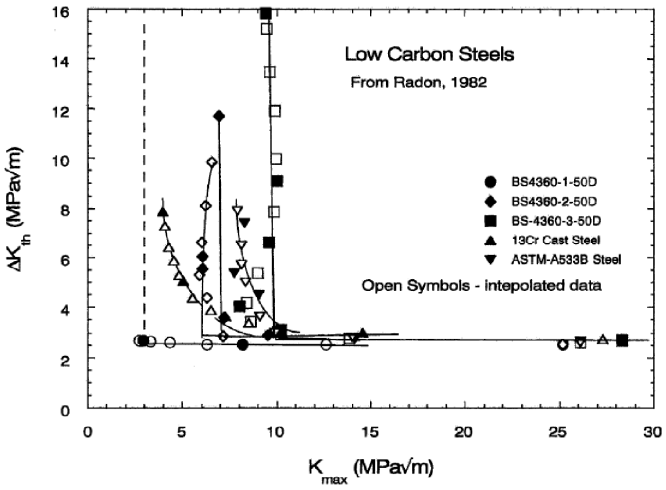

Figure 2.41: $\Delta K - K_{max}$ curve for different steels [72].

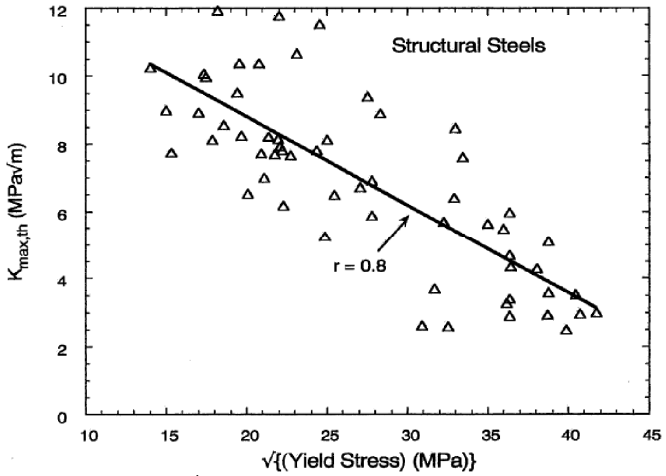

Figure 2.42: Variation of $K^*_{max,th}$ as a function of the square root of the yield stress for different steels in ambient air. A least square fit with a correlation coefficient of r = 0.8 is shown [72].

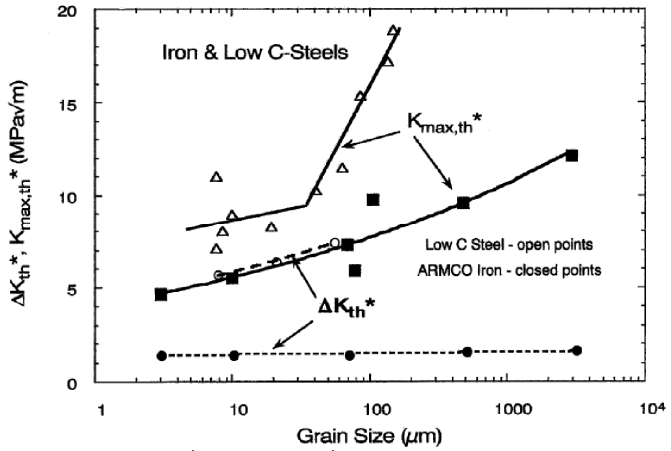

Figure 2.43: Variation of $K^*_{max,th}$ and ΔK^*_{th} as a function of grain size [72].

Figure 2.43 shows the variation of both thresholds $K^*_{max,th}$ and ΔK^*_{th} as a function of grain size for ARMCO iron [73] and low carbon steels [74]. The figure shows that ΔK^*_{th} for ARMCO iron is very small and is independent of grain size. On the other hand $K^*_{max,th}$ is larger and increases with increase in grain size. It further shows that for low alloy steels this increase is not a simple linear function of grain size. The independence of ΔK^*_{th} with the grain size is compatible with data in figure 2.41 where ΔK^*_{th} remains the same for different materials with different grain sizes. Comparison of figures 2.42 and 2.43 raises the question of whether grain size or yield stress independently affect $K^*_{max,th}$ or whether their effects are interrelated. In addition, changing grain size can also affect other microstructural features of the steels, which also can influence their thresholds. Sadananda et al. [72] tried to answer this question using the Hall-Petch relationship but their results were inconclusive.

Figure 2.44 shows the effect of the temperature on the two thresholds for a low alloyed steel [75]. With an increase in temperature from 24 to 150 °C, $K^*_{max,th}$ decreases from 8.2 to 4.4 MPa√m. When the temperature further increases to 427 °C $K^*_{max,th}$ increases again to 9.9 MPa√m. This means that the threshold reaches a minimum at an intermediate temperature around 150 °C. On the other hand ΔK^*_{th} varies very little with the temperature. The Sadananda et al. [72] expect that this behavior can be addressed completely to environmental interactions which can have a maximum effect at some intermediate temperature. This behavior is not observed for stainless steels where both thresholds were found to be independent of the temperature (between 25 and 500 °C) [76].

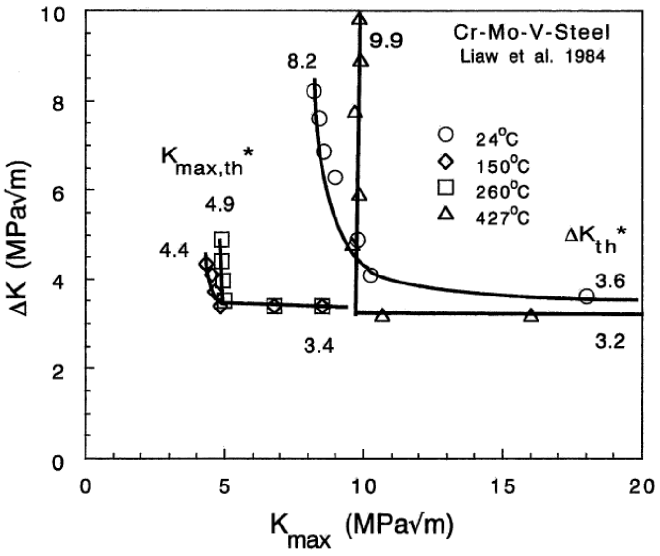

Figure 2.44: Effect of the temperature on $K^*_{max,th}$ and ΔK^*_{th} [72].

Vasudevan et al. [77] studied the influence of the environment on the fatigue thresholds. They experimentally observed that $K^*_{max,th}$ increases when a steel is tested in a more aggressive environment while ΔK^*_{th} remains unaffected. Through oxide thickness measurements at the crack tip they observed an increase in oxide thickness for a more aggressive environment. They concluded that there is a critical $K^*_{max,th}$ required to break the oxide and advance the crack. The criterion for crack propagation requires that the applied $K_{max} > K^*_{max,th}$. $K^*_{max,th}$ is probably related to the intrinsic fracture properties of the oxide, oxide/metal interface bonding, slip mode and the type of corrosion reaction at the crack tip.
Vasudevan et al. [77] made a schematic overview of their proposed mechanism which is given in figure 2.45.
The bold dashed line on figure 2.45 shows the experimentally observed oxide thickness at the crack tip as a function of the environment (which is interrelated with K_{max} at the horizontal axis). The vertical K_{max} line shows the maximum oxide thickness at the crack tip for a certain environment just before it breaks. When the oxide layer breaks the fatigue crack can continue its growth (after the vertical line the oxide thickness becomes marginal). The vertical K_{max} lines correspond with the $K^*_{max,th}$ lines of the ΔK - K_{max} graph which is given in the inset of figure 2.45.

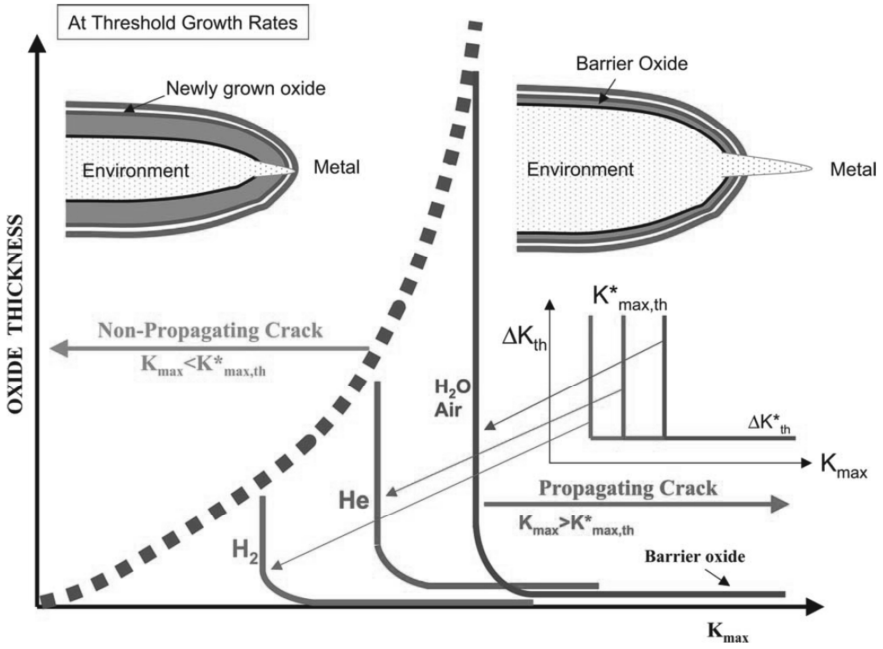

Figure 2.45: Schematic representation of the mechanism behind the increasing $K^*_{max,th}$ for a more aggressive environment [77].

2.3.6 Conclusions

This part of the literature review gives a selection of fatigue related topics that are relevant for this study.

The discussion about low and high cycle fatigue is based on high strength steels, which fracture internally at non-metallic inclusions in the high cycle fatigue regime. Around these inclusions a characteristic area, called the facet (FCT) area, is formed. A lot of effort was put in understanding the formation of FCT area and according to the author, the internal stress model of Sadananda et al. [44] describes the behavior best at the moment. All other studies that describe the FCT area assume that hydrogen, which diffuses from the inclusion into the steel, plays a crucial role in the formation of the FCT area. The authors would like to emphasize that none of the studies were able to measure the presence of hydrogen in the FCT area. In the model of Sadananda, the influence of hydrogen is mentioned but is not a necessary condition.

The internal stress model of Sadananda et al. [44] forms the basis of the unified damage approach. In the unified damage approach it is assumed that there exists only one threshold for crack growth, both in the short and the long crack growth regime. This assumption is questionable and does not fit the model that is suggested by Chapatti [65]. Although the unified damage approach is successfully applied for a broad range of different materials, caution is needed when the approach is used. On the other hand, the model of Chapetti [65] predicts significantly faster crack growth rates in the short crack growth regime compared

to experimental results (figure 2.33). Therefore it can be concluded that Chapetti's model for short crack growth is not generally applicable.
In a concluding remark the author would like to mention that, at the moment, there exists no generally accepted model which describes the short crack growth behavior.

2.4 Fatigue of drawn wires

The amount of publications that deal with fatigue related topics on cold drawn pearlitic steel wires are limited. Verpoest et al. [78] were the first authors that successfully described the fatigue behavior of cold drawn steel wires by using fracture mechanics. They experimentally measured the fatigue limit (σ_e) and the threshold stress intensity range for crack growth (ΔK_{th}) on five different pearlitic steel wires with a diameter of 2 mm and strains ranging from 0.32 to 2.51. To determine ΔK_{th} they used the AC potential drop method to measure the fatigue crack length. It is important to note that they defined the fatigue threshold at a crack growth rate of 10^{-7} m/cycle. In comparison, modern crack growth rate techniques such as a long distance microscope can measure crack growth rates as low as 10^{-11} m/cycle [79], which will have a significant influence on the measured threshold values.

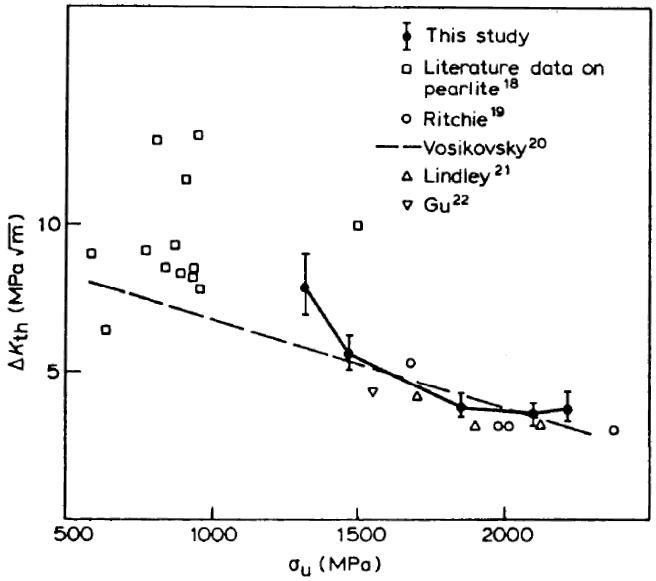

Figure 2.46: Fatigue threshold of drawn pearlitic steel wires (indicated as 'This study') as a function of the tensile strength, compared with some data from literature on pearlitic and martensitic steels [78].

Figure 2.46 shows the fatigue threshold as a function of the tensile strength for the fatigue data of Verpoest et al. [78] at R = 0 compared to fatigue data from

literature. It was observed that the fatigue threshold decreases with increasing tensile strength. For higher tensile strengths (> 1800 MPa) or wire drawing reduction (> 85%) the fatigue threshold reaches a stable value between 3.5 and 4 MPa√m. For lower tensile strengths (< 1500 MPa) however the scatter is very large making it impossible to find any correlations. This suggests that other parameters are playing a role. Verpoest et al. [78] investigated if there exists a correlation between the interlamellar distance λ and the fatigue threshold (figure 2.47). The figure shows that at R = 0 no unique relationship exists between λ and ΔK_{th}. It is however important to note that for high R values ($R \geq 0.6$) all the data points fall in a narrow band ($4 < \Delta K_{th} < 5$ MPa√m), independent of the interlamellar distance. Verpoest et al. [78] concluded that the above described behavior can be explained by crack closure. This conclusion is mainly based on the observed independence of ΔK_{th} on the interlamellar spacing for high R values.

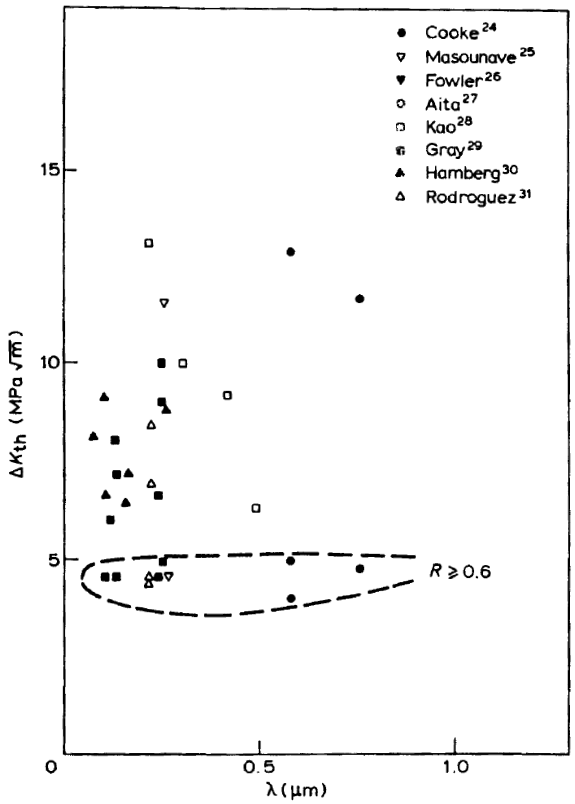

Figure 2.47: Influence of the interlamellar distance λ on the fatigue thresholds of pearlitic steels [78].

Based on the fatigue limit and the fatigue threshold which were experimentally measured, Verpoest et al. [78] calculated the initial defect depth using equation

2.26 (please note that a_0 is used for the initial defect depth by Verpoest et al. and not as the El Haddad parameter).

$$a_0 = \frac{1}{\pi}\left(\frac{\Delta K_{th}}{2 \cdot \alpha \cdot \sigma_e}\right)^2 \tag{2.26}$$

where a_0 is the initial defect depth and α is a geometrical factor that equals 0.67 for the assumed semi-circular crack. Figure 2.48 shows that the calculated initial defect depth $a_{0,c}$ decreases with increasing tensile strength or wire drawing strain. This trend was experimentally validated by microscopic observations and roughness measurements (figure 2.48).

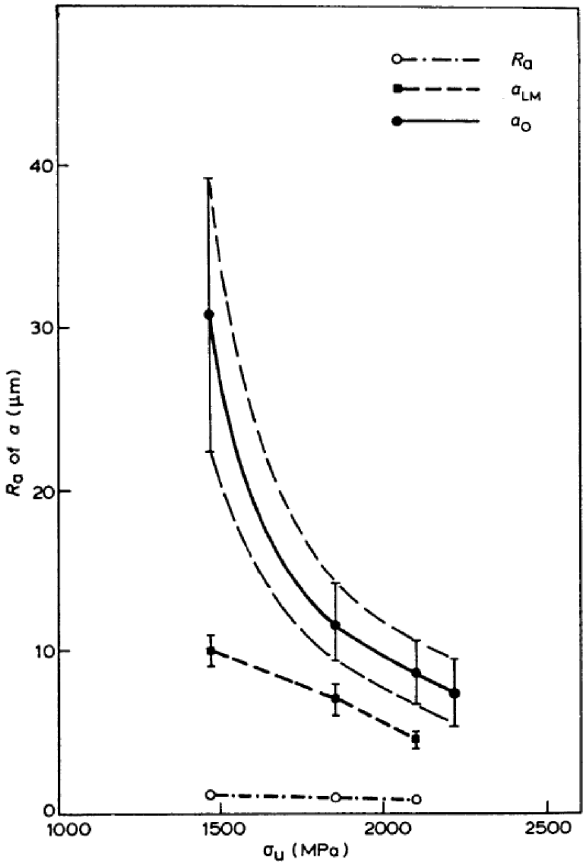

Figure 2.48: Surface roughness (R_a), surface defect depth optically measured on longitudinal sections (a_{LM}) and calculated initial defect depth (a_0) as a function of the tensile strength [78].

Through fractographical analysis Verpoest et al. [78] divided the surface stress concentration from which the fatigue cracks initiated into three groups.

- Broken martensite (figure 2.49). Due to a poor lubrication during the wire drawing process the wire can locally overheat. When the wire leaves the drawing die a thin martensitic layer is formed due to the sudden cooling. During the following drawing steps the cementite gets fragmented forming shallow cracks.

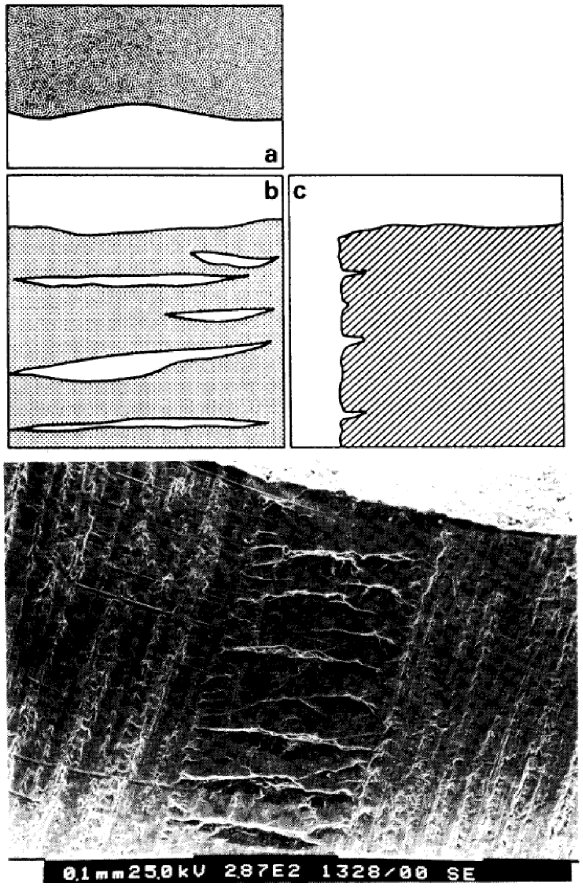

Figure 2.49: Broken martensite as a crack origin. At the top of the figure, (a) the fatigue crack fracture plane, (b) the wire surface and (c) a section through the defect are shown schematically [78].

- Two grooves (figure 2.50). Longitudinal surface grooves are typical surface features in drawn steel wires. It was experimentally found that about 1/3rd of the fatigue fractures initiated at the point where two grooves come very close to each other. Since the stress concentrations at these longitudinal grooves are very low Verpoest et al. [78] proposed the

following crack growth model (figure 2.51). Due to high stress concentrations small fatigue crack can initiate at the corners of the central ribbon (I). These cracks grow and meet forming a through crack in the central ribbon (II). Finally, this crack reaches the bottom line of the two grooves, forming a semi-elliptical crack (III).

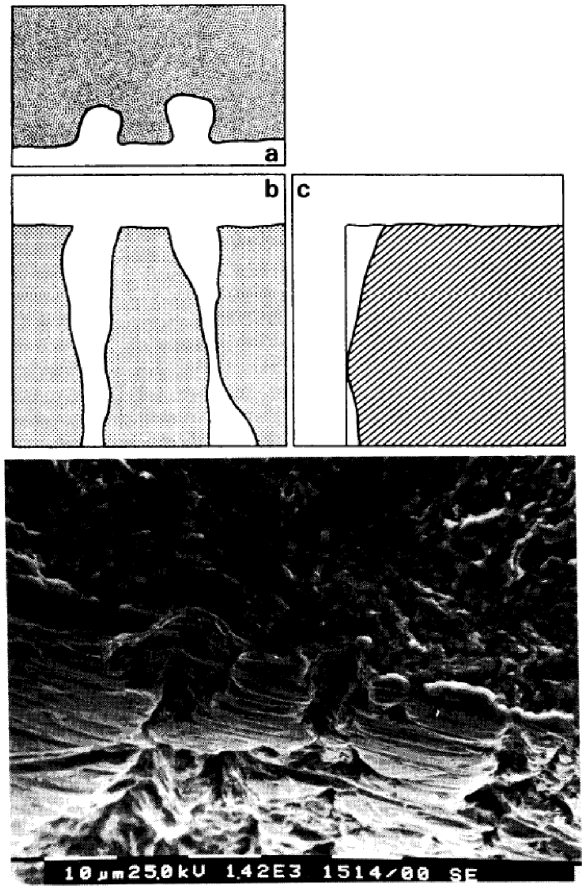

Figure 2.50: Two grooves as a crack origin. At the top of the figure, (a) the fatigue crack fracture plane, (b) the wire surface and (c) a section through the defect are shown schematically [78].

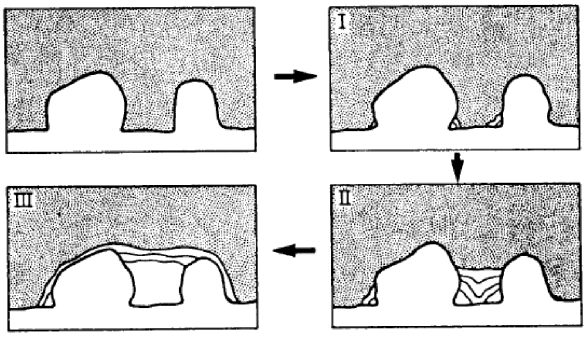

Figure 2.51: Crack initiation mechanism at two longitudinal grooves [78].

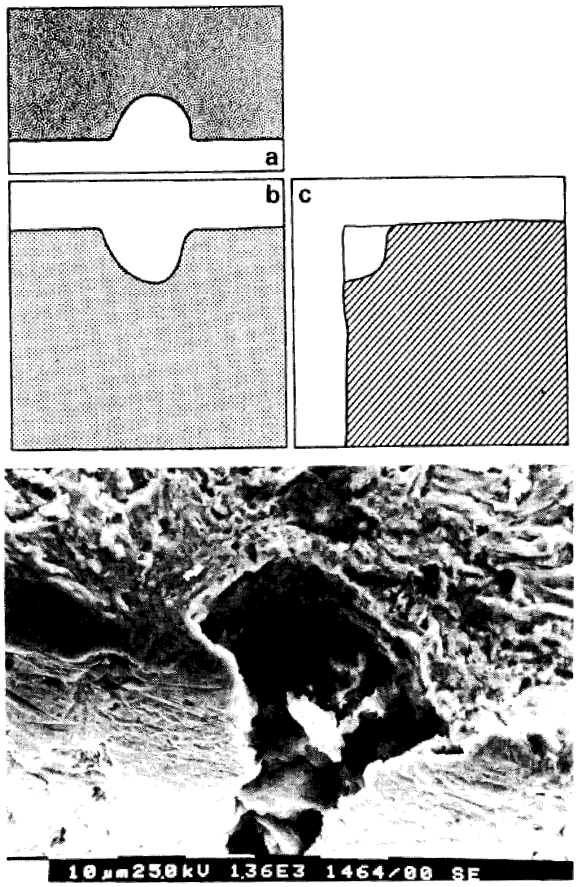

Figure 2.52: A hole or inclusion as a crack origin. At the top of the figure, (a) the fatigue crack fracture plane, (b) the wire surface and (c) a section through the defect are shown schematically [78].

– Holes (figure 2.52). These are mainly caused by surface inclusions which drop out during wire drawing or fatigue testing. Sometimes the inclusions are still present. A similar crack growth model as for the 'two grooves' is suggested.

Based on their fractographical results Verpoest et al. [78] concluded that every surface defect can be approached as a two dimensional semi-elliptical crack which is characterized by a depth a and a width 2c (or a geometrical factor a/c). Therefore they suggested to calculate the stress intensity factor of the surface defects using the geometrical factor α as is given by equation 2.27, which should be used to calculate the initial defect size (equation 2.26).

$$\alpha = -0.139\left(\frac{a}{c}\right)^2 - 0.314\left(\frac{a}{c}\right) + 1.12 \tag{2.27}$$

Through extensive experimental validation Verpoest et al. [78] developed a model that allows the prediction of the fatigue limit based on the surface defects size and geometry (equation 2.28).

$$\sigma_e = \frac{\Delta K_{th}}{2 \cdot \alpha \cdot \sqrt{\pi \cdot a_0}} \tag{2.28}$$

Figure 2.53 shows that fatigue limit of cold drawn steel wires can not only be improved by an increase in ΔK_{th} or a decrease in defect depth a_0, but also by an increase of the geometrical ratio a/c of the surface defects.

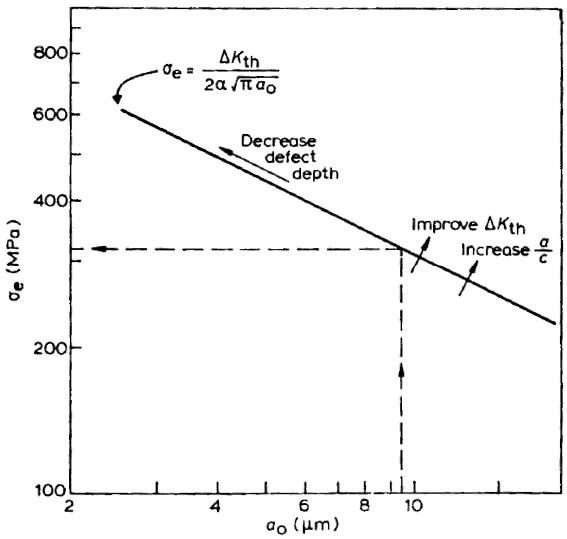

Figure 2.53: Suggested ways to improve the fatigue limit of steel wires [78].

Verpoest et al. [78] also investigated the influence of electropolishing the wire surface on the fatigue properties. Figure 2.54 shows that the fatigue life doubles after only 30 seconds of polishing and triples after 1 minute. Longer polishing times have only a marginal effect on the fatigue life. This can be explained by the presence of surface inclusions which can not be removed by the polishing operation. Verpoest et al. [78] were able to calculate the fatigue life from this limited data. They found that the fatigue life increased with 40% by the electrolytic polishing.

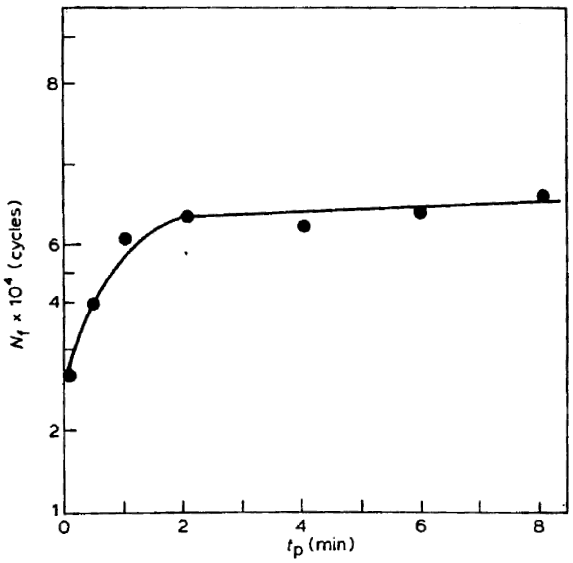

Figure 2.54: Number of cycles to failure at a fixed applied stress as a function of the polishing time [78].

Some years later Llorca and Sanchez-Galvez [80] studied the influence of the stress ratio R on the threshold stress intensity factor range ΔK_{th} of cold drawn wires with a diameter of 7 mm. The wires were drawn to a total strain of 1.08. To measure the crack growth rate the fatigue test was stopped, the samples were heated for 10 to 15 minutes at 200°C and the test was continued. In this way the different regions of crack growth can easily be distinguished due to the presence of an oxide film for the part of the fatigue crack that was heated. Using this method, Llorca and Sanchez-Galvez [80] were able to measure crack growth rates as low as 10^{-11} m/cycle.

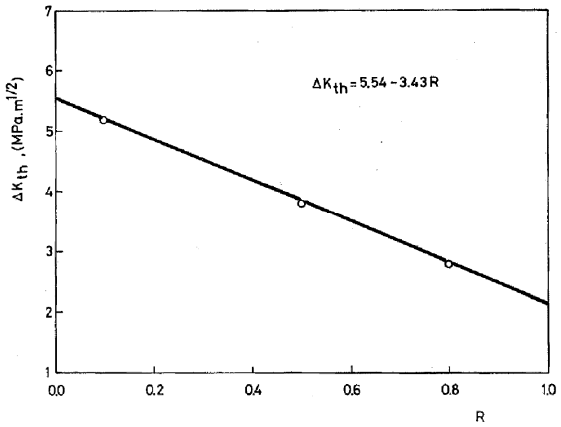

Figure 2.55: ΔK_{th} as a function of R [80].

Llorca and Sanchez-Galvez [80] determined ΔK_{th} for three different R values and defined the fatigue threshold at a crack growth rate of 10^{-11} m/cycle. Figure 2.55 shows the ΔK_{th} as a function of R. It was observed that the experimental results follow the Barsom [50] linear fit (equation 2.15) with A = 5.54 and B = 3.43. Although their results are in agreement with the observations of Verpoest et al. [78] and the Barsom linear fit is followed almost perfectly, it is necessary to make some comments on their obtained results. First of all it can be expected that the crack growth rate measurement method that was used for this study alters the fatigue thresholds of the material since the thickness of the oxide layer is increased. This can alter the results in two ways. Firstly, due to an increase in oxide thickness the amount of oxide induced crack closure will increase. Secondly the oxide thickness at the crack tip can influence $K^{*}_{max,th}$ [77] which will have an impact on ΔK_{th} for low R values. Further it is important to notice that the scatter of the experimentally measured ΔK_{th} is very large (ΔK_{th} = 2.8 ± 0.5 MPa√m for R = 0.8) for high R ratios due to limitations in the experimental methods that were used. This is important since a horizontal asymptote could be expected for high R values based on modern literature (see paragraph 2.3.2 and 2.3.4).

Llorca and Sanchez-Galvez [80] also observed a linear relationship between ΔK_{th} and the tensile strength for low R values (R = 0, 0.1) but were not able to draw the same conclusions for high R ratios (R > 0.6) due to excessive scatter of the fatigue data.

Based on this data Llorca and Sanchez-Galvez developed a model to predict the fatigue limit and the fatigue life and published this a few years later [81]. Using linear elastic fracture mechanics (LEFM) and the experimentally obtained linear relationship between ΔK_{th} and R they derived equation 2.29.

$$\sigma_F = \frac{5.54 - 3.43 \cdot R}{F\left[a_0, (a/c)_0\right]} \tag{2.29}$$

Where σ_F is the fatigue limit and $F\left[a_0,(a/c)_0\right]$ is the crack intensity factor at the tip of a semi-elliptical crack loaded by a unit stress (unit: $\sqrt{m}$). Figure 2.56 shows the calculated fatigue limit as a function of R. Taking into account that the maximum stress in a cycle can never be higher than the ultimate tensile strength equation 2.29 is limited by:

$$\sigma_F = \sigma_u (1-R) \tag{2.30}$$

From figure 2.56 it can be concluded that the fatigue limit decreases with an increasing defect size and that residual stresses alter the fatigue life considerably. These calculated predictions are in good agreement with the experiments and with results from literature. Llorca and Sanchez-Galvez [81] further observed that the fatigue limit strongly depends on R, the defect depth and residual stresses and to a lesser extent on the shape of the defect.

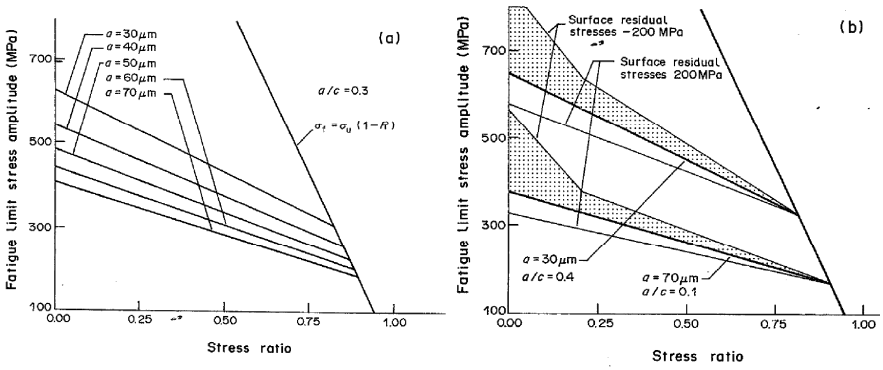

Figure 2.56: Fatigue limit as a function of the R value calculated with equation 2.29. (a) influence of the defect depth, (b) influence of residual stresses [81].

Almost 10 years later Beretta and Matteazzi [82] investigated the short crack growth behavior of eutectoid steel wires. They used wires with a diameter of 1.97 mm which were drawn to a total strain of 2.05. They developed a crack growth model that takes the short crack growth regime into consideration and that is based on the model of El haddad et al. [63] (equation 2.19). Based on experimental results Beretta and Matteazzi [82] calculated the El Haddad parameter a_0 with a geometrical factor of 0.74 for semi-circular crack in an infinite solid:

$$a_0 = \frac{\left(\Delta K_{th} \Big/ \left((1-R)\cdot\sigma_{cyc}\cdot 0.74\right)\right)^2}{\pi} \tag{2.31}$$

with σ_{cyc} the cyclic yield stress. Figure 2.57 shows the Kitagawa-Takahashi diagram of the experimental and calculated results. The figure shows that the

developed model predicts the crack growth behavior of the steel wires very well, both in the long and the short crack growth region.

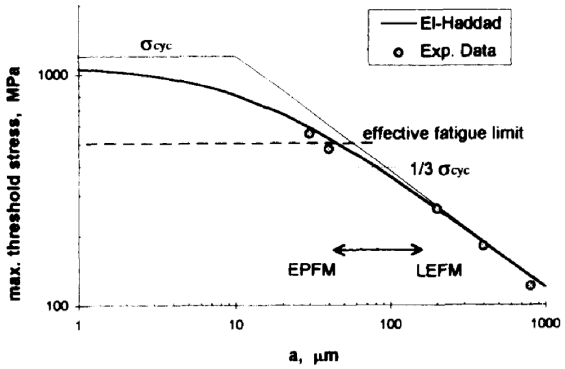

Figure 2.57: Kitagawa-Takahashi diagram with the experimental and the calculated data [82].

When the model is however used to predict the fatigue life of steel wires it predicts a conservative life compared to the experimental results (figure 2.58).

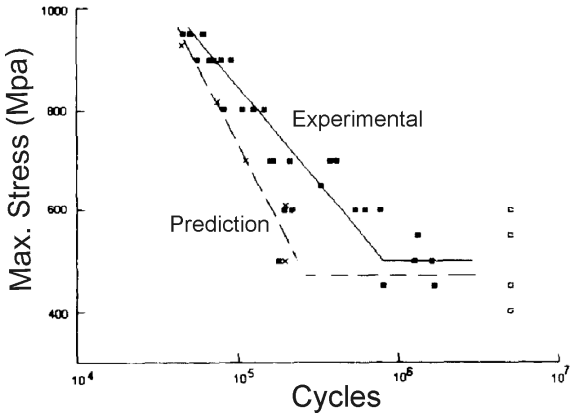

Figure 2.58: Experimental and predicted fatigue lives presented in a SN graph [82].

Recently, Yang et al. [83] investigated the possibility of improving the bending fatigue resistance of steel wires by post processing heat treatments. They used hyper-eutectic steel cord filaments with a diameter of 180 μm that were drawn to a strain of 4.12. The wires were annealed to temperatures ranging from 100 to 500 °C for 60s and then cooled down to room temperature in air. For each sample the fatigue limit was determined using a Hunter rotating beam fatigue machine. Figure 2.59 shows the influence of the annealing temperature on the fatigue limit and the tensile strength.

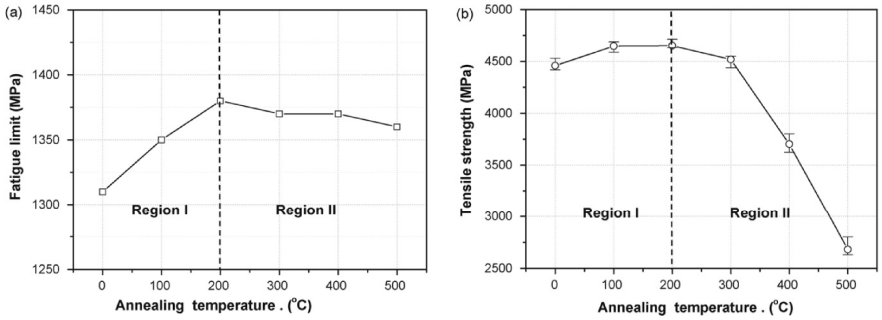

Figure 2.59: Behavior of the mechanical properties of steel wires depending on the annealing temperature: (a) bending fatigue resistance and (b) tensile strength [83].

The figure shows that the fatigue limit as well as the tensile strength are strongly influenced by the annealing temperature and show different behaviors in the temperature Regions I (0–200 °C) and II (200–500 °C). The optimum temperature to obtain the maximum fatigue resistance is 200 °C and corresponds with the maximum in the tensile strength. This behavior was explained by a combination of strain aging and the relaxation of residual stress in temperature region I and by the increase in surface roughness in Region II.
It is important to note that based on the ΔK_{th} which are reported in literature it is not possible to explain the decrease in fatigue limit in temperature region II by the marginal increase in surface defect size (from 0.1 to 0.5 μm based on surface roughness measurements). Since the tensile strength strongly decreases in temperature region II the mechanisms behind the decrease in fatigue limit is most probably related to a change in microstructure.

In 2010 Petit et al. [79] published an article about the fatigue crack propagation in thin wires of ultra high strength steels. The fatigue threshold for crack growth was measured using crack growth rate measurements on wires with a diameter of 0.95 mm which were drawn to a strain that is larger than 2. The wires were mechanically machined to remove the surface layers and obtain a rectangular section of the wire (which simplifies the crack growth rate measurements). The crack growth rate was measured using a long distance microscope and the threshold value was defined at a crack growth rate of 10^{-11} m/cycle.
Figure 2.60 shows the results of pull-pull stress driven fatigue tests at an R ratio of 0.4 and 0.7. It is observed that for high ΔK values the fatigue data corresponds with the same curve for both R values ($da/dN > 10^{-9}$ m/cycle) and follows the Paris regime. When the fatigue data however starts to deviate from the Paris regime ($da/dN < 10^{-9}$ m/cycle) the scatter becomes very large.

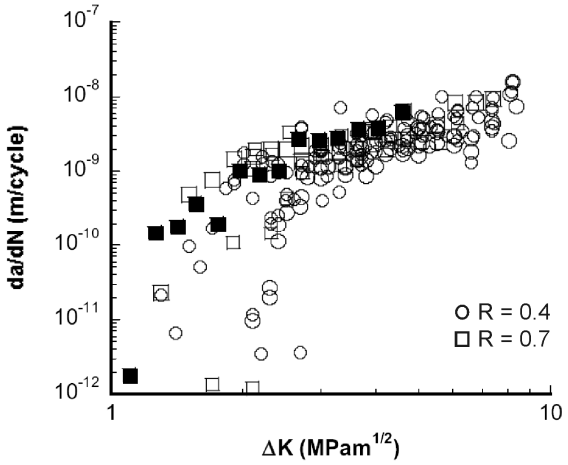

Figure 2.60: Crack growth rate (da/dN) as a function of ΔK for R = 0.4 and R = 0.7 [79].

Although Petit et al. [79] claim a generally lower fatigue threshold for the higher R value, the difference is not statistically significant, and therefore it is not right to draw such a conclusion. Figure 2.61 shows the measured fatigue thresholds of this study compared to data from literature.

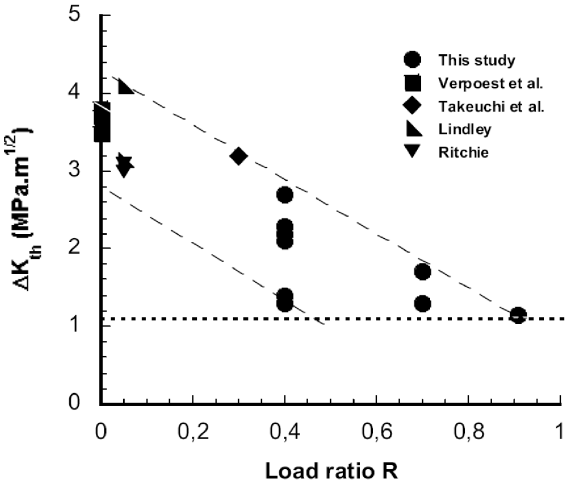

Figure 2.61: ΔK_{th} dependence on R [79].

Figure 2.61 shows that for R = 0.4 ΔK_{th} ranges from 1.3 to 2.8 MPa$\sqrt{m}$. The scatter for R = 0.7 appears to be smaller, however, since they did only two tests at this R value these results are not conclusive and it could be misleading to draw the dashed trend lines in figure 2.61.
Petit et al. [79] tried to explain their results by a substantial contribution of crack closure in combination with the presence of residual stresses. It is however very

doubtful that the observed large scatter can be explained by the presence of crack closure. First of all it is shown in several publications [84-87] that plastic crack closure is insignificant around ΔK_{th}. Further, Vasudevan et al. [88] showed that the decrease of ΔK_{th} with R is more dependent on environmental effects that alter the fatigue crack growth than on roughness/oxide induced closure. Due to the high applied R ratios (≥ 0.4) other crack closure effects such as roughness and oxide induced crack closure are expected to be marginal. This means that based on the present knowledge on crack closure it is highly unlikely that crack closure can cause such extreme scatter in ΔK_{th}. Secondly there is no reason why two identical samples that are tested under exactly the same conditions would show a completely different crack closure behavior.

It is more likely however that the experimental results of Petit et al. [79] are disturbed by local environmental changes. The possible mechanisms involved are explained in detail in paragraph 4.1.2 (Environmentally assisted fatigue crack initiation) of this book and it is experimentally shown that local environmental changes can lead to a very large scatter in the fatigue properties.

Further it is important to note that, due to the removal of surface material in order to create the samples, the internal stress state will be changed completely. Therefore, even if the scatter of ΔK_{th} was low, it would be impossible to interpret the results without the measurement of the residual stresses inside the newly created test sample.

2.5 Conclusions

At the moment the author is not aware of any publications that describe the fatigue properties of heavily drawn steel wires. The work of Verpoest et al. [78] which was done 30 years ago and the work of Beretta and Matteazzi [82] which was done 15 years ago successfully describe the fatigue properties of wires with a diameter of 2 mm. Both observed that the fatigue properties of these wires are controlled by surface stress concentrations which are mostly introduced by the wire drawing process itself. Since the wires that will be investigated in this study have a diameter that is one order of magnitude smaller, it is interesting to check whether or not surface stress concentrations are still controlling the fatigue properties of these very thin wires.

Yang et al. [83] did do bending fatigue tests on wires with a diameter of 180 μm. They investigated the influence of a heat treatment after drawing on the fatigue limit of heavily drawn steel wires, but they did not perform (or reported) a fractography study and therefore didn't describe the fatigue crack initiation or propagation mechanisms. This lack of understanding governed the decision to investigate the fatigue mechanism for heavily drawn steel wires in this study.

It is important to note that, at the moment, the mechanisms behind the cementite decomposition are not understood well. Further, the relation between the microstructure and the fatigue properties of heavily drawn steel wires hasn't been reported yet. A research proposal on this topic is described in paragraph 9.3.

3 Materials and methods

3.1 Materials

All the fatigue tests in this study are performed on brass coated steel wires. Table 3.1 gives the used abbreviation (type), diameter, strength class, total strain, Ultimate Tensile Strength (UTS) of all the wires used in this study.

Table 3.1: Properties of brass coated steel wires used in this study.

Type	∅ (μm)	Strength class	Total strain (ε)	UTS (MPa)
175 NT	175	Normal tensile	3.5	3187 ± 37
175 HT	175	High tensile	3.5	3378 ± 51
300 HT	300	High tensile	3.6	3300 ± 100

The difference in the strength class, between normal and high tensile, is related to the composition of the steel, more specifically to the carbon content. For confidentiality, the exact composition of the steels is not given.
Within one strength class the wires have the same carbon equivalent (%CE = %C + %Mn/6). It is important to note that the wire rod used to draw the wires comes from different suppliers, meaning that differences in inclusion properties (size, composition and distribution) can be expected.

3.2 Methods

3.2.1 Fatigue tests

Fatigue tests were performed on a hydraulic Schenk fatigue machine with a linear actuator PLZ 7 and a 1 kN load cell. The experiments done in this study are load driven pull-pull fatigue tests performed at a frequency of 60 Hz and with a gauge length of 80 mm.
It was intentionally chosen to do pull-pull fatigue tests in stead of bending fatigue tests. This choice is based on results of finite element modeling (FEM, done by NV Bekaert SA) of the application (steel cords used in a tire). The FEM analysis showed that the load ratio ($R=\sigma_{min}/\sigma_{max}$) is between 0.4 and 0.6 for the final application. Therefore almost all of the fatigue tests were performed with an R value of 0.5. For an R value of 0.5 about 5% of the samples fractures inside the clamps of the fatigue machine. These fractures are not taken into consideration.

In order to check the influence of the environment on the fatigue properties, fatigue tests were done on reference wires (69 samples), coated wires (104 samples), wires that are submerged in isopropanol (7 samples) and on cleaned wires (123 samples).
The reference wires are the wires in the as received state (after production). When the reference wires are cleaned by whipping the surface with acetone and ethanol they are called cleaned wires. When a coating is applied on these cleaned wires

they are called coated wires. Three different coatings were used namely cyanoacrylate glue (84 samples), benzotriazole (BTA, 9 samples) and rubber (11 samples).
Except for the fatigue tests in isopropanol, the fatigue tests were performed in a controlled environment with a relative humidity of 54 ± 4 % and a temperature of 20.4 ± 0.3 °C.

In total more than 300 successful fatigue tests were performed on the 175 µm wires (175 HT and NT) at a R value of 0.5. The reference wires are tested at five different stress amplitudes σ_a = 416, 520, 624, 707 and 748 MPa. Figure 3.1 gives a schematic illustration of the stress during the fatigue tests at σ_a = 416, 520 and 624 MPa and R=0.5.

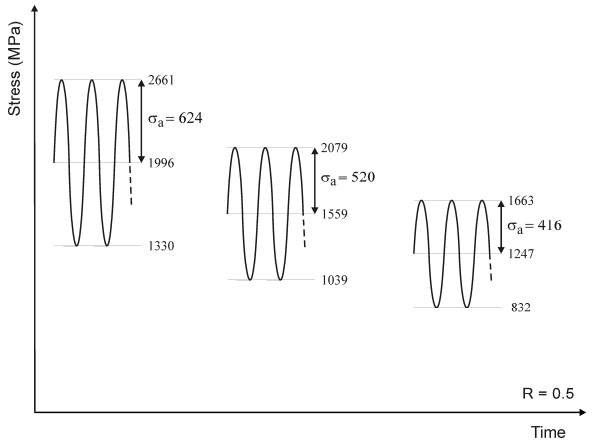

Figure 3.1: Schematic illustration of the stress during fatigue tests at different σ_a and R=0.5.

Table 3.2: Overview of the loading conditions and the amount of repetitions for the different R ratios for the 175 µm wires.

R	σ_a (MPa)	σ_{mean} (MPa)	σ_{min} (MPa)	σ_{max} (MPa)	# samples
0.05	956	1060	104	2016	7
0.2	1123	1705	582	2827	29
0.4	854	1996	1142	2850	43
0.5	416	1247	832	1663	11
0.5	520	1559	1039	2079	77
0.5	624	1996	1330	2661	15
0.5	707	2120	1414	2828	164
0.5	748	2245	1497	2993	36
0.6	561	2245	1684	2806	5

In order to check the influence of the load ratio 175 µm wires were fatigue tested at 5 different load ratios ($R=\sigma_{min}/\sigma_{max}$): 0.05, 0.2, 0.4, 0.5 and 0.6. Table 3.2 gives an overview of the loading conditions and the amount of repetitions for the

different R values. Figure 3.2 shows a schematic illustration of the stress during fatigue tests at different R ratios.

To study the influence of inclusions on the fatigue properties wires with a diameter of 300 μm were used (43 samples). The wires were loaded at σ_a = 670 MPa and R = 0.5 (σ_{max} = 2680 MPa).

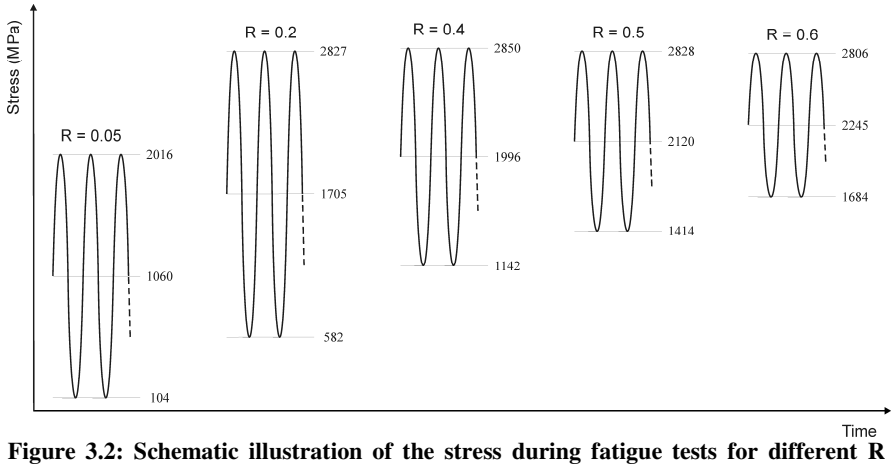

Figure 3.2: Schematic illustration of the stress during fatigue tests for different R values.

3.2.2 Fractography

A fractography study was performed on all fatigue fractures with scanning electron microscopy (SEM) using a FEI XL30 FEG or a FEI XL40 Lab6 system. In order to look at the fracture surface of the wires (perpendicular to the wire axis), the fatigue fractures are positioned vertically in the vacuum chamber of the SEM. The SEM image is then used to position the fracture surface perpendicular to the indecent electron beam, which is schematically illustrated in figure 3.3. When the wire is not positioned completely vertical a part of the wire surface will be visible in the SEM image (left side of figure 3.3). The stage of the SEM is tilted until only the fracture surface can be seen in the SEM image. By following this procedure it is possible to position the fracture surface perpendicular to the indecent electron beam with an estimated error of about ± 2°, leading to a negligible error of ± 0.06 % on the geometries that are measured on the fracture surface. It is important to note that in some cases the wires are curved which makes the above described procedure less accurate. When it is assumed that the error increases for this case to ± 5°, the error on geometrical measurements is still only ± 0.4%.

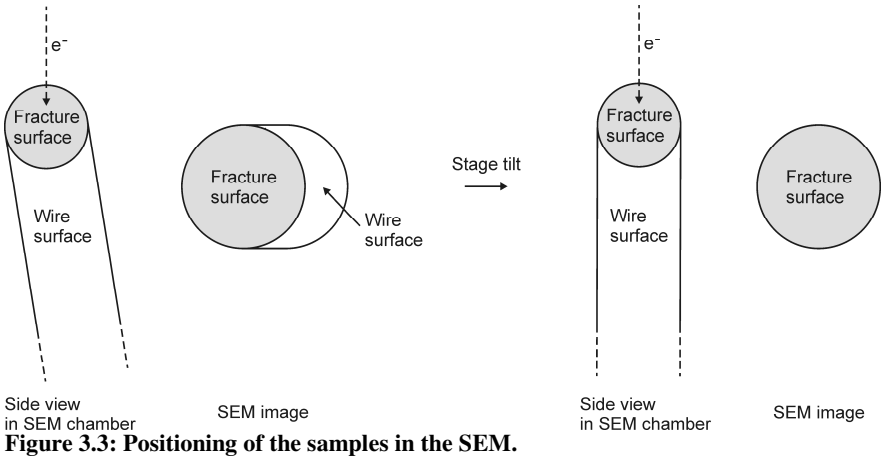

Figure 3.3: Positioning of the samples in the SEM.

To measure geometries on the SEM image, a freeware image processing software, ImageJ (http://rsbweb.nih.gov/ij/), is used. Each dimension (length or area) is measured three times and the average of the three measurements is used. To estimate the error of the geometry measurement technique 10 different SEM images are analyzed. On each SEM image a characteristic length and a characteristic area is measured 5 times and the 95 % confidence intervals are calculated. The average of the 95% confidence intervals of the 10 different SEM images is used as an approximation of the error. For the length measurements the error is estimated to be ± 0.3 % and for the area measurements ± 1.4 %.

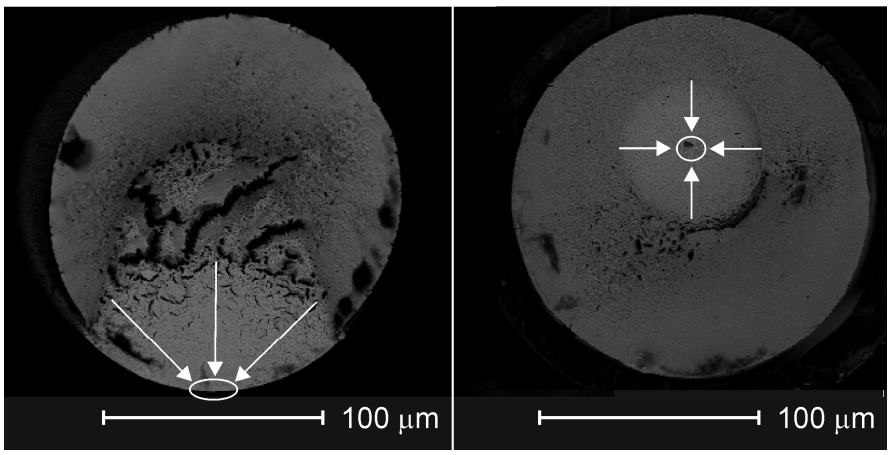

Figure 3.4: Determination of the fatigue crack initiation area of a surface (left) and internal (right) fatigue fracture.

To be able to determine the cause of failure (=fractography study) it is assumed that the fatigue cracks grow semi-circular or semi-elliptical when the fatigue crack initiates from the surface and circular or elliptical when the fatigue crack

initiates internally. Since the residual fracture plane, which is an overload fracture that fails by micro void coalescence, can be distinguished easily from the fatigue fracture, it is possible to determine the fatigue crack initiation area. Figure 3.4 gives an example of a surface and an internal fatigue fracture. The white arrows point from the residual fracture towards the fatigue crack initiation area.
By investigation the fatigue crack initiation area in depth it should be possible to determine the active fatigue crack initiation mechanism.

To study the microstructure around non-metallic inclusions a SEM/FIB (focused ion beam) FEI Dual beam Nova 600 Nanolab system is used to etch material away from the surface of the wire to the place of interest. The material was etched away using a FIB current of 0.92 nA. The microstructure around the inclusion was made visible by FIB imaging with a current of 9.3 pA.

4 Fatigue mechanisms

This chapter explains all the fatigue crack initiation and growth mechanisms that are observed for the steel wires investigated in this study. No differences in initiation or growth mechanisms were observed between the different wire diameters, nor between the different applied loading conditions.

4.1 Fatigue crack initiation mechanisms

Based upon multiple experimental results it was possible to determine the different fatigue crack initiation mechanisms that are active for the heavily drawn steel wires investigated in this study. For the reader's convenience an overview of the different active crack initiation mechanisms is made and is shown here, before the different initiation mechanisms are described (figure 4.1).
It is observed that fatigue cracks can initiate from the surface or from the interior of the wire (called fracture modes in the following discussion).
The different fatigue crack initiation mechanisms are schematically shown in figure 4.1. Two different fracture modes were observed, namely surface and internal crack initiation. Two fatigue crack initiation mechanisms were found to be active, namely environmentally assisted fatigue crack initiation and crack initiation at stress concentrations. Both initiation mechanisms were observed for surface crack initiations while internal fatigue cracks always initiated at stress concentrations.

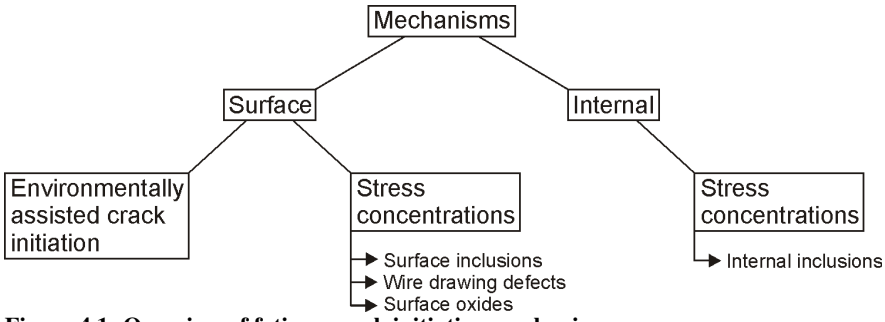

Figure 4.1: Overview of fatigue crack initiation mechanisms.

4.1.1 Fracture modes

Two different fracture modes were observed for the heavily drawn steel wires investigated in this study, namely surface and internal fatigue crack initiation. The left side of figure 4.2 shows a surface fatigue crack initiation, the right side shows an internal fatigue crack initiation (Also referred to as fish eye fracture in literature). The fatigue crack initiation area is indicated with a white ellipse.

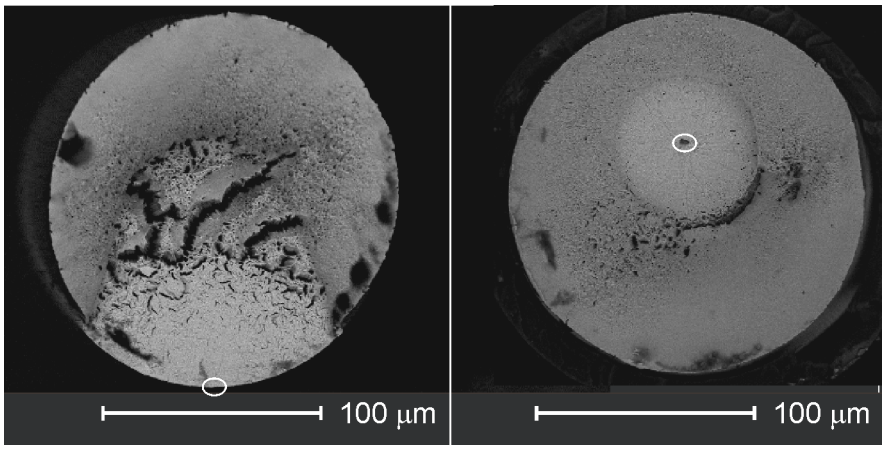

Figure 4.2: Fracture modes of heavily drawn steel wires.

There are two important differences between both fracture modes.
Firstly, there is the difference in stress intensity factor (SIF) range due to the difference in boundary conditions between surface and internal fatigue cracks. Murakami's formulae [45] for fatigue cracks with an arbitrary shape show a difference of 30% in geometrical factor (0.65 versus 0.5).

$$\Delta K_{surface} = 0.65 \cdot \Delta\sigma \cdot \sqrt{\pi\sqrt{area}} \qquad (4.1)$$

$$\Delta K_{internal} = 0.5 \cdot \Delta\sigma \cdot \sqrt{\pi\sqrt{area}} \qquad (4.2)$$

with ΔK the stress intensity factor range [MPa$\sqrt{}$m], $\Delta\sigma$ the applied stress range (= $2\sigma_a$, [MPa]) and $\sqrt{area}$ the root of the area of the fatigue crack projected on the plane perpendicular to the wire axis [m].
Secondly, there is the difference between the environmental condition between surface and internal fatigue cracks. Environmental interactions can have an effect on surface fatigue crack initiations (paragraph 4.1.2). Since internal fatigue cracks are not in contact with the environment, no environmental interactions are possible during fatigue crack initiation.

4.1.2 Environmentally assisted fatigue crack initiation

It is observed that if the heavily drawn steel wires investigated in this study are subjected to a cyclic load when they are in the as received state (after production, without cleaning or coating), fatigue cracks will initiate due to environmental interactions rather than at pre-existing surface stress concentrations. This environmentally assisted fatigue crack initiation was discovered due to an observed difference in fatigue life between as-received wires and cleaned and coated wires.

4.1.2.1 Coated wires.

To investigate the influence of coating the wires two different coatings are used, namely a Sicomet 50 cyano-acrylate glue coating (referred to as glue) and a benzotrialzole coating (referred to as BTA). Before coating, the wires are cleaned intensively by wiping the surface at least 5 times with acetone to remove dirt and residual lubricant, followed by wiping the surface at least 2 times with ethanol to remove the residual acetone. The glue coating has a varying thickness between 2 and 50 μm, the BTA coating has a more homogeneous thickness that is smaller than 1 μm. Both coatings completely cover the wire surface. After cleaning and coating, the wires are fatigue tested within 2 weeks.

Figure 4.3 shows the fatigue data of reference (as received after production) and coated 175 HT wires in an SN-graph. The fatigue tests were performed at three different stress levels (σ_a = 416, 520 and 624 MPa) and an R value of 0.5.

It is observed that coated wires have a higher fatigue life than the reference wires. No difference in fatigue life is observed between both coatings.

Since the BTA coating is very thin (submicron) it can not have any mechanical retardation effect (the coating doesn't change the stress state at the surface of the wire) on the fatigue crack initiation mechanisms. Therefore the improved fatigue properties of the coated filaments can be addressed completely to environmental effects. To confirm this hypothesis fatigue tests are done in isopropanol, in which corrosion should be impossible (paragraph 4.1.2.2). Further it is important to check the influence of cleaning on the fatigue properties (paragraph 4.1.2.3).

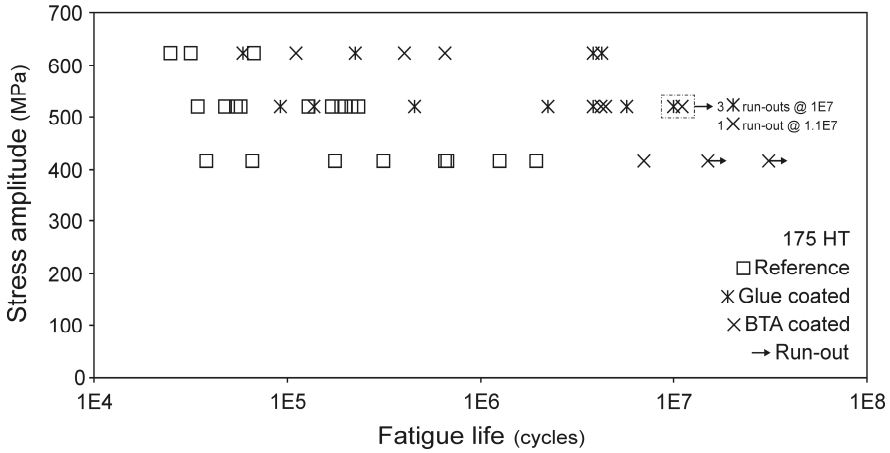

Figure 4.3: Fatigue data of reference and coated 175HT wires.

To confirm the improved fatigue life of coated filaments, the experiments were repeated on 175 NT wires. Since no difference in fatigue life was observed between different applied stress amplitudes, the new tests were only performed on one stress level. Further it was chosen to compare the reference state of the wire with only the glue coating.

Figure 4.4 shows the fatigue data of the 175NT wires. Although the fatigue tests on the reference and the glue coated wires are performed on the same stress level (σ_a = 707 MPa), they are depicted on a different position on the vertical axis in figure 4.4 to improve its readability. This means that the figure should be viewed without consideration of the vertical axis.

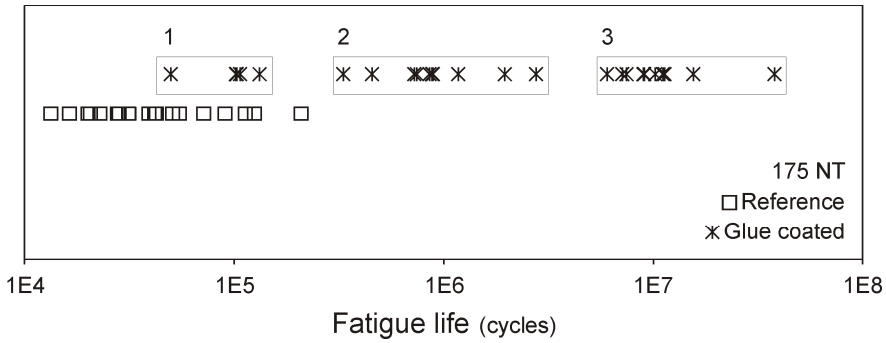

Figure 4.4: Fatigue properties of reference and glue coated 175 NT wires.

For the 175 NT filaments it is observed that the coated filaments have a higher fatigue life than the reference wires. It is however important to note that the scatter of the coated filaments is much higher than for the reference filaments. When looking closer to the fatigue data of the 175 NT wires the data points can be subdivided in three different groups, indicated as 1, 2 and 3 in figure 4.4.
To check whether or not the groups are significantly different, an analysis of variance (ANOVA) was used. One of the assumptions of ANOVA is that the data are normally distributed. Therefore it is not possible to use the fatigue life (no normal distribution) in the data analysis. When however the logarithm of the fatigue life is taken, the data become normally distributed. Therefore, the logarithm of the fatigue life will be used throughout the complete study in stead of the fatigue life (all graphs will have a logarithmic scale and the logarithm of the fatigue life is given in all tables).
It is calculated that all groups are significantly different from each other (ANOVA, α=0.05). Table 4.1 gives the mean, standard deviation, minimum, maximum and the lower and upper confidence limit (LCL, UCL) of the logarithm of the fatigue life of each group.

Table 4.1: Statistical data of the logarithm of the fatigue life for the different groups.

Group	Mean	Standard deviation	Min.	Max.	LCL (95%)	UCL (95%)
1	4,97	0,16	4,70	5,12	4,77	5,17
2	5,95	0,27	5,52	6,44	5,76	6,15
3	7,02	0,22	6,78	7,58	6,88	7,17

Figure 4.5 shows the box plot of the fatigue data which is a good tool to give a graphic representation of several groups of fatigue data and helps to see the spread, skewness and possible outliers. The box represents the first quartile (Q_1),

the median (Q_2) and the third quartile (Q_3). This means that the inter quartile range (IQR) represents 50 % of all data. The whiskers (vertical lines starting from the box) show the lowest and the highest data still within 1.5 times the IQR. All data outside the whiskers (if any) is considered as an outlier.
The box plot in figure 4.5 clearly shows the difference between the three groups.

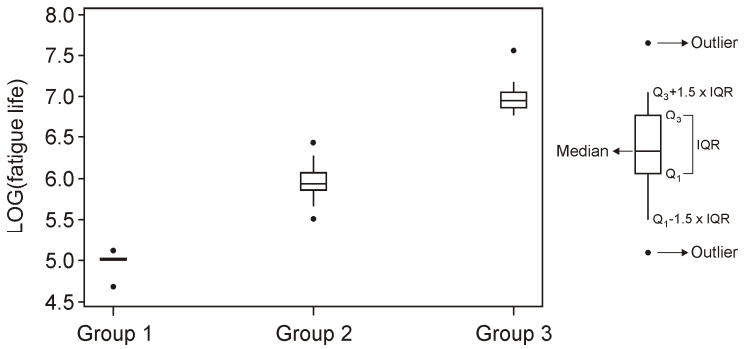

Figure 4.5: Box-plot of the coated wires.

Since the fatigue data of the coated wires can be subdivided into three significantly different groups and all the coated wires are believed to be identical (same wire rod material, wire drawing production process, coating procedure and time between production and fatigue testing), it can be expected that different fatigue mechanisms are active. Therefore a fractography study was done on all fatigue fractures.

To be able to explain that there are three different fatigue crack initiation mechanisms active for the three groups, it is necessary to compare the ΔK value of the stress concentration to the threshold value for crack growth ($\Delta K_{th,R}$). $\Delta K_{th,R}$ is calculated in chapter 5 using a newly developed threshold determination method. For R = 0.5, $\Delta K_{th,R} = 3.82 \pm 0.09$ MPa$\sqrt{m}$.

Group 1
The fractography study shows that there is only one fatigue crack initiation mechanism active for the coated wires in group 1, namely fatigue crack initiation at surface stress concentrations with a stress intensity factor that is larger than the fatigue threshold. This initiation mechanism is explained in detail in paragraph 4.1.3.1.

Group 2
The fractography study shows there is only one fatigue crack initiation mechanism active for the coated wires in group 2, namely fatigue crack initiation at surface stress concentrations with a stress intensity factor that is smaller than the fatigue threshold. This initiation mechanism is explained in detail in paragraph 4.1.3.1.

Group 3

The fractography study shows there is only one fatigue crack initiation mechanism active for the coated wires in group 3, namely fatigue crack initiation at internal stress concentrations. This initiation mechanism is explained in detail in paragraph 4.1.3.2.

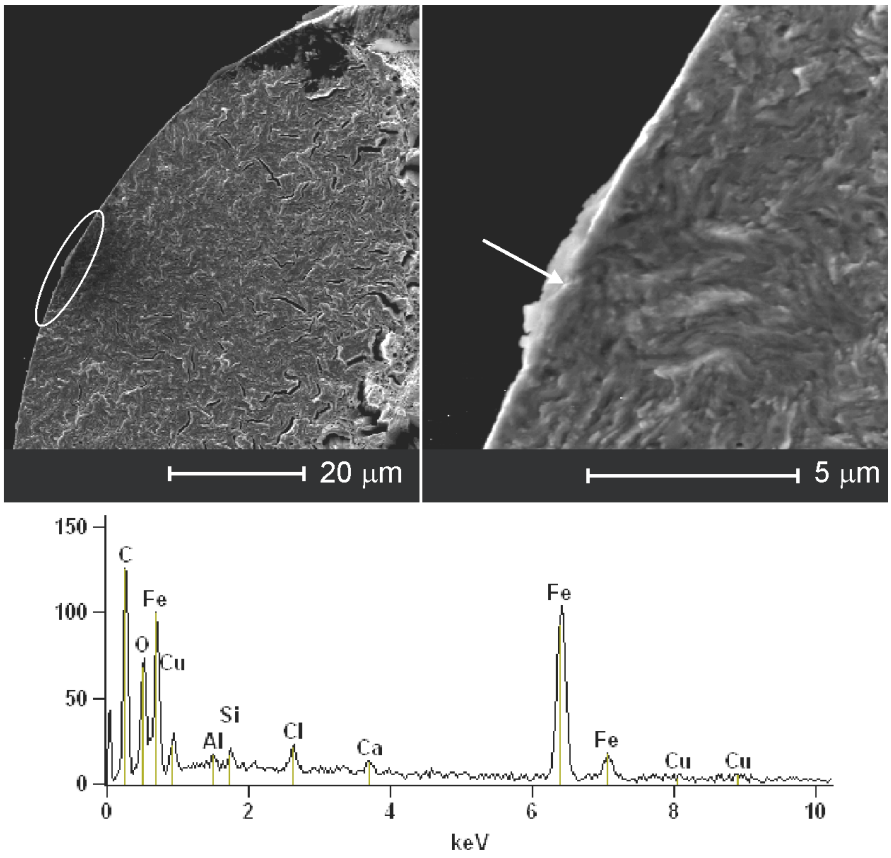

Figure 4.6: Fatigue fracture of uncoated wire that fracture due to environmental influences.

For the reference wires (uncoated) no subdivision can be made based upon the fatigue life. The different fatigue behaviour could be explained by environmental effects as described above. To get a better understanding about the possible active mechanisms, all fatigue fractures are investigated using SEM/EDX analysis.

The majority of the fatigue fractures (about 3 out of 4 fractures) show no stress concentrations at the fatigue crack initiation area. Figure 4.6 gives an example of such a fracture. The fatigue crack initiation area is shown by the white ellipse on the left top side of figure 4.6 and the right top side shows a magnification of this region. The SEM pictures show no defect in the initiation area, but on most of the

fractures some dirt is found at the surface of the wire. The bottom of figure 4.6 shows the EDX spectrum of the point indicated by the arrow on the right SEM picture. Besides some traces of Al, Si and Ca, chlorides were found on the surface of the wire. The presence of chlorides, which are known as corrosion accelerators, can play a role in environmentally assisted fatigue crack initiation. The combination of the absence of stress concentrations and the presence of chlorides further confirms the hypothesis of environmentally assisted crack initiation. To confirm the influence of chlorides, fatigue tests are done on cleaned wires and on cleaned wires whereon chlorides are added intentionally (paragraph 4.1.2.3). To confirm the influence of environmental effects, fatigue tests are performed in isopropanol (paragraph 4.1.2.2).

In reference to the final application of the steel cord filaments, fatigue tests are done on rubber coated wires. The rubber coating is applied by Bekaert using the same process conditions as requested by the tyre companies (customers of Bekaert). Therefore all the rubber coated wires have a gauge length of about 43 cm (in stead of 8 cm for all the other fatigue tests done in this study). The higher gauge length does not change the active fatigue mechanisms itself, but caution is needed when the data are analyzed statistically. Since the failure probability is constant for a certain gauge length, the probability of having a critical defect (environmentally assisted crack initiation or surface stress concentrations which are larger than the fatigue threshold) increases when the gauge length increases. Therefore it is expected that more wires fail at a lower amount of cycles compared to fatigue tests on smaller gauge lengths.
Fatigue tests are performed at a stress amplitude σ_a = 520 MPa and an R value of 0.5. Figure 4.7 shows the box plot of the fatigue data. It is observed that part of the rubber coated wires (8 out of 11 fractures, indicated as Rubber 1) have a fatigue life that is comparable with the reference wires (uncoated 175 HT wires). The other fractures (3 out of 11, indicated as Rubber 2) have a significantly higher fatigue life (ANOVA α = 0.05).

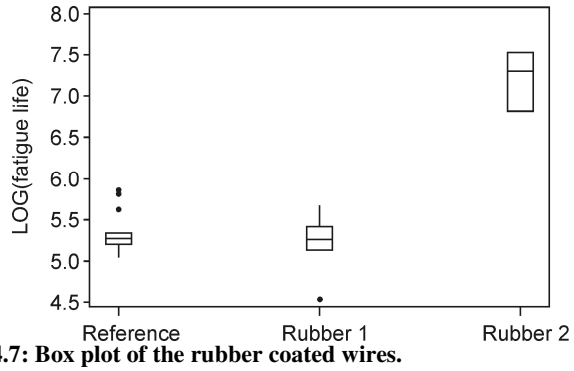

Figure 4.7: Box plot of the rubber coated wires.

A fractography study confirms that the wires from the group 'Rubber 1' fractured at surface stress concentrations with a stress intensity factor which is larger than

the fatigue threshold. On some of these fractures chlorides were present at the crack initiation area. For the wires of the group 'Rubber 2' all the fatigue cracks initiated at surface stress concentrations with a stress intensity factor which is lower than the fatigue threshold.

4.1.2.2 Tests in isopropanol

To confirm the assumption that environmentally assisted fatigue crack initiations determine the fatigue life of uncoated wires, fatigue tests are performed in isopropanol (C_3H_8O) instead of lab air. Isopropanol is intentionally chosen as a test medium in stead of other alcohols due to the possibility of producing completely water free isopropanol. The absence of water is important because otherwise it is still possible for corrosion mechanisms to take place.
In practice it was necessary to design a vessel that could be mounted in between both clamps on the fatigue machine. The vessel is shown in figure 4.8.

Following procedure is followed to set-up the tests in isopropanol:

- The wire is cleaned using the same procedure as for coated wires.
- Two aluminium plates are glued to the bottom of the wire which will be used to fix the wire to the bottom of the machine.
- The wire is put through the bottom hole of the vessel. The bottom of the vessel is sealed with glue.
- The top part of the wire is coated with glue to protect it from environmental influences.
- The vessel is mounted on the lower clamp and the aluminium plates are fixed to the bottom of the machine using the lower clamp.
- The vessel is filled with isopropanol until the uncoated part of the wire is completely submersed.
- The top of the vessel is closed.
- Two aluminium plates are glued on the top of the wire and are used to clamp the top of the wire into the fatigue machine.

When the above procedure is used correctly, there is an uncoated part of the wire with a length of about 80 mm completely submerged in isopropanol and there is no uncoated part of the wire in contact with the environment. Only the fatigue fractures that occur at the uncoated submerged part are taken into consideration in this study.

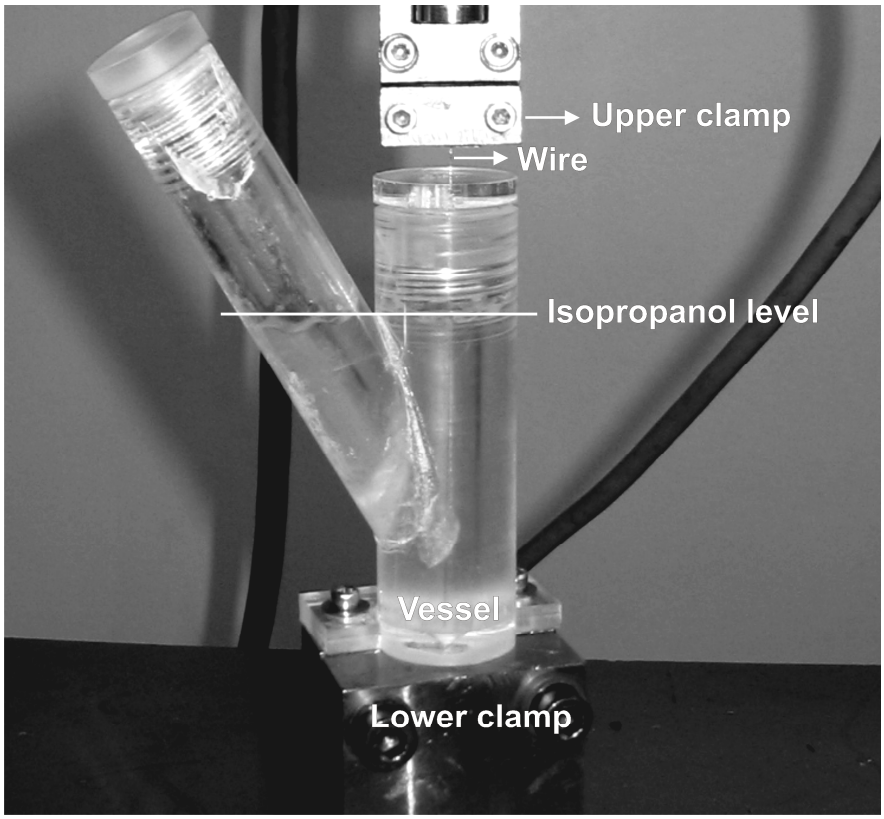

Figure 4.8: Fatigue test set-up isopropanol tests.

Figure 4.9 shows the fatigue data of the tests in isopropanol together with the reference wires (both 175 HT wires). Due to the difficult test set-up the amount of fatigue data is limited. Nevertheless one can clearly see that the fatigue properties of the wires submerged in isopropanol are better than the reference wires.
There are however two wires that fractured early (at the same fatigue life as the reference wires). A fractography study shows the presence of surface oxides together with chlorides. Figure 4.10 shows a SEM picture of one of the early fractures. At the fatigue crack initiation area surface oxides (white arrow) together with chlorides are observed (left side and bottom of figure 10). The surface oxides are located inside the brass layer and are connected with other surface oxides (dark spot right of the white arrow) by cracks inside the brass layer and at the interface between the brass layer and the steel. The right side of figure 10 shows that these surface oxides follow the wire axis over a length of more than 10 μm (dark lines at the surface of the wire). Although the fatigue tests are performed in isopropanol it is expected that moisture is captured inside the surface oxides and in the pre-existing cracks. This moisture together with chlorides can initiate an environmentally assisted fatigue crack. This could explain the short fatigue life of the two early fractures.

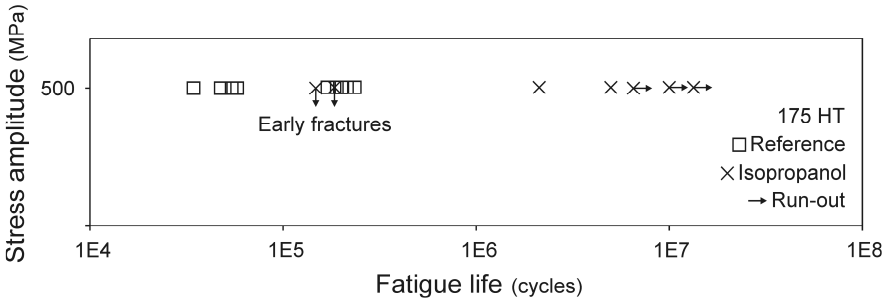

Figure 4.9: Fatigue data of reference and isopropanol 175 HT wires.

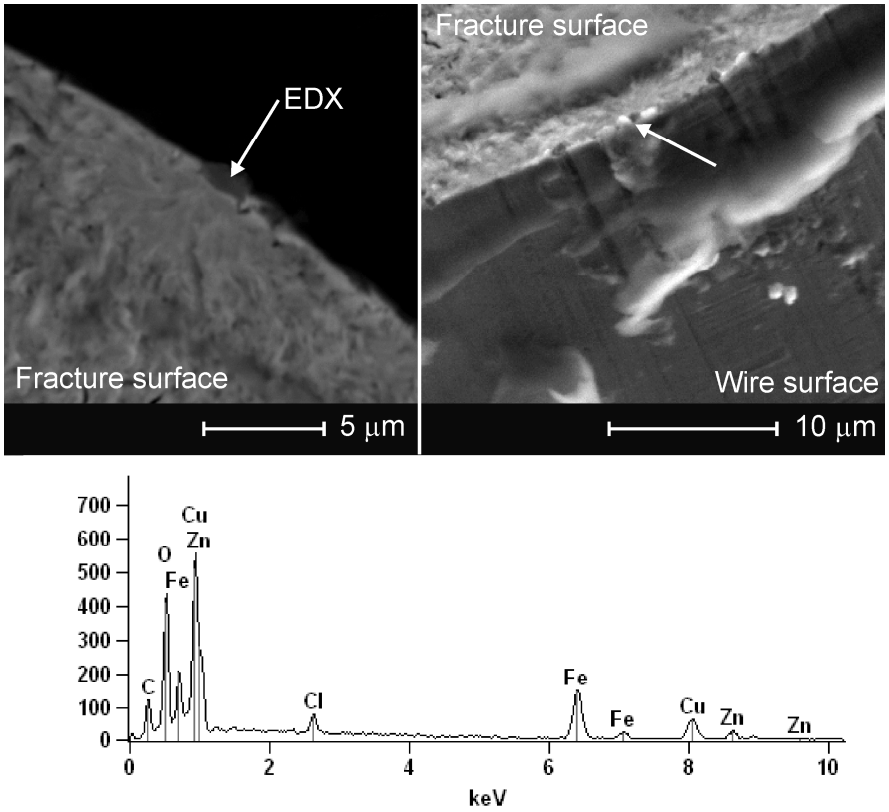

Figure 4.10: Fatigue crack initiation area of the early fractures of the isopropanol wires.

Since the two early fractures can be explained and the other wires submerged in isopropanol fracture at large fatigue lives or are stopped before fracture, it can be concluded that the improved fatigue life of coated wires is completely environmentally driven.

4.1.2.3 Cleaned wires

To confirm the influence of chlorides on the fatigue properties (Paragraph 4.1.2.1) fatigue tests are launched on cleaned wires and on cleaned wires on which chlorides are intentionally added.
The cleaning procedure is the same as the one that is used before the glue coating is applied (wiping with acetone and ethanol, described in paragraph 4.1.2.1). After a batch of wires is cleaned they are randomly separated into two groups of equal size. One group is used as cleaned samples for fatigue testing. On the other group chlorides are added. To add the chlorides, a droplet of a NaCl – solution is added to the surface of the wire while the wire is placed on a pre-heated metal plate (90-110°C). Due to the heat, the water will evaporate very quickly (some seconds), leaving only NaCl crystals on the surface of the wire (Figure 4.11). The wires are removed from the heat source as soon as possible to limit the possible aging process as much as possible. To avoid corrosion before fatigue testing the chloride containing wires are immediately tested. This means that the chlorides are added on one sample at the time.

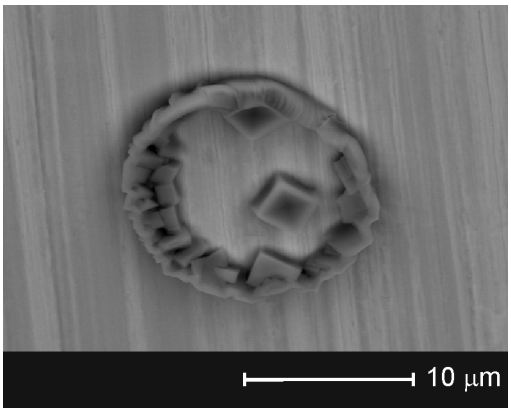

Figure 4.11: Intentionally added NaCl crystals on the wire surface.

The box-plot of the fatigue data is shown in figure 4.12. It is observed that the cleaned wires have significantly higher fatigue lives than the reference wires (175 NT, confirmed with ANOVA, $\alpha = 0.05$). The fatigue life of the cleaned wires increases to the same degree as the fatigue lives of the coated (Paragraph 4.1.2.1) and the isopropanol wires (Paragraph 4.1.2.2). When chlorides are added on the cleaned wires a decrease of the fatigue life to the same level as for the reference wires is observed. Therefore it can be concluded that the presence of chlorides critically influences the fatigue properties of these heavily drawn steel wires. The environmentally assisted crack initiation mechanism is accelerated significantly by the presence of these chlorides.

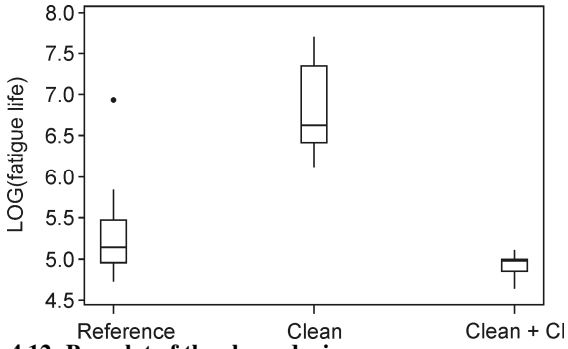

Figure 4.12: Box plot of the cleaned wires.

4.1.2.4 Corrosion mechanisms

S. Chanel and N. Pébère [89] investigated the corrosion behaviour of heavily drawn brass coated steel wires submerged in a 0.25M Na_2SO4 solution. They observed that before immersion the brass coating is covered by a thin layer of zinc oxide. The first step of the degradation (0 – 6 hours of immersion in the electrolytic solution) is the selective dissolution of zinc followed by the corrosion of the underlying steel. In a second step (> 6 hours of immersion) a copper oxide film (Cu_2O) is formed on the dezincified brass by hydrolysis of the primary cuprous corrosion products. The local anodic dissolution (LAD) of the steel is enhanced by the galvanic couple between the brass and the steel.
Toribio et al. [90-96] showed in several studies that uncoated drawn steel wires are very sensitive for hydrogen assisted cracking (HAC) and almost completely resistant to LAD. Further he showed that due to LAD fatigue cracks get blunted, which is beneficial for fatigue [97]. On the other hand there are some publications which describe the preferential fatigue crack initiation at corrosion pits [98, 99].
Based on literature two corrosion mechanisms can be active, namely hydrogen assisted cracking (HAC) and/or localized anodic dissolution (LAD).

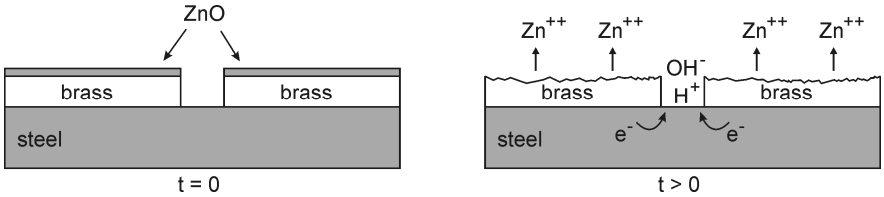

Figure 4.13: Schematic representation of the HAC corrosion mechanism.

Hydrogen assisted cracking (HAC)
The HAC corrosion mechanism is schematically represented in figure 4.13. A galvanic couple is created due to the selective dissolution of the zinc, making the steel surface locally cathodic. Due to the reduction of water (reaction in equation 4.3) hydrogen is created at the steel-water interface. This hydrogen could diffuse into the steel causing hydrogen embrittlement.

$$2 \cdot H_2O + 2 \cdot e^- \rightarrow 2 \cdot OH^- + H_2 \qquad (4.3)$$

Assumptions:

- There are defects present in the brass coating assuring the direct contact of the environment with the steel.
- Water is available at the steel surface.
- The selective dissolution of zinc happens first and lasts long enough for hydrogen to form and diffuse into the steel.

Localized anodic dissolution (LAD)

The LAD corrosion mechanism is schematically represented in figure 4.14. Since the brass coating is more noble than the steel a galvanic couple is created with a very large cathodic area (brass coating) and some localised anodic spots (steel surface). The anodic steel will go into solution (Fe^{++}) and will start at the brass-steel interface because the potential difference is higher there. This creates an undercutting of the brass layer.

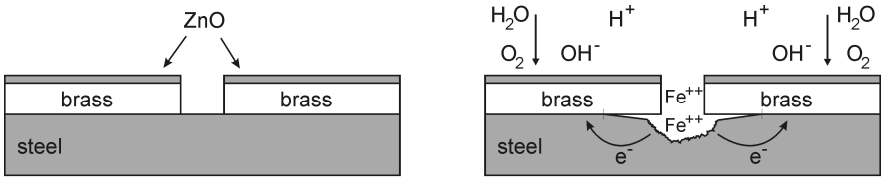

Figure 4.14: Schematic representation of the LAD corrosion mechanism.

Assumptions:

- There are defects present in the brass coating assuring the direct contact of the environment with the steel.
- Water is available at the steel surface.
- The selective dissolution of zinc does not occur during the timeframe of the experiments.

Discussion

Both mechanisms need the presence of defects in the brass layer. To confirm this assumption, the surface of the wire is scanned with SEM for cracks in the brass layer. Figure 4.15A shows an example of a longitudinal surface crack in the brass layer of a wire that has not been subjected to fatigue. Figure 4.15B and C show sections of these longitudinal surface cracks which are made using a focussed ion beam (FIB). From these two examples it seems that the longitudinal surface cracks stay in the brass layer and do not grow into the steel.

To confirm these observations, FIB sections were made on wires from which the brass coating is chemically removed. It is chosen to remove the brass coating because the difference between the brass coating and the steel can not always be seen clearly in SEM.

To remove the brass coating following procedure is followed:

- Submerge the wire for about 30 seconds in an ammoniumpersulfate solution to remove the brass layer. Ammoniumpersulfate solution = 40 ml 10% $(NH_4)_2S_2O_8$ + 30 ml NH_4OH + dilute with water until 250 ml.
- Put the wire for about 3 seconds in demineralised water to stop the reaction and to remove the ammoniumpersulfate.
- Put the wire between 3 and 5 seconds in a 1M HCl solution to remove the iron oxide layers from the surface.
- Rinse with demineralised water between 2 and 3 seconds to stop the reaction.
- Rinse with ethanol or isopropanol to remove the water.
- Rinse with ether to remove the ethanol or isopropanol.
- Submerge the wire in hexane for storage (can be contained for several months).

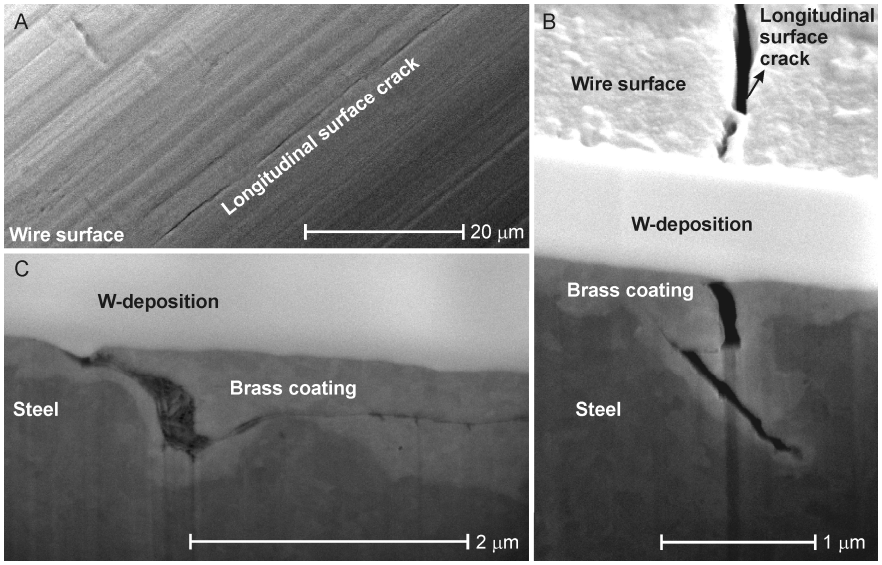

Figure 4.15: FIB sections through longitudinal surface cracks.

Figure 4.16 shows a section through a wire from which the brass coating is removed. The magnified view on the right of the figure shows that the cracks in the brass coating can grow into the steel. It is important to note that the root of the cracks was already attacked by the chemical procedure to remove the brass coating. Further it can be observed that when the brass coating is removed the surface roughness increases significantly, as will be shown in chapter 6.

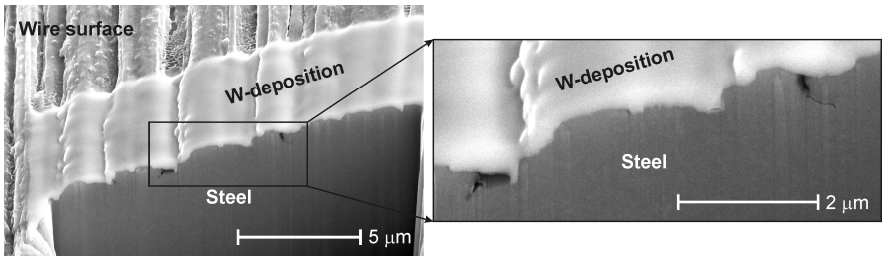

Figure 4.16: FIB section through wire wherefrom the brass coating is removed.

Figure 4.17 shows a typical fatigue crack initiation area of a sample that failed due to environmentally assisted fatigue crack initiation (note that no surface stress concentrations are present). Multiple cracks in the brass coating are observed at the fatigue crack initiation area, indicating the existence of a relation between these cracks and environmentally assisted fatigue crack initiations.

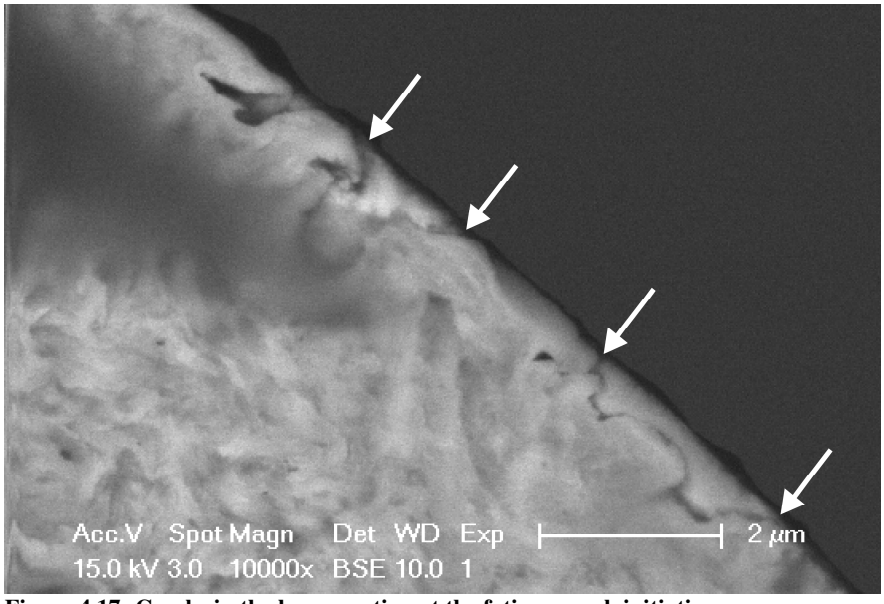

Figure 4.17: Cracks in the brass coating at the fatigue crack initiation area.

A second assumption that has to be valid for both HAC and LAD is the presence of water at the defects in the brass layer. This water is a necessary condition for environmentally assisted fatigue crack initiations to occur. Due to the observed increase in fatigue life for coated wires and wires in isopropanol, it can be assumed that water is sufficiently available during normal lab air fatigue experiments.

The third assumption about the occurrence of the selective dissolution of zinc is different for the HAC and LAD mechanism. Literature on the corrosion of brass

coated steel wires [89] states that the selective dissolution of zinc will happen first when the wires are submerged in a 0.25M Na_2SO4 solution. If the selective dissolution of zinc would also occur in lab air conditions, it is most probably that the HAC mechanism is active.
Some Bekaert experts however experimentally validated that the selective dissolution of zinc does not happen in normal circumstances ($2 < pH < 11$). The difference with the existing literature could be explained by a misinterpretation of the experimental results in literature. This would mean that the LAD mechanism is more likely to occur.

Since it is not possible to exclude one of both mechanisms from literature slow strain rate tests (SSRT) are performed to check whether or not hydrogen embrittlement plays a role in the environmentally assisted fatigue crack initiations. If hydrogen embrittlement would occur, the SSRT would have a significantly lower ultimate tensile stress (UTS) than tensile tests performed at a normal speed [100]. Other researchers also found a relation between the decrease in ductility and hydrogen embrittlement in SSRT [101].
Two SSRT tests were performed and compared to five normal tensile tests. The SSRT tests are performed with a speed of 0.5 µm/min and the normal tensile tests with a speed of 0.5 mm/min. For both tests a gauge length of 80 mm is used. Since no extensometer was used during the experiments, the total strains are not measured accurately, and therefore are not given. Table 4.2 gives the UTS together with the 95% confidence intervals (LCL = lower confidence limit, UCL = upper confidence limit) of both the SSRT and the tensile tests. It is observed that the UTS of the SSRT is not significantly different from the UTS of the normal tensile tests. This indicates that the influence of hydrogen embrittlement is not critical (doesn't has a significant effect on the mechanical properties) for the wires studied in this research. It is however important to note that only two SSRT were done.

Table 4.2: UTS of the SSRT and tensile tests on 175 HT wires given in MPa.

Sample	UTS	LCL 95%	UCL 95%	± 95%
Tensile	3379	3327	3429	51
SSRT	3334	3296	3372	38

Conclusion
Due to the knowledge which was gained from the SSRT and multiple fractography studies that showed the presence of corrosion products at the fatigue crack initiation area (figure 4.18), it is most probably that the mechanism behind the environmentally assisted fatigue crack initiations is localized anodic dissolution.

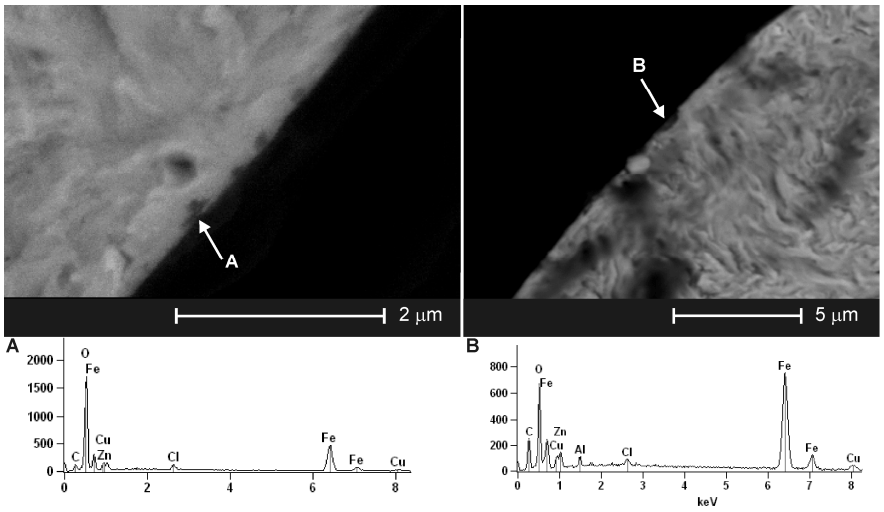

Figure 4.18: Presence of corrosion products together with chlorides at the fatigue crack initiation areas of environmentally assisted fatigue cracks.

4.1.2.5 Storage time dependence

Since the environmentally assisted fatigue crack initiation mechanism is dominant and critical for the heavily drawn steel wires investigated in this study, it can be expected that the fatigue properties of these wires degrade as a function of time. To check this hypothesis, the fatigue properties of freshly made wires are determined over the time span of several months. The freshly made wires are stored in a desiccator during the experiments.

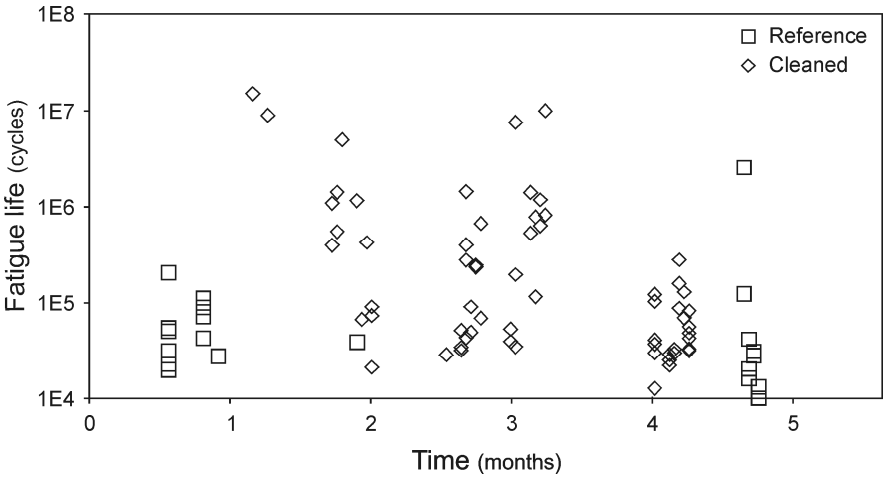

Figure 4.19: Fatigue properties as a function of the time between production and fatigue testing.

Figure 4.19 shows the fatigue properties as a function of the time between production and fatigue testing for both reference and cleaned wires. The cleaned wires clearly show a decrease in fatigue life as a function of the time between production of the wires and fatigue testing, while no time dependence is observed for the reference wires. A fractography study showed that these shorter fatigue lives can be explained by the formation of corrosion spots on the surface of the wire as a function of time. These corrosion spots act as surface stress concentrations, leading to a decrease in fatigue life.
The corrosion spots don't influence the fatigue properties of the reference samples since the environmentally assisted fatigue crack initiation mechanism is active (presence of chlorides) for the reference samples. This means that the environmentally assisted fatigue crack initiation mechanism is at least as critical as the fatigue crack initiation at corrosion spots with a $\Delta K > \Delta K_{th}$ (this is shown in paragraph 4.1.4).
Based on these results it is suggested to minimize the time between production and the rubber embedment (for the final application) or to protect the wires against corrosion in another way in order to avoid a decrease in fatigue properties.

4.1.2.6 Conclusions

Based upon multiple experimental results it can be concluded that the environmentally assisted fatigue crack initiation mechanism is a dominant and critical fatigue mechanism that leads to low fatigue lives. In most cases the environmentally assisted fatigue crack initiation mechanism can be associated with the presence of chlorides at the surface of the wire. The removal of the surface chlorides by a cleaning operation leads to a significant increase in the fatigue life in the majority of the cases. The cleaning operation does not improve the fatigue life whenever chlorides are captured inside corrosion spots or when environmentally assisted fatigue crack initiation is not the active fatigue mechanism.
The coating of the wires with cyanoacrylate glue also significantly improves their fatigue properties. This is due to the cleaning operation that is applied before the coating operation, but it can also be related to the fact that the cyanoacrylate hardens out due to a reaction with water. When the glue is applied it will react with the water that is present at the surface of the filament. Without the presence of water no corrosion is possible.
The mechanisms behind the environmentally assisted fatigue crack initiations is localized anodic dissolution (LAD) where the steel (anode) will dissolve preferentially due to the large galvanic couple which is created between the brass coating and the steel wire.

4.1.3 Stress concentrations

The second fatigue crack initiation mechanism for the surface fracture mode is the fatigue crack initiation at pre-existing surface stress concentrations, as is shown schematically in figure 4.1. Paragraph 4.1.3.1 describes this fatigue crack

initiation mechanism in detail. Paragraph 4.1.3.2 describes the fatigue crack initiations at internal stress concentrations for the internal fracture mode.

4.1.3.1 Surface stress concentrations

The second fatigue crack initiation mechanism that is active for the heavily drawn steel wires investigated in this study is the fatigue crack initiation at pre-existing surface stress concentrations. Unlike for the environmentally assisted crack initiations which are described in detail in paragraph 4.1.2, it is possible to calculate the stress intensity factor range (ΔK) for stress concentrations. To calculate the ΔK values Murakami's formulae [45] are used (equation 4.1 and 4.2).
The initial ΔK value of the surface stress concentration will determine the fatigue life of the material. Therefore a subdivision is made between surface stress concentrations with a ΔK value that is smaller than the threshold value for crack growth (ΔK_{th}) and surface stress concentrations with a ΔK value that is larger than ΔK_{th}.

$\Delta K > \Delta K_{th}$
When $\Delta K > \Delta K_{th}$ long fatigue cracks can immediately start growing. This leads to low fatigue lives which are comparable to the fatigue lives of the environmentally assisted fatigue crack initiation mechanism. By analyzing all the fatigue fractures it was possible to further subdivide the fatigue crack initiations at surface stress concentrations in three groups of different surface stress concentrations. Figure 4.20 shows a typical fatigue crack initiation area of each group.
Figure 4.20A shows an example of a surface defect that was introduced by the wire drawing production process, figure 4.20B shows an example of a surface inclusion and figure 4.20C shows an example of surface oxides. These surface oxides are introduced by corrosion that occurred before fatigue testing.
From a fracture mechanics point of view all the three groups of surface stress concentration can be approached as one group. The fatigue life of the wires is not determined by the kind of surface stress concentration but by the size of the defect. It is important to note that it is necessary to model the defect as a crack in order to apply fracture mechanics. In chapter 7, which deals with the influence of non metallic inclusions, it will be shown that the size of the crack that models non-metallic inclusions is significantly larger than the size of the inclusion itself. Therefore it is necessary to use an adapted form of Murakami's formulae [45] for non-metallic inclusions in heavily drawn steel wires.

$\Delta K < \Delta K_{th}$
When $\Delta K < \Delta K_{th}$ it is in principle not possible for fatigue cracks to grow. It is experimentally observed that below ΔK_{th} the growth of fatigue cracks is still possible, however at much lower crack growth rates. In this study the fatigue cracks that grow when $\Delta K < \Delta K_{th}$ are called short fatigue cracks and the fatigue cracks that grow when $\Delta K > \Delta K_{th}$ are called long fatigue cracks. The growth

mechanisms of short and long fatigue cracks of heavily drawn steel wires are explained in detail in paragraph 4.2.1.
Two different kinds of defects are observed when $\Delta K < \Delta K_{th}$ and a typical example of both defects is shown in figure 4.21.

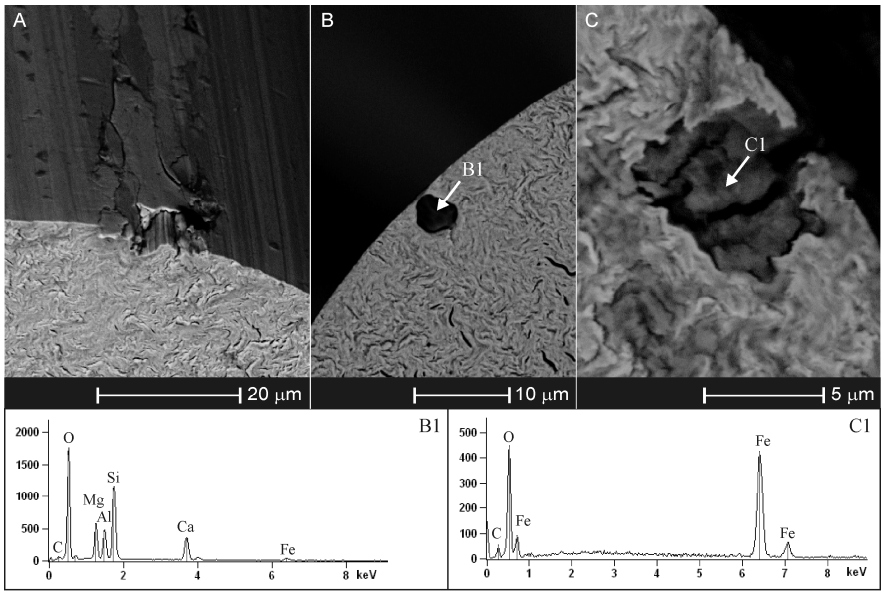

Figure 4.20: A. Surface defects due to the wire drawing process. B. Surface inclusion. C. Surface oxides.

Figure 4.21A shows an example of the fatigue crack initiation area of a longitudinal surface crack which follows the wire axis (perpendicular to the plane of the paper) for several hundreds of μm. Figure 4.21B shows an example of the fatigue crack initiation area of a subsurface SiO_2 inclusion. It is observed that short fatigue cracks can initiate and grow starting from these defects.
Different from internal crack initiations, no characteristic area is formed around the surface stress concentration with a $\Delta K < \Delta K_{th}$ (FCT area, see paragraph 4.1.3.2). No transition between the short and the long crack growth regime can be observed. The size of a semi circular crack with a $\Delta K = \Delta K_{th}$ is shown as the dashed white line in figure 4.21B. The radius of the crack is calculated to be 4.39 μm using equation 4.1 with $\Delta K_{surface} = \Delta K_{th} = 3.82$ MPa$\sqrt{m}$, $\Delta\sigma = 1414$ MPa and area $=\pi r^2/2$. At the moment it is not clear why the growth of short fatigue cracks that initiate from the surface doesn't form a FCT area, while short cracks that initiate internally do form a FCT area. A possible explanation could be found in the difference in residual stresses or in a possible difference in microstructure between the surface and the interior of the wire. Due to time limitations no efforts were made to validate the hypotheses above.

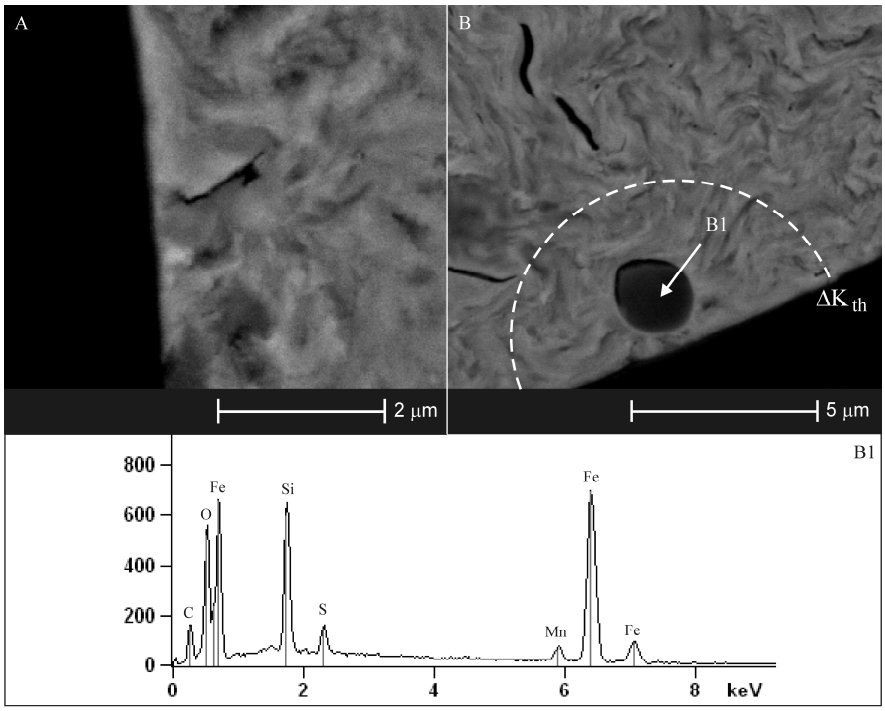

Figure 4.21: A. Longitudinal surface crack. B. Subsurface SiO_2 inclusion.

4.1.3.2 Internal stress concentrations

For the internal fracture mode only one fatigue crack initiation mechanism is active, namely fatigue crack initiation at internal stress concentrations. Since the fatigue crack is located completely inside the material, no environmentally assisted crack initiation is possible for the internal fracture mode.

It is observed that internal fatigue cracks always initiate at internal non-metallic inclusions. Similar as for surface stress concentrations, the size of the internal inclusion (which determines the initial ΔK value) will determine the fatigue life of the material. Therefore a subdivision is made between internal stress concentrations with a ΔK value that is smaller than the threshold value for crack growth (ΔK_{th}) and internal stress concentrations with a ΔK value that is larger than ΔK_{th}.

$\Delta K > \Delta K_{th}$

When $\Delta K > \Delta K_{th}$ long fatigue cracks can immediately start growing. This leads to low fatigue lives. The fatigue lives are however bigger than for a surface stress concentration with the same in plane area due to the difference in geometrical factor between surface and internal fatigue cracks (equation 4.1 and 4.2). It is important to note that this fatigue crack initiation mechanism was only observed for one single fracture and therefore will not be taken into account in the

discussion on the relation between the fatigue crack initiation mechanisms and the fatigue lives (paragraph 4.1.4).
Figure 4.22A gives an example of a fracture surface of an internal fatigue crack that initiated at an internal non-metallic inclusion for which $\Delta K > \Delta K_{th}$.

$\Delta K < \Delta K_{th}$
When $\Delta K < \Delta K_{th}$ short fatigue cracks have to grow until ΔK_{th} is reached. Figure 4.22B gives an example of a fracture surface of an internal fatigue crack that initiated at an internal non-metallic inclusion for which $\Delta K < \Delta K_{th}$. It is important to note that the fracture surface around the inclusion has a significantly higher roughness than a normal fracture surface. This rough area around the non-metallic inclusion is only observed for internal inclusions with a $\Delta K < \Delta K_{th}$ and can be associated with the growth of internal short fatigue cracks. The region of short crack growth around internal non-metallic inclusions is called facet (FCT) area in this study (also known as optically dark area, granular bright facet and fine granular area).. The growth mechanisms of short and long fatigue cracks are described in detail in paragraph 4.2.1.

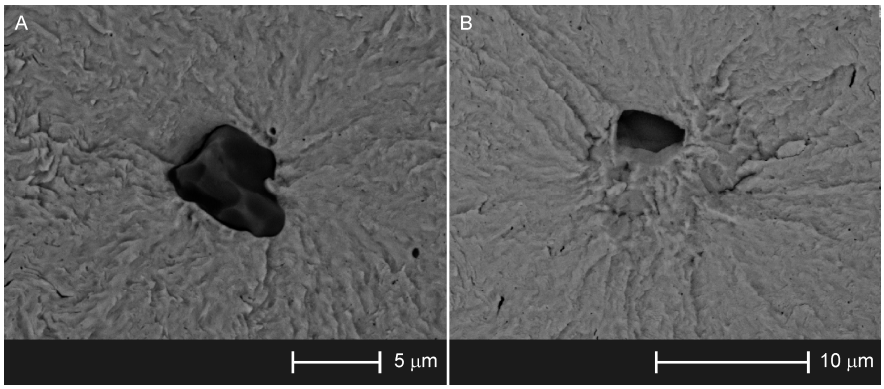

Figure 4.22: A. Internal fatigue crack initiation at a non-metallic inclusion for which $\Delta K > \Delta K_{th}$. B. Internal fatigue crack initiation at a non-metallic inclusion for which $\Delta K < \Delta K_{th}$.

4.1.4 Influence of the fatigue crack initiation mechanism on the fatigue life

The total fatigue life of the heavily drawn steel wires investigated in this study is mainly caused by the fatigue crack initiation mechanism that is active, as was already indicated in the description of the different fatigue crack initiation mechanisms. Figure 4.23 gives a schematic overview of the different fatigue crack initiation mechanisms and their fatigue lives. The environmentally assisted fatigue crack initiation mechanism and the fatigue crack initiations at surface stress concentrations with $\Delta K > \Delta K_{th}$ lead to low cycle fatigue behavior. Figure 4.24 which shows the fatigue data of 175 NT wires in a SN graph, gives an idea about the absolute value of the fatigue lives. It is important to note that a

combination of both mechanisms can be active and that it is not possible to make a distinction between both mechanisms based on the fatigue life.

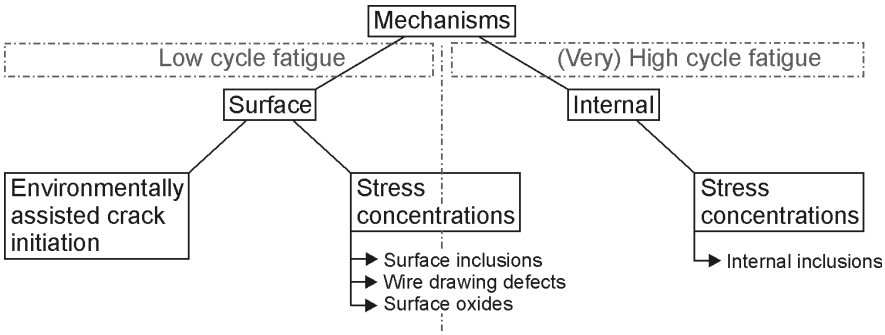

Figure 4.23: Overview of the fatigue crack initiation mechanisms and their fatigue lives.

Surface stress concentrations with $\Delta K < \Delta K_{th}$ lead to high cycle fatigue behavior and internal stress concentrations with $\Delta K < \Delta K_{th}$ lead to very high cycle fatigue behavior. Figure 4.24 gives an idea on the absolute value of the fatigue lives.
In figure 4.24 a log-normal distribution is superimposed on the fatigue data at the 707 MPa stress amplitude level to show the significant difference in fatigue life between the different fatigue crack initiation mechanisms.

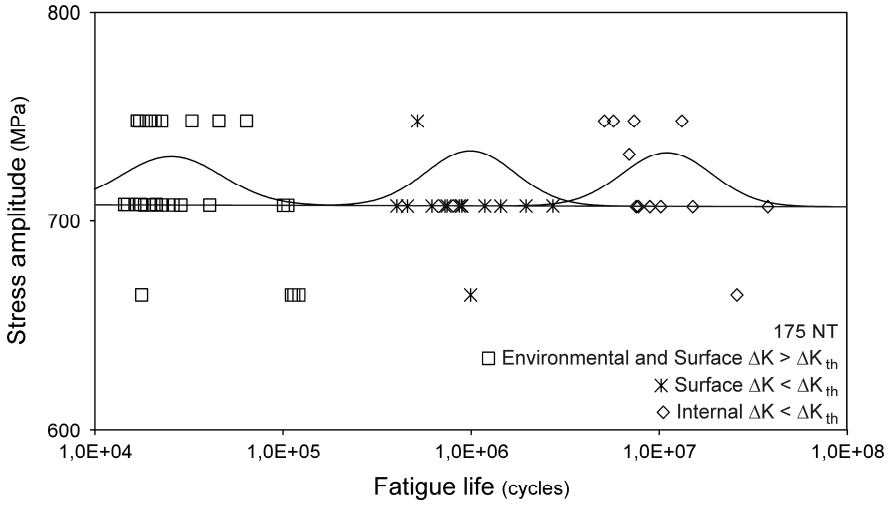

Figure 4.24: Fatigue data of the different fatigue crack initiation mechanisms presented in a SN graph. On the 707 MPa stress level a log-normal distribution is plotted for each individual fatigue crack initiation mechanism.

Figure 4.25 gives a schematic representation of a prospective SN-graph of the heavily drawn steel wires investigated in this study. Since the four different

fatigue crack initiation mechanisms lead to three different groups of fatigue data, a triplex SN graph is observed for these heavily drawn steel wires in stead of a duplex SN graph which is observed for high strength steels. The prospective SN graph is based on multiple fatigue tests which were performed on stress levels which are always larger than the conventional fatigue limit (fatigue limit which is based on surface crack initiations and run-out values of 10^6 to 10^7 cycles). The 95% confidence intervals of the curves are based on the calculated 95 % confidence intervals at a stress range of 1414 MPa.

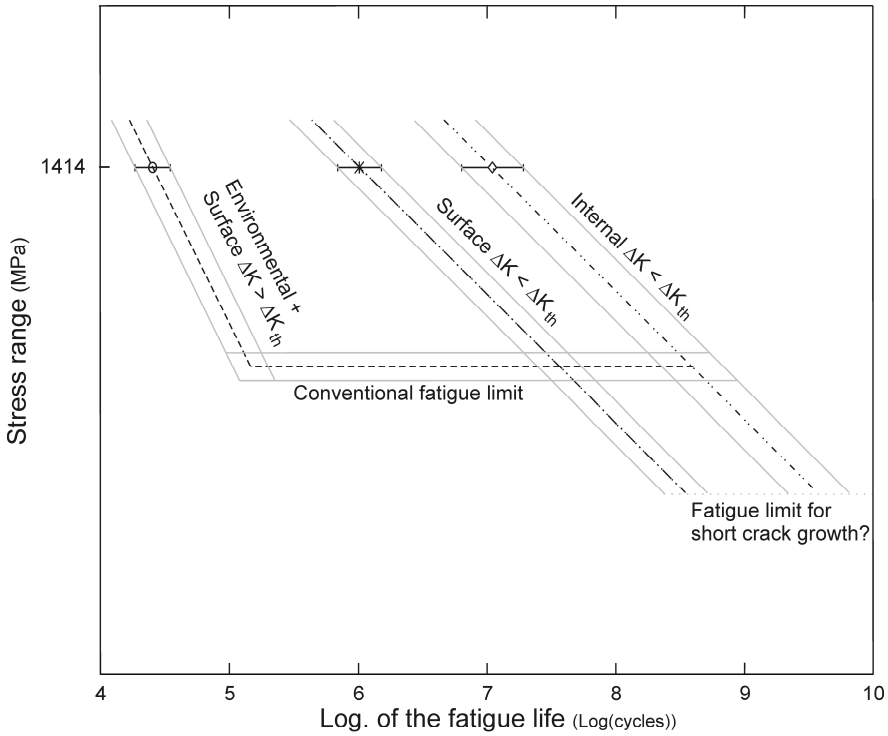

Figure 4.25: Prospective SN graph together with the 95 % confidence intervals for the heavily drawn steel wires investigated in this study.

Based on ΔK_{th} (= 3.82 ± 0.09 MPa$\sqrt{m}$, see chapter 5 and 8) and on the experimentally obtained defect distribution (obtained through fractographical analysis on all the surface stress concentrations) it is possible to calculate the conventional fatigue limit ($\Delta\sigma_e$) by equation 4.1. A Weibull distribution is fitted on the experimentally obtained defect distribution of the steel wire and is used to estimate the largest defect (taken at 99% of the distribution). The largest defect is estimated to have a projected area of 98 μm² (equivalent diameter of 11.2 μm). To calculate $\Delta\sigma_e$ equation 4.1 is used in the following form:

$$\Delta K_{th} = 0.65 \cdot \Delta\sigma_e \cdot \sqrt{\pi \sqrt{area_{max}}} \qquad (4.4)$$

where $area_{max}$ is the largest defect present in the material. The conventional fatigue limit is calculated to be 1054 ± 25 MPa.

Since the threshold value for short crack growth is smaller than ΔK_{th} the fatigue limit for the fatigue crack initiation mechanisms at surface and internal stress concentrations with $\Delta K < \Delta K_{th}$ has to be smaller than the conventional fatigue limit. It is however important to note that the fatigue limit for short crack growth has not been experimentally observed yet and is even questioned by some [47].

4.1.5 Conclusions

Experimental results show that four different fatigue crack initiation mechanisms are active for the heavily drawn steel wires investigated in this study. Fatigue crack initiations at surface stress concentrations with $\Delta K > \Delta K_{th}$ and environmentally assisted fatigue crack initiations are the most critical fatigue mechanisms which always lead to low cycle fatigue behavior. Surface stress concentrations with $\Delta K < \Delta K_{th}$ lead to high cycle fatigue behavior while internal stress concentrations with $\Delta K < \Delta K_{th}$ lead to very high cycle fatigue behavior.
It is important to note that the fatigue mechanisms that lead to (very) high cycle fatigue behavior can only be observed when no surface stress concentrations with $\Delta K > \Delta K_{th}$ are present on the sample during fatigue testing and when environmentally assisted fatigue crack initiation is not possible.

4.2 Fatigue crack growth mechanisms

4.2.1 Growth of short and long fatigue cracks

Two different fatigue crack growth mechanisms are observed for the heavily drawn steel wires investigated in this study, namely the growth of short and long fatigue cracks. It is important to note that these crack growth mechanisms can be accelerated by environmentally assisted fatigue crack growth (paragraph 4.2.2) Which fatigue crack growth mechanism is active is determined by the size of ΔK compared to ΔK_{th} and is independent of the fracture mode (surface or internal fatigue crack initiation). $\Delta K < \Delta K_{th}$ is the short fatigue crack growth region while $\Delta K > \Delta K_{th}$ is the long fatigue crack growth region.

4.2.1.1 Growth of long fatigue cracks

It is observed by fractographical investigations that long fatigue cracks grow in a plane perpendicular to the wire axis (figure 4.26). Since the load is applied following the wire axis, the long fatigue cracks grow in a plane perpendicular to the applied load. The fatigue crack grows from the white arrow until point 1,

where the fracture toughness of the material is reached and the fatigue crack continues by micro void coalescence (MVC), leading to its final failure.

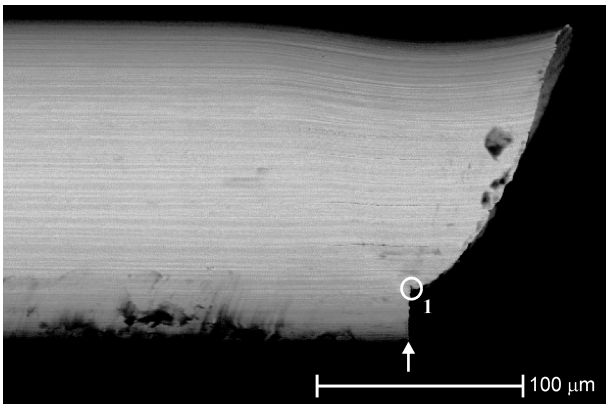

Figure 4.26: Growth of long fatigue cracks perpendicular to the wire axis.

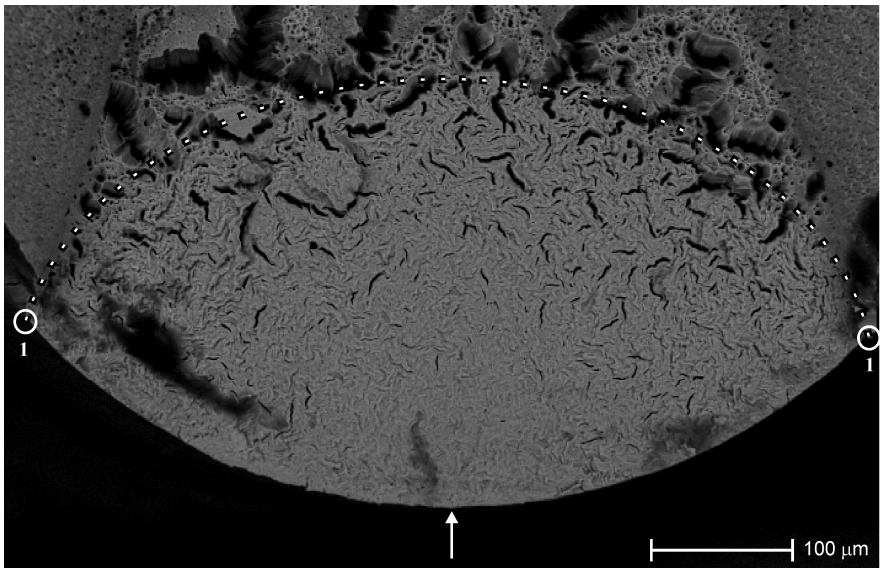

Figure 4.27: Typical fracture plane of a surface crack initiation.

Figure 4.27 shows the fracture plane of a typical surface crack initiation viewed from the top. The white arrow indicates the area where the fatigue crack initiated and the dotted white line indicates the end of the fatigue fracture. One can see that besides the main fatigue crack, a lot of secondary cracks are present at the fracture surface. These secondary cracks follow the wire axis (90° deflection from the crack plane, figure 4.31) and are formed during fatigue crack growth to relieve existing crack tip stresses in the radial direction. When the size of the fatigue crack increases, the stresses at the crack tip will also increase. It is

important to note that the applied tensile stress in the Y direction (figure 4.28) will lead to a three dimensional stress state at the crack tip. The early work of Westergaard [102] and Irwin [103] showed that the crack tip stress in the X direction equals the one in the Y direction (figure 4.28) for the case that the crack is present in an infinite medium.

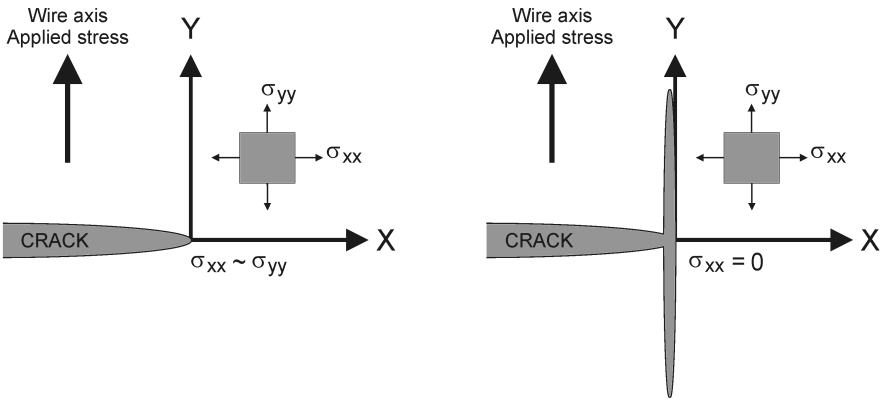

Figure 4.28: Schematic representation of the formation mechanism for secondary cracks.

Whenever a secondary crack is created, stresses are relieved at the free surface of this secondary crack. Locally, the X component of the stress will become zero. Due to this stress relief, deep secondary cracks are often followed by more shallow ones (figure 4.29A). Due to the fact that the crack tip stresses increase with the crack length, there is an overall tendency that the secondary cracks become deeper with an increasing fatigue crack length (figure 4.27 and 4.29B).

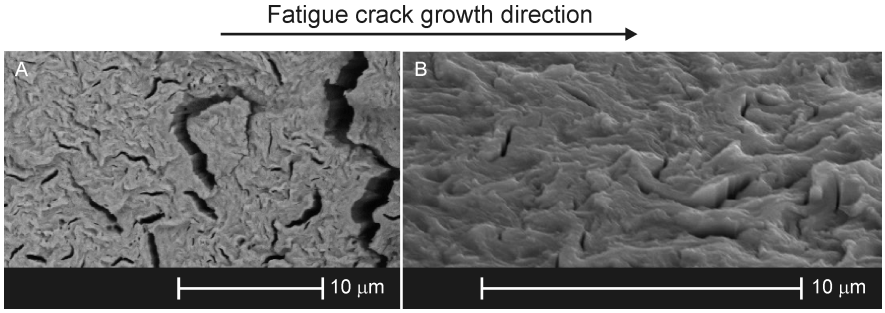

Figure 4.29: Fatigue fracture surface with secondary cracks. A. Secondary crack become deeper with increasing crack length. B. Fatigue crack jumps up and down after secondary cracks.

Secondary cracks have a wavy shape when observed on the fracture plane. Figure 4.30 shows the microstructure of a cross section of a drawn steel wire next to a fatigue fracture surface. It shows that the pearlite colonies and the secondary

cracks both have the same wavy form. Therefore it is most probable that the secondary cracks are formed on pearlite colony grain boundaries during fatigue crack growth.
After the formation of a secondary crack, the fatigue crack continues to grow in mode I (perpendicular to the wire axis), but not necessarily on the same plane as it was growing on. The fatigue crack will continue its growth on the place where the resistance against crack growth is locally at a minimum. (e.g. at grain boundaries, slip planes or pre-existing microcracks). This leads to a fatigue fracture plane that is not completely flat, but jumps up and down at secondary cracks. In figure 4.29B these jumps are shown. Figure 4.31 shows a fatigue fracture plane with a cut-out at a secondary crack showing the possible multiple fatigue crack growth from a secondary crack. A focused ion beam (FIB) was used to make the cut-out; therefore a W layer (white area in figure 4.31) was deposited to protect the fatigue fracture plane. Note that the secondary crack is almost completely filled with W.

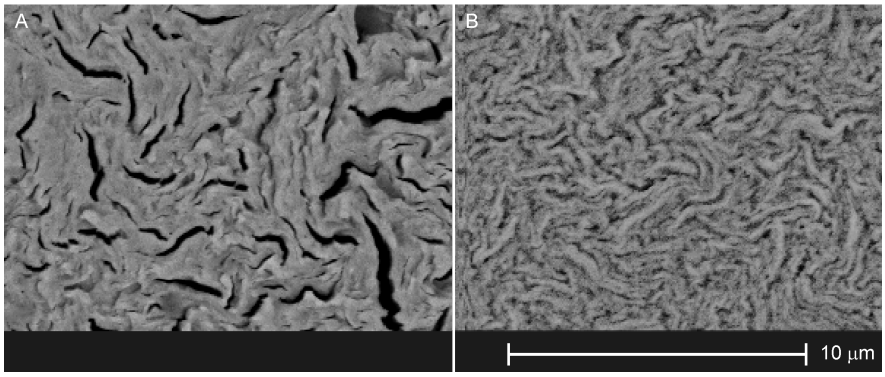

Figure 4.30: A fatigue fracture surface (A) is shown next to the microstructure of the cross section (B) to indicate that secondary cracks will most probably be formed at the grain boundaries of pearlite colonies.

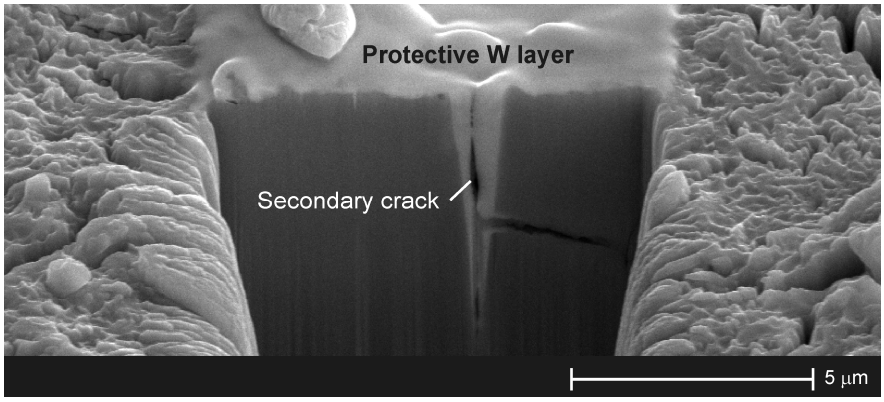

Figure 4.31: Fatigue fracture plane with a cut-out at a secondary crack showing the possible multiple fatigue crack growth from a secondary crack.

Since the fatigue life of wires for which the fatigue crack initiated at surface stress concentrations with $\Delta K > \Delta K_{th}$ is determined by the growth of long fatigue cracks, it is possible to predict the total fatigue life by using the fatigue crack growth model of Paris [104]. The Paris formula is shown in equation 4.5:

$$\frac{da}{dN} = C \cdot \Delta K^m \tag{4.5}$$

With *da/dN* the crack growth speed and *C* and *m* are material parameters. To determine the material parameters only the fatigue data of cleaned and coated wires that failed at surface stress concentrations are used in order to make sure that the environmental fatigue crack initiation mechanism is not active. Further only the surface stress concentrations with a $\Delta K > 1.1\Delta K_{th}$ are used to make sure that the crack growth behavior follows the Paris regime (figure 2.26). Equation 4.1 is used to calculate the initial ΔK value of the surface defects and the defect is idealized as a semi-circular crack (equation 4.6).

$$area = \frac{\pi \cdot a^2}{2} \tag{4.6}$$

With *a* the radius of the semi-circular crack. The combination of equation 4.1 and 4.5 is integrated starting from a semi-circular crack with a radius *a* until final failure of the wire at N_f cycles and a crack length a_f (equation 4.7). Both *a* and a_f can be measured during fractography.

$$\int_0^{N_f} dN = \int_a^{a_f} \frac{1}{C \cdot \left(0.65 \cdot \Delta\sigma \cdot \sqrt{\pi \cdot \sqrt{\pi/2}}\right)^m} \cdot \frac{da}{a^{m/2}}$$

$$N_f = \frac{2\left(a^{1-0.5m} - a_f^{1-0.5m}\right)}{C(m-2)\left(0.65 \cdot \Delta\sigma\sqrt{\pi\sqrt{\pi/2}}\right)^m} \tag{4.7}$$

In equation 4.7 only the material parameters *C* and *m* are unknown. To solve equation 4.7 the fatigue data of cleaned and coated 175NT wires loaded at a stress amplitude of 707 MPa for which the fatigue crack initiated at surface stress concentrations is used (figure 4.24). Following material parameters are calculated:

$$\begin{aligned} C &= 7.68 \cdot 10^{-13} \\ m &= 4.3 \end{aligned} \tag{4.8}$$

The material parameters given in equation 4.8 can be used to estimate the fatigue life of the 175 NT wires for which the fatigue crack initiated at stress concentrations with $\Delta K > \Delta K_{th}$. This approach is only valid when it is assumed that the fatigue crack growth can be modeled by the Paris law [104].

4.2.1.2 Growth of short fatigue cracks

When however $\Delta K < \Delta K_{th}$ short fatigue cracks have to grow. The growth of short fatigue cracks is not a cycle by cycle based crack growth mechanism and depends strongly on local microstructural properties. Therefore no successful predictive fatigue models for the growth of short cracks can be found in literature nowadays. It is possible however to estimate the fatigue life that is spent in the short crack growth region by comparing the total fatigue life to the fatigue life that is spent in the long crack growth region. To estimate the amount of cycles that is spent in the long crack growth region, the size of the FCT area (= transition between short and long crack growth, see paragraph 4.2.1) is taken as the initial crack size in the Paris model. Using equation 4.7 it is estimated that it takes about 60,000 cycles for a crack to grow from the FCT area to final failure when $\Delta\sigma$ = 1414 MPa. Compared to the total fatigue life of internal fatigue crack initiations at non-metallic inclusions with a $\Delta K < \Delta K_{th}$, it is estimated that the formation of the FCT area can take over 99% of the total fatigue life. This was also observed in literature [39,105,106].

It is observed from fractographical analysis that short fatigue cracks that initiated from internal non-metallic inclusions do not only grow on a plane perpendicular to the wire axis but also on planes with different angles with respect to the wire axis, leading to a rough area around the non-metallic inclusion. This rough area, which corresponds with the short crack growth area, is called the FCT area.

Figure 4.32 clearly shows the different appearance of the FCT area. The edge of the FCT area is characterized by the transition of mixed mode crack growth to mode I crack growth. In SEM this transition can be identified quite clearly (figure 4.32).

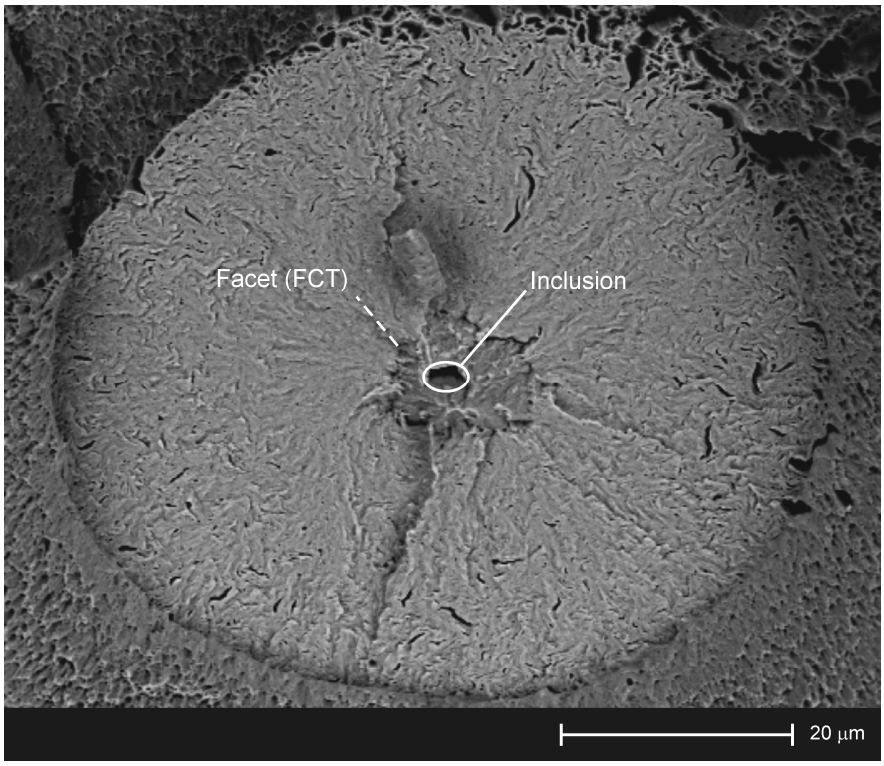

Figure 4.32: SEM image of an internal fatigue fracture.

Figure 4.33 shows a section of the FCT area. The section is made by an ion beam and cuts perpendicularly to the fatigue fracture plane and through the inclusion. It is shown that the short fatigue cracks do not only propagate in a plane perpendicular to the wire axis, but grow in a more random way, contributing to the rough surface of the FCT area. The smallest angle that is measured between the short fatigue crack and the wire axis is 28°. Zelin [8] observed that for drawn steel wires with a total strain of 3.5 (same strain as the wires investigated in this study) the angle between the microscopic shear bands and the wire axis is between 30 and 45 degrees. Therefore it can be assumed that in some parts of the FCT area, short cracks grow via microscopic shear bands. For the example in figure 4.33 this could be the case for the segments indicated with the white dotted arrows. In the other parts of the FCT area it can be assumed that the short fatigue cracks grow via grain boundaries or other low energy paths.

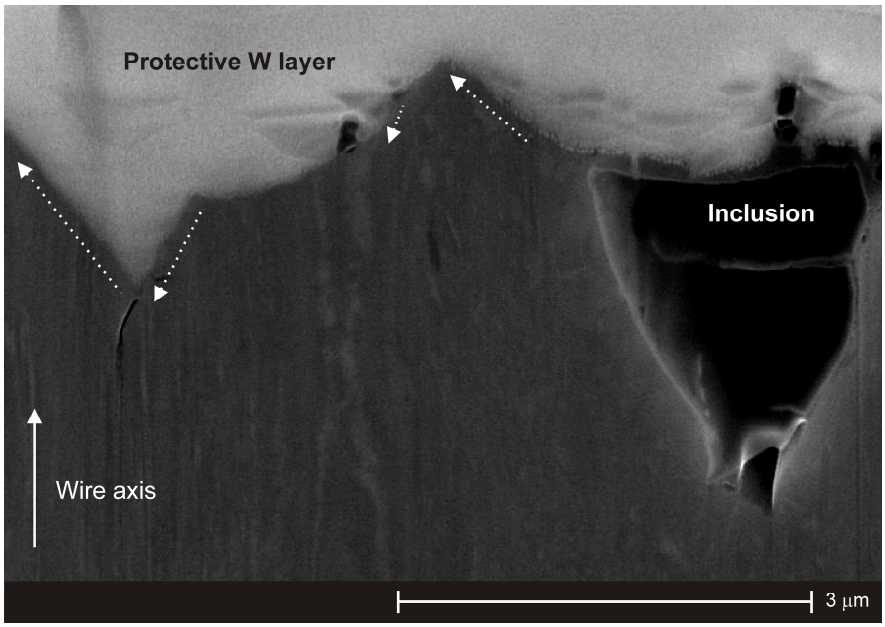

Figure 4.33: Ion beam section of the FCT area. The section is made perpendicular to the fatigue fracture plane and trough the inclusion. The white dotted arrows indicate the regions of short crack growth that make an angle of 30 to 45° with the wire axis.

4.2.2 Environmentally assisted fatigue crack growth

It is already known from the research on the environmentally assisted fatigue crack initiations (paragraph 4.1.2) that the environment can have a critical influence on the fatigue properties of the heavily drawn steel wires investigated in this study. Analogue to the environmentally assisted fatigue crack initiations, the mechanism behind environmentally assisted fatigue crack growth will be localized anodic dissolution in combination with a cyclic load. It is important to note that the presence of a cyclic load is essential, which can be concluded from the slow strain rate test. Also it can be expected that the presence of chlorides increases the crack growth speed significantly. Since this crack growth mechanism is corrosion related, the exposure time of the environment on the steel will play an important role. Therefore it is expected that environmentally assisted fatigue crack growth is more pronounced for relatively low crack growth rates (small crack lengths). It is even possible that the environmental influences become negligible from a certain crack growth speed. At this point, the crack growth mechanism will change from environmentally assisted crack growth to pure fatigue crack growth.
Although the environmentally assisted fatigue crack initiations fracture in the low cycle fatigue regime and the fatigue data has a reasonably low scatter, it is difficult to develop a predicting fatigue model due to the large amount of influencing factors. Since no successful models exist in literature and due to time

limitations, it was chosen not to develop such a predictive environmentally assisted fatigue model for heavily drawn steel wires.

4.2.3 Conclusions

The two different fatigue crack growth mechanisms that were found to be active for the heavily drawn steel wires investigated in this study are described. The long crack growth region was modeled by the Paris law and based hereon it was possible to conclude that over 99% of the total fatigue life is spent in the short crack growth region.

It is observed that short fatigue cracks don't grow solely in mode I, but show a mixed mode crack growth behavior. The combination of the investigation of the short crack growth region and microstructural characterizations from literature lead to the assumption that short fatigue cracks grow via microscopic shear bands, grain boundaries and other low energy paths.

5 Fatigue thresholds

For the heavily drawn steel wires investigated in this study, it is observed that fatigue cracks can initiate internally at non-metallic inclusions (described in detail in chapter 4). This internal fracture mode shows a fish eye appearance, which was also observed for high strength steels [38]. Around the non-metallic inclusion a very rough area is observed, which is called FCT area in this thesis (chapter 4). The edge of the FCT area is characterized by the transition of mixed mode crack growth to mode I crack growth and corresponds with the transition from short to long crack growth. Therefore, it is possible to estimate the threshold value for long crack growth ($\Delta K_{th,lc}$) by the FCT area. Paragraph 5.1 describes a threshold determination method that is based on the FCT area. Paragraph 5.2 uses the Kitagawa-Takahashi diagram [62] to validate the threshold determination method from paragraph 5.1.

5.1 Threshold determination method

To estimate the threshold value for long crack growth it is suggested to use the size of the FCT area of internal fatigue fractures. To use the size of the FCT area, it is necessary to check if the size of the FCT area is constant for a certain applied stress and if the ΔK value of the FCT area is independent of the applied stress.
Figure 5.1 shows the relation between the area of the FCT and the fatigue life for different applied stresses and an R value of 0.5. It is observed that the area of the FCT region is constant for a certain applied stress and that the FCT area increases with a decreasing applied stress. When the ΔK value of the FCT area is calculated for each internal fracture using equation 5.1 (equivalent with equation 4.2) it becomes clear that ΔK_{FCT} is constant and independent of the stress level (no significant difference ANOVA, $\alpha = 0.05$) for a given R value (R = 0.5).

$$\Delta K_{FCT} = 0.5 \cdot \Delta\sigma \cdot \sqrt{\pi \sqrt{area_{FCT}}} \qquad (5.1)$$

Figure 5.2 shows the ΔK value of the FCT area as a function of the fatigue life. ΔK_{FCT} is calculated to be 3.82 ± 0.09 MPa$\sqrt{m}$. Akiniwa et al. [46] also observed that ΔK_{FCT} is constant and independent of the stress level for high strength steels.
The observed independence of the applied stress on ΔK_{FCT} indicates the possibility of using ΔK_{FCT} to estimate $\Delta K_{th,lc}$. Since it is expected that the transition from mixed mode crack growth to mode I crack growth corresponds with the transition from short to long crack growth, it is assumed that $\Delta K_{th,lc} = \Delta K_{FCT}$. The validity of this estimation is described in detail in paragraph 5.2. It is intentionally chosen not to call $\Delta K_{th,lc}$ the threshold value for long crack growth anymore. This decision is based on the unified damage approach of Sadananda and Vasudevan [44,109] (paragraph 2.3.4) which shows the existence of a single fatigue threshold. For this reason the term ‘threshold for long crack growth’ will

be replaced by the fatigue threshold for crack growth ($\Delta K_{th,R}$). $\Delta K_{th,R}$ can be estimated using equation 5.2.

$$\Delta K_{th,R} = \Delta K_{FCT} = 0.5 \cdot \Delta\sigma \cdot \sqrt{\pi \sqrt{area_{FCT}}} \qquad (5.2)$$

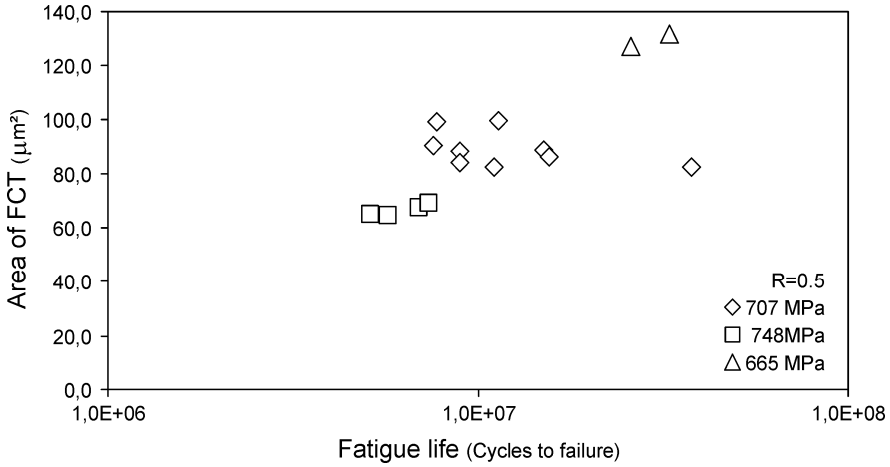

Figure 5.1: FCT area as a function of the fatigue life.

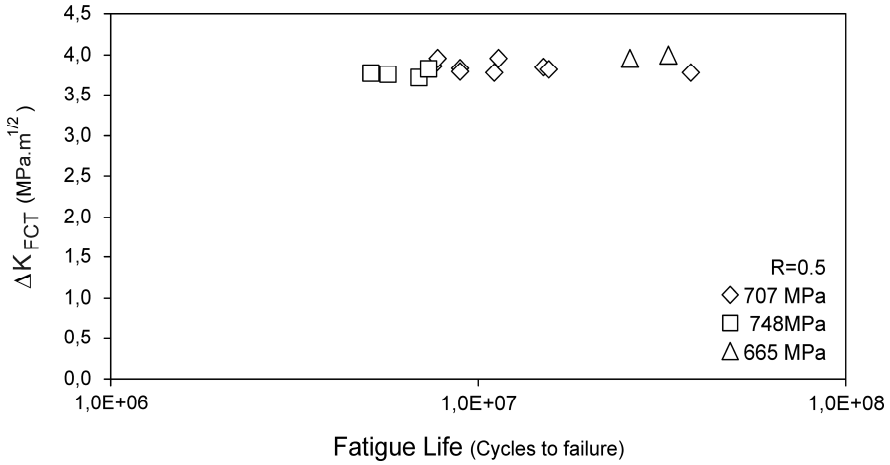

Figure 5.2: Stress intensity factor of the FCT area as a function of the fatigue life.

$\Delta K_{th,0.5}$ is calculated to be 3.82 ± 0.09 MPa√m. The value of $\Delta K_{th,0.5}$ compares quite well with the experimentally measured values of Verpoest [78,110] who performed crack growth rate measurements to determine the fatigue threshold. He measured $\Delta K_{th,R}$ for drawn wires with a UTS between 1321 and 2218 MPa to be between 3.5 and 4 for R = 0 and between 4 and 5 for R ≥ 0.6. It also compares well to the experimental values obtained by Llorca and Sanchez-Galvez [80].

5.2 Kitagawa-Takahashi diagram

5.2.1 Threshold determination method

To get a better understanding on the relevance of the FCT area, an effort is made to present the internal fatigue crack growth in a Kitagawa diagram [62]. It is important to note that the Kitagawa diagram which is explained in the literature review (paragraph 2.3.3) is constructed for surface fatigue crack growth in the low cycle fatigue (LCF, $N_f < 10^5$) and the high cycle fatigue (HCF, $10^5 < N_f < 10^7$) region. When the fatigue crack initiates internally in the very high cycle fatigue (VHCF, $N_f > 10^7$) region it is observed that fatigue cracks can grow for stress-crack length combinations that lie within the Kitagawa-Takahashi diagram. In figure 5.3 the fatigue data of this study are used to explain this behavior.

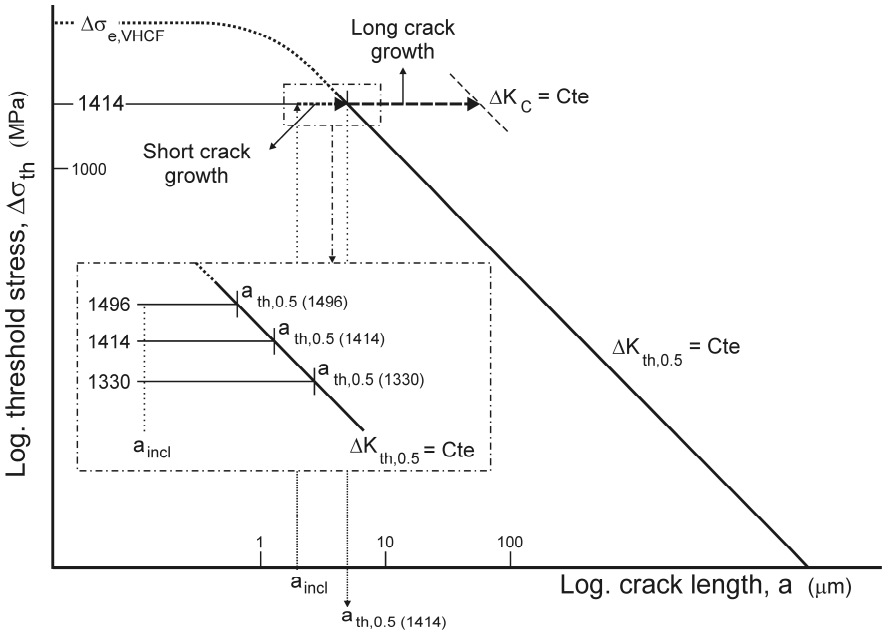

Figure 5.3: Kitagawa-Takahashi diagram for internal fatigue fractures at non-metallic inclusions in heavily drawn steel wires for R = 0.5.

For the heavily drawn steel wires investigated in this study the combination of the defect distribution and the gauge length results in three different crack initiation mechanisms: surface defects in LCF, small surface defects in HCF and internal non-metallic inclusions in VHCF (chapter 4). When for example the gauge length is increased, the probability of finding a critical surface defect will also increase, leading to a higher probability of a surface crack initiation in LCF. This implies that when only the samples that failed in the VHCF region are taken into account, the conventional fatigue limit will be defined by the largest surface defect of these samples. Since the surface defects are less critical than the internal defects,

the conventional fatigue limit has to be higher than the externally applied stress. The conventional fatigue limit of the VHCF samples is indicated as $\Delta\sigma_{e,VHCF}$ in figure 5.3. Since the value of $\Delta\sigma_{e,VHCF}$ and the shape of the transition between $\Delta\sigma_{e,VHCF}$ and $\Delta K_{th,R}$ are unknown, they are shown as a dotted line in figure 5.3.
In this study the applied stress is kept constant during fatigue testing. The majority of the fatigue tests were performed at R = 0.5 and $\Delta\sigma$ = 1414 MPa (σ_a = 707 MPa), which is higher than $\Delta\sigma_e$ but lower than $\Delta\sigma_{e,plain}$. The inclusions from which internal fatigue cracks initiated have a radius between 0.9 and 2.8 μm. To show the fatigue crack growth from an internal inclusion on the Kitagawa diagram an inclusion radius of 2 μm is taken as an example. Figure 5.3 shows that when an internal inclusion of 2 μm (a_{incl}) is loaded to a $\Delta\sigma$ of 1414 MPa the applied stress is lower than $\Delta\sigma_{e,plain}$ and the inclusion size is lower than the critical crack size for long crack growth ($a_{th,0.5\ (1414)}$ calculated to be 5.2 μm by filling in $\Delta K_{th,0.5}$ = 3,82 MPa$\sqrt{m}$ and $\Delta\sigma$ in equation (5.2) and assuming a circular crack (area = $\pi.a^2_{th,0.5}$). Note that this value is only valid for $\Delta\sigma$ = 1414 MPa). Therefore no fatigue crack growth should be possible at all.
Sadananda et al. [44] already addressed this problem using their unified damage approach and suggested that fatigue cracks can still grow due to the presence of internal stresses. These internal stresses (pre-existing or in situ generated) are required for crack growth until $\Delta K_{th,R}$ is reached. This crack growth regime is addressed as short crack growth in this study. When however the short cracks grow away from a pre-existing internal stress field (for example an inclusion) they can get arrested and a non-propagating short crack is formed. At that point the internal stresses have to be created in situ by localized plasticity which is not a cycle by cycle based crack propagation. Therefore the majority of the fatigue life will be in the FCT formation stage, explaining the large fatigue lives of the internal fatigue fractures. When $\Delta K > \Delta K_{th,0.5}$ it is possible for long fatigue cracks to grow until the fracture toughness (ΔK_C) of the material is reached.
In the inset on figure 5.3 $a_{th,0.5}$ is shown for the three different stress amplitudes σ_a = 665, 707 and 748 MPa that were tested in this study for R=0.5. All the $a_{th,0.5}$ are situated on the straight $\Delta K_{th,0.5}$ line, indicating that the fatigue tests are all performed in the long crack growth region of the Kitagawa-Takahashi diagram and that there exists a sharp transition between the short and the long crack growth for these internal crack initiations. Therefore it is concluded that the determination of $\Delta K_{th,R}$ by using the size of the FCT area is correct and that $\Delta K_{th,R} = \Delta K_{FCT,R}$.

5.2.2 Short crack growth

The Kitagawa-Takahashi diagram is a good graphical tool to explain the short crack growth mechanism in relation to the existence of a single fatigue crack growth threshold which is described by the unified damage approach of Sadananda and Vasudevan [44,109] (see chapter 2). It is important to note that the assumption of a single fatigue threshold for crack growth (as described paragraph 2.3.4) may not be valid for the heavily drawn steel wires investigated

in this study. Fractographical investigations show that short fatigue cracks don't grow solely in mode I but in a mixed mode. This can be incorporated in the unified damage approach (internal stress model) by redefining the internal stress triangle (figure 5.4). In stead of using $\Delta K_{th,R}$ as a criterion for crack growth $\Delta K_{th,mixed}$ should be used. This will not change anything to the threshold determination method, which is based on the size of the FCT area (transition between mixed mode and mode I crack growth).
Since $\Delta K_{th,mixed}$ is unknown and in order to allow a clear graphical illustration of the mechanisms, it is assumed that there exists a single fatigue threshold for crack growth. Therefore the unified damage approach is used in its original form to describe the short crack growth behavior of heavily drawn steel wires.
In the unified damage approach it is described that short fatigue cracks can grow due to the presence of pre-existing internal stress concentrations or the in situ generation of internal stresses via cyclic plasticity. The magnitude of the required internal stresses for short crack growth are given by the triangular area which is created on the Kitagawa-Takahashi diagram when the linear segment ($\Delta K_{th,R}$) is extrapolated to lower crack lengths. This triangular area is schematically shown in figure 5.4.

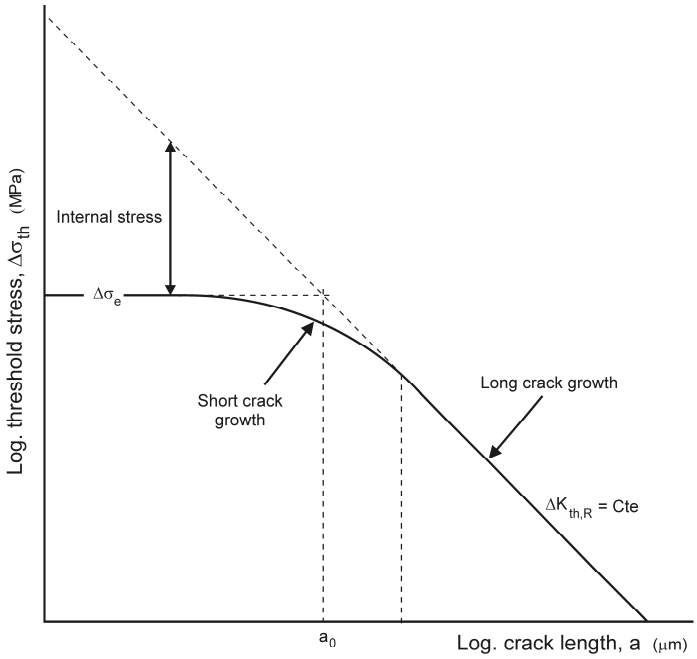

Figure 5.4: Internal stress region on the Kitagawa-Takahashi diagram.

The unified damage approach can be used to explain the short crack growth behavior that is observed for the internal fatigue fractures of the heavily drawn steel wires investigated in this study. Figure 5.5 shows an example (identical as in

paragraph 5.2.1) of an internal fatigue crack initiation at an inclusion with a radius of 2 μm on a Kitagawa-Takahashi diagram, for a constant applied stress ($\Delta\sigma$ = 1414 MPa) and R = 0.5. The inset of figure 5.5 shows a magnification of the short crack growth region. In the initial stage (when the material is loaded for the first time) the inclusion site is located at the intersection of a_{incl} (2 μm) and the applied stress (1414 MPa). It is assumed that a small fatigue crack is pre-existing at the edge of the inclusion or that it has just nucleated (this assumption is microstructurally validated and described in paragraph 7.4). The necessary condition for the growth of this small fatigue crack is to exceed the threshold value for crack growth ($\Delta K_{th,0.5}$). To do so, the gap between the initial stage and $\Delta K_{th,0.5}$ has to be bridged. This is possible by the high internal stresses that exist around pre-existing stress concentrations and/or by the in situ generation of internal stresses by cyclic plasticity. In the inset of figure 5.5 the gap is indicated by 'Minimum required internal stress for crack growth'.

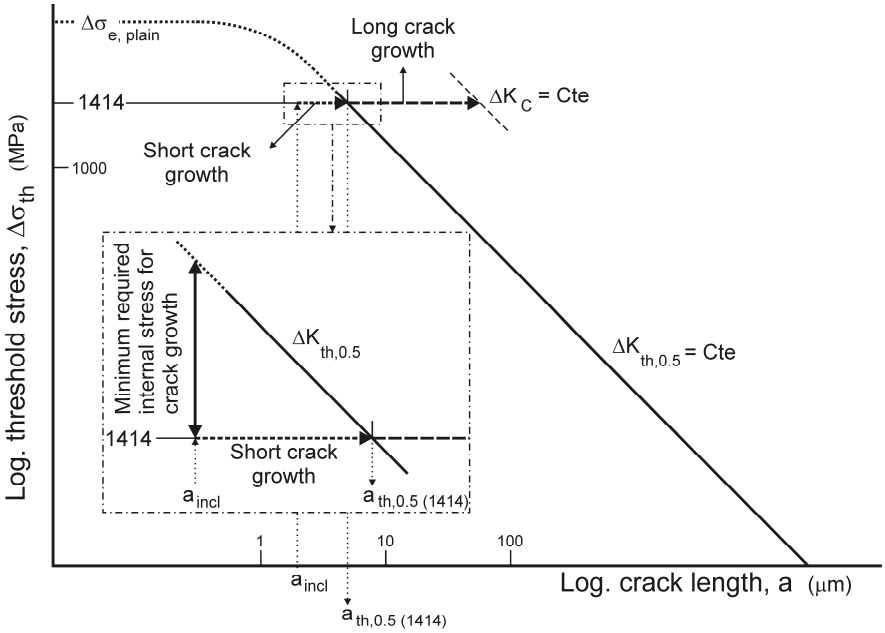

Figure 5.5: Short crack growth of internal fatigue fractures shown on a Kitagawa diagram.

The three different internal stress profiles of the pre-existing stress concentrations, which are causing non-propagating, arresting or growing fatigue cracks, are described in detail in the literature review (chapter 2). Here, case 2 (arrested fatigue crack) will be used to describe the active mechanisms of short crack growth for internal fatigue fractures.

Very high internal stresses can be present around non-metallic inclusions. If the inclusion is idealised as a circular hole, the maximum tensile stress around the inclusion is 3 times larger than the applied stress. Besides the absolute value, the

stress gradient is important. It is generally known that the internal stress field around inclusions are very steep and can already approach the stresses in the bulk of the material after 2 to 3 times the inclusion radius.
In the frame of the master thesis of Peter Masschelein (2008-2009), the equivalent Von Mises stresses in and around an inclusion are calculated with finite element modeling (FEM). A linear elastic model is used for three octahedral inclusions with a different composition (Al_2O_3, TiO_2, SiO_2) in a steel matrix. The bonding between the inclusions and the matrix is assumed to be perfect. The Youngs modulus and the Poisson coefficients that are used are given in table 5.1.
Since the FEM is linear elastic, it is possible to extrapolate the results for other applied stress levels. Therefore it is chosen to give the resulting stresses as a percentage of the stress that is applied on the matrix. Table 5.2 gives the maximum stress inside the inclusion and the matrix.

Table 5.1: Youngs modulus and Poisson coefficient of inclusions and matrix.

Material	Youngs modulus (GPa)	Poisson coefficient
Al_2O_3	402	0,233
TiO_2	287	0,268
SiO_2	95	0,082
Fe-matrix	210	0,29

Table 5.2: Maximum stress inside the inclusion and matrix as a percentage of the externally applied stress (FEM results)

Inclusion	Max. stress inside the inclusion (% of the applied stress)	Max. Stress in the matrix (% of the applied stress)
Al_2O_3	160	120
TiO_2	125	108
SiO_2	107	104

The FEM results show that Al_2O_3 inclusions lead to the highest stresses inside the surrounding matrix due to the large difference between the Youngs modulus of the inclusion and the matrix. The FEM results also show that the stresses in the matrix approach the bulk stress of the material after 1 to 2 times the inclusion radius. Further it is shown that the stresses around inclusions are much less than around a circular hole. Caution is needed however when the FEM results are interpreted because some important idealizations are made. The most important one is the assumption that the bonding between the inclusion and the matrix is perfect. This is not the case. Microstructural characterization (paragraph 7.4, chapter 7) around inclusions even show the presence of cracks at the interface between the inclusion and the matrix. This indicates that the calculated Von Mises stresses can not be used for further analyses. It is expected that the real stresses that will be present in the matrix around an inclusion will be between the ones that are calculated by the FEM model (perfect interface bonding) and the analytical calculations. Nevertheless, the FEM gives an indication of the relative importance of the inclusion composition.

Figure 5.6 shows a schematic representation of a possible internal stress field around an internal inclusion on the triangular internal stress region of the Kitagawa-Takahashi diagram (hypothetical, only used to illustrate the concept of crack arrest). Close to the inclusion the internal stresses are larger than $\Delta K_{th,R}$, meaning that fatigue cracks can grow. Due to the steep gradient of the internal stress profile the internal stress can drop below $\Delta K_{th,R}$. At this point the crack gets arrested, leaving a non-propagating fatigue crack behind. The further growth of this non-propagating fatigue crack is only possible by the in situ generation of internal stresses via cyclic plasticity. The non-propagating fatigue crack will continue its growth when the in situ generated internal stresses exceed $\Delta K_{th,R}$, It is expected that the in situ generation of the internal stresses causes the high fatigue lives observed for the internal fatigue fractures.

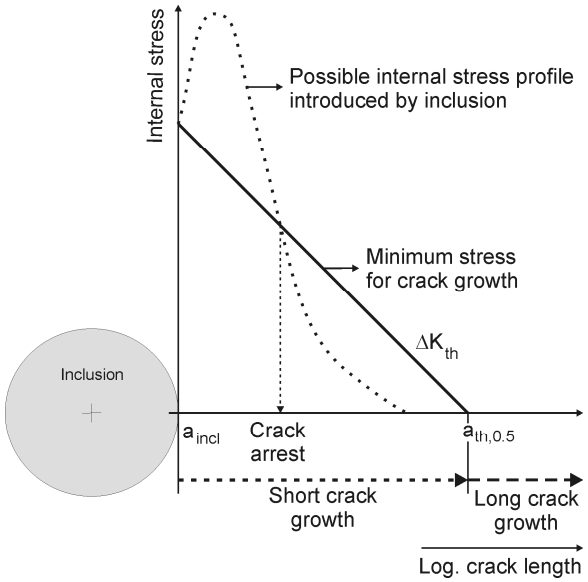

Figure 5.6: Possible internal stress profile introduced by an inclusion represented on the triangular internal stress region of the Kitagawa-Takahashi diagram.

There exist two other possible internal stress profiles around stress concentrations with respect to the triangular internal stress region of the Kitagawa-Takahashi diagram (literature review in chapter 2). In case 1, the internal stress profile is always larger than $\Delta K_{th,R}$. The fatigue crack grows without any arrest. Case 2 is already described in detail above and in case 3, the internal stress profile never exceeds $\Delta K_{th,R}$, meaning that the fatigue crack can not grow without the in situ generation of additional internal stresses.
Some similar approaches are described in literature [44]. The main difference with the approach discussed in this paragraph is that in literature the internal fatigue fractures are presented in the area above $\Delta\sigma_e$. This means that both the short and the long crack growth region are located outside the Kitagawa-

Takahashi diagram, while this approach successfully locates the short crack growth region within the Kitagawa-Takahashi diagram.

5.3 Conclusions

A new threshold determination method to determine the threshold for long crack growth is developed. Due to a lack of other experimental techniques to measure the threshold for long crack growth for such small diameter wires, it was not possible to validate these results. The author would strongly suggest validating the results whenever another experimental method becomes available.

The discussion on the growth of short fatigue cracks is completely based on the unified damage approach since this approach explains the short crack growth mechanism best according to the author. However it is important to note that the assumption of a single threshold for crack growth (unified damage approach) may not be valid for the heavily drawn steel wires investigated in this study. Based on fractographical results it is observed that short fatigue cracks grow in mixed mode, indicating that it is not correct to use the mode I threshold value. This can be incorporated in the unified damage approach (internal stress model) by redefining the internal stress region in the Kitagawa Takahashi diagram. In stead of using $\Delta K_{th,R}$ as a criterion for crack growth $\Delta K_{th,mixed}$ should be used. This will not change anything to the threshold determination method, which is based on the size of the FCT area (transition between mixed mode and mode I crack growth).

6 Surface roughness

In the frame of a master thesis which was performed by Bart Ballet in the academic year 2007-2008, the influence of decreasing the surface roughness on the fatigue properties and more specifically on the fatigue crack initiation mechanisms of heavily drawn steel wires is investigated. A brass coated heavily drawn steel wire with a diameter of 350 µm is used (further called reference material) for the analyses. The wire is electro-chemically polished and the roughness of both the reference and the polished wires is measured. Further, stress driven pull-pull fatigue tests are performed on both wires to be able to compare their fatigue properties.

6.1 Experimental methods

6.1.1 Polishing method

To reduce the surface roughness of the wires an electrochemical polishing method is used. It is important that the method is reproducible in order to create wires with the same surface roughness after polishing. Further the polish method must create a smooth wire surface without any chemical degradation of the surface layer: the existing surface defects should be removed without introducing other surface defects. It is also important that the polishing method creates a constant wire diameter over a large wire length. If this would not be the case, the stresses caused by the applied load during fatigue testing would be maximum at the place where the diameter of the wire is minimum. The driving factor for crack growth (ΔK) would also be maximum at this place, leading to a local preferential crack initiation. This would lead to a large scatter between the different wires which is strongly affected by the surface defect distribution of the wires.
The polishing procedure consists of following steps:

- Removal of the brass coating
- Polishing test setup
- Electrochemical polishing
- Protection and storage

Removal of the brass coating

The first step of the polishing procedure is the removal of the brass coating (the procedure is described in paragraph 4.1.2.4). The wire is submerged in a hydrous ammoniumpersulfate solution at room temperature. The brass coating is dissolved according to the following reactions:

Reduction:

$$S_2O_8^{-2} + 2e^- \Rightarrow 2SO_4^{2-} \qquad (6.1)$$

Oxidation:

$$Zn \Rightarrow Zn^{2+} + 2e^{-} \tag{6.2a}$$

$$Cu \Rightarrow Cu^{2+} + 2e^{-} \tag{6.2a}$$

Since ammonium is present in the solution it reacts with Cu and Zn:

$$NH_4OH \Rightarrow NH_3 + H_2O \tag{6.3a}$$

$$Zn^{+} + 4NH_3 \Rightarrow \left[Zn\left(NH_3\right)_4 \right]^{2+} \tag{6.3b}$$

$$Cu^{+} + 4NH_3 \Rightarrow \left[Cu\left(NH_3\right)_4 \right]^{2+} \tag{6.3c}$$

and the Fe react with the persulfate:

$$Fe + S_2O_8^{-2} \Leftrightarrow Fe^{2+} + 2SO_4^{2-} \tag{6.4}$$

Due to the formation of a FeO surface layer the steel wire itself will not go into solution. This oxide layer will be removed by submerging the wire in a HCl solution:

$$FeO + 2HCl \Rightarrow H_2O + Fe^{2+} + 2Cl^{-} \tag{6.5}$$

After each step the wires are rinsed with distilled water to stop the reaction, and remove the residual chemicals. After the last step the wires are rinsed with ethanol to dry the wires and they are finally stored in hexane to prevent any interactions with the environment.

Polishing test setup

Figure 6.1 shows a schematic representation of the polishing test setup.

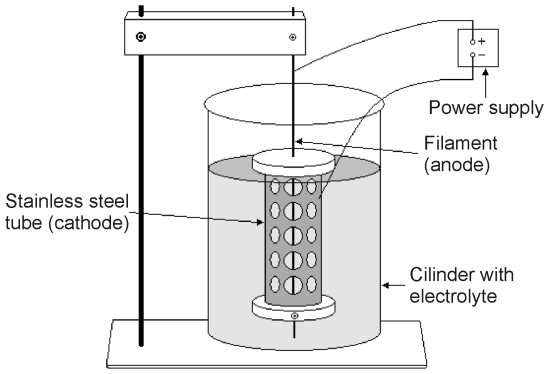

Figure 6.1: Schematic representation of the polishing test setup.

The wire is clamped in a plastic holder at the bottom and the top of the perforated stainless steel tube (with a length of 15 cm and a diameter of 4 cm) in such a way that the wire is located exactly in the middle of the tube. The construction is hung with the wire and due to the weight of the tube the wire gets straight and aligned in the middle of the electrolyte. The positive side of the power supply is connected to the filament (anode) and the negative side to the stainless steel tube (cathode).

Electrochemical polishing
In the PhD thesis of H. Delrue [111] it is described that the best polishing conditions for steel wires are obtained with an electrolyte with following composition: 133 ml acetic acid (CH_3COOH), 25 g chromium trioxide (CrO_3) and 7 ml water (H_2O). The strongly oxidizing chromium trioxide dissolves potentially formed metal oxides on the wire surface and therefore avoids the formation of pits in the surface.
According to Faraday's law the amount of oxidized material is direct proportional to the quantity of electricity that is passed through the cell. Therefore the current density is one of the most important parameters for the electrochemical polishing. Based on the polarization curves that were made by Shigolev [112] for this electrolyte, it is best to use a current density between 0.1 and 0.2 A/cm². For the tests performed in this study an initial current density of 0.15 A/cm² is chosen.

Protection and storage
As was already shown in paragraph 4.1.2 environmental interactions can deteriorate the fatigue properties of these highly drawn steel wires. Although the brass coating is removed for the polished samples (galvanic couple) the wire is very reactive due to the newly created surface. Therefore all the wires are rinsed with water (to remove residual electrolyte), dried with ethanol and coated with glue. The glue coating should prevent any environmental interactions that can disturb the fatigue properties.

6.1.2 Roughness measurements

To quantify the effect of the electrochemical polishing the roughness of the wires is measured with a Wyko Optical Profiling System. This system is based on white light interferometry and allows a contactless high resolution 3D measurement of the wire surface. The roughness of the surface is characterized by the use of R values which are defined by:

$$R_a = \frac{1}{M \cdot N} \sum_{j=1}^{M} \sum_{i=1}^{N} \left| Z_{ij} \right| \tag{6.6}$$

$$R_t = R_p = R_v \tag{6.7}$$

with

M: amount of datapoints in the x-direction
N: amount of datapoints in the y-direction
Z: difference in height compared to the mean plane
R_a: average roughness
R_t: difference between the lowest valley and the highest peak
R_p: maximum profile peak height compared to the mean
R_v: maximum profile valley depth compared to the mean

The roughness measurements were done on a wire with a brass coating, without a brass coating and on three polished wires.

6.2 Results

6.2.1 Polishing method

The polishing time was varied between 45 and 75 minutes and the diameter was measured for all polished wires. It was observed that due to the test setup the diameter at the top of the wire is much smaller than at the bottom, leaving a very small useful length for fatigue testing. An optimum between the obtained surface roughness and the variation in wire diameter was found at a polishing time of 60 minutes. Due to the decrease in wire diameter as a function of time the current density will increase during the polishing process. After one hour of polishing the wire diameter has decreased 70 μm (∅ 350 to 280 μm) which causes an increase in current density from 0.15 to 0.19 A/cm². This is still within the region which was suggested by Shigolev [112] for this electrolyte.
Due to the internal resistance of the wire which causes a difference in voltage between the top and the bottom of the wire, the wire is etched inhomogeneously leading to a variation in diameter. This change in diameter is measured using the scanning electron microscope (SEM). After 1 hour of polishing the variation in diameter is 28.6 ± 2.6 μm over 12 cm of wire, or 2.4 ± 0.2 μm per cm wire length. For the fatigue tests performed in this study this change in diameter leads to a stress difference between the top and the bottom of the wire between 120 and 135 MPa. Although the influence of this stress profile is rather small, the diameter of all fatigue fractures is measured and the actual applied stress calculated and used for further analyses.
Figure 6.2 shows a SEM image of a wire after removing the brass coating and after polishing. It can be observed clearly that the surface roughness is decreased significantly (below $1/10^{th}$ of the initial roughness) by the polishing method.
This change in surface roughness is quantified using white light interferometry measurements. For each wire an area of 4000 μm² is measured. Figure 6.3 gives the results of the unpolished wires with and without the brass coating. Figure 6.4 gives the results of the polished wires. Table 6.1 gives the R_a values of the wires.

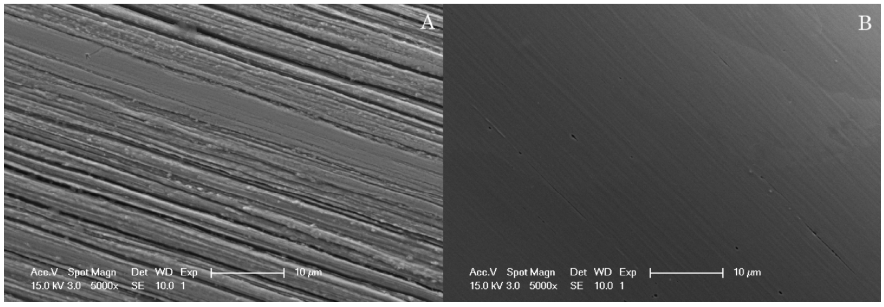

Figure 6.2: SEM picture of a wire (a) after removing the brass coating and (b) after the polishing process.

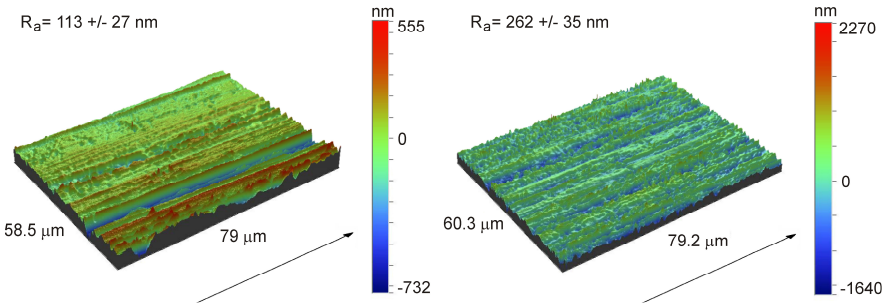

Figure 6.3: 3D roughness profile of (left) wire with brass coating and (right) without brass coating. The arrow gives the drawing ditection.

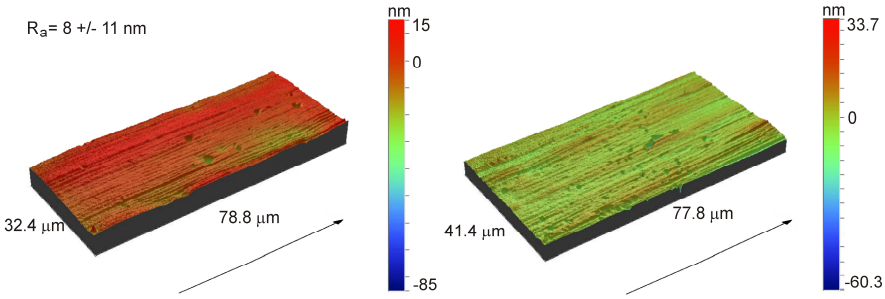

Figure 6.4: 3D roughness profile of polished wires. The arrow gives the drawing detection.

Table 6.1: R_a values of the different wires.

	Reference wire	Wire without brass coating	Polished wire
R_a	113 ± 27 nm	262 ± 35 nm	8 ± 11 nm

From the roughness measurements it is observed that the surface roughness doubles due to the removal of the brass coating. This can be explained by the wire drawing production process. Since the brass is much softer than the steel, it will

act as a lubricant during the wet wire drawing process. Therefore the brass coating will be smeared out over the wire surface covering the drawing lines in the steel (left side of figure 6.2). When however the wires are polished the roughness decreases significantly (more than one order of magnitude compared to the wire without brass coating).
It is however important to note that it is expected that the roughness of the filaments has very little influence on the fatigue properties of the wires due to the low values (sub-micron) on one hand and the strong orientation of the grooves following the wire axis (grooves are oriented with the applied load) on the other hand. As is known from literature and our own experimental results, the fatigue properties will be controlled by surface stress concentrations (when the environmental fatigue crack initiation mechanism is not active). Due to the removal of a large portion of the surface (diameter decreases from 350 to 280 μm) these surface stress concentration will also be removed. When the surface of the polished wires is investigated with SEM it is observed that there still exist some small surface stress concentrations (figure 6.5).

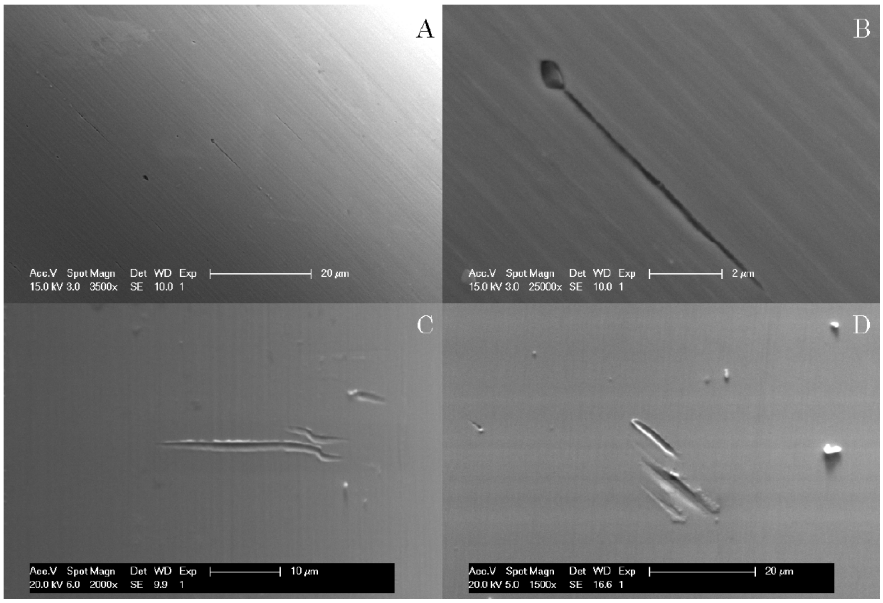

Figure 6.5: Surface stress concentrations on polished wires.

Figure 6.5 A and B show some typical surface defects of polished wires. These are caused by the presence of inclusions in the wire, which was also observed by Verpoest et al. [78]. Figure 6.5 B shows a detailed view of a former inclusion. At the left top the elliptical hole indicated where the inclusion was present. Below the inclusion some kind of tail is present. This indicates that the material behind the inclusion has different properties compared to the bulk material and therefore is etched away preferentially.

Figure 6.5 C and D show scratches on the wire surface that were caused by handling the wires after the polishing process. Therefore special care is needed for handling heavily drawn steel wires in general.

6.2.2 Fatigue tests

The fatigue tests are performed at an R value of 0.5 and a maximum stress level between 60 and 75 % of the ultimate tensile strength (UTS). The UTS of the reference wires and the polished wires is measured and given in table 6.2.

Table 6.2: UTS of the reference and the polished wire.

	Reference wire	Polished wire
UTS	3622 ± 139 MPa	3600 ± 330 MPa

Although the scatter is larger for the polished wires, there is no significant difference between the UTS of the reference and the polished wires.
Due to severe problems with clamp fractures only 20% of the fatigue tests were successful, leaving only 9 fatigue fractures. Figure 6.6 shows the results of the fatigue tests on the polished wires.

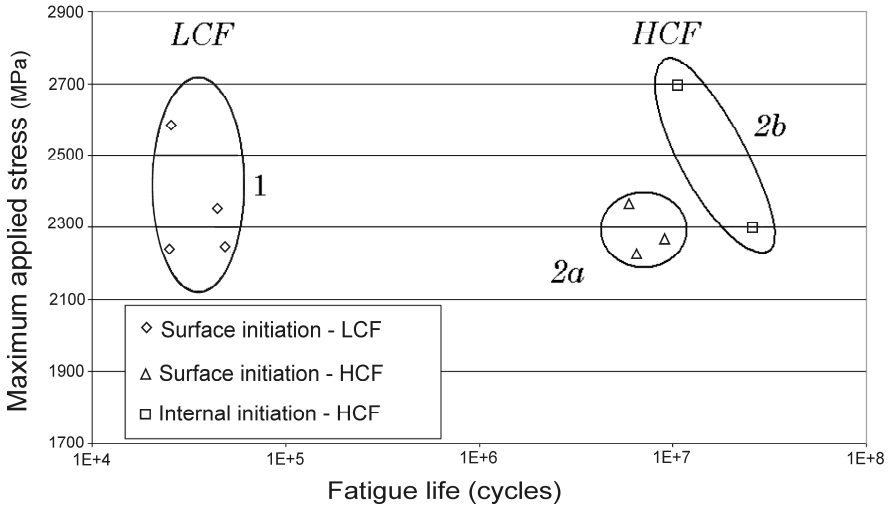

Figure 6.6: Fatigue data of the polished wires.

Based on fractography it was observed that three different fatigue fractures occurred for the polished samples. Therefore the successful fatigue tests are subdivided in three groups: surface crack initiations in low cycle fatigue (LCF), surface crack initiations in high cycle fatigue (HCF) and Internal crack initiations in HCF. Figure 6.7 A and B show the fatigue crack initiations in LCF, where small surface defects can be detected at the fatigue crack initiation area. Three out of four of the surface crack initiations in low cycle fatigue have these small stress concentrations at the initiation area, one wire doesn't show any stress

concentration at the crack initiation area. Since one of the samples failed in LCF without the presence of any stress concentration it is very likely that environmental influences play a dominant role in the fatigue crack initiation stage (paragraph 4.1.2). Figure 6.7 C and D show the surface fatigue crack initiations in HCF, where no significant stress concentrations can be found. The mechanism behind these surface crack initiations in HCF is already described in paragraph 4.1.3.1.

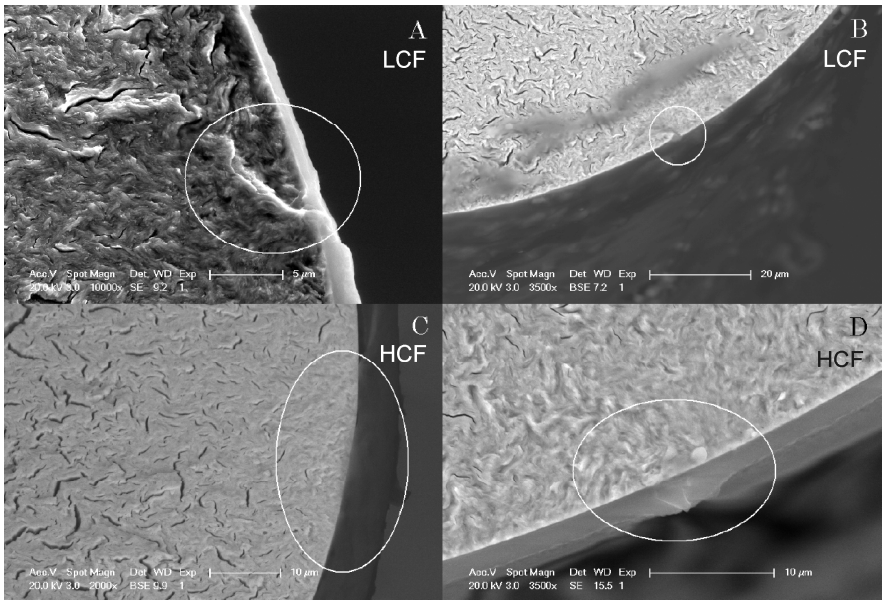

Figure 6.7: SEM picture of fatigue crack initiation areas of surface fractures in (A and B) LCF and (C and D) HCF.

The internal fatigue crack initiations (only two fractures) show the typical fish eye appearance which is described in detail in paragraph 4.1.3.2. Figure 6.8 gives an example of such a fracture.

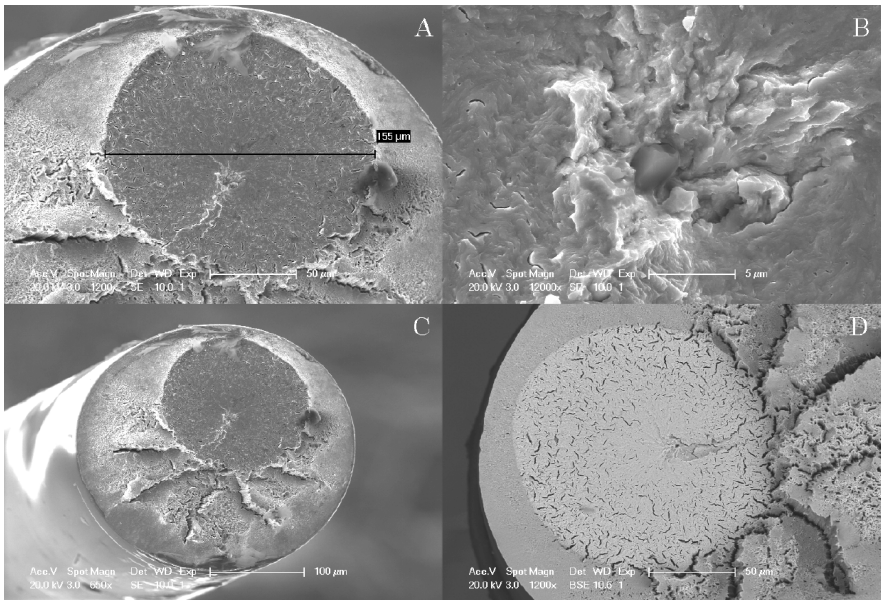

Figure 6.8: Internal fatigue crack initiation in HCF showing a typical fish eye fracture.

Figure 6.9 shows the fatigue data of the polished samples together with the reference samples. The figure shows that the reference wires all fail in the LCF and that the cracks all initiate from the surface.

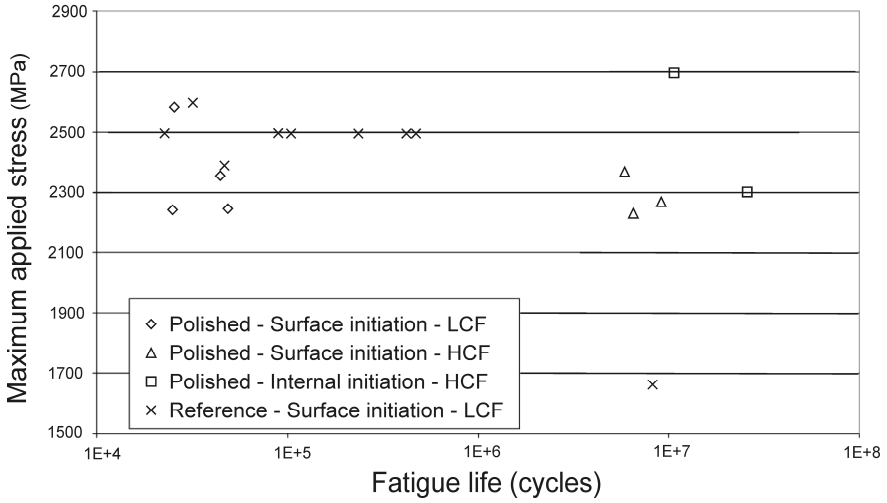

Figure 6.9: Fatigue data of the polished and reference wires.

6.3 Conclusions

Although it is tempting to conclude that the reduced roughness leads to an increase in the fatigue life it is not right to do so. First of all, due to the removal of a large portion of the material it is likely that the internal stress distribution changes completely. A change in internal stress distribution will change the fatigue properties of the filaments due to a change in the local stress state at the fatigue crack initiation region. Secondly, the surface roughness in the reference material is already too small (submicron) to cause a significant stress concentration for fatigue. The reduction in diameter by etching can however remove the pre-existing surface stress concentrations (surface inclusions, surface oxides, big drawing defects) that lead to large stress concentrations (paragraph 4.1.3.1). It is however important to note that new surface defects are created during the etching process by the presence of inclusions in the steel (figure 6.5), which can also lead to significant stress concentrations.

Since it is shown already that environmentally assisted fatigue crack initiations can be very dominant (paragraph 4.1.2) it is very plausible that the observed increase in fatigue life is caused by the removal of chlorides on the surface by the polishing procedure and by the protection of the wires from the environment by a glue coating after polishing.

Although no conclusions can be drawn from the experiments due to the reasons stated above, it was still decided to include this chapter since it describes a successful procedure to polish very thin filaments. Further it shows the roughness profile of a heavily drawn steel wire and of the same wire without a brass coating. Also the author of this thesis is convinced that the described polishing procedure can be helpful to determine the intrinsic fatigue properties (fatigue properties of a material without surface stress concentrations) of materials for which the fatigue properties are governed completely by large surface stress concentrations.

7 Influence of non-metallic inclusions

7.1 Introduction

It is known from research on high strength steels (literature review, chapter 2) that the presence of non-metallic inclusions (further referred to as inclusions) can affect the fatigue properties in a negative way. Several studies on high strength steels show that both the short and long fatigue lives are affected by the presence of inclusions. In all cases the short fatigue lives are controlled by surface crack initiations at surface defects and the long fatigue lives are controlled by internal crack initiations at inclusions. In the literature on high strength steels the influence of the inclusion size and location is clear, but little research is done on the influence of the inclusion composition and the inclusion geometry on the fatigue properties. Since the inclusion composition and the inclusion geometry have an influence on the stress state in and around the inclusion [113] it is interesting to study the influence of these factors on the fatigue life.
Due to the extensive plastic deformations during the wire drawing process it is not possible to extrapolate the findings on high strength steels to heavily drawn steel wires. Therefore, the influence of inclusions on the fatigue properties of heavily drawn steel wires is investigated in this chapter (paragraph 7.3). In paragraph 7.2 the inclusion content and composition of two different wire rods is investigated. This part of the research was performed in the frame of a master thesis by Peter Masschelein in the academic year 2008-2009.

Material
Two different brass coated steel wires are used to study the influence of inclusions on the fatigue properties. The first wire has a diameter of 175 µm and an ultimate tensile strength (UTS) of 3187 ± 37 MPa and was cold drawn to a strain of 3.5. The wire has a threshold stress intensity factor range for crack growth ($\Delta K_{th,0.5}$) of 3.82 ± 0.09 MPa$\sqrt{m}$ (chapter 5). The second wire has a diameter of 300 µm and a UTS of 3300 ± 100 MPa and was cold drawn to a strain of 3.6. The $\Delta K_{th,0.5}$ is calculated to be 4.14 ± 0.05 MPa$\sqrt{m}$ by using the methodology which is described in chapter 5. Both wires have the same carbon equivalent (%CE = %C + %Mn/6). It is important to note that the wire rod used to draw both wires comes from different suppliers, meaning that differences in inclusion properties (size, composition and distribution) can be expected.

Fatigue tests
Two different loading conditions were used for the wires with a diameter of 175 µm. The majority (about 80%) of the tests were done at a stress amplitude (σ_a) of 707 MPa and a load ratio (R) of 0.5 (σ_{max} = 2828 MPa). The other wires with a diameter of 175 µm were loaded at σ_a = 1123 MPa and R = 0.2 (σ_{max} = 2827 MPa). The wires with a diameter of 300 µm were loaded at σ_a = 670 MPa and R = 0.5 (σ_{max} = 2680 MPa).

Microscopy
A fractography study was performed on all fatigue fractures with scanning electron microscopy (SEM) using a FEI XL30 FEG system. Only the fatigue fractures that failed due to the presence of inclusions are described in this chapter. The microstructure around inclusions is characterized with a SEM/FIB (focused ion beam) using a FEI Dual beam Nova 600 Nanolab system. The material was etched away using a FIB current of 0.92 nA and the microstructure was made visible using FIB imaging with a current of 9.3 pA.

7.2 Inclusions in wire rod

The morphological and chemical properties of inclusions in wire rods that are described in this paragraph are performed automatically by the NSS software on the FEI XL40 SEM-Lab6 system. The software automatically detects the inclusions on sections of the wire rod based on the difference in contrast and chemical composition between the inclusion and the surrounding matrix on a back scattered electron (BSE) image. For each inclusion the geometry and the chemical composition is measured.
The inclusions are measured on two different types of wire rods (called wire rod A and B in the following text). Wire rod A is made from a high grade steel and is used to draw the 300 µm wire that is used to study the influence of inclusions in this chapter. Wire rod B is made from a low grade steel.

7.2.1 Wire rod A

An area of 2 mm² is scanned for inclusions. In total 110 inclusions were identified, leading to an area density of 55 mm^{-2}. figure 7.1 shows the distribution of inclusion composition in a ternary diagram. The inclusions are subdivided into two groups: 53 inclusions (48%) completely exist of oxides (further referred to as oxide inclusions) while 57 inclusions (52%) also contain sulfur and nitrogen (further referred to as sulfide inclusions).

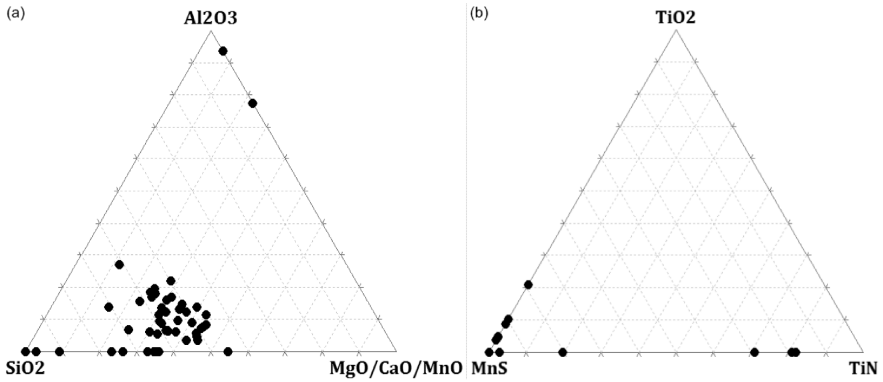

Figure 7.1: Distribution of the inclusion composition of (a) oxide inclusions and (b) sulfide inclusions in wire rod A.

Most of the oxide inclusions have a composition of about 60 % SiO_2, 10 % Al_2O_3 and 30 % of a mixture of MgO, CaO and MnO. Some inclusions have a very high concentration of Al_2O_3. Most of the sulfide inclusions consist almost completely of MnS (90-100%). In most of these inclusions Ti is present and some of the inclusions consist of a large amount of TiN.
Figure 7.2 shows the logarithm of the inclusion density as a function of the inclusion size. The inclusion density is defined as the amount of inclusions per unit of volume divided by the statistical interval length (the length which is chosen to group the data to form a histogram), which has as unit length^{-4}. The inclusion size is defined as the equivalent diameter (the diameter of a perfect sphere that has the same volume as the inclusion itself).
It is important to note that the inclusion density was incorrectly calculated in the master thesis of Peter Masschelein. To calculate the inclusion density, he divided the inclusion area density (55 mm^{-2} for wire rod A) by the average inclusion size, which leads to a significant overestimation of the inclusion density. This erroneous calculation was corrected by dividing the inclusion area density by the average distance between two inclusions. For wire rod A the average distance between two inclusions was estimated to be 134.8 μm (1/√area density).

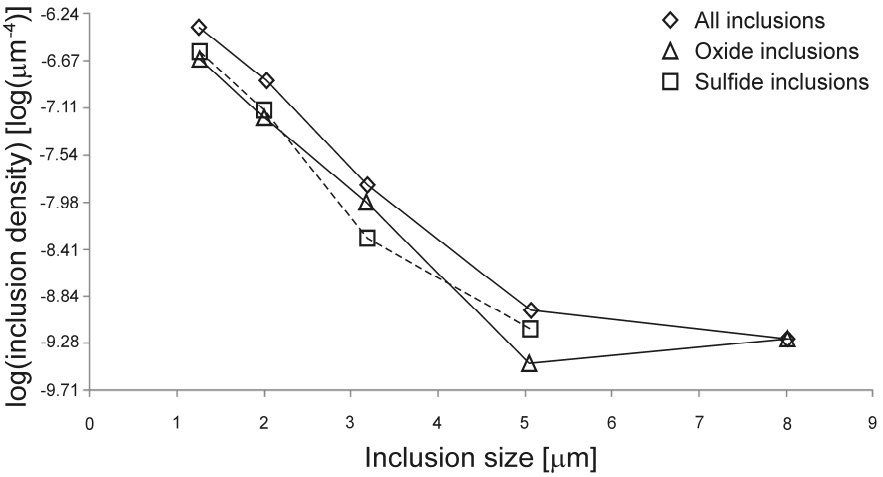

Figure 7.2: Logarithm of the inclusion density as a function of the inclusion size in wire rod A.

Figure 7.2 shows that the amount of oxide and sulfide inclusions is more or less the same. The sulfide inclusions are smaller with a size up to 5 μm while the oxide inclusions have a size up to 8 μm. The majority of the inclusions is smaller than 2 μm.
Based on these data it is possible to calculate the volume density of the inclusions, which is shown in table 7.1. In total there are 408 inclusions present in each mm³ of wire rod.

Table 7.1: volume density of the inclusions in wire rod A.

Type of inclusion	Volume density (mm^{-3})
All inclusions	408
Oxide (Al_2O_3, SiO_2, MgO, CaO, MnO)	199
Sulfide (MnS, TiO_2, TiN)	209

7.2.2 Wire rod B

An area of 4.5 mm² is scanned for inclusions. In total 219 inclusions were identified, leading to an area density of 48 mm^{-2}. Figure 7.3 shows the distribution of inclusion composition in a ternary diagram. The inclusions are subdivided into two groups: 52 inclusions (24%) are oxide inclusions while 167 inclusions (76%) are sulfide inclusions.

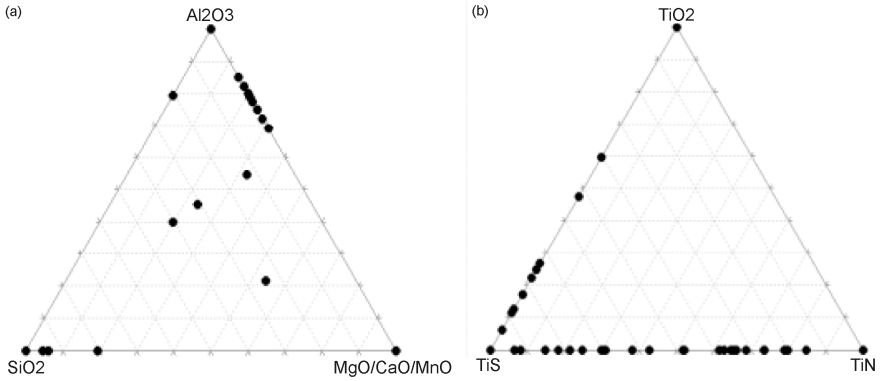

Figure 7.3: Distribution of the inclusion composition of (a) oxide inclusions and (b) sulfide inclusions in wire rod B.

About 35 % of the oxide inclusions in wire rod B have a composition of about 70 % Al_2O_3, 30 % of a mixture of MgO, CaO and MnO and no SiO_2. 55 % of the oxide inclusions have a composition of almost 100% SiO_2. Most of the sulfide inclusions consist almost completely of MnS (90-100%). In most of these inclusions Ti is present and some of the inclusions consist of a large amount of TiN or TiO_2.

Figure 7.4 shows the logarithm of the inclusion density as a function of the inclusion size. For wire rod B the average distance between two inclusions was estimated to be 144.3 µm (1/√area density). It is observed that there are more sulfide inclusions than oxide inclusions present in wire rod B. The sulfide inclusions are smaller with a size up to 8 µm while the oxide inclusions have a size up to 20 µm. The majority of the inclusions is smaller than 5 µm.

Based on these data it is possible to calculate the volume density of the inclusions, which is shown in table 7.2. In total there are 27,000 inclusions present in each mm³ of wire rod.

Table 7.2: volume density of the inclusions in wire rod B.

Type of inclusion	Volume density (mm^{-3})
All inclusions	333
Oxide (Al_2O_3, SiO_2, MgO, CaO, MnO)	81
Sulfide (MnS, TiO_2, TiN)	252

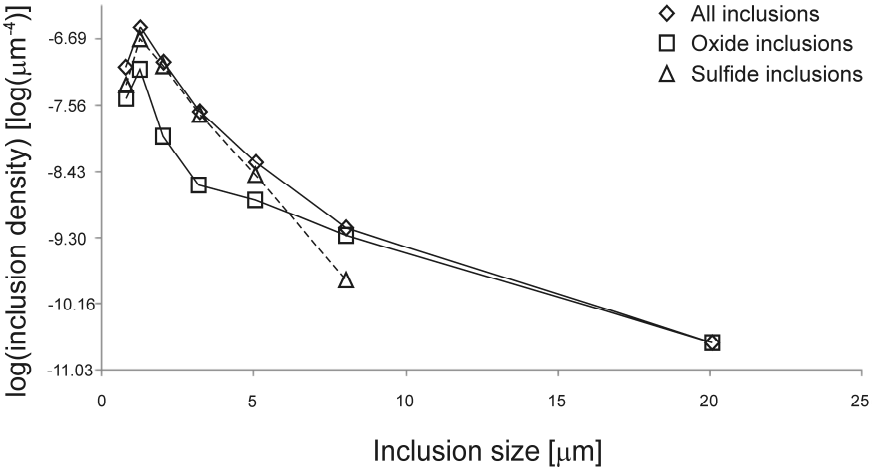

Figure 7.4: Logarithm of the inclusion density as a function of the inclusion size in wire rod B.

It is important to note that, although wire rod B has a lower inclusion content (volume density) than wire rod A, it contains much larger inclusions. Further it contains a larger portion of Al_2O_3 inclusions compared to wire rod A. Therefore it can be expected that wires that are drawn from wire rod A will have better fatigue properties than the ones that will be drawn from wire rod B. This was experimentally validated in the master thesis of Peter Masschelein.
In the next paragraph the influence of the inclusion size, location, composition and geometry will be experimentally shown.

7.3 Inclusion properties

7.3.1 Inclusion size and location

The influence of the inclusion size and location can be deduced directly from Murakami's formulae [114] for surface and internal inclusions. For the readers convenience both formulae are shown again in this chapter (equation 7.1 and 7.2).

$$\Delta K_{surface} = 0.65 \cdot \Delta\sigma \cdot \sqrt{\pi\sqrt{area}} \tag{7.1}$$

$$\Delta K_{internal} = 0.5 \cdot \Delta\sigma \cdot \sqrt{\pi\sqrt{area}} \tag{7.2}$$

ΔK is the stress intensity factor range, Δσ is the applied stress range and *area* is the area of the inclusion projected on a plane perpendicular to the loading direction. For surface inclusions the weakened area [114] is added to the inclusions projected area.

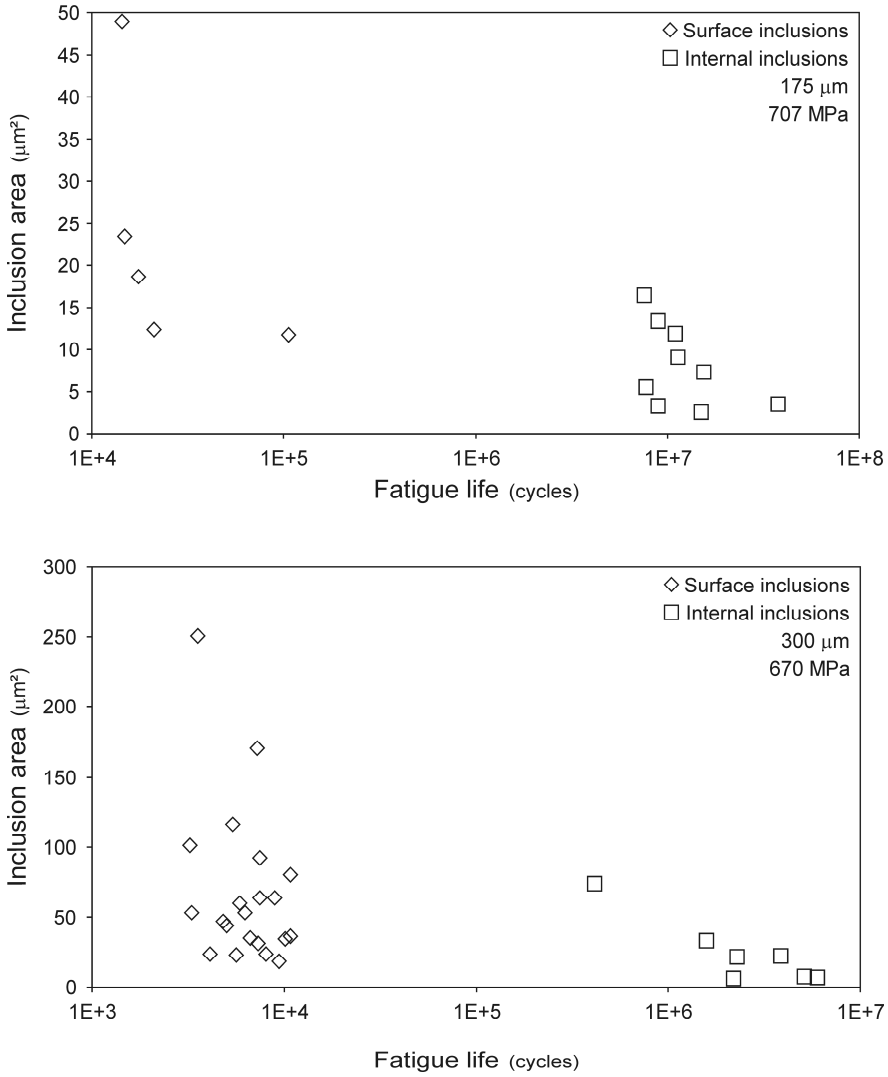

Figure 7.5: Inclusion area as a function of fatigue life.

The ΔK value for both surface and internal crack initiations is calculated using the square root of the inclusion size (√√inclusion area). Since the ΔK value is the driving factor for the crack growth rate, there is a tendency of a decreasing fatigue life with an increasing inclusion size. This tendency is also observed for

high strength steels [39-41,43,46,115-120]. Figure 7.5 shows the relation between the inclusion area of the fatigue fractures and the fatigue life. Although the scatter is large, both wire diameters show a tendency of decreasing fatigue life for an increasing inclusion size. In figure 7.6 the ΔK value is shown as a function of the fatigue life.

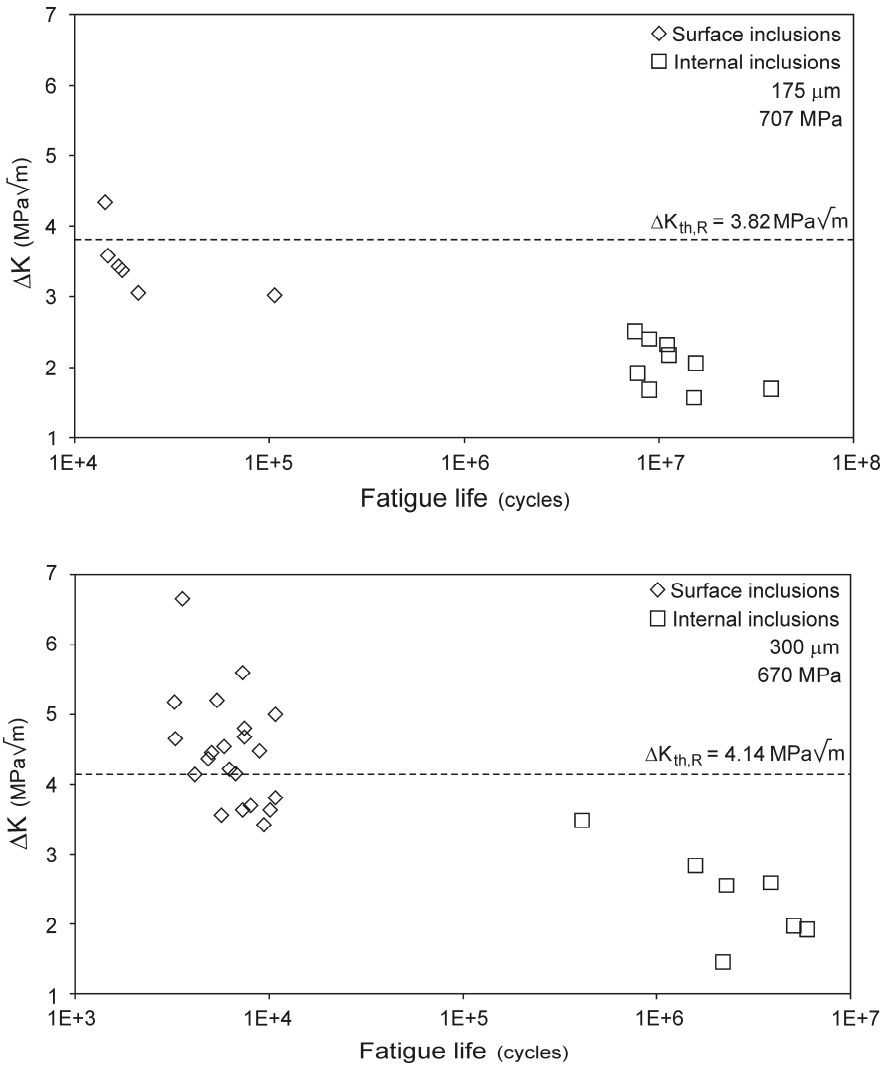

Figure 7.6: ΔK value calculated with equations 7.1 and 7.2 as a function of the fatigue life.

The influence of the inclusion location (surface or bulk) on the fatigue properties is taken into account in equation 7.1 and 7.2 by the difference in geometrical factor between both (0.65 – 0.5). This difference is related to the different

boundary conditions between surface and internal fatigue cracks. In figure 7.5 it can be seen clearly that for a certain inclusion size, the fatigue life of surface crack initiations is significantly lower than for internal crack initiations.

In order to further emphasize the difference in fatigue mechanism between surface and internal fatigue crack initiations, the relation between the experimental and the calculated fatigue life is illustrated in figure 7.7. The fatigue lives are calculated by using equation 4.7 (chapter 4), which is based on the Paris law. Since the 175 μm and the 300 μm wires don't have the exact same composition and aren't produced with identical process parameters, it is necessary to calculate the material constant (C and m from the Paris law) for both wires individually. It is important to remember that the Paris law can only be applied when $\Delta K > \Delta K_{th}$. Therefore, only the surface fractures are used to calculate the material constants.

175 NT $\quad C_L = 7.68 \cdot 10^{-13}$

$\quad m_L = 4.3$

300 HT $\quad C_L = 1.95 \cdot 10^{-13}$

$\quad m_L = 5.44$

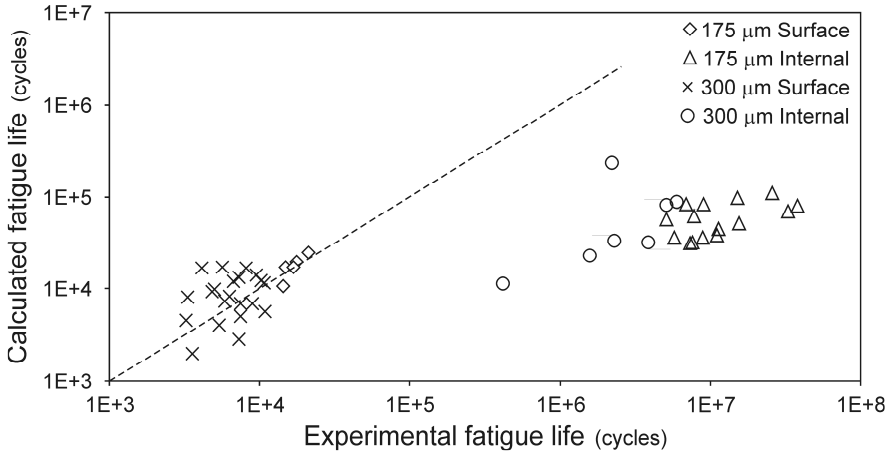

Figure 7.7: Relation between the experimental and the calculated fatigue life (based on the Paris law).

Figure 7.7 shows a clear 1 on 1 relationship between the experimental and the calculated fatigue life for the surface fractures. This proves that surface cracks that initiated from surface inclusions can be modeled by the Paris law. Further it is observed that the internal fatigue crack initiations don't show a 1 on 1 relationship. This clearly shows that there are two different fatigue mechanisms active for surface and internal crack initiations.

Although the relationship between the experimental and the calculated fatigue life is not 1 on 1 for the internal fatigue crack initiations, there exists a linear relationship between both. This implies that the internal fatigue crack initiations, for which the fatigue life is controlled by the growth of short fatigue cracks (paragraph 4.2.1.2, chapter 4), can be modeled by an equation similar to the Paris law.
By using equation 4.7 for the internal fatigue data it is possible to calculate the material constants for the short crack growth region.

175 NT (short cracks) $C_S = 2.8 \cdot 10^{-18}$

$m_S = 12.8$

300 HT (short cracks) $C_S = 1.6 \cdot 10^{-15}$

$m_S = 5.95$

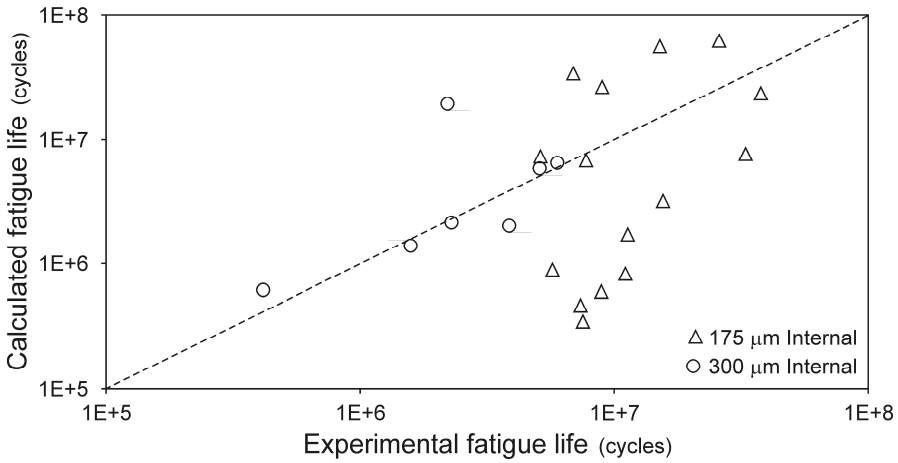

Figure 7.8: Relation between the experimental and the calculated fatigue life (based on the Paris law) for short cracks.

Figure 7.8 shows the relation between the experimental and the calculated fatigue life for the short crack growth regime. The calculated data corresponds well with the experimental data for both wires, although the scatter is large for the 175 μm wires.

Since the material constants for both crack growth mechanisms are known, it is possible to draw the complete crack growth curve based on the Paris law (equation 4.5). Figure 7.9 shows the crack growth curve based on the equation according to Paris. Both the short and the long crack growth region are modelled. It is important to note that both crack growth regions have different C and m values. Figure 7.9 is drawn for the 175 μm wires and an R value of 0.5. A similar curve can be drawn for the 300 μm wires.

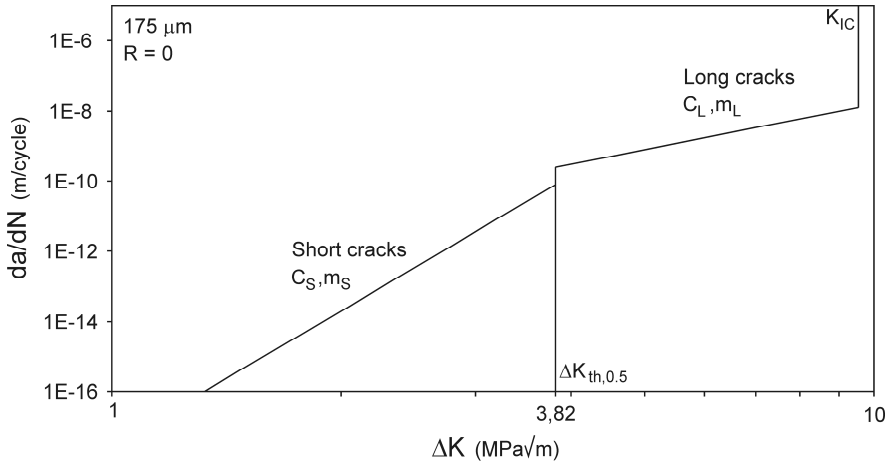

Figure 7.9: Crack growth curve based on the Paris law for both the short and long crack growth regime for the 175 μm wires and an R value of 0.5.

The total fatigue life (N_f) can be calculated as follows:

$$N_f = N_S + N_L \tag{7.3}$$

With N_f the total fatigue life, N_S the fatigue life that is spend in the short crack growth regime and N_L the fatigue life that is spend in the long crack growth regime. When $\Delta K_{inclusion} < \Delta K_{th,R}$, equation 7.3 can be written as:

$$N_f = \frac{2\left(a_{defect}^{1-0.5m_S} - a_{FCT}^{1-0.5m_S}\right)}{C_S\left(m_S - 2\right)\left(Y \cdot \Delta\sigma\sqrt{\pi\sqrt{\pi/2}}\right)^{m_S}} + \frac{2\left(a_{FCT}^{1-0.5m_L} - a_f^{1-0.5m_L}\right)}{C_L\left(m_L - 2\right)\left(Y \cdot \Delta\sigma\sqrt{\pi\sqrt{\pi/2}}\right)^{m_L}} \tag{7.4}$$

With a_{defect} the crack length of the stress concentration (the inclusion radius for internal inclusions), a_{FCT} the radius of the FCT area, a_f the fatigue crack length at final failure (= radius of the fish-eye), Y the geometrical factor of equation 7.1 and 7.2 (0.5 for internal cracks and 0.65 for surface cracks), C_S and m_S the material constants for short crack growth and C_L and m_L the material constants for long cracks.
When equation 7.4 is used for internal fatigue cracks it is observed that the fatigue life for long crack growth is always smaller than 0.7% of the fatigue life for short crack growth ($N_S > 0.99\ N_f$). Therefore equation 7.4 can be simplified:

$$N_f = \frac{2\left(a_{incl}^{1-0.5m_S} - a_{FCT}^{1-0.5m_S}\right)}{C_S\left(m_S - 2\right)\left(Y \cdot \Delta\sigma\sqrt{\pi\sqrt{\pi/2}}\right)^{m_S}} \tag{7.5}$$

In equation 7.5 a_{incl} is used in stead of a_{defect} since it is experimentally observed that all internal cracks initiate at inclusions.
When $\Delta K_{inclusion} > \Delta K_{th,R}$, long fatigue crack can directly start growing, meaning that $N_S = 0$ in equation 7.3.

$$N_f = \frac{2\left(a_{defect}^{1-0.5m_L} - a_f^{1-0.5m_L}\right)}{C_L\left(m_L - 2\right)\left(Y \cdot \Delta\sigma\sqrt{\pi\sqrt{\pi/2}}\right)^{m_L}} \tag{7.6}$$

By the use of equations 7.5 and 7.6 it is possible to predict the fatigue life of the heavily drawn steel wires that are investigated in this study. It is however important to remember that the scatter is large for the internal crack initiations and it is therefore suggested to use equations 7.5 and 7.6 only to get an idea about the order of magnitude of the fatigue life and further look at the 95% confidence intervals of the experimental data of this study (different initiation mechanisms, paragraph 4.1.4, chapter 4).

In the following paragraphs it is investigated if the inclusion properties (composition and geometry) have an influence on the experimental fatigue life and, by taking the possible influence into account, if the calculated fatigue lives correspond better to the experimental fatigue lives.

7.3.2 Inclusion composition

When the influence of the inclusion composition on the fatigue properties is studied, two different influencing factors can play a role: the difference in thermal expansion coefficient and the difference in mechanical properties between the inclusion and the steel matrix. It is important to note that the difference in thermal expansion coefficient is not taken into account here because it manifests itself immediately after patenting but the stress state in and around the inclusion will be changed completely due to the extensive plastic deformation caused by the wire drawing production process after patenting. Therefore only the difference in Young's modulus (ΔE), which is caused by the difference in chemical composition of the inclusions and the steel matrix, will be taken into account. ΔE can have an influence on the fatigue properties because it will influence the stress state in and around the inclusions. Further it is possible that ΔE has an influence on the deformation behavior during the wire drawing production process.
To study the influence of the inclusion composition (and the inclusion geometry) on the fatigue properties only the internal fatigue fractures are investigated into

depth because it is possible that when the fatigue crack initiates at the surface of the wire, environmental influences overshadow the influence of the inclusion properties.
The inclusion composition of all internal fatigue fractures is analyzed with microanalysis. It is observed that the 300 μm wires all have more or less the same composition: a mixture of Al_2O_3, MgO and SiO_2. There are however 2 fractures for which it was not possible to measure the inclusion composition. These fractures are labeled with unknown in figure 7.10. Due to a lack of information it is not possible to study the influence of the inclusion composition based on the 300 μm wires.

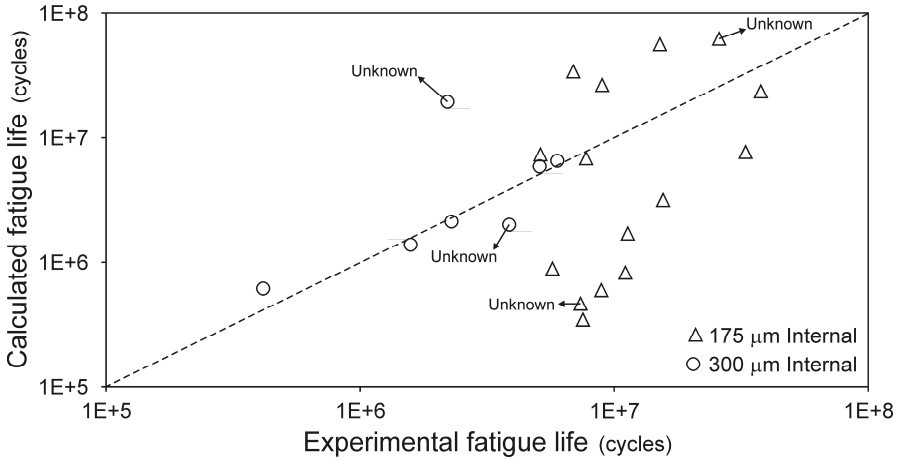

Figure 7.10: Relation between the experimental and the calculated fatigue life (based on the Paris law) for short cracks.

The internal fractures of the 175 μm wires can be divided in two groups according to their inclusion composition. One group of inclusions consists almost completely out of SiO_2 (more than 90%) while the other group is composed of a mixture of MgO, Al_2O_3, SiO_2, CaO and MnO. There are also 2 inclusions with an unknown composition (figure 7.10) which are not taken into account here.

Figure 7.11 shows the two different inclusion groups on the fatigue life graph. It is observed that the SiO_2 inclusions have an experimental fatigue life that is equal to, or smaller than the calculated fatigue life. On the other hand the inclusions which are composed of a mixture of MgO, Al_2O_3, SiO_2, CaO and MnO have an experimental fatigue life that is larger than the calculated fatigue life. In other words, the SiO_2 inclusions lead to a lower fatigue life than the other inclusions. These data could indicate that, if the observed difference in fatigue properties can be addressed completely to a difference in inclusion composition, ΔE between the inclusion and the matrix is significantly larger for the SiO_2 inclusions than for the inclusions that consist of a mixture of MgO, Al_2O_3, SiO_2, CaO and MnO.

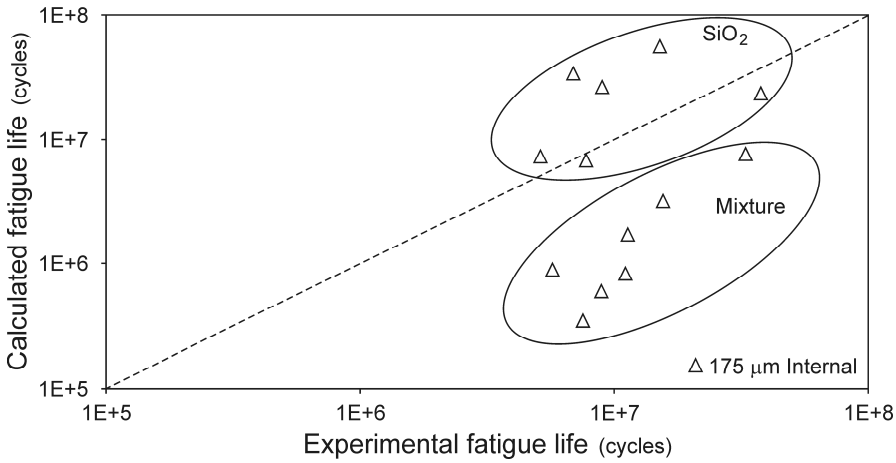

Figure 7.11: Influence of the inclusion composition on the fatigue life.

Since it is not possible to calculate the E-modulus of the mixture in a reliable way, it is not possible to draw strong conclusions on the relation between the inclusion composition and the fatigue properties. Nevertheless it is clear that the SiO_2 inclusions have worse fatigue properties than the other inclusions, which indicates the existence of a correlation between the inclusion composition and the fatigue properties.

7.3.3 Inclusion geometry

It has already been shown that the inclusion geometry has an influence on the fatigue properties for high strength steels [124]. The maximum inclusion stress ($\Delta\sigma_{incl,max}$) that occurs at internal inclusions is calculated using equation 7.7 [124]:

$$\Delta\sigma_{incl,max} = 2 \cdot \Delta\sigma \cdot (a/b) \tag{7.7}$$

with $\Delta\sigma$ the applied stress range and a and b respectively the longest and shortest semi-axis of the ellipse that is used to approach the inclusion geometry. Equation 7.7 shows that $\Delta\sigma_{incl,max}$ is determined by a/b, meaning that the more an inclusion approaches the geometry of a perfect sphere, the lower $\Delta\sigma_{incl,max}$ will be.
Figure 7.12 shows the relation between $\Delta\sigma_{incl,max}$ and the fatigue life. Although some correlation between $\Delta\sigma_{incl,max}$ and the fatigue life can be observed for the 175 µm wires, there is no correlation for the 300 µm wire. Therefore it is not possible to conclude that the inclusion geometry has a significant effect on the fatigue properties. It is possible that the other effects, such as inclusion size, location and composition overshadow the effect of the inclusion geometry.

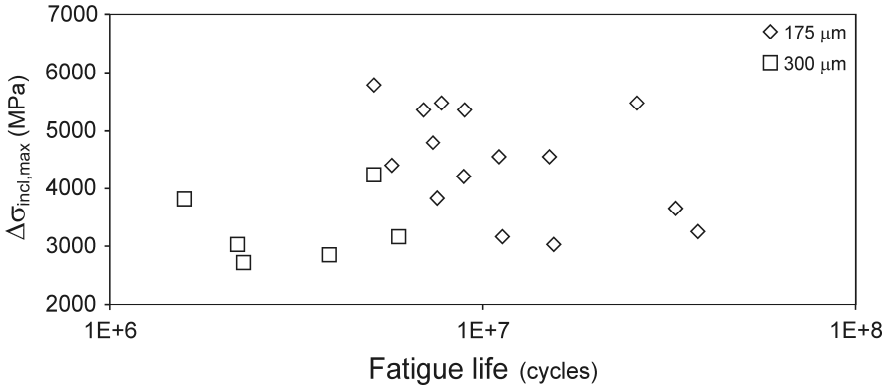

Figure 7.12: Influence of the inclusion geometry on the fatigue properties.

7.4 Stress intensity factor calculation

When looking at the fatigue crack initiations at surface inclusions in figure 7.6 it is important to note that more than 1/3 of the inclusions have a ΔK value that is smaller than $\Delta K_{th,R}$. Whenever $\Delta K < \Delta K_{th,R}$ short fatigue cracks have to grow until $\Delta K_{th,R}$ is reached. For internal fatigue crack initiations it was already shown that the growth of short fatigue cracks results in very high fatigue lives by the formation of a facet area [41, 43]. Therefore it can be expected that the fatigue life of these surface crack initiations should also increase significantly. When however the fatigue lives of the surface inclusions with $\Delta K > \Delta K_{th,R}$ are compared to the surface inclusions with $\Delta K < \Delta K_{th,R}$ no discontinuity can be observed. This indicates that no short fatigue crack growth occurs, meaning that the ΔK value of the inclusions is actually larger than $\Delta K_{th,R}$. Therefore it is expected that Murakami's way of calculating ΔK for inclusions can not be applied for heavily drawn steel wires. To validate this assumption the microstructure around surface inclusions is investigated in depth using a SEM/FIB dual beam microscope.

To study the microstructure around inclusions, it is not possible to use fatigue fractures since possible microstructural changes can be caused by the fatigue testing itself. Therefore only wires without any load history after the production process are used. SEM is used to scan the surface of these wires for inclusions. Whenever an inclusion is found, sections of about 500 nm are made starting before the inclusion and ending after it. Between each section the microstructure around the inclusion is made visible with the FIB. The sections are made following the wire axis. For each section the depth of the inclusion and the altered microstructure is measured. After all sections are made and analyzed, the data are put back together and the projected area of the inclusion and the altered microstructure is estimated. A schematic representation of this experimental procedure is shown in figure 7.13. Since the inclusions present in the 300 μm wire are significantly larger than the inclusions present in the 175 μm wire (figure

7.1), only the 300 µm wire is investigated to increase the probability of finding surface inclusions.

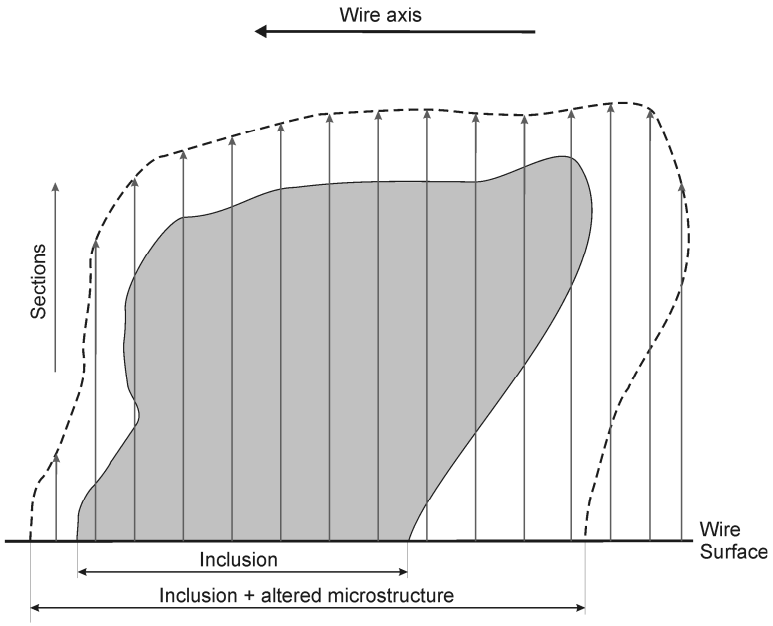

Figure 7.13: Representation of the experimental procedure to make the microstructure around non-metallic inclusions visible.

Figure 7.14 and 7.15 show FIB images of sections through surface inclusions. Around the inclusion the microstructure is clearly different from the bulk of the material which shows elongated grains parallel to the wire axis. Also microcracks are observed. The presence of the alterations in the microstructure and the microcracks can be explained by the inhomogeneous deformation of the steel matrix around the inclusion during the wire drawing production process. In total 6 surface inclusions were investigated.

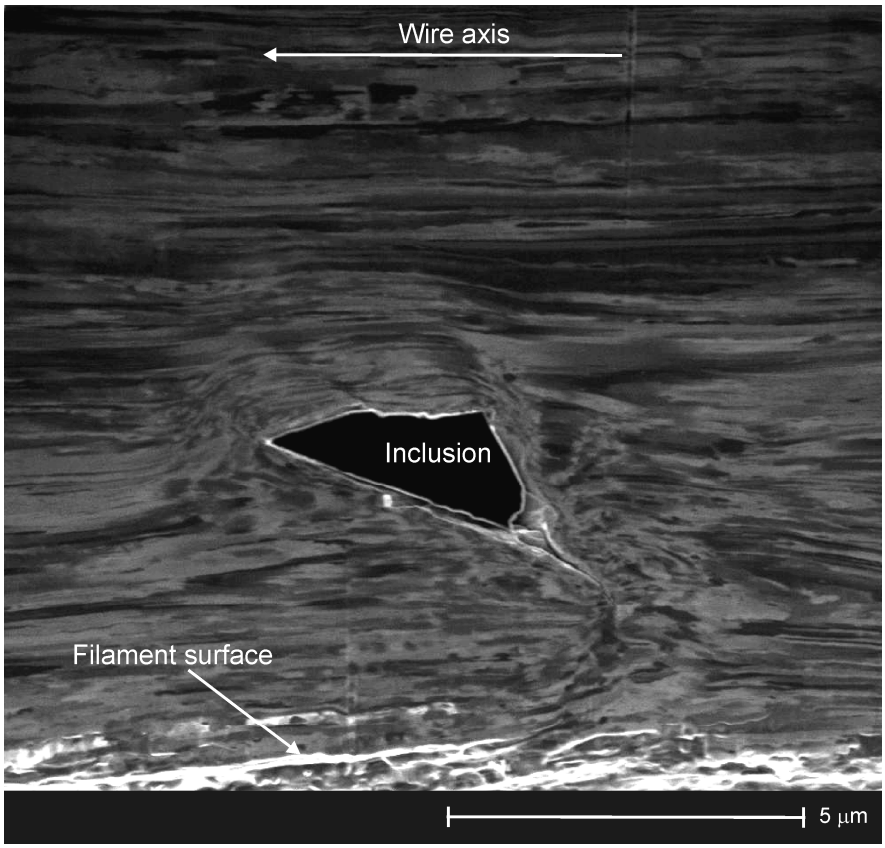

Figure 7.14: Section through a surface inclusion. Around the non-metallic inclusion microcracks and alterations in the microstructure can be observed.

Murakami [114] observed that it is not sufficient to use the inclusion area to calculate ΔK of surface inclusions. Therefore Murakami suggested to add a weakened area to the inclusion area. Since the observations on heavily drawn steel wires show that Murakami's approach underestimates the ΔK value, adaptations are necessary.

It is important to know that equation 7.1 is based on Murakami's formula for a surface crack of arbitrary shape and that inclusions can be modeled as cracks because cracks can immediately initiate due to the high stresses present around them. Since microcracks and alterations in the microstructure are observed around inclusions in heavily drawn steels, it is reasonable to use the projected area of the altered microstructure together with the inclusion projected area in equation 7.1.

Table 7.3: Altered microstructure around non-metallic inclusions.

Estimated projected area (μm²)			Difference in ΔK (%)	
Inclusion	Inclusion + weakened area	Inclusion + microstructure	(Inclusion + microstructure) x100 / inclusion	(Inclusion + microstructure) x100 / (inclusion + weakened area)
5.5	5.8	9.5	14.8	13.1
9.9	9.9	20.4	19.9	19.9
16.3	16.9	31.8	18.1	17.1
23.7	23.7	50.6	20.9	20.9
24.6	25.2	45.1	16.3	15.6
35.6	40.3	64.7	16.1	12.6
		Average	17,7 ± 2.5	16.5 ± 3.6

Table 7.3 shows the estimated projected areas of 6 surface inclusions together with the difference between the ΔK values. It is calculated that the ΔK value of the inclusion + the altered microstructure is 17.7 ± 2.5 % larger than the ΔK value of the inclusion alone. The ΔK value of the inclusion + the altered microstructure is 16.5 ± 3.6 % larger than the ΔK value suggested by Murakami (with the weakened area only). Figure 7.16 shows the ΔK values of the surface inclusions as a function of the fatigue life when the alterations in the microstructure are taken into account. The ΔK values in figure 7.16 are calculated using equation 7.8.

$$\Delta K_{surface} = 0.65 \cdot x \cdot \Delta\sigma \cdot \sqrt{\pi\sqrt{area}} \qquad (7.8)$$

with x = 1,165 ± 0,036 for the 300 μm wire. Using equation 7.8, all fatigue fractures of the 300 μm wire have a ΔK value that is larger than, or at least falls within the 95% confidence limits of, $\Delta K_{th,R}$. Therefore it can be concluded that the suggested adaptations of Murakami's model (equation 7.4) are valid for these 300 μm wires.

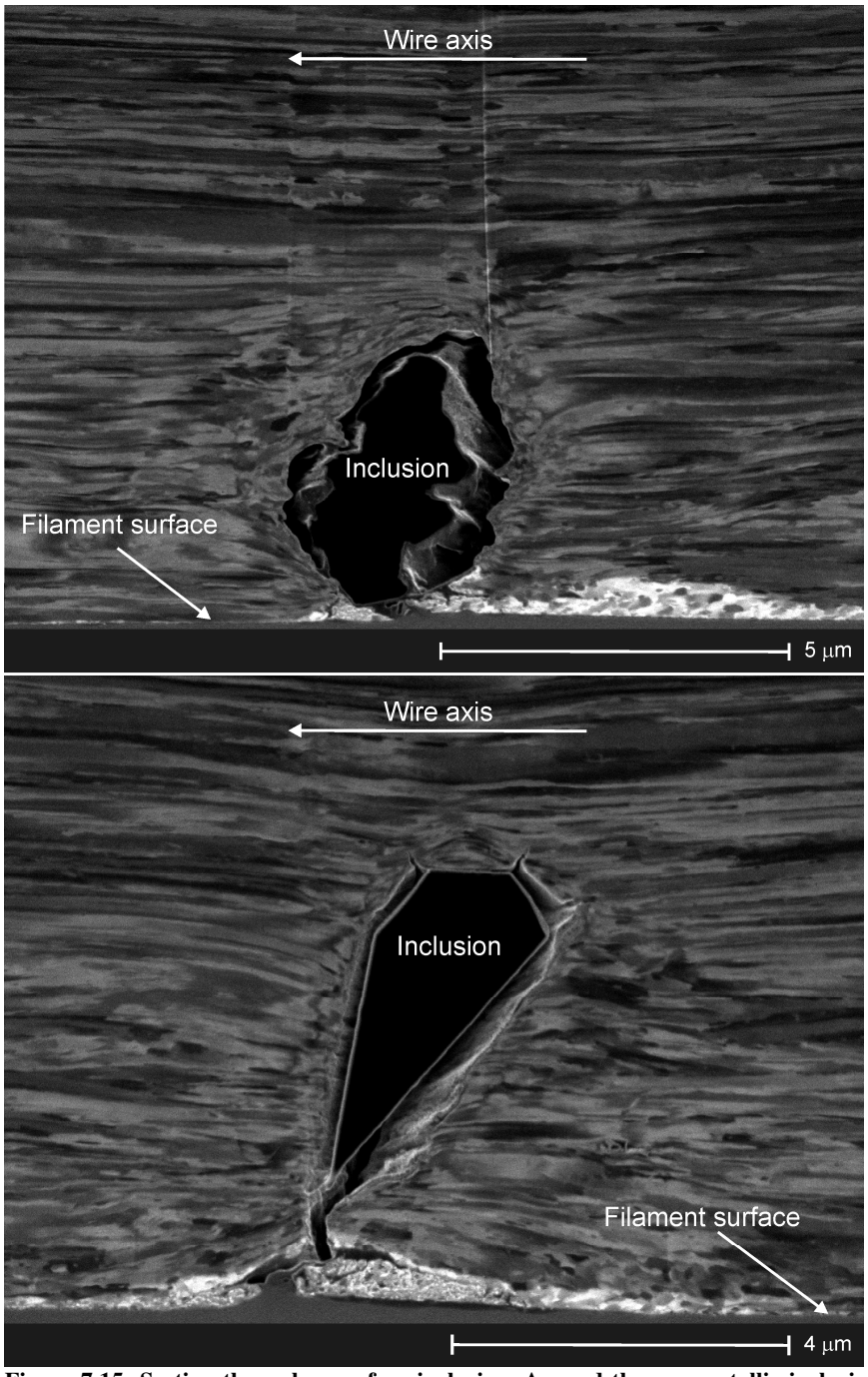

Figure 7.15: Section through a surface inclusion. Around the non-metallic inclusion microcracks and alterations in the microstructure can be observed.

If equation 7.8 is also used for the 175 µm wires there are still two fatigue fractures with a ΔK value that is smaller than $\Delta K_{th,R}$ (top of figure 7.16). Therefore it is not possible yet to say whether or not equation 7.8 can be used for other wires with a comparable production process. More research is needed to make a general conclusion hereon. Nevertheless it should be clear that Murakami's formula underestimates the ΔK value of inclusions in heavily drawn steel wires because microcracks and alterations in the microstructure are present around inclusions due to the wire drawing production process.

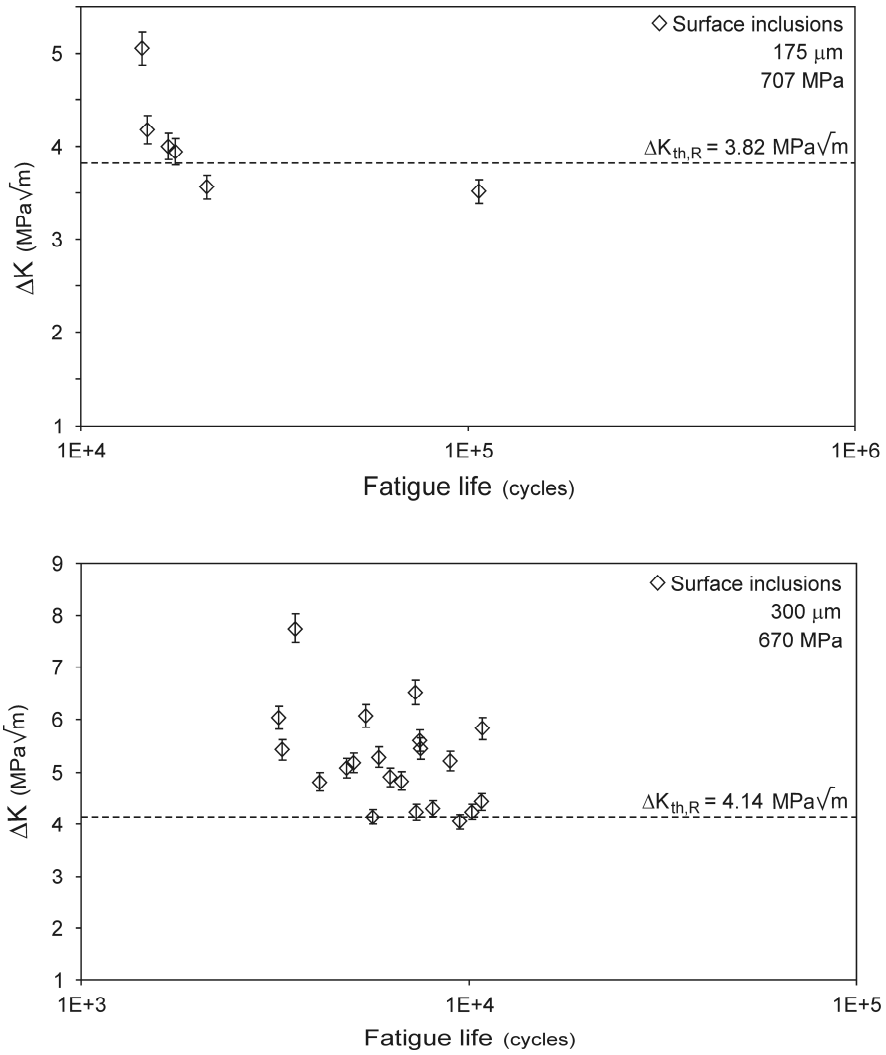

Figure 7.16: ΔK values of the surface inclusions calculated using equation 7.4 as a function of the fatigue life.

7.5 Conclusions

The influence of non-metallic inclusions on the fatigue properties of heavily drawn steel wires is investigated in this chapter. Beside the influence of the inclusion size and location, it was possible to observe some influence of the inclusion composition and geometry.

By plotting the relation between the experimental and the calculated fatigue life (Paris model for long cracks) it is possible to show that different fatigue mechanisms are active for surface and internal crack initiations. Interestingly, the graph shows a linear relationship between the experimental and calculated fatigue life of internal fractures. This indicates that it is possible to model the internal fatigue fractures with the Paris law. Since the fatigue life of the internal fatigue crack initiations is determined by the growth of short fatigue cracks, the Paris law can be used to model the growth of short fatigue cracks in heavily drawn steel wires.

Through an extensive experimental investigation of the microstructure around inclusions it was observed that microcracks can be present around inclusions in drawn steel wires. Further it was observed that the microstructure around the inclusions was different from the bulk of the wire. Based on these observations and on a discrepancy between the fatigue data and the threshold value it was concluded that the actual defect size of an inclusion that is used to calculate ΔK is about 18% larger than the inclusion size itself. An adaptation of Murakami's formula is suggested.

8 Load ratio effects

8.1 Introduction

The threshold value for crack growth is the most important material property for fatigue since it defines the minimum loading conditions necessary for a fatigue crack to grow. This threshold value is usually expressed as the threshold stress intensity factor range for crack growth ($\Delta K_{th,R}$). $\Delta K_{th,R}$ depends on microstructural parameters, temperature and environment, but also on the load ratio (R = minimum applied stress / maximum applied stress). In the early seventies Elber [54] explained the influence of the load ratio by using a crack closure mechanism that originates from the plastically deformed wake of the crack that makes contact with itself while some tensile loading is still applied. Other closure mechanisms such as closure due to the surface roughness and oxidation were extensively described in literature [125-128].

More recent literature [34,85-87] shows that plastic closure is insignificant for very small crack growth rates (at or around $\Delta K_{th,R}$). Vasudevan et al. [88] showed that the decrease of $\Delta K_{th,R}$ with R is more dependent on environmental effects that alter the fatigue crack growth than on roughness/oxide induced closure. These experimental observations spurred interest in using two intrinsic material thresholds to explain the load ratio effects.

Vasudevan et al. [60] introduced a unified damage approach in which the fatigue crack growth is dictated by two crack tip driving forces, namely ΔK (causing cyclic plastic damage) and K_{max} (causing crack tip rupture). In this approach the fatigue data can be plotted for any crack growth rate in terms of ΔK - K_{max} rather than ΔK-R. Such ΔK - K_{max} plots at the near threshold crack growth rates yield toward two critical values for ΔK and K_{max}, namely ΔK^*_{th} and K^*_{max}, which are the necessary requirements for a crack to advance. In literature it was shown that this unified damage approach successfully accounts for the load ratio effect [72,128,129] and is applicable for all R values [130].

By the use of a new threshold determination method which is described in detail in chapter 5, it is possible to determine the threshold values for crack growth for these small diameter wires. In this chapter fatigue tests are performed on several R values in order to determine ΔK^*_{th} and K^*_{max} for the heavily drawn steel wires used in this study.

Material

Brass coated steel wires with a diameter of 175 μm and an UTS (ultimate tensile strength) of 3187 ± 37 MPa are used to investigate the influence of the R value on $\Delta K_{th,R}$. The wires were cold drawn to a total strain of 3.5. After wire drawing the wires are straightened (bent over pulleys in perpendicular planes) to introduce compressive residual stresses at the surface. At the moment, the magnitude of the residual stresses is not known.

Fatigue tests

The fatigue tests were performed at 5 different load ratios: R = 0.05, 0.2, 0.4, 0.5 and 0.6. The fatigue tests at R=0.5 are performed at three different stress amplitudes σ_a = 665, 707 and 748 MPa. The other fatigue tests were performed at stress amplitudes of 956 (R=0.05), 1123 (R=0.2), 854 (R=0.4) and 561 (R=0.6) MPa. Figure 8.1 gives a schematic illustration of the different applied loading conditions (R values) that are used in this study.

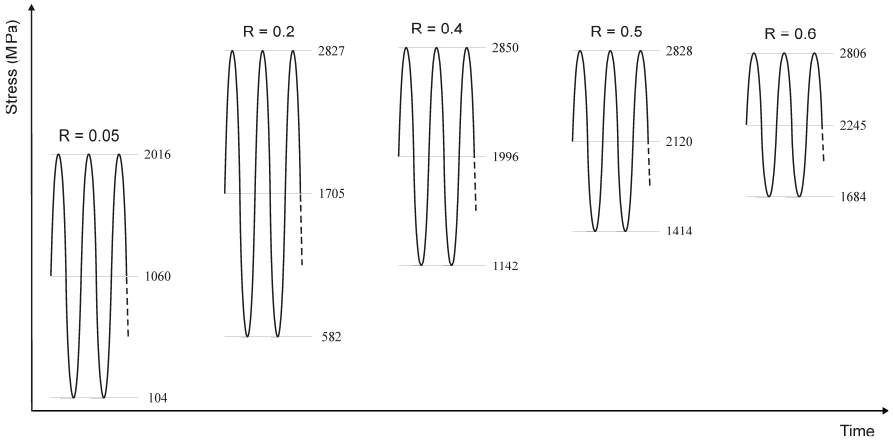

Figure 8.1: Schematic illustration of the stress during fatigue tests for different R values.

8.2 Influence of the load ratio on the fatigue thresholds

$\Delta K_{th,0.5}$ is calculated to be 3.82 ± 0.09 MPa√m using the area of the FCT area as is described in detail in chapter 5. Although the existing literature on drawn steel wires is only available for much larger wire diameters, a good agreement can be found between $\Delta K_{th,0.5}$ which is measured in this study and the values from literature. Verpoest [110] measured ΔK_{th} for steel wires with an ultimate tensile strength (UTS) between 1321 and 2218 MPa (∅ 2 – 1.85 mm). For R = 0 $\Delta K_{th,0}$ = 3.5 – 4 MPa√m and for R ≥ 0.6 ΔK_{th} = 4 – 5 MPa√m. LLorca and Sanchez-Galvez [80] measured ΔK_{th} for steel wires with a UTS of 1720 MPa (∅ = 7mm). Depending on the R value following results were obtained: $\Delta K_{th,0.1}$ = 5.2 MPa√m, $\Delta K_{th,0.5}$ = 3.8 MPa√m and $\Delta K_{th,0.8}$ = 2.8 MPa√m.

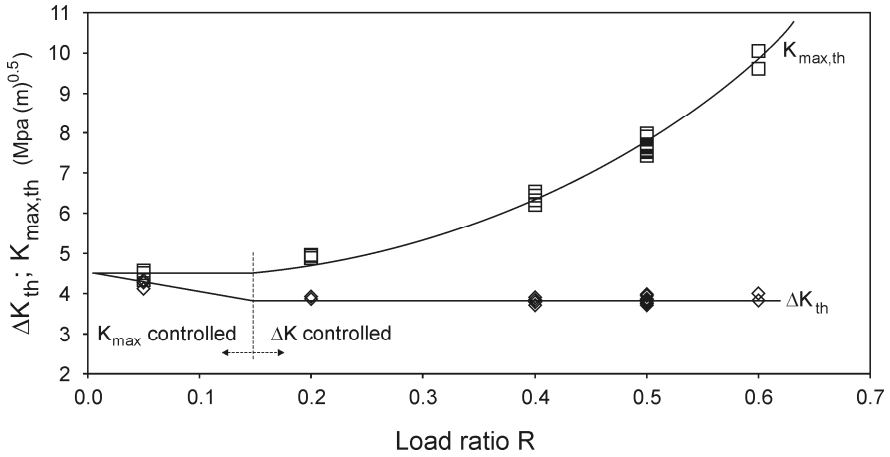

Figure 8.2: ΔK_{th} and $K_{max,th}$ dependence on R.

Figure 8.2 shows the dependence of ΔK_{th} and $K_{max,th}$ on R ($K_{max,th}$ is calculated using equation 8.1). It is observed that ΔK_{th} is independent of R for high R values (R = 0.2, 0.4, 0.5, 0.6) and increases for low R values (R = 0.05). At R = 0.05, ΔK_{th} = 4.24 ± 0.15 MPa$\sqrt{m}$, which is significantly different from ΔK_{th} = 3.82 ± 0.09 MPa$\sqrt{m}$ for R = 0.2, 0.4, 0.5 and 0.6 (ANOVA, α = 0.05).
Although it is not possible to perform fatigue tests on lower R values (tension-compression region) with the fatigue testing system used for this study, it can be assumed that $K_{max,th}$ is independent on R for low R values [60, 72, 87, 88, 128-130]. The region with the ΔK_{th} independency is called the ΔK controlled crack growth region and the region with the K_{max} independency is called the K_{max} controlled crack growth region.
These observations are different from the results in literature. For steels in general the fatigue crack growth is K_{max} controlled for R ratios below 0.5 and for steel wires with a diameter of 7 mm it was observed that the fatigue crack growth is K_{max} controlled for R ratios smaller or equal than 0.8 (paragraph 2.3.2 and 2.4). This difference can be explained by environmental influences. It is observed that when the reactivity of an environment increases (more aggressive environment), the K_{max} controlled crack growth region also increases (transition from K_{max} to ΔK controlled crack growth happens at a larger R value), which was already shown in the literature review (paragraph 2.3.5). Since ΔK_{th} is measured from internal fatigue fractures, and therefore, is measured in a situation where environmental influences are excluded, the transition from K_{max} to ΔK controlled crack growth happens at a lower R value than in literature.

$$K_{max,th} = 0.5 \cdot \sigma_{max} \cdot \sqrt{\pi \sqrt{area_{FCT}}} \qquad (8.1)$$

The ΔK – K_{max} curve is shown in figure 8.3 where the ΔK controlled crack growth region is defined by the horizontal line ΔK^*_{th} = 3.82 ± 0.09 MPa$\sqrt{m}$ and

the K_{max} controlled crack growth region is defined by the vertical line K^*_{max} = 4.47 ± 0.16 MPa√m. The transition from ΔK to K_{max} controlled crack growth is calculated from the intersection of the ΔK^*_{th} and the K^*_{max} line and takes place at R = 0.16. Therefore the fatigue crack growth will be ΔK controlled when R > 0.16 and K_{max} controlled when R < 0.16. The necessary condition for fatigue crack growth is to exceed both threshold values, ΔK^*_{th} and K^*_{max}, simultaneously.

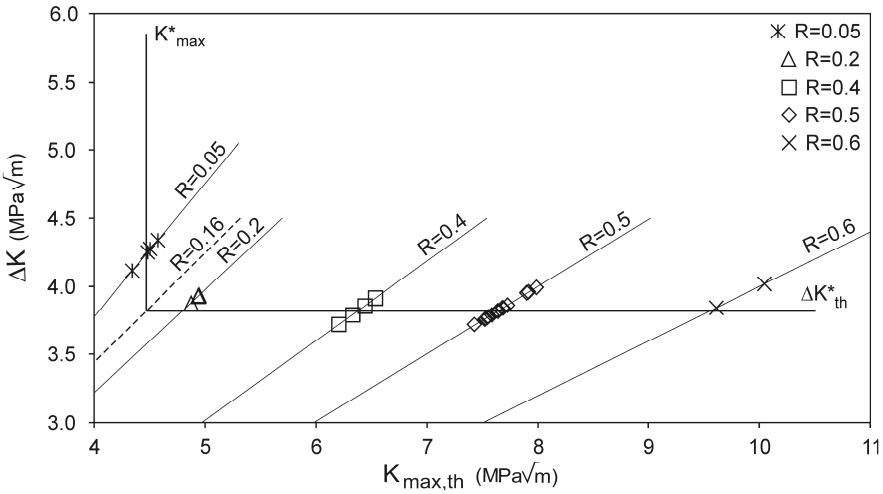

Figure 8.3: ΔK_{th} - $K_{max,th}$ graph.

It is however important to note that all threshold values were determined using internal fatigue fractures, meaning that no environmental influences could have played a role. If the heavily drawn wires used in this study are subjected to fatigue in a humid environment it can be expected that ΔK_{th} decreases [77,131] or remains unaffected [72] and that $K_{max,th}$ increases [77].

The transition from ΔK (R > 0.16) to K_{max} (R < 0.16) controlled crack growth is observed clearly during fatigue testing. The amount of internal fractures and the amount of clamp fractures increase significantly for the R = 0.05 tests compared to the tests at the other R values. At R = 0.2, 0.4, 0.5 and 0.6 about 25% of the tests fail internally compared to 75% at R = 0.05. The amount of clamp fractures increases from about 5 % of the tests at R = 0.2, 0.4, 0.5 and 0.6 compared to 80% at R = 0.05. This indicates that there is indeed a different fatigue crack growth mechanism active for R = 0.05 compared to the other fatigue tests.

The increase in internal fatigue fractures can be explained by the presence of residual stresses. Due to the straightening operation after wire drawing it is expected that residual compressive stresses are present at the surface of the wire and residual tensile stresses are present at the core. Since the residual stresses should be added to the applied stress to calculate the stress intensity factor, the K_{max} value will be larger in the core of the wire than on the surface. Since the fatigue crack growth is K_{max} controlled and $K_{max,internal} > K_{max,surface}$, it is more

likely for a fatigue crack to initiate internally in stead of at the surface of the wire. Since the clamping force will also have an influence on K_{max}, the increase in the amount of clamp fractures can be explained accordingly.

8.3 Conclusions

By using the newly developed threshold determination method (chapter 5) it was possible to determine the influence of the load ratio (R) on the threshold value for long crack growth. By using the unified damage approach the two intrinsic threshold values, ΔK^*_{th} and K^*_{max} are determined to be 3.82 ± 0.09 MPa$\sqrt{}$m and 4.47 ± 0.16 MPa$\sqrt{}$m correspondingly. The transition between K_{max} controlled and ΔK controlled crack growth was calculated to happen at an R value of 0.16. This transition could also be observed clearly during fatigue testing by an increase in the amount of internal and clamp fractures.

When one wants to use the intrinsic threshold values for these heavily drawn steel wires in practice, it is important to remember that they are measured based on internal fatigue crack initiations. This means that these threshold values can only be used in comparable circumstances (where no environmental influences are possible). When the environment can play a role, it is expected that K^*_{max} will increase and that ΔK^*_{th} will decrease.

9 Conclusions

9.1 Results and evaluation

Based on a large amount of experimental fatigue data the active fatigue mechanisms for heavily drawn steel wires are determined. Two different fracture modes are observed namely surface and internal fatigue crack initiations. The surface crack initiations mostly lead to low cycle fatigue behavior and therefore they will determine the fatigue properties of the wires. Two different surface fatigue crack initiation mechanisms are observed: fatigue crack initiations at surface stress concentrations with $\Delta K > \Delta K_{th}$ and environmentally assisted fatigue crack initiations. The environmentally assisted fatigue crack initiations where found to be closely related to the presence of chlorides on the surface of the wires. It is important to note that both mechanisms can be active at the same time.
To improve the fatigue properties of these heavily drawn steel wires the author would suggest tackling the problem of environmentally assisted fatigue crack initiations first. This suggestion is based on the experimental results on cleaned and coated wires which are explained in detail in chapter 4. It was observed that when the surface defect distribution (surface stress concentrations) remains the same and the wires were completely protected from environmental influences by cleaning and coating, the fatigue properties improve significantly. Further, the reduction of the amount and size of surface stress concentrations can only lead to a significant improvement of the fatigue properties when the environmentally assisted fatigue crack initiations are not dominant.
When no environmental interactions are possible a further improvement in the fatigue properties could be achieved by reducing the amount and size of surface stress concentrations. Besides defects which are introduced by the wire drawing production process itself it is not possible to change the surface defect distribution by the wire drawing production process (due to the presence of non-metallic inclusions). The only possibility would be to use a very clean wire rod (which leads to a significant increase in the total cost of the wire).
Internal fatigue crack initiations can only be observed when no surface stress concentrations are present with a $\Delta K > \Delta K_{th}$ and no environmentally assisted fatigue crack initiations are possible. It was found that internal fatigue cracks always initiate at internal non-metallic inclusions and lead to high and very high cycle fatigue behavior when $\Delta K < \Delta K_{th}$. These internal fatigue crack initiations show a characteristic area around the internal non-metallic inclusion, which is called FCT area in this study. Since this FCT area defines the transitions from short to long crack growth it can be used to estimate the fatigue thresholds. This new method of estimating the fatigue threshold based on internal fatigue fractures is explained and validated in chapter 5. The new threshold determination method was used to determine the influence of the load ratio on the threshold value. Using the unified damage approach it was possible to determine the two threshold values, ΔK^*_{th} and K^*_{max}, which completely describe the fatigue behavior of these heavily drawn steel wires. It is however important to note that these threshold

values are only valid for wires that are protected from environmental influences because they are determined using internal fatigue cracks. It is interesting to note that at this moment it is not possible yet to determine the fatigue thresholds due to limitations in crack growth rate measurement techniques of such small diameter wires. Therefore it is not possible to validate the newly developed threshold determination method. Further it is not possible to include environmental influences in the two fatigue thresholds, ΔK^*_{th} and K^*_{max}, for heavily drawn steel wires yet.

The influence of non-metallic inclusions on the fatigue properties of heavily drawn steel wires is investigated in chapter 7. Beside the influence of the inclusion size and location, it was possible to observe some influence of the inclusion composition and geometry.
By plotting the relation between the experimental and the calculated fatigue life (Paris model for long cracks) it was possible to show that different fatigue mechanisms are active for surface and internal crack initiations. Interestingly, the graph shows a linear relationship between the experimental and calculated fatigue life of internal fractures. This indicates that it is possible to model the internal fatigue fracture with the Paris law. Since the fatigue life of the internal fatigue crack initiations is determined by the growth of short fatigue cracks, the Paris law can be used to model the growth of short fatigue cracks in heavily drawn steel wires.
Through an extensive experimental investigation of the microstructure around inclusions it was observed that microcracks can be present around inclusions in drawn steel wires. Further it was observed that the microstructure around the inclusions was different from the bulk of the wire. Based on these observations and on a discrepancy between the fatigue data and the threshold value it was concluded that the actual defect size of an inclusion that is used to calculate ΔK is about 18% larger than the inclusion size itself. An adaptation of Murakami's formula is suggested.

To conclude the author would like to make a comment on the influence of residual stresses. The residual stresses of the wires were not measured for this study due to the very complex and time consuming nature of the residual stress measurements, especially when they are performed on small diameter wires. It is acknowledged that the residual stresses will have an influence on the fatigue properties. Nevertheless it is believed that they will have little influence on the fatigue crack initiation mechanisms. This can be explained by looking to the fatigue crack initiation area on a micro scale. Locally, the residual stresses should be added to the applied stress to calculate ΔK, which wouldn't change the fatigue mechanisms itself. It is however possible that due to a change in residual stresses the relative position of the ΔK value compared to the threshold value changes. In this way some defects can become critical while other defect that are located in another part of the wire will not influence the fatigue properties anymore. On the other hand, it is possible that residual stresses locally change the R value, which could change the crack growth mechanism from ΔK to K_{max} controlled and vice

versa. Further it is possible that the fatigue thresholds which are determined from internal fatigue crack initiations should be altered before applying them to surface crack initiations due to the difference in residual stresses between the surface and the bulk of drawn wires. For the reasons stated above the author would like to emphasize that the influence of residual stresses is acknowledged, but since the residual stresses are not known, they can not be taken into account yet.

9.2 Applicability of the results

Since a tire is a very complex composite material, it is not possible to make a direct link between the fatigue properties of steel cord filament (the heavily drawn steel wires that were investigated in this study) and the overall performance of a tire. The steel cord filaments are first twisted together to a cord. During the formation of the cord the wires are plastically deformed which could change their fatigue properties. The cords are then embedded in rubber to form a tire. It is important to realize that the fatigue properties of rubber embedded cords can be completely different from the fatigue properties of the individual filaments since other fatigue mechanisms can be active. First of all, the fatigue properties of the filaments itself can be changed due to the cord formation (plastic deformation) and the rubber embedment (vulcanization of the rubber, typically 10 minutes at 170 °C). Secondly, when the rubber penetration between the individual filaments is not perfect, a steel-steel contact is possible which can lead to fretting fatigue.
On the other hand one can say that, if one wants to obtain good fatigue properties of the rubber embedded cords, it is a necessary condition to have good fatigue properties of the individual filaments.

The knowledge on the different fatigue crack initiation mechanisms and their relation to the fatigue life is valuable information that can be used to improve the fatigue properties of heavily drawn steel wires. It indicates which parameters (for example defect size, inclusion size and the presence of chlorides) should be controlled in the wire drawing production process in order to obtain good fatigue properties of the individual wires.
For the wires investigated in this study, a predicting fatigue model is developed which can be used to estimate the total fatigue life of a wire based on the largest defect present in that wire. This is a powerful tool that can be used to calculate the maximum allowable defect size given a desired fatigue life. In practice this means that it is possible to define a maximum allowable inclusion size in the wire rod for a certain loading condition (applied stress and R value) and a desired fatigue life.

It is important to note that this information is only available for the wires investigated in this study, while in practice a lot of different wires are used. Therefore the author would like to suggest to determine the fatigue thresholds and the Paris constants for some other wires (with different diameters and strains) and to investigate all this data statistically. The author expects that the spread on the

fatigue thresholds will be limited and that, based on this data, it will be possible to derive a generally applicable maximum defect size for heavily drawn steel wires to obtain high cycle fatigue behavior, given a certain loading condition.

9.3 Recommendations for future work

Through this study knowledge is gained on the fatigue crack initiation and propagation mechanisms of steel cord filaments. To obtain a high output this research was performed in low cycle fatigue (high applied stresses which are significantly larger than the conventional fatigue limit). All critical factors were identified and explained. This knowledge is very useful but it does not cover the influence of microstructural parameters.
When looking at the final application the filaments are not loaded to such high stresses. The occurring stresses are always below the conventional fatigue limit ($\Delta\sigma_e$). Therefore short fatigue cracks have to grow from stress concentrations until the threshold value for crack growth ($\Delta K_{th,R}$) is reached. Since the growth of short fatigue cracks is a very slow process the fatigue life of the final application will be determined by them (high cycle fatigue). The growth of short fatigue cracks will strongly depend on local material properties [44,107,132]. Therefore it is very useful to study the influence of the microstructure on the fatigue properties.

Approach
Investigating the influence of the microstructure on the fatigue properties of heavily drawn steel cord filaments is proven to be a difficult and challenging task. Up to this moment no successful and relevant relation between both was found.
Since the microstructure is influenced by the wire drawing process parameters and the high cycle fatigue properties are influenced by the microstructure (full arrows in figure 9.1), it is possible to study the influence of microstructural parameters in an indirect way (dotted arrows in figure 9.1).

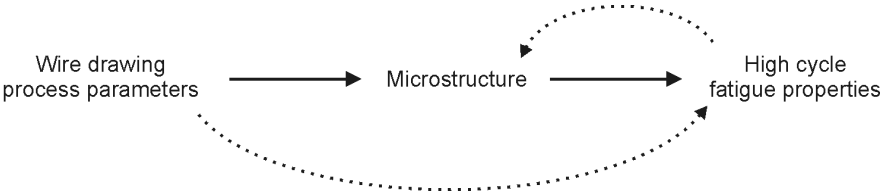

Figure 9.1: Relationship between wire drawing process parameters, the microstructure and the high cycle fatigue properties.

For industrial relevance and research efficiency it is suggested to investigate the relation between various wire drawing process parameters and the high cycle fatigue properties first. Only when a clear difference in fatigue life is observed the microstructure of the filament will be investigated in depth, searching for relevant microstructural parameters. This approach allows a quick generation of knowledge on which process parameters do alter the microstructure in such a way

that the fatigue properties of the final application will change. It is important to note that the microstructure will be investigated first on micro scale (0.1 - 10 μm) using the scanning electron microscope (SEM). It is known from literature that short fatigue cracks can get arrested by the strongest microstructural barrier [36,107,132,133].
In order to provide a high research output, transmission electron microscopy (TEM) observation will only be considered whenever the difference in fatigue life can not be explained by SEM observations or fractography. If necessary the TEM observations can be done in cooperation with Tsinghua University (Beijing).

Experimental details
To gain knowledge on both the influence of microstructural parameters and the fatigue properties of the application it is, as said before, necessary to study the growth of short fatigue cracks. This can easily be done by loading the filaments to a stress below the conventional fatigue limit. In this way, short fatigue cracks will have to grow until $\Delta K_{th,R}$ is reached. However it can be estimated from figure 4.26 (prospective SN curve) that when the filaments are loaded at or below the conventional fatigue limit, the fatigue life will be between 3.7E7 and 3.9E8 cycles. When a test frequency of 60 Hz is used the time necessary for one test to failure will be between 7 and 75 days.

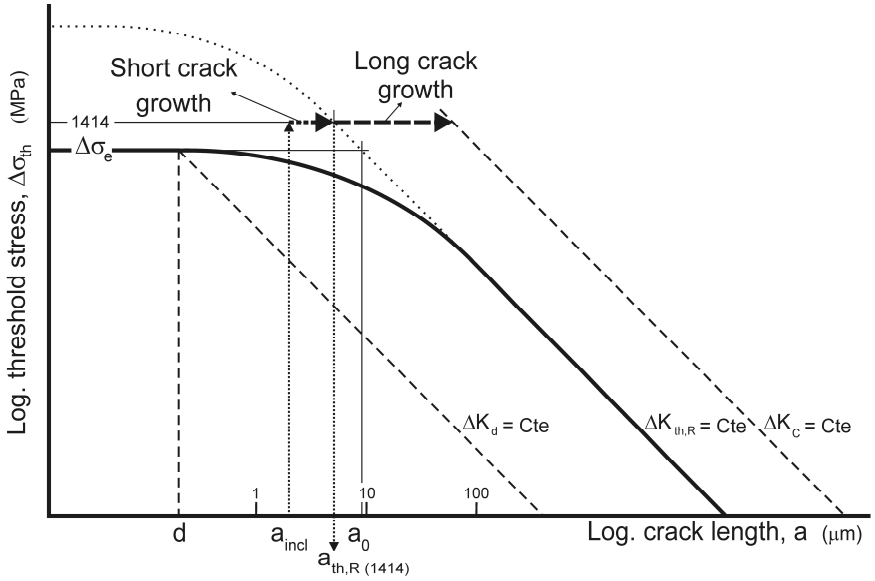

Figure 9.2: Kitagawa-Takahashi diagram.

To avoid these unacceptably long fatigue lives it is suggested to perform the fatigue tests at a stress level that is much higher than the conventional fatigue limit, for example at $\Delta\sigma$ = 1414 MPa, and investigate the fatigue fractures that initiated at internal inclusions. Figure 4.26 shows that the average fatigue life of

these internal fractures is about 1E7 cycles. For a test frequency of 60 Hz it will take less than 2 days to obtain an internal fatigue fracture.

The Kitagawa diagram in figure 9.2 shows that when the applied stress range is 1414 MPa and the fatigue crack initiates at an internal inclusion with a radius of 2 μm, short fatigue cracks will have to grow from a_{incl} (= 2 μm) until $a_{th,R(1414)}$ (= 5 μm, intersection with the line $\Delta K_{th,R}$). Although the crack path in the short crack growth regime is much smaller than in the long crack growth regime, it is calculated in paragraph 4.2.1.2 that for these internal crack initiations about 99% of the total fatigue life is spent in the short crack growth regime. Therefore the fatigue life is determined by the growth of short fatigue cracks. This means that it is possible to use a stress range that is significantly larger than the conventional fatigue limit to study the influence of microstructural parameters on the high cycle fatigue properties of steel cord filaments.
It is experimentally observed that more than 20% of all fatigue tests initiates at internal inclusions. All other fatigue fractures initiate at surface stress concentrations and have fatigue lives below 1E5 cycles. For a test frequency of 60 Hz this means that a surface crack initiation fails within 30 minutes. Therefore a high research output can be guaranteed with this approach.
If necessary following actions can be taken in order to increase the probably of internal fatigue crack initiations:

- Avoid the presence of chlorides (clean well and protect with a glue coating) to make sure that no environmentally assisted fatigue crack initiations can occur. Although it is not proven yet, it seems that it is best to use gas patenting in stead of chloride pickling.
- Use a high quality wire rod to minimize the chance of large surface inclusions.
- Corporate production technology should be used to make sure that no big surface defects are introduced due to the wire drawing process.
- Use a short gauge length to minimize the chance of having a large surface defect or surface inclusion present on the sample. It is expected that the microstructure is constant along the wire axis.

Expected outputs

- Knowledge on the influence of all relevant production process parameters (emphases on microstructural changes, not on the difference in surface stress concentration distributions) on the high cycle fatigue properties of steel cord filaments.
- Link between relevant microstructural parameters, the production process and the final fatigue properties. Knowledge on how the fatigue properties of the final application can be changed by changing the production process parameters.

Bibliography

[1] Ochiai M, Nishida S, Ohba H, Kawata H. Application of hypereutectoid steel for development of high strength steel wire. Tetsu-to-Hagane 1993;79:1101–7.

[2] ASM handbooks online, ASM international 14A (2005) 448-458.

[3] E. Siebel, Stahl und Eisen, 66-67 (11-12) (1947), 171.

[4] W.F. Hosford and R.M. Caddell, Metal forming mechanics and metallurgy, Prentice hall, Englewood Cliffs, NJ, USA (1983).

[5] G. Langford, Deformatioin of pearlite, Metallurgical transactions 8A (1977) 861.

[6] G. Sevillano, P. Van Houtte, E. Aernoudt, large strain work hardening and textures, Progress in Materials Science AQ25(2-4) 69-412 (1980).

[7] X. Zhang, A. Godfrey, N. Hansen, X. Huang, W. Liu, Q. Liu, Evolution of cementite morphology in pearlitic steel wire during wet wire drawing, Materials Characterization 61 (2010) 65-72.

[8] M. Zelin, Microstructure evolution in pearlitic steels during wire drawing, Acta Materialia 50 (2002) 4431–4447.

[9] Taniyama T. Sumitomo, 1999. Metals Ind.

[10] Zhou S, Shiflet GJ. Metall Trans 1992;23A:1259.

[11] C. Borchers, T. Al-Kassab, S. Goto, R. Kirchheim, Partially amorphous nanocomposite obtained from heavily deformed pearlitic steel, Materials Science and Engineering A 502 (2009) 131–138.

[12] T. Tarui, J. Takahashi, H. Tashiro, N. Marayuma, S. Nishida, Microstructure Control and Strengthening of High-carbon Steel Wires, Nippon steel technical report No. 91 January 2005.

[13] K. Hono, M. Ohnuma, M. Murayama, S. Nishida, A. Yoshie and T. Takahashi, Cementite decomposition in heavily drawn pearlitic steel wire, Scripta mater. 44 (2001) 977–983.

[14] M. H. Hong, W. T. Reynolds, T. Tarui and K. Hono, Atom Probe and Transmission Electron Microscopy Investigations of Heavily Drawn Pearlitic Steel Wire, Metallurgical and Materials Transactions A Vol 30 No 3 (1999) 717-727.

[15] W. J. Nam, C. M. Bae, S. J. Oh, S.J. Kwon, Effect of interlamellar spacing on cementite dissolution during wire drawing of pearlitic steel wires, Scripta mater. 42 (2000) 457–463.

[16] N. Maruyama, T. Tarui, H. Tashiro, Atom probe study on the ductility of drawn pearlitic steels, Scripta Materialia 46 (2002) 599–603.

[17] V.G. Gavriljuk, Decomposition of cementite in pearlitic steel due to plastic Deformation, Materials Science and Engineering A345 (2003) 81-89.

[18] M. Umemoto, Y. Todaka, K. Tsuchiya, Mechanical properties of cementite and fabrication of artificial pearlite, Materials science forum 426-432 (2003) 859-864.

[19] A. Taniyama, T. Takayama, M. Arai, T. Hamada, Structure analysis of ferrite in deformed pearlitic steel by means of X-ray diffraction method with synchrotron radiation, Scripta Materialia 51 (2004) 53–58.

[20] T. Tarui, J. Takahashi, H. Tashiro, N. Marayuma, S. Nishida, Microstructure Control and Strengthening of High-carbon Steel Wires, Nippon steel technical report No. 91 January 2005.

[21] X. Sauvage, X. Quelennec, J.J. Malandain, P. Pareige, Nanostructure of a cold drawn tempered martensitic steel, Scripta Materialia 54 (2006) 1099–1103.

[22] Read HG, Reynolds WT, Hono K, Tarui T. APFIM and TEM studies of drawn pearlitic wire. Scripta Mater 1997;37:1221–30.

[23] W.J. Nam, Ch.M. Bae, S.J. Oh, S. Kwon, Effect of interlamellar spacing on cementite dissolution during wire drawing of pearlitic steel wires, Scripta Mater. 42 (2000) 457-463.

[24] J. Takahashi, T. Tarui, K. Kawakami, Three-dimensional atomprobe analysis of heavily drawn steel wires by probing perpendicular to the pearlitic lamellae, Ultramicroscopy 109 (2009) 193–199.

[25] V.G. Gavriljuk, Comment on “Effect of interlamellar spacing on cementite dissolution during wire drawing of pearlitic steel wires”, Scripta Materialia 45 (2001) 1469–1472.

[26] Y.S. Yang, J.G. Bae, C.G. Park, Nanostructure and mechanical properties of heavily cold-drawn steel wires, Materials Science and Engineering A 508 (2009) 148–155.

[27] K. Shimizu, N. Kawabe. Fracture mechanics aspects of delamination occurrence in high-carbon steel wire. In: Proc. of 71st Wire & Cable Technical Symposium, Guilford, USA: The Wire Assoc Intl, p. 35 (2001).
[28] Montesin T, Heizmann JJ, Abdellaoui A, Pelletier JB. Wire J Int 4 (1993) 163.
[29] K. Van Acker, J. Root, P. Van Houtte, E. Aernoudt, Neutron diffraction measurements of the residual stress in the cementite and ferrite phases of cold drawn steel wires, Acta Mater. Vol. 44, No. 10 (1996) 4039-4049.
[30] M. ELICES, Influence of residual stresses in the performance of cold-drawn pearlitic wires, Journal of Materials Science 39 (2004) 3889 – 3899.
[31] K. Katagiri, T. Sato, K. Kasaba, S . Sasaki, H. Tashiro, ibid. 22 (1999) 753.
[32] F. Yang, J.Q. Jiang, F. Fang, Y. Wang, C. Ma, Rapid determination of residual stress profiles in ferrite phase of cold drawn wire by XRD and layer removal technique, Materials science and engineering A 486 (2008) 455-460.
[33] F. Yang, J.Q. Jiang, F. Fang, Y. Wang, C. Ma, F. Fang, K.L. Zhao, W. Li, residual stress in pearlitic steel rods during progressively cold drawing measured by X-ray diffraction, Materials letters 62 (2008) 2219-2221.
[34] S. Suresh, Fatigue of materials, Cambridge University press, 1998, 2nd edition, Cambridge, ISBN 0-521-57847-7.
[35] J. Schijve, Fatigue of structures and materials, Springer, 2009, 2nd edition, Berlin, ISBN 978-1-4020-6807-2.
[36] K.J. Miller, W.J. O'dnell, The fatigue limit and its elimination, Fatigue Fract. Engng Mater. Struct. 22 (1999) 545-557.
[37] C. Bathias, There is no infinite fatigue life in metallic materials, Fatigue Fract. Engng Mater. Struct. 22 (1999) 559-565.
[38] Y. Murakami, T. Nomoto, T. Ueda, Factors influencing the mechanism of superlong fatigue failures in steels, Fatigue Fract. Engng Mater. Struct. 22 (1999) 581-590.
[39] K . Shiozawa, L . Lu, S. Ishihara, S –N curve characteristics and subsurface crack initiation behaviour in ultra-long life fatigue of a high carbon-chromium bearing steel, Fatigue Fract. Engng Mater. Struct. 24 (2001) 781–790.
[40] K. Shiozawa and L. Lu, Very high cycle fatigue behaviour of shop-peened high-carbon-chromium bearing steel, Fatigue Fract Engng Mater Struct 25 (2002) 813-822.
[41] K. Shiozawa, Y. Morii, S. Nishino, L. Lu, Subsurface crack initiation and propagation mechanism in high-strength steel in a very high cycle fatigue regime, International Journal of Fatigue 28 (2006) 1521–1532.
[42] T. Sakai, B. Lian, M. Takeda, K. Shiozawa, N. Oguma, Y. Oshi, et al., Charactaristic S-N property of high carbon chromium bearing steel under axial loading in long life fatigue, Proceedings of the internat. Conference fatigue in very high cycle regime (2001) 51-57.
[43] K. Tanaka and Y. Akiniwa, Fatigue crack propagation behaviour derived from S-N data in very high cycle regime, Fatigue Fracture Engineering Material Structures 25 (2002) 775 – 784.
[44] K. Sadananda, A.K. Vasudevan , N. Phan, Analysis of endurance limits under very high cycle fatigue using a unified damage approach, International Journal of Fatigue 29 (2007) 2060–2071.
[45] Murakami Y., Kodama S., Konuma S. Quantitative evaluation of non-metallic inclusions on fatigue strength of high strength steels. I: Basic fatigue mechanism and evaluation of correlation between the fatigue fracture stress and the size and location of non-metallic inclusions. Int
J Fatigue 11 (1989) 291-98.
[46] Y. Akiniwa, N. Miyamote, H. Tsuru, K. Tanaka, Notch effect on fatigue strength reduction of bearing steel in the very high cycle regime, International Journal of Fatigue 28, pp. 1555–1565, 2006.
[47] Pyttel B et al. Very high cycle fatigue – Is there a fatigue limit? Int J Fatigue (2010), doi:10.1016/j.ijfatigue.2010.05.009.
[48] L. Lawson, E.Y. Chen, M. Meshii, Near-threshold fatigue: a review, International Journal of fatigue 21 (1999) S15-S34.
[49] Bulloch JH. The influence of mean stress or R-ratio on the fatigue crack threshold characteristics of steels - a review. Int J Pressure Vessels Piping;47 (1991) 263–92.

[50] Barsom J. Fatigue behavior of pressure-vessel steels. Welding Research Council Bulletin Number 194, 1974.
[51] Klesnil M, Lucas P. Effect of stress cycle asymmetry on fatigue crack growth. Mater Sci Eng 1972;9:231–40.
[52] Taylor D. Fatigue thresholds. London: Butterworth, FIRST EDITION, 1990.
[53] Christensen RH. Fatigue crack growth affected by metal fragments wedged between opening-closing crack surfaces. Appl Mater Res 2 (1963) 207–10.
[54] Elber W. Fatigue crack closure under cyclic tension. Eng Fract Mech 1970;2:37–45.
[55] Elber W. The significance of fatigue crack closure. In: Damage tolerance in aircraft structures, ASTM STP-486. Philadelphia (PA, USA): American Society for Testing and Materials, 1971: 230–42.
[56] Ritchie RO. Near threshold fatigue crack propagation in steels, review 245. Int Metals Rev 5–6 (1979) 205–30.
[57] Schmidt RA, Paris P. Threshold for fatigue crack propagation and the effects of load ratio and frequency. Progress in flaw growth and fracture toughness testing, ASTM STP 536. Philadelphia (PA, USA): American Society for Testing and Materials, 1973: 79–94.
[58] Döker H, Peters M. Fatigue threshold dependence on material, environment and microstructure. In: Beevers C, editor. Fatigue 84, 2nd International Conference on Fatigue and Fatigue Thresholds. Cradley Heath, Warley, UK: EMAS, 1984:275–85.
[59] Marci G. A fatigue crack growth threshold. Eng Fract Mech 41 (1992) 367–85.
[60] Vasudevan AK, Sadananda K, Louat N. Two critical stress intensities for threshold crack propagation. Scr Metall 28 (1993) 65–70.
[61] Vasudevan AK, Sadananda K. Fatigue crack growth in advanced materials. In: Lütjering G, Nowack H, editors. Fatigue '96: Proceedings of the 6th International Conference on Fatigue and Fatigue Thresholds. New York: Pergamon Press, 1996:473–8.
[62] Kitagawa H, Takahashi S. Symposium on second international conference on mechanical behavior of materials. Metals Park: American Society of Metals; 1976. p. 627–31.
[63] M.H. El Haddad, T.H. Topper, K.N. Smith, prediction of non propagating cracks, Engineering fracture Mechanics Vol 11 (1979) 573-584.
[64] K.J. Miller, The short crack problem, fatigue of engineering materials and structures, vol 5 no 3 (1982) 223-232.
[65] M.D. Chapetti, Fatigue propagation threshold of short cracks under constant amplitude loading, International Journal of Fatigue 25 (2003) 1319–1326.
[66] Zheng X, Hirt MA. Eng Fract Mech 18(5) (1983) 965–73.
[67] Akiniwa Y, Tanaka K, Kinefuchi M. J Soc Mater Sci Jpn 38(434) (1989) 1275–81.
[68] Sadananda K, Vasudevan AK. Acta Mater 52 (2004) 4239–49.
[69] K. Sadananda, A.K. Vasudevan, N. Phan, Analysis of endurance limits under very high cycle fatigue using a unified damage approach, International Journal of Fatigue 29 (2007) 2060–2.
[70] Usami S. In: Blacklund I, Bloom A, Beevers CJ, editors. Symposium on fatigue threshold. Stockholm, Sweden: EMAS; 1981. p. 205–38.
[71] Tanaka K, Nakai Y. Fatigue Eng Mater Struct 6 (1985) 315.
[72] K. Sadananda, A.K. Vasudevan, Fatigue crack growth mechanisms in steels, International Journal of Fatigue 25 (2003) 899–914.
[73] Pippan R. Mater Sci Engng A138 (1991) 1–13.
[74] Taira S, Tanaka K, Hoshina M. ASTM STP 675 (1979) 135.
[75] Liaw PK, Saxena A, Swaminathan VP, Shih TT. In: Fatigue crack growth thresholds concept. Warrendale PA: AIME; 1984. p. 205–23.
[76] S; Matsuoka, E. Takeuchi, S. Nishijima, AJ. McEvily, Metall Trans 20A (1989) 741–9.
[77] A.K. Vasudevan, K. Sadananda, R.L. Holtz, Analysis of vacuum fatigue crack growth results and its implications, International Journal of Fatigue 27 (2005) 1519–1529.
[78] I. Verpoest, E. Aernoudt, A. Deruyttere, M. De Bondt, The fatigue threshold, surface condition and fatigue limit of steel wire, International Journal of Fatigue 7 No 4 (1985) 199-214.
[79] J. Petit, C. Sarrazin-Baudoux and F. Lorenzi, Fatigue crack propagation in thin wires of ultra high strength steels, Procedia Engineering 2 (2010) 2317–2326.
[80] J. Llorca, V. Sanchez-Galvez, Fatigue threshold determination in high strength cold drawn eutectoid steels wires, Engineering Fracture Mechanics 26, No 6 (1987) 869-882.

[81] J. Llorca, V. Sanchez-Galvez, Fatigue limit and fatigue life prediction in high strength cold drawn eutectoid steel wires, Fatigue fracture and engineering materials 12, No 1 (1989) 31-45.
[82] S. Beretta, S. Matteazzi, Short crack propagation in eutectoid steel wires, International Journal of Fatigue 18, No 7 (1996) 451-456.
[83] Y.S. Yang, J.G. Bae, C.G. Park, Improvement of the bending fatigue resistance of the hyper-eutectoid steel wires used for tire cords by a post-processing annealing, Materials Science and Engineering A 488 (2008) 554–561.
[84] Suresh S. Fatigue of materials. Cambridge, MA: Cambridge University Press; 1998.
[85] Louat N, Sadananda K, Vasudevan AK, Duesbery MS. Metall Trans A 1993; 2225.
[86] Weertman J. Phys Status Solidi B 172 (1992) 27.
[87] Vasudevan AK, Sadananda K, Louat N. Mater Sci Eng A 188 (1994) 1.
[88] Vasudevan AK, Sadananda K, Holtz RL. Analysis of vacuum fatigue crack growth results and its applications. Int J Fatigue 27 (2005) 1519-29.
[89] S. Chanel, N. Pebere, An investigation on the corrosion of brass-coated steel cords for tyres by electrochemical techniques, Corrosion Science 43 (2001) 413-427.
[90] J. Toribio, O.M. Lancha, Effect of cold drawing on environmentally assisted cracking of cold-drawn steel, Journal of materials science 31 (1996) 6015-6024.
[91] J. Toribio, E. Ovejero, Effect of Cold Drawing on Microstructure and Corrosion Performance of High-Strength Steel, Mechanics of Time-Dependent Materials 1: 307-319, Kluwer Academic Publishers, 1998.
[92] J. Toribio, E. Ovejero, Micromechanics of hydrogen assisted cracking in progressively drawn steels, Scripta Materialia, vol. 40, No. 8 (1999) 943 – 948.
[93] J. Toribio, E. Ovejero, Corrosion assisted cracking in progressively drawn pearlitic steels: a materials science approach, Materials Science, Vol. 35, No. 6 (1999) 802-810.
[94] J. Toribio, E. Ovejero, Microstructure-based modelling of hydrogen assisted cracking in pearlitic steels, Materials Science and Engineering A319-321 (2001) 540-543.
[95] J. Toribio, FJ. Ayaso, E. Ovejero, Evolution of hydrogen-assisted micro-damage in progressively drawn pearlitic steel, Materials Letters 58 (2004) 2541– 2544.
[96] J. Toribio, E. Ovejero, Failure analysis of cold drawn prestressing steel wires subjected to stress corrosion cracking, Engineering failure analysis 12 (2005) 654-661.
[97] J. Toribio, E. Ovejero, Role of crack tip blunting in stress corrosion cracking of high-strength steels, International journal of fracture 98 (1999) L31-L36.
[98] G. Murtaza, R. Akid, Corrosion fatigue short crack growth behaviour in a high strength steel, Int. J. Fatigue, Vol. 18, No. 8 (1996) 557-566.
[99] R. Akid, I.M. Dmytrakh, J. Gonzalez-Sanchez, Fatigue damage accumulation: the role of corrosion on the early stages of crack development, Corrosion Engineering, Science and Technology, Vol. 41, No. 4 (2006) 328-335.
[100] M. Wang, E. Akiyama, K. Tsuzaki, Effect of hydrogen on the fracture behavior of high strength steel during slow strain rate test, Corrosion Science 49 (2007) 4081–4097.
[101] T. Zakroczymski, A. Glowacka, W. Swiatnicki, Corros. Sci. 47 (2005) 1403.
[102] H.M. Westergaard, Bearing pressures and cracks, Journal of applied Mechanics 6 (1939) A49-A53.
[103] Irwin, G.R., Kies, J.A. and Smith, H.L., Fracture strengths relative to onset and arrest of crack propagation, Proc. Am. Soc. Test. Mater., 58 (1958) 640-657.
[104] P.C. Paris, M.P. Gomez, and W.E. Anderson. A rational analytic theory of fatigue. The Trend in Engineering 13 (1961) 9-14.
[105] Q.Y. Wang et al., "Gigacycle fatigue of ferrous alloys", Fatigue fract. Eng. Mater. Struct. 22 (1999) 667-672.
[106] Q.Y. Wang et al., "Technical note high cycle fatigue crack initiation and propagation behaviour of high strength spring steel wires", Fatigue fract. Eng. Mater. Struct. 22 (1999) 673-677.
[107] M.D. Chapetti, T. Tagawa, T. Miyata, Ultra-long cycle fatigue of high-strength carbon steels part I: review and analysis of the mechanism of failure, Materials Science and Engineering A356 (2003) 227-235.
[108] M. Nakajima, N. Kimiya, H. Itoga, K. Tokayi, H.N. Ko, Experimental estimation of crack initiation lives and fatigue limit in subsurface fracture of a high carbon chromium steel, International Journal of Fatigue 28 (2006) 1540–1546.

[109] K. Sadananda, S. Sarkar, D. Kujawski, A.K. Vasudevan, A two-parameter analysis of S–N fatigue life using Δσ and σmax, International Journal of Fatigue 31 (2009) 1648–1659.
[110] I. Verpoest, The fatigue threshold, the surface condition and the fatigue limit of steel wire, 1984, ISBN 90-6569-674-1.
[111] H. Delrue (2001). Invloed van de trekparameters op microstructuur en mechanische eigenschappen van perlietische staaldraad. PhD thesis, Katholieke Universiteit Leuven, Departement Metaalkunde en Toegepaste Materiaalkunde (in Dutch).
[112] P. Shigolev (1974). Electrolytic and chemical polishing of metals. Tel-Aviv: Freund publ. house.
[113] T. Antretter, F.D. Fischer, The stress state around two spatially arranged ellipsoidal inclusions – A case study for high-speed tool steel. Comput Mat Sci 7 (1996) 247-52.
[114] Y. Murakami, S. Kodama, S. Konuma, Quantitative evaluation of non-metallic inclusions on fatigue strength of high strength steels. I: Basic fatigue mechanism and evaluation of correlation between the fatigue fracture stress and the size and location of non-metallic inclusions. Int J Fatigue 11 (1989) 291-98.
[115] Y. Oshi. T. Matsumura, K. Masaki, S. Yoshida, High-cycle rotating bending fatigue property in very long-life regime of high-strength steels. Fatigue Fract Engng Mater Struc 25 (2002) 823-30.
[116] Q.Y Wang., C. Bathias, N. Kawagoishi, Q. Chen, Effect of inclusion on subsurface crack initiation and gigacycle fatigue strength. Int J Fatigue 24 (2002) 1269–74.
[117] K. Shiozawa, T. Hasegawa, Y. Kashiwagi, L. Lu. Very high cycle fatigue properties of bearing steel under axial loading condition. Int J Fatigue 31 (2009) 880-8.
[118] K. Shiozawa, M. Murai, Y. Shimatani, T. Yoshimoto, Transition of fatigue failure mode of Ni-Cr-Mo low alloy steel in very high cycle regime. Int J Fatigue 32 (2010) 541-50.
[119] Z.G. Yang, S.X. Li, Y.D. Li, Y.B. Liu, W.J. Hui, Y.Q. Weng, Relationship among fatigue life, inclusion size and hydrogen concentration for high-strength steel in the VHCF regime. Mater Sci Eng A527 (2010) 559-64.
[120] W. Li, T. Sakai, Q. Li, L.T. Lu, P. Wang, Reliability evaluation on very high cycle fatigue properties of GCr15 bearing steel. Int J Fatigue 2010; doi:10.1016/j.ijfatigue.2009.12.008.
[121] D.W Richerson. Modern ceramic engineering: properties, processing and use in design. 2nd ed. New York: Dekker; 1992
[122] D.J. Green. An introduction to the mechanical properties of ceramics. Cambridge: Cambridge University press; 1998
[123] D. Munz, T. Fett, Ceramics: mechanical properties, failure behaviour, materials selection. Berlin: Springer; 1999
[124] G.M.D Almaraz, Prediction of very high cycle fatigue failure for high strength steels, based on the inclusion geometrical properties. Mech Mater 40 (2008) 636-40.
[125] A. Ohta, M. Kosuge, E. Sasaki, Fatigue crack closure over the range of stress ratios from -1 to 0.8 down to stress intensity threshold level in HT80 steels and SUS 304 stainless steel. Int J Fract 14 (1978) 251-64.
[126] DL. Chen, B. Weiss, R. Stickler, Contribution of cyclic loading portion below the opening load to fatigue crack growth. Mater Sci Eng A208 (1996) 181-7.
[127] JK. Donald, Introducing the compliance ratio concept for determining effective stress intensity. Int J Fatigue 19-1 (1997) S191-5.
[128] S. Dinda, D. kujawski, Correlation and prediction of fatigue crack growth for different R-ratios using Kmax and ΔK parameters. Eng Fract Mech 71 (2004) 1779-90.
[129] AH. Noroozi, G. Glinka, S. Lambert, A study of the stress ratio effects on the fatigue crack growth using the unified two-parameter fatigue crack growth driving force. Int J Fatigue 29 (2007) 1616-33.
[130] AK. Vasudevan, K. Sadananda, Application of unified fatigue damage approach to compression-tension region. Int J Fatigue 21 (1999) S263-73.
[131] AK. Vasudevan, K. Sadananda, Classification of environmentally assisted fatigue crack growth behavior. Int J Fatigue 31 (2009) 1696-708.
[132] O. Düber et al., Experimental characterization and two-dimensional simulation of short-crack propagation in an austenitic-ferritic duplex steel, International Journal of Fatigue 28 (2006) 983-992.

[133] Y. Murakami, T. Nomoto, T. Ueda, Y. Murakami, Fatigue, On the mechanism of fatigue failure in the superlong life regime (N>107 cycles). Part II: influence of hydrogen trapped by inclusions, Fract. Eng. Mater. Struct. 23 (2000) 903-910.

List of publications

Book chapters, internationally recognised scientific publisher

Lambrighs, K., Wevers, M. (2009). Applications of acoustic emission for SHM: A review. In: Boller C., Fujino Y. (Eds.), *Encyclopedia of Structural Health Monitoring* (pp. 289-301). UK: John Wiley & Sons, Ltd.

Papers at an internationally published journal

Lambrighs, K., Verpoest, I., Verlinden, B., Wevers, M. Fatigue properties of cold drawn steel wires: crack initiation and growth mechanisms, submitted to Fatigue & Fracture of Engineering Materials & Structures (first submission august 2009).

Lambrighs, K., Verpoest, I., Verlinden, B., Wevers, M. Influence of non-metallic inclusions on the fatigue properties of heavily cold drawn wires, Procedia Engineering 2 (2010) 173–181. *Presented at "10th International Fatigue Congress. Prague, Czech Republic, 6-11 June 2010"*.

Lambrighs, K., Verpoest, I., Verlinden, B., Wevers, M. Influence of the load ratio on the threshold stress intensity factor range for heavily drawn steel wires, submitted to Engineering Failure Analysis (august 2010). *Presented at "Fourth International Conference on Engineering Failure Analysis, Churchill College, Cambridge, UK, 4–7 July 2010"*.